Catalytic Steam Reformer Tubes Non-destructive Inspection Technology Investigation and Advancement

A dissertation presented in partial fulfillment of the

Requirements for the degree of

Doctor of Philosophy

in

Engineering

at Massey University, Manawatu Campus

New Zealand.

Morio Fukuoka

Dec 2018

Abstract

Catalytic Steam reforming is a chemical synthesis process used in the production of hydrogen by mixing hydrocarbon with steam in the presence of a metal-based catalyst. This is achieved in a steam reformer plant where the mixture of gases is elevated to high pressure and temperature through a continuous process for efficient mass production of syngas to meet the global hydrogen demand. One of the challenges in operating a steam reformer plant is monitoring and maintaining the tubular reactors (Reformer tube). Under the severe service conditions the tubes a subjected to various degradation mechanism which ultimately determine the service life. With the tubes accounting to over 20% of the capital cost of a reformer plant, it is of great significance to maximise the service life of each tubes, which has been the motivation to the advancement in metallurgy and NDT technology around reformer tubes from the introduction of Catalytic Steam reforming in the early 20th century.

Under the influence of long-term exposure of mechanical stressing and elevated temperature, reformer tube is subjected to a material degrading phenomenon call creep deformation. In 1952, F.R. Larson and J. Miller devised the Larson-Miller Parameter which predicts the lifetime of a material based on service temperature and stress-rupture time and for decades this method was used design and managed reformer tubes on a time-based strategy of 10,000 service hour. However, case studies have time and time shown premature rupture of reformer tube causing unexpected downtime resulting in significant loss in production and asset. Hence engineers and researchers have worked on a more direct method of assessing the remaining service life of reformer tubes.

Inline pipe inspection is a hot area of research in robotics and automation. Eddy current, laser profilometry, ultrasonic and infrared thermography is the four technology that is currently dominating the Reformer industry, of which laser profilometry assessment being the only method capable of early stage creep detection. While other fields of pipe inspection have advanced and industrially applied over past decades, it is the author's opinion that NDT technology for reformer tube is outdated with areas of innovation. The aim of this research is to investigate an alternative solution to overcome the challenges and limited faced in modern systems and contribute to the advancement of NDT of Catalytic Steam reformer tubes.

Presented in this dissertation is a new framework for an autonomous Reformer Tube inspection system, which incorporates a number of innovative elements for improved creep

damage assessment. The program for this work is comprised of three studies. In the first study, the challenges around process profilometry dataset is demonstrated, the limitation in the available methods is discussed, and the impacts in regards to detection creep deformation is identified. Based on the finding, a three-stage creep detection algorithm (CDA) is derived, offering a dynamic solution to distinguish two modes of isotropic and anisotropic creep deformation. The system is experimentally assessed using a set of profilometry measurements collected from retire reformer tube.

In the second study, a novel method for tracking a motion of an object moving inside a reformer tube is devised. Literature study showed that conventional profilometry system suffers from measurement uncertainty cause from an uncontrolled rotation of measurement instruction during an inspection. Because location information gives valuable insight as to the performance of the plant, the long-range optic solution is conceptualised, based on polarising filters and Malus Law, to overcome these limitations. In this research, a proof of concept experiment is conducted to evaluate and justify the conceptual method through the development of a working prototype. This novel technique is named Optical Position Tracking (OPT) system.

Presented in the final study is an autonomous reformer tube inspection system developed on the basis of the results and finding in the first portion of the research. The contribution of this research is demonstrated with a working prototype justifying the practicality of CDA and the OPT system. The design incorporates wireless communication, modular design, and modern semiconductor sensing technology. In conclusion, this research met the first milestone for an ongoing research to progress the NTD industry

Acknowledgement

I would like to thank my supervisors and colleagues at the School of Engineering and Advanced Technology , Massey University, for providing the opportunity to conduct this research. It was a privilege to work with such professional, highly creative, and solution-oriented team in both academic and technical staffs.

Sincere thanks to my wife and three kids for the continuous love, patient, and support you gave throughout the years in conducting this research.

And foremost, I must express my very profound gratitude to my parents who've supported my passion and decisions through love and wisdom throughout the years of conducting and writing this thesis. This accomplishment would not have been possible without them, and for that I would like to dedicate this work to them.

Thank you to all.

Table of contents

List of figures

List of Table

1 Introduction

1.1 Background

In-situ condition monitoring of Reformer Tube plays a critical role in the petroleum industry providing a mean of evaluating the key components of a reformer plant under the operational condition. In the last five-decade, research has advanced the field of non-destructive testing (NDT) of such pressure vessels, making a major contribution towards the advancement of modern reforming technology for a safer and more economical system. Where traditional reformer tube has been managed on an ineffective time-based strategy, NDT has enabled plant operators to gain an insight into the plant operation through condition based methodology for a more economical and reliable management scheme.

Catalytic steam reforming (CSR) is a process of breaking down high-level hydrocarbon in the presence of steam into hydrogen and carbon monoxide gas, commonly referred to as syngas. Syngas is used as a feedstock for production of other high-value products such as ammonia and methanol. With the use of Methanol-to-gasoline (MTG) process methanol can also be further synthesized into gasoline, contributes to the global automotive industry [1]. CSR is correspondingly the most common large-scale process for mass production of high purity hydrogen. Hydrogen having the highest combustion energy release per unit of weight of any commonly occurring material, it is fed into the world energy matrix to satisfy the high demand of energy generation. One of the most recognized example of this being the Fuel Cell technology for 'zero' emission solution for transportation. While hydrogen has been used extensively historically in the industry as a coolant product, rocket fuel, metallurgical application, etc. [2], research is continually being conducted in academia and industry for improving energy harvesting application.

There are various kinds of hydrocarbons used as feedstock for CSR, such as naphthas and residual refinery gas, depended on the availability [3], but by far natural gas is considered to be the most rational raw material for CSR. Natural gas is made up of over 80% methane and found abundantly in nature reserves, associated or not with petroleum. According to work by L.S. Neiva and L. Gama [4], interest in natural gas is directly related to the replacement of fossil fuel. With CSR accounting for over 50% of the global processes of conversion of natural gas for hydrogen production, and over 90% in countries such as the US, it is considered one of the most important technology for inserting natural gas into the world

energy matrix. As the world trend continuously shifts towards a cleaner and sustainable energy source, CSR of natural gas will continue to attract industry and researchers' interest.

The process of CSR is as follows. A mixture of steam and hydrocarbon is fed into a radiant tube (commonly referred to as primary reformer or reformer tube) which is filled with nickel metal catalyst. With the use of external gas burners, the reformer tube along with the feedstock and catalyst is heated to 800-1000°C and the internal gas pressure is elevated to 10bars. This activates the highly endothermic reforming reaction which breaks down the hydrocarbon into Syngas. Syngas is then extracted out the bottom section of the tube (reducer) and gathered into a collector manifold for further processing. For the benefit of thermal efficiency, reformer tubes are installed inside large-scale furnaces (Reformer Furnace) which is internally coated with a radiant material. In a large plant, over 500 reformer tubes of 10-15m in length with 80-150mm internal bore are vertically mounted inside a single furnace, with over 60 burners located on the furnace ceiling, producing over 2600 tons of syngas per day. Reformer tubes are constructed out of heat resistance HP40-mod stainless-steel alloy which accounts for over 50% of the plant cost in both material and maintenance. Because the service parameters of the furnace has direct influence on the efficiency of the plant production and the equipment service life, it is of the business best interest to understand the true condition of the plant during operation.

Reformer tube is designed with an intended minimum service life of 100,000hr, equating to approximately 11 years of operation. With numerous design discipline to resistance various mechanical wear during operation, the ultimate service life is predominately determined by creep damage. Creep is a time dependent gradual degrading of material commonly characteristic by the Larson and Miller parameter (LMP) [5]. Over exposure to the severe reforming environment will ultimately result in a rupture along the length of the reformer tube wall, a phenomenon known as creep rupture. The rate of creep damage is dependent on the operating temperature and the hoop stress caused by the internal gas pressure. Due to the exponential correlation between these parameters, small variation in the operation conditions can greatly influence the service life of the reformer tubes.

In-service failure of reformer tube is very hazardous and expense, and is considered to be a catastrophic event. A sudden rapture in the tube wall can release high pressure gas which will propagate pressure waves through the furnace, damaging the neighboring tubes and surround furnace structure. A case study by M. Rogers [6] present records of human operators being injured from such event as metal debris piercing through the furnace roof and launched in

trajectory to the neighboring plant. While the re-tubing cost of single reformer tube can cost over $20,000USD, the production lost due to unplanned downtime is of more concern. To this, design and plant level inspection for safety precaution is of significant importance for reforming natural gas in fertilizer and petrochemical industries.

1.1.1 Reformer Tube Inspection Technology

Inspection and examination of material property are divided into two categories; destructive (DT) and non-destructive testing (NDT). DT as the name suggests use destructive methods to quantify the mechanical property of a sample, leaving the specimen unfit for service after the inspection. This method is generally considered to be the more accurate then NDT and finds its niche in offsite, laboratory environment. For the application of Reformer Tube inspection, DT is used by researchers for studying material degrading phenomenon and failure mechanism to further the understanding of reforming technology. Traditionally, metallographic examination technique is used to study the microstructural changes resulted from creep damage in the reformer tube wall under long-term service at elevated temperature, such as in work by J.labanowski [7]. Correspondingly, in more modern work by M. Szkodo [8] the same technique is used to study the mechanism of metal dusting corrosion phenomenon. In the study by A.A. Wahab [9] a combination of electron microscopy, energy dispersive spectroscopy and other optical microscopy and x-ray inspection, along with computing tomography techniques are used to reconstruct a 3D model of creep void in ex-service reformer tube as shown in Figure 1-1.

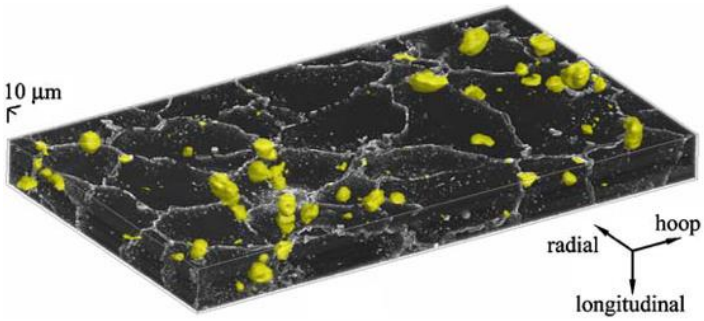

Figure 1-1: 3D reconstruction of retired reformer tube wall with austenite shown in black, voids in yellow, and precipitates in gray [9]

One of the common and considerable limitation of DT for reformer tube health monitoring is the destructive nature of the inspection method. According to R.D. Roberts [10], the cost for single reformer cost approximately $20,000USD. Because multiple samples must be taken to accurately evaluate a furnace of 500 tubes, the cost could easily accumulate to hundreds of thousands of dollars while the quality of the resulting data being greatly subjective to the

sampling method, sample location, etc. On top of this, there is also the cost of re-tubing, transports, and labor for the preparation of the examination which also must be considered. While DT is the most accurate and reliable inspection method for detecting creep damage, implementation of DT for the entire batch of reformer tube for any mass production plant is impractical and very uneconomical.

The second limitation of DT for reformer tube health monitoring is the time required in performing the assessment. Relatively speaking, DT is a very slow process requiring a lot of preparation and examination time. For all metallographic inspection, samples must first be removed and transported to the laboratory, segments extracted from selected areas of the tube, and further samples must be grinded, polished, etched and many other steps are necessary for acquiring an accurate result. According to the literature from Quest Integrity Group [11], around $250,000USD is lost for every 24hr of reformer plant downtime due to production loss. To this, many of the DT such as metallographic and microscopy examination for in-service reformer tube health monitoring is not viable. In a similar way, radiography inspection is not preferable due to low productivity (time to carry out the procedure) and safety related issues [12].

From the reason stated in the leading passage, reformer plant owners and operators generally prefer the practice of Non-destructive examination method for an in-situ examination of the reformer tubes. There are several inspection methods used for in-situ evaluation of creep strain, among them Ultrasonic, Eddy Current and Laser profilometry being the three most recognized approach.

Ultrasonic technique measures creep damage by using the acoustic property of the tube material. A controlled beam of ultrasound is passed through the full thickness of the tube wall, and the attenuation of the signal is measured to determine the amount of internal creep void, micro cracks, and macro cracks. The advantage of this technique is that it can detect mild initial stage of creep that is not detectable by radiography [13]. Also, as the system is usually used in external systems, the inspection can be conducted without the need for catalyst unloading.

Eddy current testing similarly is an effective surface inspection technique to detecting later stage creep damage in reformer tubes. Electromagnetic induction is used to measure the materials conductivity and magnetic permeability properties to characterize the extinct of creep damage in the tube wall. In theory, any defects in the material such as cracks, pitting,

wall loss or other discontinuities will disrupt the flow of the eddy currents and be detected by the instrumentation [14].

Laser profilometery uses a combination of vision and laser technology to directly measure the creep strain via diametrical measurement. Using a rotating head at 1800rpm the laser is used to mark the internal wall of the tube and pixel level vision analysis is used to measure the wall distribution. Laser NDT technology is capable of inspecting one hundred percent of the tube's interior surface and can gather more than two million data readings on a 50-foot (15m) long tube [15].

There are various advantages and disadvantages in each of the NDT techniques, as discussed further in chapter 2. There are many documents comparing the various inspection technologies, but there is mixed thought as to the effectiveness of each methodology depending on the author [14, 16]. However, a study performed by one of the world's largest petrochemical manufacturers was able to compare the different inspection techniques based on historical data, destructive testing, and field inspection comparison, and determined that the laser profilometry was the only technique capable of identifying creep strain in its earliest stages [15]. This is recognized by many studies; hence profilometry base analysis is highly regarded in this research. Shown in Figure 1-2 commonly used creep strain vs time chart demonstrating the applicability of the various NDT techniques for reformer tubes.

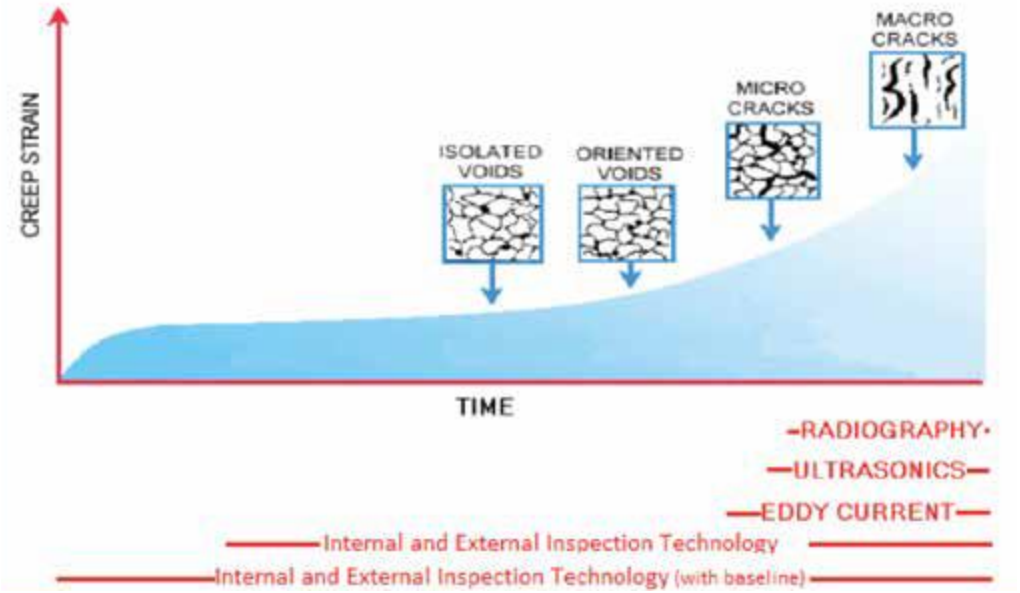

Figure 1-2: Inspection Technology Comparison [11]

Early detection of creep damage is of great advantage over other technique as it allows the plant owner/operator to have time to make operational changes to extend the tubes life. The

application of laser profilometry can be implemented even earlier when baseline data, collected before tubing, is available as common manufacturing defects, such as over boring and cross-sectional deformation, can be accounted for.

1.1.2 Issues & challenges

Despite the abundance of many proven material testing technology that is available, only a few of the techniques are implemented for reformer tube inspection. In developing a system that is niche to reformer tube health monitoring, researchers are faced with numerous technological, economical, and practical issues and challenges that must be addressed which often limiting the implementation of many available technologies.

One of the greatest constraints in performing tube inspection is the accessibility to the reformer tubes. Due to the severe operating conditions, reformer tube is not accessible during operation. Some long range contactless sensing technology such as the infrared thermography inspection are being implemented through the furnace peek windows [17] during operation. However, the performance of such technique is limited primary due to the limitation of the acquired information and the limit of the measurement resolution. Naturally, in-depth inspection is conducted during periodic planned downtime for maintenance and catalyst replacement, where the furnace is cooled and the tubes are emptied. Considering the economics of the retubing cost, the inspection must be conducted in situ with the tube oriented vertically inside the reformer furnace, resulting in a physical accessibility limitation in which the inspection may be demanding. For an external system, access to the lower portion of the tube is impeded by the flue gas extraction tunnel, and the top portion is also challenging to reach with no work working platforms. Consequently, a compact autonomous climber robotic is required to access the bottom of the tubes while having enough power to reach the top of the tube. Alternatively, an internal system can be used but is considerably restricted for physical space as access is only available from the top of the tube through the circular opening of the same size as the reformer tube internal diameter (typically 70-150mm diameter). The advantage of this alternative is that the full length of the tube can be evaluated, and inspection probe can be suspended with a cable, with the assist of gravity, which has proven to be more time efficient than external crawlers [10, 15, 18, 19]

From an economic perspective, a more general issue concerns how quickly the inspection can be conducted while achieving reliable and repeatable measurement data. A typical syngas plant loses approximately $250,000 per day when shutdown [11]. To this, it is of the plant

owners' best interest to reduce the downtime which is directly influenced by the inspection time of the tube.

Procedure for a reformer tube inspection can be generalized into three steps; setup, measure and evaluate. Setup time is dependent on the simplicity and practicality of the system preparation. While some systems require multiple operators for operation, and other requiring high voltage power source. Hence it is important that the resources are available and accessible within the inspection environment. Mobility influenced by system physical form factor is also a major aspect that must be considered. The mechanical design must be viable with the in-situ environment of the tubes with appropriate mechatronic control system and sensing technology to cover the entire length of the reformer tube as much as possible. Increase data quantity and quality is often compromised with reduced inspection speed and larger system form factor, hence developers must work in balancing the two aspects. The data collected must contain enough data point for accurate evaluation of the tube condition with minimal loss of information through filtering, sampling and data interpolation.

In the recent years, as the quality of the inspection data has improved, inspection data has proved useful not just for estimating the remaining service life of individual reformer tubes but also for plant diagnostic and optimization. By evaluating the modern 3D contour presentation of the data, such as the one shown in Figure 1-3, plant operators are able to identify and act on furnace faults such as flame impingements, manufacturer flaws, and tunnel port effect. From this trend, the demand for better reformer tube inspection data has risen, and the need for precise and accurate measurement is at its peak.

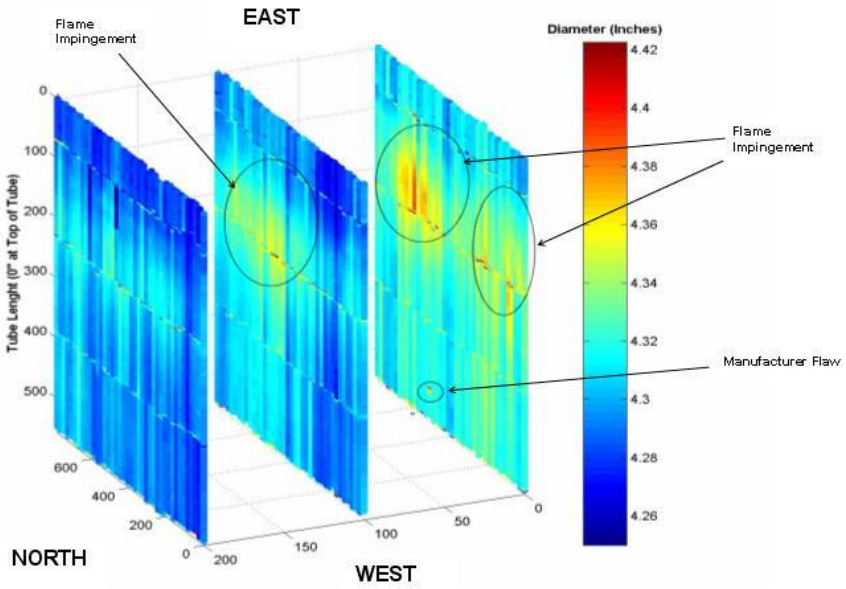

Figure 1-3 3D isometric representation of LOTIS profilometry measurement [18]

1.2 Research Problem

NDT of reformer tube has proven to play a critical role in providing valuable insight into the furnace operation, creating a powerful decision-making tool for plant operators. Significant advancement here can lead to improved reformer operation, reducing creep damage, a better-balanced furnace and improved planning of tube replacement, eliminating unnecessary/unplanned outages [15]. A considerable amount of research has been carried out in the past three decades, where four technologies have extensively been reviewed (ultrasonic, eddy current, infrared thermography, and laser profilometry). The latest enhancement of laser profilometry technology has revealed the reliability of early stage creep detection and the effectiveness for providing valuable insight into the furnace operation. However, it has been determined that there are knowledge gaps in specific elements of the inspection systems that could potentially be limiting the performance of the inspection quality. To further the advancement of NDT technology in the reforming industry this research will focus on resolving issues in the following three aspects.

- Although there is mention of some data analysis software, such as the software used in the LOTIS system for graphically displaying the inspection data [15], there is minimal literature on the processing of profilometry measurement for creep damage analysis. As sensor measures are prone to errors and uncertainties in the real world, signal filtering, linearization, and other signal conditioning techniques are commonly implemented for reducing noise-to-signal ratios and improving measurement accuracy. In this research a focus is given towards advancing profilometry data processing techniques better interpretation of creep damage. In particular, the focus has been directed at detection and correction of datum misalignment that may result from mechanical stabilizing mechanisms and anisotropy in tube geometry.

- With the advancement of graphical interpretation software to accommodate the increased number of inspection data points, positional data has proven to be of more value than it has traditionally been. Accurate location of creep damage will provide a powerful diagnostic and furnace evaluation tool, exploiting the techniques full potential [15]. Whilst axial location (depth) data is typically associated with profilometry data collected at a given plane, the radial position is only considered relative to the measuring device. Hence, as the inspection instruments rotate during

the measurement duration (especially with internal systems) resulted data is prone to distortion.

- The accuracy of profilometry measurement has significantly improved with the advancement of laser technology, where the LOTUS system claims to achieve a maximum precision of 0.05mm [10]. But it has been identified that creep deformation is still measured based on diametrical evaluation and not radial distribution. While the performance of diametrical evaluation is comparable in reformer tube with uniform creep deformation, the ability to quantify creep deformation is limited for reformer tube with inhomogeneous expansion (bulging) as averaging phenomenon takes effect.

1.1.3 Benefits & Potential

The fundamental purpose of a Reformer Tube Inspection System (RTIS) is to provide a conditional evaluation of the reformer tube by performing and collection conditional measurement of the tube as accurately and quickly as possible. Advancement made in the three areas identified in the previous section, a more accurate knowledge of the reformer tube condition will be possible, allow for improved estimation of the remaining service life of each tube and assisting plant operators in making critical decisions. Early detection of localized tube degrading with improved RTIS will help evaluate the performance of the reformer furnace. With this knowledge, operators are able to adjust the operation parameters for a long term improvement in production and efficiency. Additionally, Reformer tube can be operated safer, and service life can be extended beyond the 100,000hr design life for a more financially economical system.

1.3 Research Program

1.1.4 Research Outline

The proposed research program is motivated by the advancement of modern sensing technology and its potential in improving existing RTIS system. With a considerable review of existing technology, the effort is directed at developing a new framework for an in-situ RTIS with significant performance improvement. In particular, effort is directed in implementing numerical data processing technique combined with a mechatronic design for an internal system. In this study, data interpretation for remaining tube service life and plant optimization is assumed, and the focus of the work is on the measurement data acquisition and data optimization. This includes the acquisition of reformer profilometry information, displacement measurement and its relative location, data transmission for simultaneous processing, and the post-processing of the data for improved data interpretation. Depicted in Figure 1-4 is a graphical representation of the proposed research areas with respect to the generic in-situ reformer tube inspection. Data interpretation for Remaining Service Life analysis and ultimate decision-making aspect (shown in the shaded box) is not considered in this study.

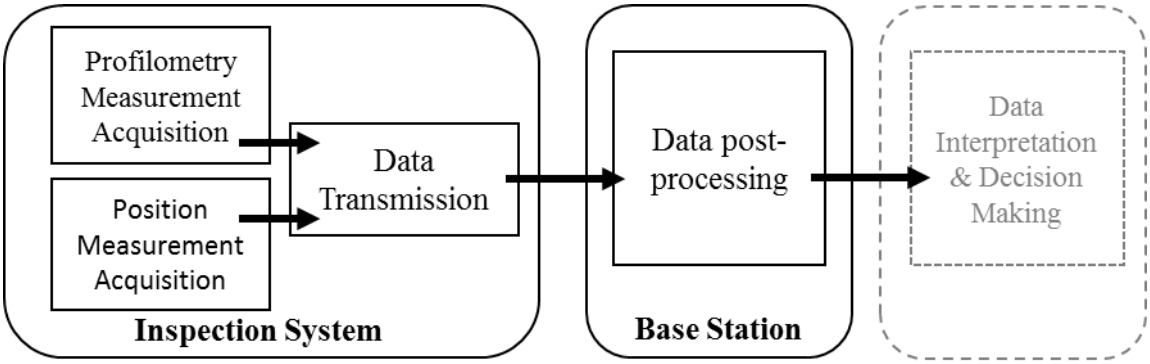

Figure 1-4 Proposed research area with respect to the generic reformer tube inspection system.

Considering the issues and challenges discussed in the preceding sections, and the importance of addressing the association of practical perspectives, an explicit consideration of RTIS constraints inherent within the environment of the Reformer Furnace is placed throughout this research. In many cases, practical implementation of NDT technology is limited by the physical environment in which it operates. In this work, industrial application and realistic assumptions regarding the physical limitation of confined environment of RT is considered.

1.1.5 Proposed Methodology

Proposed in this research is a new profilometry based NDT reformer tube inspection system with a unique designed of a system architecture. The proposed methodology has been developed in a bottom-up approach to advance NDT technology, featuring three components directly aimed at filling the knowledge gaps identified in the currently used technologies.

The first component of the proposed FTIS addresses the improvement of collected profilometry data for a better detection of creep strain. In existing FTIS systems creep strain is being measured based on diametrical measurement. While this approach is adequate for reformer tubes with uniform deformation, the quality of the measurement is reduced when applied to tubes with inhomogeneous deformation as averaging effect takes place between the opposing radial measurements. To improve this, this research will investigate into implementing a radius based analysis of creep strain from reformer tubes profilometry data. This includes the development of a data processing algorithm to simultaneously process the measurement data, accounting for measurement datum detection, detection of uniform and localized creep damage, and quantifying the extinct of the detected creep strain. Compared to diametrical analysis, evaluation of creep damage using radius measure is considerably difficult as higher level of measurement datum alignment with the tube axis is necessary.

The second component of the proposed research addresses the area of data acquisition and transmission. The key feature here is the implementation of radio communication technology to wirelessly transfer the profilometry measurement data and various other control data between the inspection probe and the control station. With a wide range of advanced wireless protocol that is currently available, a balance between data transmission speed and power consumption must be investigated. By eliminating thick umbilical cord currently used in the internal system, the proposed RTIS will be significantly compact with practical advantages.

The third component of the proposed research addresses the improvement the locating of the profilometry data. As discussed previously in the chapter, and discussed more in the remaining body of the thesis, the location of the measurement data is typically detected only along the length of the reformer tube, especially for internal systems. Hence, as the inspection probe can rotate during the inspection, the profilometry data can be distorted as seen in the 3D isotropic image in Figure 1-5. To improve on this, the proposed FTIS will investigate long-range optical sensing technology to track the angular movement of the inspection probe during the period of the inspection.

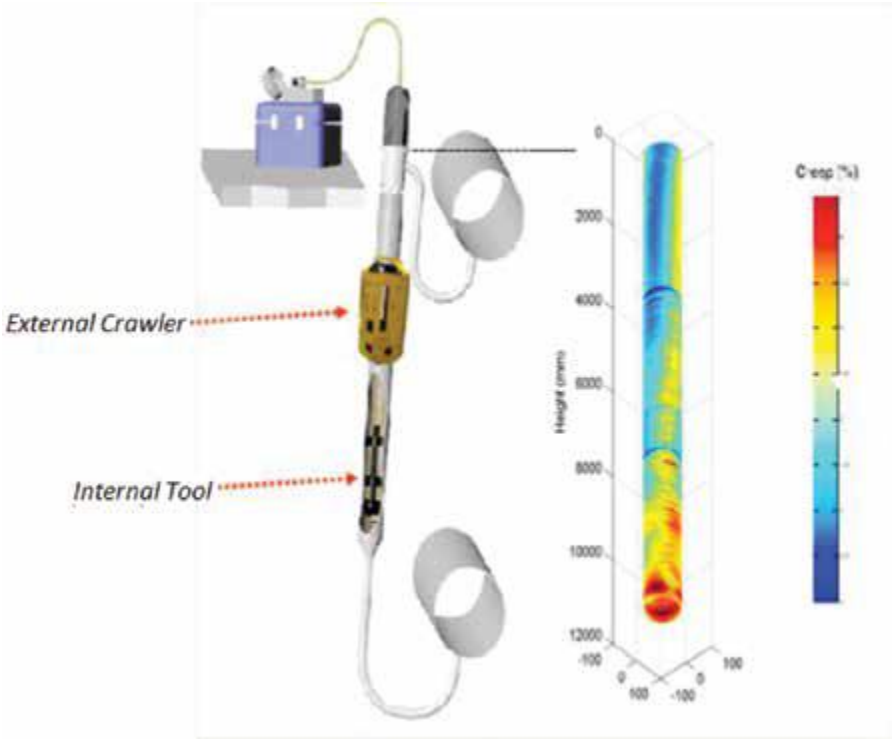

Figure 1-5 Twisting distortion of 3D model of single reformer tube collected from Internal and External Inspection tools [11]

1.1.6 Research Aim and Scope

The aim of this research is to develop a new reformer tube inspection system for profilometry assessment to advance the NDT technology in the petroleum industry. The scope of this research is bound by the consideration of the FTIS demand in industry, contribution from existing work, and the availability of the resources. Elements considered in this research are as follows:

- Reformer tubes are evaluated based on Creep damage. There are numerous failure mechanisms that are prone to reformer tube (such as Liquid metal Embrittlement, metal dusting, and surface oxidation) of which it has been determined that creep damage is the most dominant factor in determining the service life of the tube [5, 9, 10, 15, 18, 20-38].
- Creep damage is classified in two modes of either isotropic or anisotropic deformation. General creep damage is the uniform increase in the tube diameter resulting from uniformly distributed hoop straining under balance operation. Localized creep damage refers to anisotropic deformation of tube resulted from the hot spot of the tube from burner misalignment or catalyst deactivation.

- Reformer tube is inspected along the main reformer body. Creep damage in the inlet and outlet ‘pig tail’ piping is not considered in this research.
- Reformer tube of 90-150mm nominal internal diameter is considered. There are records, or wide arrange of the tube from 70mm up to 200mm, but it has been decided that consideration on all existing sizes is uneconomical for this work.
- Experimental studies are conducted as proof of concept approach. Segments of reformer tube with various extinct of degrading is used as a sample specimen for performing the practical analysis.
- Inspection measurement is located in both axial and radial positions. While radial position is commonly ignored in existing system, it has been determined that this accurate position data is valuable for plant evaluation and optimization.

Following are key assumptions made in this research. Assumptions in this work are implicitly justified throughout the thesis with relevant literature or supporting statements.

- Baseline data is available prior to tube installation
- Reformer tube is accessible from the top flange end during catalyst replacement procedures.
- Sufficient workspace is available for the operators (platform, area for carry case and laptop e.g.) in the furnace inlet area.

1.4 Contribution & Significance

The main contribution of this research is to further progression of Reformer Tube inspection and health monitoring technology. Consequently, a number of significant theoretical and practical contributions advancing the implementation of optical and displacement sensing fields are presented. Specifically, the research makes a total of 5 significant contributions as described below.

- **Contribution 1** Improved detection and quantifying of creep damage in reformer tubes.

A development of a profilometry data post-processing algorithm for improving creep strain evaluation. This includes the research into understanding the nature of creep strain and formulating a mathematical model to detect and quantify the severity of creep strain. Experimental result has shown that presented post-processing algorithm is capable of accurately correct for datum offset resulted from mechanical three-point stabilizing design and classify creep strain in terms of general and localized deformation.

- **Contribution 2** Angular Position Tracking inside reformer tube

A study of a novel long-range Position Tracking system. This includes an investigation of a new scheme for tracking the rotational motion of the object inside a reformer tube using optical technology and evaluating the approach using practical experimentation. It was found that adequate long-range orientation tracking of an object inside an enclosed tube is possible using a combination of linearly polarized light source, light filters and precision illuminance sensors. The finding is not only novel but also constitutes to the first implementation of dynamic angular orientation tracking for reformer tube inspection.

- **Contribution 3** Reformer Tube data interpolation

The first implementation of creep deformation interpolation in reformer tube cross-section profile. This includes sampling reformer tube internal radial displacement measurement and reconstructing the data using piecewise cubic spline interpolation. This work has shown that Cubic Spline interpolation is sufficient in modeling the creep strain deformation of reformer tubes from minimum of 12 radial measurement points.

- **Contribution 4** Displacement Sensor

A development of a novel displacement sensor for accurate and rapid radial displacement measurement. This includes a design and researching a system capable of measuring radial displacement measurement of the internal profile of the reformer tube. Findings have shown the use of mechatronic design integrating with modern embedded magnet encoding technology can achieve displacement measurement at 0.026mm precision and 400hz sample rate with significantly small footprint. This work has also demonstrated practical implementation of the sensor design for reformer tube inspection, justifying the potential for industrial application.

Reformer tube Inspection and health monitoring problem for the reformer plant is considered to have a great impact on the petrochemical industry. Limitation of conventional inspection methods and systems has restricted the realization of the full potential of reforming technology. This work represents a significant effort to contribute toward such difficult global problem on multiple levels.

- **Contribution 5** Wireless Communication

This research contributes to the first implementation of wireless communication technology inside an empty reformer tube. This includes the investigation of common phenomenon of radio wave propagation inside a circular waveguide and design consideration to implementing the technology under the unique FTIS constraints. It was found that integration of wireless system greatly reduces the complexity and size of the inspection system when compared with an alternative wired system. With the elimination of thick data transmission cable, the size of the spooling system in reduced.

1.5 Thesis Outline

Remainder of the thesis is organised in five sections as follow:

Chapter Two

This chapter starts by presenting the background information on Catalytic Steam Reforming technology, identifying the nature of the process and the significance of Reformer Tube Inspection. Existing inspection techniques are presented and the positive, and negative aspects of each approach is reviewed. Methods of improving the inspection performance are discussed, focusing on opportunities for incorporating numerical data process, improved measurement acquisition, and a mechatronic design. A preliminary study conducted to study the feasibility wireless communication and mechatronic internal diameter acquisition design is also presented.

Chapter Three

Presented in this section are the strain creep detection and quantifying approach using statistical modelling. First, the fundamental limitations of the mechanical stabilizer design are presented, and the importance of measurement datum offset is given. A mathematical model correlating the datum offset and measurement data is derived and a systematic architecture for implement the model using MATLAB is presented. Finally, the performance of the proposed algorithm is evaluated through experimental analysis.

Chapter Four

Presented in this section is the derivation and development of a long-range optical position tracking system for improving creep detection on the radial axis. The fundamental principle of the approach is discussed and characterized. A two-stage signal processing algorithm is presented, and results from laboratory experiments are presented.

Chapter Five

In this chapter the system architecture of the proposed FTIS integrated with the key elements from chapter three and four is presented. The features and considerations of the system design is presented and its benefit is discussed. The design and performance of the unique Displacement Encoder are presented and the practicality of the proposed methodology is demonstrated with a fully functional inspection probe design.

Chapter Six

In this concluding chapter, the research findings are presented, summarizing the results from each chapter along with the limitations of the presented work. Finally recommendations for future opportunity are discussed to further the research progress.

2 Literature Review

2.1 Introduction

The operation, management, and inspection of reformer tube is an important element in various aspects of Steam Reforming process. To best understand the contribution of this work it is viable that the current knowledge of Catalytic Steam Reforming process and the associated non-destructive testing (NDT) techniques are reviewed.

The first section of this chapter reviews the Catalyst Steam Reforming technology, and it's advancement over the past five decades. Various tube degrading mechanisms are presented, and the impact of tube failure in service is elaborated. Then the four NDT inspection methods that are currently used for reformer tubes are reviewed, and the limitation of each technology is discussed. Finally, the key finds in the literature is summarized, highlighting the identified knowledge gaps in Reformer Tube Inspection systems.

2.2 Catalytic Steam Reforming Technology

Catalytic Steam Reforming (CSR) is a well-established and most commercially available process for mass production of Syngas. From its first appearance in the year 1913 for the production of hydrogen in two ammonia Harber-Bosch plant [39], the use of catalytic steam reforming in industry has continued to increase. Now there are many large-scale reformer plants around the world using this technology to meet the global demand of hydrogen for the production of critical chemical products, such as Gasoline, Methanol, and Ammonia. In America alone, over 2.6 billion gallons of methanol is produced annually, account for estimated 80% of methanol production. Overall Catalytic Steam Reforming accounts for over 80% of the world's methanol capacity.

CSR is a process of breaking down hydrocarbon into hydrogen-rich Syngas. As the name indicates, the technology reacts hydrocarbon, typically natural gas, with steam in the presence of a metal catalyst to produce syngas; a gas product with a mixture of primarily hydrogen and carbon monoxide. This process is conducted in a furnace plant called a reformer often referred to as Steam Methane Reformer (SMR). In a CSR process two main reactions are involved:

$$CH_4 + H_2O = CO + 3H_2, \qquad \triangle H = 206kJ/mol \qquad (1)$$

$$CO + H_2O = CO_2 + H, \qquad \triangle H = -41kJ/mol \qquad (2)$$

Reaction (1) is the reforming process itself where the H2O in the steam reacts with the hydrocarbon to produce carbon monoxide and hydrogen. As indicated by the positive enthalpy value (ΔH), reforming process is an endothermic reaction. Also, high steam to carbon ratio and low pressure is favoured to meet equilibrium condition with lower carbon dioxide emission. Reaction (2) is a partial water-gas shift reaction that concurrently occurs, where the carbon monoxide resultant from the reforming reaction (1) reacting with the H2O to produce Carbon Dioxide and Hydrogen. This reaction is exothermic and is favoured for production of Syngas with higher hydrogen level. The overall reaction is described as follows:

$$CH_4 + 2H_2O = CO + 4H_2, \qquad \triangle H = 165kJ/mol \qquad (3)$$

The overall reaction of CSR is highly endothermic, and therefore it is necessary to supply thermal energy to move the equilibrium to the right. This is accomplished by using fuel burners in a direct-fired or indirectly fired furnaces arrangement. To achieve a complete conversion of methane to hydrogen and carbon monoxide, long residence time and temperature above 1000°C must be kept, resulting in high energy loss and large CSR plant. In contradiction to the optimal equilibrium condition, high pressure inside tubes is used under practical considerations, such as equipment size minimisation and requirement of down-stream process units. By increasing the pressure and using metal catalysts, it is possible to reduce the temperature necessary for total conversion of the methane and tars to below 1000°C, within considerable short residence time. There is no doubt that the right equilibrium conditions during reforming process are critical. However, reaction kinetics and diffusional limitations are also of importance [40, 41]. Modern reforming processes are generally designed to operate around 800-900°C and at internal pressure 20-30bar.

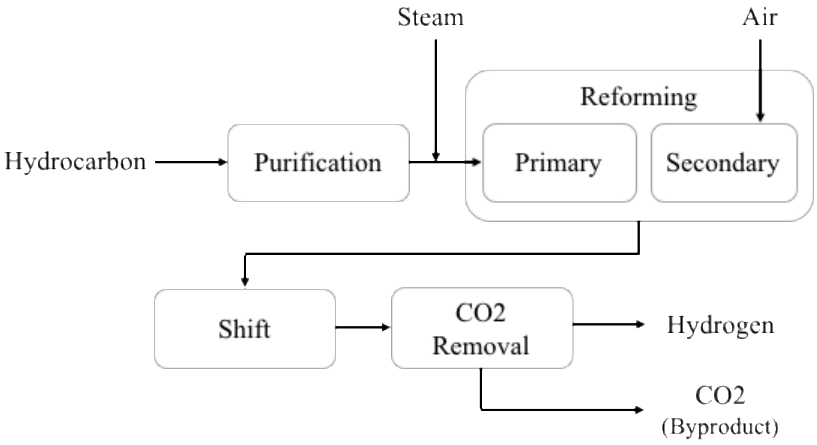

Figure 2-1 Generic flow chart of Catalytic Steam Reforming process

Figure 2-1 is an illustration of a generic flowchart of the CSR process. This process can be categorised into three sections: Purification, Reforming, and Shift. Natural gas and naphtha are the two commonly used hydrocarbon feedstock. The two products are not a commodity with uniform composition. Although methane is the dominant component in the makeup, the impurity in the feedstock will significantly reduce the efficiency and the performance of the reforming process. Of particular importance is the presence of sulphur compounds, non-methane hydrocarbons, and hydrocarbon liquids. Table 2-1 provides a representative range of natural gas composition [42].

Table 2-1 Natural Gas Composition, mole %[42]

Component	***Normal Range***
Methane	87.0-96.0
Ethane	1.8-5.1
Propane	0.1- 1.5
Iso-Butane	0.01-0.3
n-Butane	0.01-0.3
Iso-Pentane	Trace-0.14
n-Pentane	Trace-0.04
Hexanes and higher	Trace-0.06
Nitrogen	1.3-5.6
Carbon Dioxide	0.1-1.0
Oxygen	0.01-0.1
Hydrogen	Trace-0.02
Mercaptan	4.9mg/m^3
Water	16-32 mg/m^3
Hydrogen Sulphide	4ppmv
HHV, dry, MJ/m^3	36.0-40.2

Limitations in the Reformer plant dictate the necessary quality requirements for the Hydrocarbon Feedstock. To meet the requisite stock quality permitted for CSR, Sulpha and Chlorides content level must be minimised to less than 0.1ppmv as they are poison to the catalysts in the SMR. The presence of Sulpha and Chloride in the reformer tube will deactivate the metal catalyst which becomes one of the root cause of equipment failure as discussed later in the chapter.

Once the sulpha and chloride has been removed, the feed stock is mixed with steam and enters the tubular catalytic reactor in the primary reformer. In this step, the majority of the hydrocarbon and water is converted to hydrogen through the highly endothermic reforming

reaction. In the secondary reformer, the remaining hydrocarbon remaining in the gas is partly combusted with air for heat generation, and the rest is reformed for further hydrogen conversion. In the shift converter, more hydrogen is produced from remaining water and carbon monoxide through the previous reaction (2). And in the final stage hydrogen is extracted from the syngas producing hydrogen and CO^2 by-product.

While the presented layout is the conventional scheme proposed for decades, new schemes are being developed by scientist and industry. There are many research being undertaken to develop improved and more energy efficient solution of hydrogen production as an alternative to CSR, such as Auto-thermal reformation (ATR), Steam-iron process, and electrolysis. Revamp schemes are also used to improve the existing CSR plant performance. In 2004 an ammonia plant at Sala, Slovak Republic undertook a Uhden's dual pressure ammonia process upgrade, improving plant capacity while decreasing specific energy consumption [43]. Further, a tremendous amount of research is being pursued towards the development of hydrogen production technology from renewable resources such as biomass and water with less dependency on fossil fuels. Considering the global trend towards environmental preservation, which emphasises clean and sustainable energy generation, the interest of researchers towards natural gas will increase [40]. However, CSR continuous to be the favoured method for large-scale hydrogen production. More information on the alternative scheme can be found in [44-46].

2.2.1 Steam Methane Reformer Design

The main process of CSR takes place in a large scale furnace, most commonly known as the Steam Methane Reformer (SMR). Inside the furnace are hundreds of vertically mounting tubular reactors, known as Reformer Tubes or Reformer Columns, where the hydrocarbon is converted in the syngas. There is a number of variations in the furnace layout that is currently available on the market, of which it can be separated into two distinctive types; top fired and side fired furnaces. However, most manufacturers are offering and recommending the top fired reformer as the layout benefits with comparatively less number of burners are required with much higher radiant efficiency can be achieved than the side fired reformers [47]. Shown in Figure 2-2 is a depiction of the general layout of the top fired primary and secondary SMR.

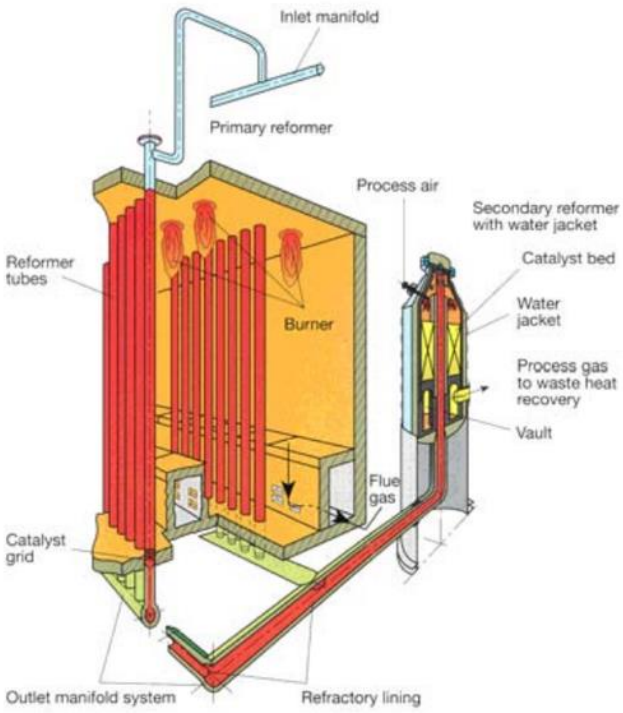

Figure 2-2 Primary Reformer furnace layout [47]

Majority of the SMR plant is comprised of the convex furnace. The reformer tubes are mounted vertically, penetrating through the ceiling and the floor of the furnace. Counter weighting hanger systems are used to suspend the tube to account for thermal expansion (not depicted in the diagram). Alternating with these radiant tubes are downwards-firing burners situated on the roof of the reformer furnace. This unit operates concurrently with the gas and steam flowing downwards through the tubes. The burner provides the heat required for the highly endothermic reaction to reach equilibrium. Located between the rows at the bottom of the tubes are flue gas tunnels for extracting the Flue gas out of the furnace. The internal walls of the reformer and outlet manifolds are coated with refractory lining for thermal insulation.

The natural gas feedstock flows from the top of the furnace through the inlet manifold into the reformer tubes, exiting the furnace from the outlet manifold at a nominal temperature between 850-950°C. Before entering the steam reformer through the inlet manifold, the natural gas feed undergoes saturation with steam and is pre-heating to 550-650°C. There have been no appreciable changes made in the front end of conventional SMR plant over the last decades. However, there have been considerable developments in the components and inspection technology associated with the primary reformer.

According to the article [47], the global trend is the development of a larger-scale SMR plant. One of the world's largest top fired ammonia plant contains 408 tubes and has a capacity of

3,300mtpd. A significant increase from the production capacity of 400mtpd in an ammonia plant designed in the 1960's with under 200 tubes. With no foreseeable future capacity limitation for a primary reformer and the improved economy of production cost per ton of syngas with increasing plant capacity, this trend is expected to continue for many decades to come.

2.2.2 Reformer Tube Design

Reformer tube is one of the most important and costly component of Steam Catalyst Reformers, accounting for more than 25% of the overall plant assets. There are variations in the design, but generally the tube dimension ranges between 60-160mm internal diameter, with a wall thickness of 10-25mm, and a total length of 10-15m. These parameters are selected to meet the requirement for different productions, but all are based on the American Petroleum Institute (API) Recommendation Practice 530 to achieve a nominal service life of 100,000h (11.4 years) [48]. Diameter straining value of roughly 3% at service temperature at the internal pressure of up to 980 and 35bar is commonly used [5]. Presented in Figure 2-3 is a schematic diagram of a general construction of a Reformer Tube.

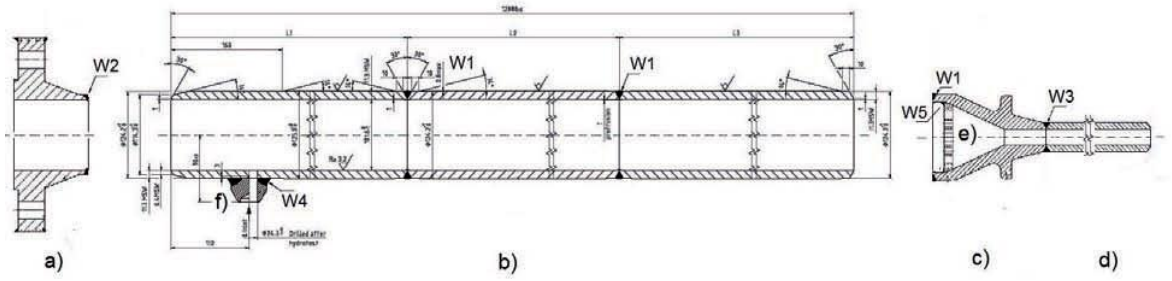

Figure 2-3 General Reformer Tube Design [49]

The construction of a reformer tube can be categorised into three components; Upper Flange, radiant tube, and the reducer. At the top of the tube, located above the furnace ceiling (shown on the left-hand side of the depiction labelled *a*) is the upper flange. This static cast constructed component is used for mounting the spring or constant hanger of the counter balance system to the reformer tube. The inner bore, matching the internal diameter of the radiant tube, is the only access to the reformer tube when installed, and is used for various tube maintenance scheme, such as loading and unloading of the nickel catalyst pallets. It is also important to note that the design of the upper flange is critical for internal NDT test equipments as it is the only practical way accessing the insides of the reformer tube during service for internal profilometry inspection.

The radiant tube, extending between the furnace ceiling and the floor, is made up of multiple 4-5m length segments butt welded together. This section makes up the majority of the Reformer Tube assembly where majority of the reaction occures. At the top of the tube is the gas inlet nozzle where the natural gas and steam mixture feedstock enters the tube at 500-600°C, making its way down the tube through the catalyst pallets, activating the reforming reaction as the temperature increasing as the heat from the gas burner radiates through the tube wall. Shown in Figure 2-4 is the graph showing the relative tube skin temperature at the different location of the tube for various SMR design.

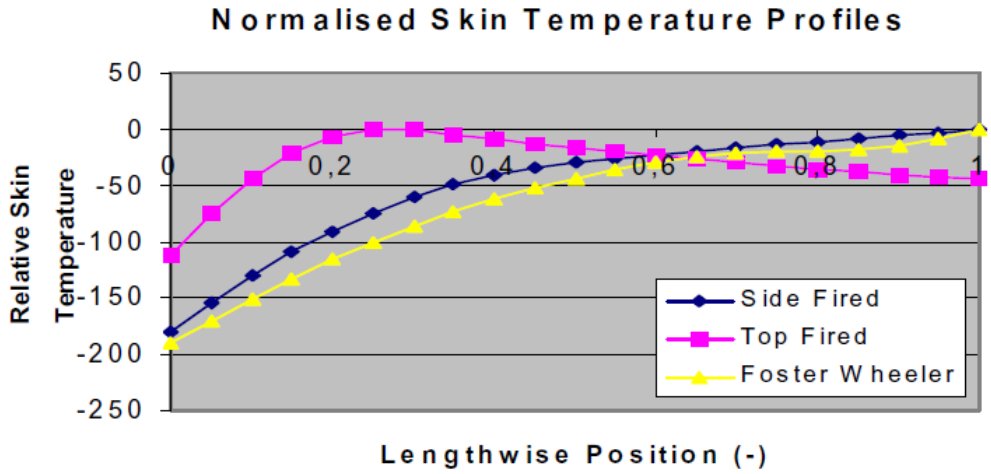

Figure 2-4 Ammonia Plant Tube Wall Temperature profile [50]

At the bottom of the tube is the reducer, located below the furnace floor, where the diameter of the tube dynamically reduces to the match the outlet manifold, commonly referred to as the outlet pigtail. By the time the feedstock gas reached the Reducer outlet, majority of the gas has converted into syngas and the temperature has reached above 850°C. The syngas from each tube is then collected through the manifold outlet system to be further processed in the secondary reformer unit.

Due to properties of the heat resistant material, tubes are not easily drawn or extruded. Thus centrifugal casting is generally used to form a more even structured tube with the molecular grains orientation in the radial direction, forming a grain matrix with greater strength and creep resistance [51]. In the article by A. Ray [52] a centrifugal casting process combined with electromagnetic field is discussed. Presented in Figure 2-5 is a schematic representation of an electromagnetic centrifugal casting equipment use for reformer tube construction. Study shows the effect of adjusted cooling rate and electromagnetic field exposure has significant effect on the granular morphologies of the tube wall. Increased cooling rate markedly

promotes the development of the columnar grains, while an applied electromagnetic field during the centrifugal solidification results in a notable grain refining, increasing the eutectic carbides along the grain boundary hence improving the creep rupture strength. The phenomenon of the granular formation by controlled centrifugal cooling rate and the magnetic field is summarised in [53]. A ratio of 2:1 of columnar and equiaxed grains regions are typically used for Reformer Tubes.

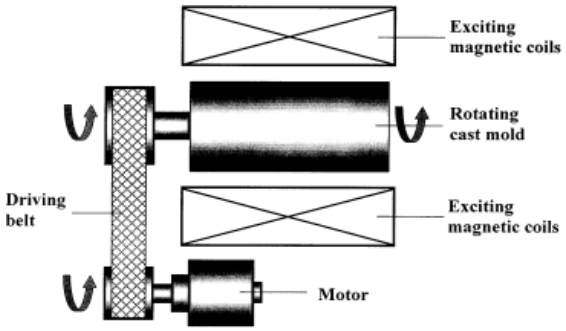

Figure 2-5 Schematic diagram of the electromagnetic centrifugal casting equiptment [53]

The most commonly used material for the production of Reformer Tube is heat-resistant stainless steel alloy denoted HK40, HP40, and HP40-mod. In this last 50 year heat-resistant alloys compositions has advanced significantly in Steam Reformers with scientific research focusing on the investigation of creep composition and relative strength of heat resistant alloys [54]. Summarised in Table 2-2 are the chemical composition and relative strength of heat resistant alloys developed during the last 50 years.

Table 2-2 Heat-resistant Alloys Compositions Developed During the Last 50 Years

Decade	**Chemical Composition (wt%)**							**Relative**
	Cr	Ni	C	Si	Nb	Other	Fe	**Strength**
1960s	25	20	0.2-0.6	1-2			Bal.	1.0
1970s	25	24	0.2-0.6	1-2			Bal.	1.4
1980s	23	22	0.2-0.6	1-2	~1	Ti	Bal.	1.7
1990s onwards	23	35	0.2-0.6	1-2	~1	Ti, Zr, W, and Cs	Bal.	2.2

Broadly speaking, the development of chemical composition of Reformer Tube can be divided into two generations. The first generation alloys constituents used between 50-ties to the 70-ties is mainly nickel and chromium. The amount of Ni was later increased giving greater mechanical strength and corrosion resistance at service temperature.

From around the 80-ties onwards commenced the second generation of reformer tube chemical composition, along with growing number of research investigating new alloying elements and additive with better carbide-forming elements were introduced. Other corrosion resistance alloys were also introduced, such as the presence of Si improving the carburization resistance. With more stable carbide between the grain boundaries, the relative strength against creep damage increased making possible for thinner tube wall which reduces the temperature differential, significantly reducing creep stress during start-up and shutdown [35]. At the same time, there is a trend shifting towards higher internal pressure and temperature for productivity enhancement.

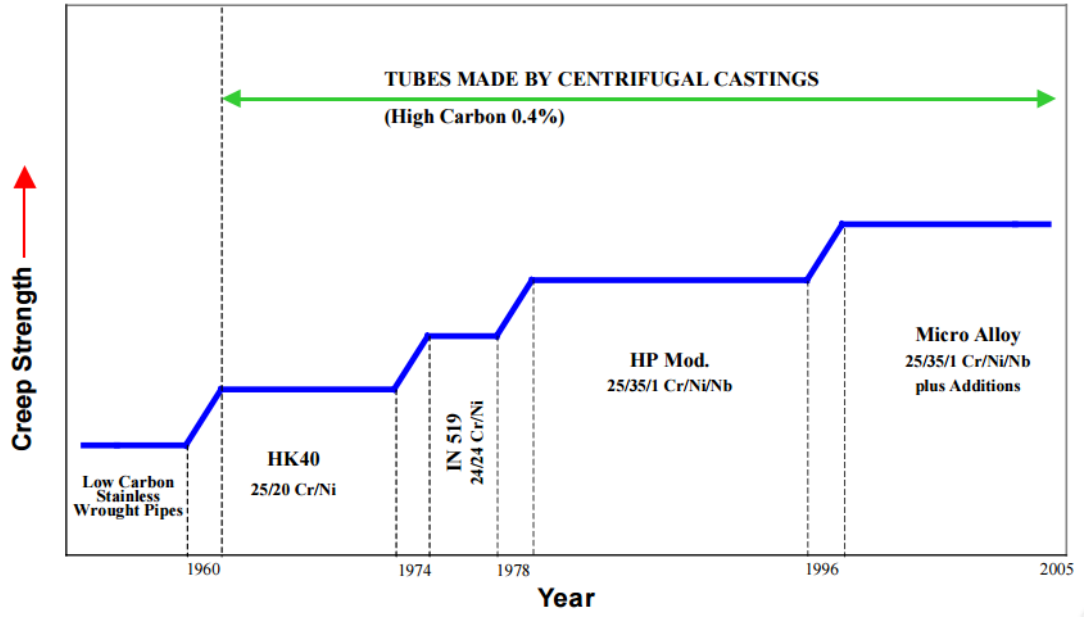

Figure 2-6 Increase in Creep Strength of centrifugal casted tube over time [47]

2.3 Degrading mechanism

Under the server working condition, reformer tubes are subjected to numerous degrading phenomena causing accumulation of microstructural damages in the tube wall. Prolong operation will result in a gradual decrease in the materials load bearing capacity, ultimately resulting in failure. Such failure under service exhibits major economic problems that often result in damaging of expensive components, production loss due to unscheduled downtime, and health and safety hazards to personal within the premises. Thus, numerous scientific research in collaboration with industry has been conducted to understand the root cause of Reformer Tube failure [20, 55-57].

Table 2-3 Common Failure Mode of Reformer Tube

FAILURE MODE	MECHANISM	RESPONSE
CARBON FORMATION	Formation of carbon inside the reformer tube resulting in reduced process activity.	In order to reduce the risk of carbon formation, steam-to-carbon ratio of about 3 is used [58]. Also potassium additive in the catalyst helps prevent carbon formation [59].
CORROSION	Corrosion on the internal and external walls causing rapid degrading of reformer tube, commonly caused by sulpha.	Inclusive of silicon in the heat resistance alloy for formation of protective oxide layer and removal of sulpha in flue gas and process gas.
CREEP	Gradual degrading of tube strength over service exposure.	Creep is unavoidable phenomena experienced by all material in elevated temperature application. To reduce the risk of premature retirement, the plant is diagnosed using NDT inspection technique for furnace balancing.
LIQUID METAL EMBRITTLEMENT	Environmental cracking caused by contact with a liquid metal.	Removal or avoidance of using metal with low-melting point.
METAL DUSTING	Corrosion of metal with high carbon activity	

Listing in Table 2-3 are the five failure mode common to reformer tube. Factors other than the creep are very complicated metallurgical phenomena to manage and are taken care in design indirectly by very conservative safety factor, thus degrading of materials mechanical properties due to creep damage is often considered to be dominant factor limiting the life of the reformer tubes [23]. From study of tube failure incidences [7, 60, 61] deterioration of mechanical properties are mainly due to the increased service temperature and pressure, composition variation of impure hydrocarbon feedstock, difference in coefficient of thermal expansion between the tube and catalyst, and presence of blow holes and pin holes in centrifuged as-solidified tubes [62].

Creep damage is a time dependent straining that occurs in all application of heat-resistant high-alloy castings. At atomic leave, creep is caused due to dislocations in the crystal structures along the grain carbide boundaries that causes an irreversible deformation, ultimately leading to creep failure mode called Creep Rapture. The rate at which creep damage progresses (creep rate) and the resulting degrading in the mechanical property is governed by the elevated temperature, stress, and the creep resistance property of the materials. Creep is typically described as having three distinct stages; primary, secondary, and tertiary creep. The creep characteristic for a given material under constant stress and elevated temperature is best described using a Strain-time curve called creep curve (Figure 2-7).

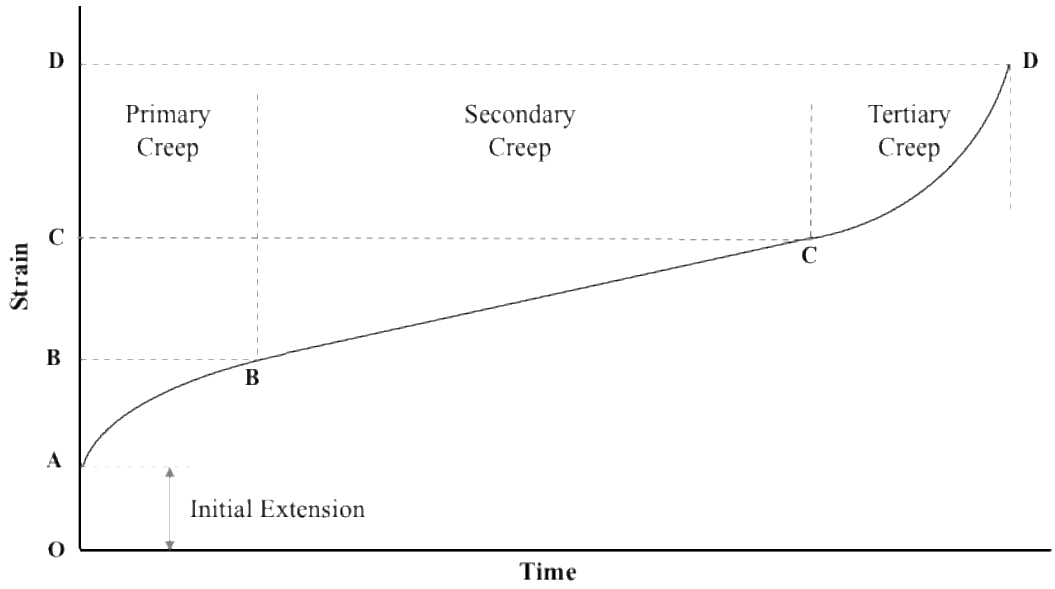

Figure 2-7 Creep Curve

Initially, when the tube is put into service, a rapid straining occurs between point O and A, which includes elastic and plastic deformation. Between point A and B the creep rate decreases to a stable minimum value with the formation of fine secondary carbides within the austenite grain, increasing creep resistance. This is termed the primary creep. In the second stage, the creep rate stays relatively constant over time, often termed steady-state creep rate. This portion of the creep curve is the area of engineering interest as the majority of the service life is spent in this state with a gradual tube diameter increase. In the final tertiary stage, the creep rate exponentially increases with time until the strain limit is reached resulting in a sudden failing under creep rupture, causing the tube wall to crack in the longitudinal direction. It has been determined that the key to the accelerated creep rate is due to the changes in the microstructural with service exposure, causing a rapid decrease in the material strength. This progression in creep failure in the metallographic structure can also be categorised into several stages, like in the Creep curve.

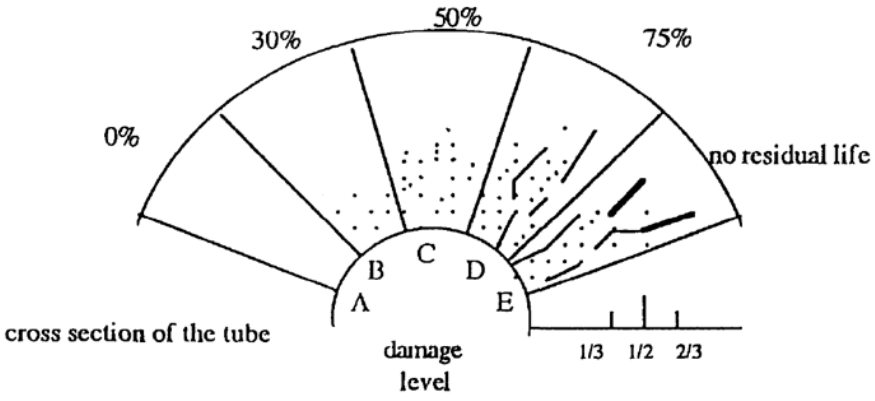

Figure 2-8 Classification of the damage in the wall of a reformer tube [26]

Shown in Figure 2-8 is the progression of creep damage within the wall of a reformer tube and the manner in which it can be classified [26]. This approach describes creep damage in 5 distinct level of metallographic stages. Level A has no detectable voids indicating a tube with considerable creep resistance. At Level B signs of isolated cavities are seen at approximately one-third of the wall thickness from the inner surface. At Level C, oriented cavities are visible along the primary grain boundary which eventually joins to form microcracks favoured in the direction normal to the principal tensile stress, indicating Level D damage level. At Level E the microcracks propagate further to the internal surface and later to the external surface to produce leakage, forming a macro size cracks. In industry, components are retired at two later levels of creep damage. Although this process starts later in the service life, the progression is sufficiently slow that a sufficient forecast of the remaining life expectancy can be made.

Reformer Tubes are designed to meet the American Petroleum Institute (API) Recommendation Practice 530 stating minimum service life of 100,000 hours (11.4 years). Under optimal condition, because this figure is very conservative, the service life can extend much beyond the manufactures design life [36]. However, it is common for a tube to prematurely fail within 3-8 years, resulting in an emergency shutdown of the plant which causes a great deal of financial and safety risks to the business. To this, research is continually being conducted to correlate the relationship between the mechanical strength and microstructural observations for remaining life assessments, contributing to more efficient and reliable operation.

In 2002, a team of researchers from National Metallurgical Laboratory analysed two raptured modified HK40 reformer tube samples failed during start-up after 4 years of operation [31]. The tubes are taken from an ammonia plant containing 288 12m length catalyst tubes with 152mm OD and 10.7mm wall thickness, arranged in two radiant chambers of 144 tubes each. A feed gas of naphtha and steam is processed at design temperature and pressure of 870-890°C and 32kg/cm^2. Tubes were investigated for failure mechanism and life evaluation using tensile test, hardness measurement, dimensional measurement, microscopy, and accelerated creep test. Research revealed that the longitudinal crack was caused by overheating that resulted from the choking of damaged catalyst Figure 2-9. Following in 2007, a collaborative research team analysed three segments of 96000hr, 105,120hr, and 131,400hr service exposed reformer tubes [36]. Microstructural changes, tensile strength and accelerated

stress rupture strength were evaluated. The sample used for the study was selected based on non-destructive ultrasonic scanning results. Progressive degradation of creep strength was observed mainly due to variation in temperature experienced by the tube.

Figure 2-9 Broken pieces of catalyst on the retaining ring [31]

Further, in 2008 the same team in collaboration with Material Science and Technology Division, India, evaluated more tubes failed in the same plant after 2, 4, and 8 years of service [5]. Same set of destructive testing was conducted, and localised overheating, possibly by flame irregularities, was determined to be the cause of significantly reduced service life. Compared with the other portion of the tube, the failed segments showed more degree of coarsening of the precipitated phases and continuity of creep cavitation either in aligned or isolated. All the tubes had diametric expansion above 2.5%, with 8 tubes showing more than 3.9%. The rupture was confined to the bottom portion of about 1-1.5m length, where the operating temperature is typically at its maximum.

Remaining Life Assessment (RSL) is an essential element necessary for Reformer Tube management. RSL techniques are used to determine the remaining service life available in individual reformer tubes by estimating the level of material degradation in the tube walls. Failure of a reformer tube during operation is considered detrimental to the operating business, resulting in significant financial loses. Accurate and reliable RLA is critical for making the important decision of tube retirement and parametrical adjustments. One of the dominant mathematical models used for RSL is the Larson-Miller Parameter (LMP) used mainly in analysing reformer tube condition[5, 23, 25, 31, 36, 63]. LMP correlate creep rapture time and the service temperature based on the Arrhenius rate equation and is described as:

$$\mathrm{LMP} = \mathrm{T}.(\mathrm{K} + \log t_r) \qquad [2\text{-}1]$$

Where T (kelvin) is the exposed temperature of the material, K is the specific material constant provided by the tube manufacturer, and t_r is the time of creep rapture (hours). Alloy data sheet provided by the manufacturer also includes creep-rupture properties and the creep-stress property in the unit of % creep strain per hour[64]

By combining the results from an accelerated creep rapture time test, service temperature stress can be described as a function of temperature and rapture time, allowing faster RLA assessment. Shown in Figure 2-10 is stress vs LMP curve constructed from failed sample tubes after four years of service [31]. The black line and the dashed line show the average and lower scatter band of the HK40 material based on the manufacturers' value. K value of 22.9 or thereabouts is the common value for HK grade material. Creep rapture data collected from the top of the tube (triangle point) matches the lower boundary of the manufacture's value indicating significant creep strength left in the material. This agrees with the lower service temperature experience near the top of the furnace. On the other hand, the data collected from the bottom of the tube show lower LMP indicating a reduction in the creep strength. This also agrees with the high service temperature experienced at the bottom of the tube. In such manner, data can be interpolated to predict the t_r of the tube at higher temperatures.

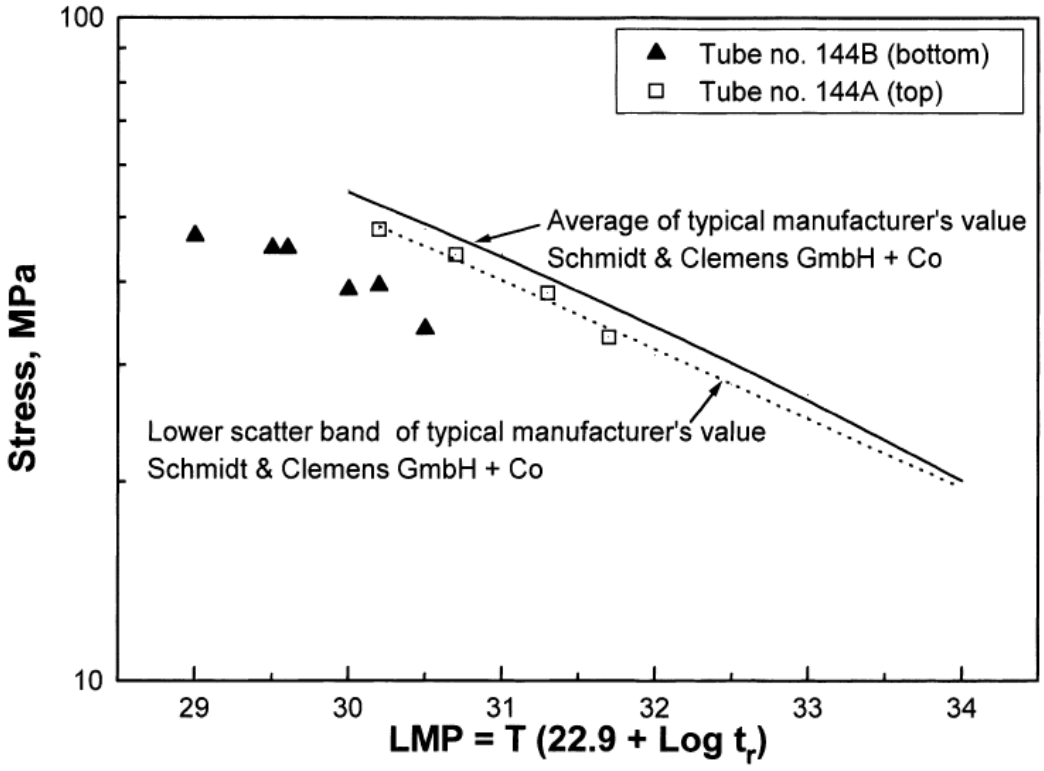

Figure 2-10 Experimental data superimposed on stress vs LMP curve [31]

It is evident that overheating appears to be the dominant factor limiting the serviceability of the reformer tubes. Unbalanced furnace will result in a localised heating above design specification in the tube wall, creating hot spots and heat band the will accelerate the degradation of the reformer tubes.

Common causes of tube over heating are:

- Choking of steam flow from broken Catalyst
- Misalignment of burners
- Unbalanced flue gas flow caused by furnace layout (e.g. tunnel ports, tube alignment)

The stress due to the pressure in the tubes under the design pressure is too low to cause significant creep, but the stresses caused by the temperature gradient through the tube wall are an order of magnitude higher [35]. The temperature gradient in this context is the temperature difference between the internal and external surface of the tube, where the outer wall temperature is greater than the internal wall in contact with the catalyst and the process gas. Such difference in the wall will result in variation in the thermal expansion creating internal stressing in three dimensions. To tackle this phenomenon effort has been directed at reducing the thickness of the tube wall by developing better alloy (as discussed in Chapter 2.2.2) and lowering the tube wall temperature (TWT) by improving the performance of the Catalyst. The key component affecting the performance of the catalyst is Heat Transfer Coefficient predominantly determined by the amount of geometric surface area (GSA) per unit volume. The first true shaped catalyst was introduced in 1941 in the form of a ring pallet, having a considerable increase in the GSA compared with former solid cylinders. The manufacturer continues to improve the catalyst performance by implementing more complex shapes to increase the GSA further while considering longer lasting metallurgical aspects. In the modern studies advanced computer modelling software, such as COMSOL, are used to simulate and analyse the catalyst design [65]. Another area that is continually researched is improving the catalyst packing and contact mechanism with the tube wall, and decreasing catalyst bed pressure drop by increasing the pellet voidage and size. Shown in Figure 2-11 is a comparison of various catalyst performance with the KATALCO^{TM} generations of Ring, 4-hole, and Quadrolobe catalyst [47].

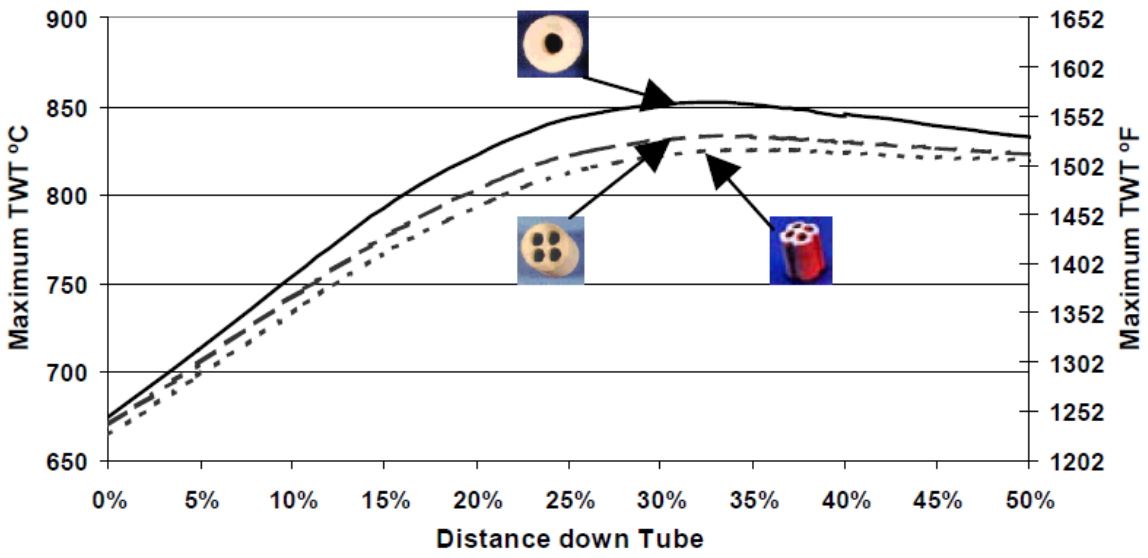

Figure 2-11 Tube Wall Temperature (TWT) with different KATALCO catalyst generation [47]

One of the biggest cause of thermal stress is due to thermal cycling. When the temperature gradient is changed by varying the heat flux, as might happen during start-up and shutdown, the metal will go through cycles of alternate tension and compression, which will eventually result in enough creep damage to cause failure. Hence increased number of plant start-up and shutdown resulted from tube failure will reduce the service life of every tube in the plant. Shown in Figure 2-12 is the effect of wall thickness and number of thermal cycling on the life of Hp-40 Mod Nb and HK-40. It also shows that TWT increase of 28°C can reduce the relative tube life by more than 40%.

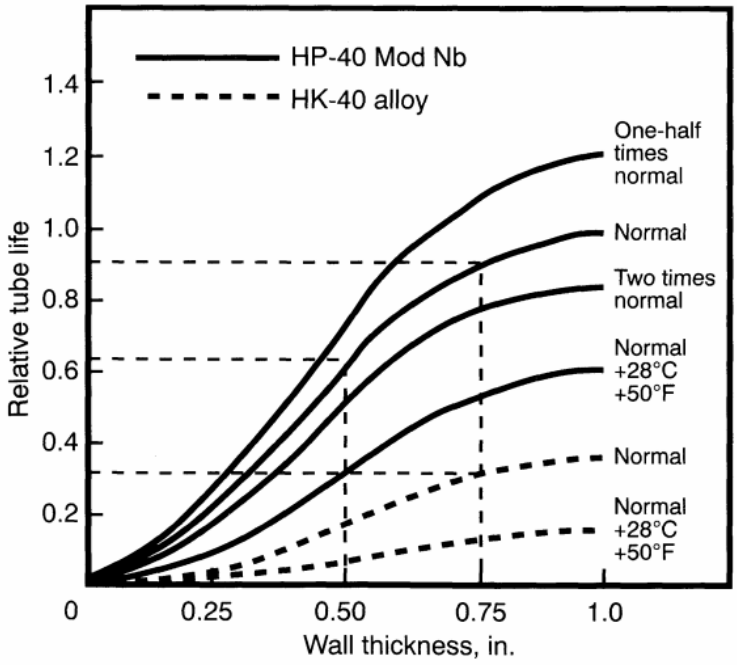

Figure 2-12 Wall thickness and amount of thermal cycling are important considerations in tube life [66]

2.4 Reformer Tube Inspection Technology

Failure of reformer tube under creep rupture is considered to be a major factor that results in gas leakage that will disrupt the thermal dynamics of the furnace which can if not directly, affect the adjacent tubes. Inherently, the plant must be shut down for plant inspection and failed components must be replaced. A typical retubing of a single tube can cost $20,000USD, not including the cost of the catalyst. In addition, while typical syngas plant loses approximately $250,000 USD per day when shutdown, procurement lead time of tubes can be 17 weeks or more [11]. Tube nipping technique on the inlet and outlet tube commonly used to isolate the failed tube to start the plant quickly, but is a preliminary solution. While production is reduced with less tube in service, the nipped tube will suffer high temperatures resulting in bowing. Prolong service under this condition will cause the nipped tube to bow excessively which will eventually be effecting the neighbouring tube to failure. Overall, unplanned shutdown due to tube failure can cost the business millions, making managing the integrity of this asset crucial.

Traditionally, reformer tube has been managed based on time-based scheme developed based on materials behavior models, such as the Larson-Miller Parameter previously discussed. However, with various variation in the plant design and unknown system parameters, it is impossible to derive a single model that works all cases. Element such as tunnel port design and flue gas flow can cause uneven temperature on the tube causing significant increasing the creep rate. Manufacturing deficiency in both mechanical properties and inherent geometrical defects can also impact the service life of the reformer tubes. Hence time-based evaluation is limited as calculation of the resulting creep is more complicated because the available data scattered and do not relate to the situation in a reformer tube where variable stresses are applied in three directions at once.

Naturally, industry has inherited in-situ NDT technoloy to aid RLA using conditional-based assessment. For an effect application under the unique environment at which the reformer tube exist, a specially design Reformer Tube Inspection System (FTIS) has been developed and are continued to be developed. Ultrasonic, Eddy Current, Infrared Thermography, and Laser Profiloetry are the four dominate NDT technologyies that are used today. For an operating facility to change from a time-based to condition-based reformer tube managing philosophy requires confidence in the methods and techniques used to determine the tube condition [50].

The fundamental purpose of a Reformer Tube Inspection System (RTIS) is to provide conditional evaluation of the reformer tube by performing and collecting conditional measurement of the tube as accurately and quickly as possible. Achieving this task will provide plant operators and engineer's number of key operations benefits. First, accurate knowledge of the reformer tube condition will allow for estimation of the remaining service life of each tube, aiding plant operator in making critical decision. And also, early detection of localized tube failure from advanced RTIS has helped evaluate the performance of the reformer furnace. With these knowledge, operators able to adjust the operation parameters for improved production and efficiency. Reformer tube can be operated safer and service life can be extended beyond the 100,000hr design life for a much more economical system.

2.4.1 Ultrasonic

Ultrasonic Inspection is a commonly used NDT technique in the industry for detecting material detects. While there are numerous sensor topologies that exist for detection of different material characteristics (e.g. wall thickness, crack detection), an "ultrasonic attenuation" technique is used for condition assessment of Reformer Tube by directly detecting and quantifying mid-wall intergranular creep damage.

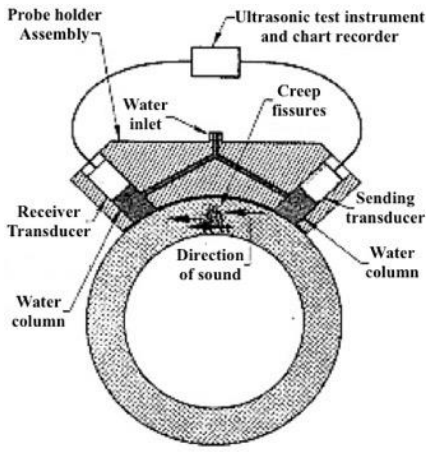

Figure 2-13 Transmit-Receive mode configuration of Ultrasonic Inspection [28]

Depicted in Figure 2-13 is the basic layout of Transmit-Receive mode configuration for reformer tube Ultrasonic inspection. Using the Sending Transducer, a beam of ultrasound energy is transmitted through the middle of the wall section and received by the Receiving Transducer. The Water Column is filled with water to act as an acoustic coupling media between the transducers and the tube wall. As the beam passes through the material defect, the signal scatters result in a signal attenuation as seen by the receiver. Prolonged exposure to high temperature, precipitation of secondary carbides and creep voids are formed creating

additionally signal scattering as presented in Figure 2-14. Thus, greater the attenuate indicate higher level creep damage. Mid-wall fissuring can, however, cause significant or complete loss of ultrasound energy which requires confirmation by other inspection techniques [67]. Results of measurement performed on sample reformer tube is presented in the reference [28].

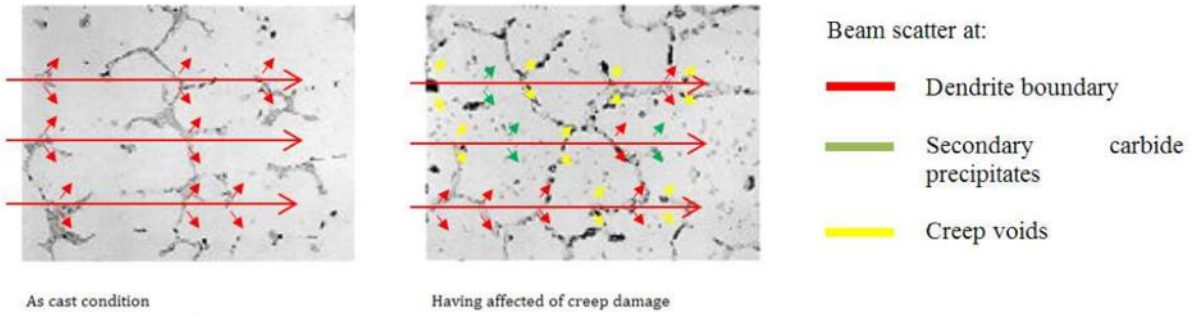

Figure 2-14 Ultrasound attenuation [68]

Another aspect affecting the performance of ultrasound attenuation is the granular characteristic of the tube. The centrifugally cast tube possess two regions of equiaxed and columnar structure on the inner and outer circumference. The columnar structure scatters ultrasound beam more than the equiaxed structure. Thus variation in the equiaxed and columnar ratio (typically 1:3) will result in attenuation variation even in an unused tube. Therefore, the ultrasonic "attenuation measurement" inspection technique has limitations based on the surface condition, the ratio of columnar and equiaxed grain, and carbide size, which can lead to false reading [36]. To this, an integrated approach of using other NDT methods along with microstructural examination can help in a more accurate and reliable RLA evaluation [67].

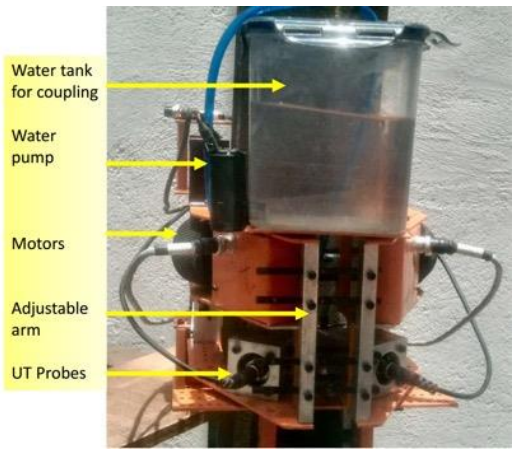

Figure 2-15 Automated Reformer Tube Inspection System (ARTiS) from TCR Engineering Services [67]

To perform an in-situ ultrasonic inspection a robotic tube crawler design is used to aid inspection in a systematic manner. One of the best example of this is the Automated

Reformer Tube Inspection System (ARTiS) developed by TCR Engineering Services in India. Shown in Figure 2-15 is the ARTiS crawler assembly, highlighting the main components of the design. Using four metal gear motors with total capacity of 200watts, the crawler moves along the reformer tube wall running on four mechanical wheels. The relatively compact design allow the unit to fit between flue gas tunnels for full coverage across the length of the tube. Up to four pairs of ultrasonic transducers can be installed which makes possible to examine four separate axial zones. The system also uses precision infrared sensors and gyro-sensors for diametrical and tube bowing detection. Computer control system combined with data acquisition and analysis system also for an automated inspection solution. Creep damage is quantified at three level as described in Table 2-4.

Table 2-4 Creep Damage Classification based on Ultrasonic attenuation

Attenuation Level	*Creep Damage*
35-55 dB	Unused tube having only dendritic columnar austenite grains oriented perpendicularly to tube wall.
55-62 dB	Detection of isolated and aligned creep voids
62-72 dB	Detection of inter dendritic micro cracks and secondary carbide coarsening indicating 10-20% remaining service life.

One of the disadvantages of the ultrasonic inspection method is the need of the ultrasound coupling media. As the ARTiS moves along the tube, the water is lost between the clearances between the tube wall and the water column. Thus the water column must continuously be filled throughout the entire inspection session. The rate at which the water is lost is dependent on the surface finish of the tube wall. Consequently, a reservoir tank and a pumping system are required, reducing the mobility and the practicality of the time-critical reformer tube inspection. The added weight will require more energy to manoeuvre the system along the tube, which is not beneficial. However, ultrasonic inspection system benefits from:

- Inspection without the need of catalyst removal
- No surface cleaning required
- Automated inspection solution avoiding the need for scaffolding
- Full coverage across the length of the radiant tube

2.4.2 Eddy Current Testing

Eddy current technology is one of the oldest technique for advanced materials testing with its origins with Michael Faraday's discovery of electromagnetic induction dating back to the year 1831 [69]. With the development of various coil configurations, eddy current technology has proved to be successful in surface crack detection, non-ferrous metal sorting, sub-surface crack/corrosion detection, and for remnants service life evaluation of heat exchanger tubes including primary reformer tubes.

The fundamental principle of Eddy Current material testing is as follows. A coil driven by an AC voltage is used to induce an alternating magnetic field into the reformer tube wall, creating an eddy current opposing the magnetic effect of the coil according to Lenz's law. The current flow through the coil is determined by the impedance of the complete electric circuit. As the mechanical properties of the wall of the reformer tube changes with the development of failure mechanisms, such as creep voids, micro and macrocracking, and corrosion, a change in the overall circuit impedance is detected with typically increased self-inductance of the coil. By analysing the circuit impedance characteristic, the properties of the tube wall can be evaluated. Eddy Current technology is considered to be the most sensitive method of NDT and, theoretically, any defects in the material such as cracks, pitting, wall loss or other discontinuities will disrupt the flow of the eddy current and be detected. However, due to the constraints of practicality limiting the depth of penetration of the eddy current related to material and frequency of the signal, the technique is more suited to later stage detection of internal creep damage and surface flaws[12].

Eddy Current inspection technique is a well-established NDT technique with many systems utilizing the technology for reformer tube inspection. One of the most recognised eddy current based NDT inspection system that is currently available is the Laser Eddy current Outside Scanning Reformer Tube Inspection system, abbreviated as LEO-SCAN, proprietary to the Magnetische Pruefanlagen GmbH (MP). MP is a German company specialising in developing non-destructive materials testing by means of eddy current technology.

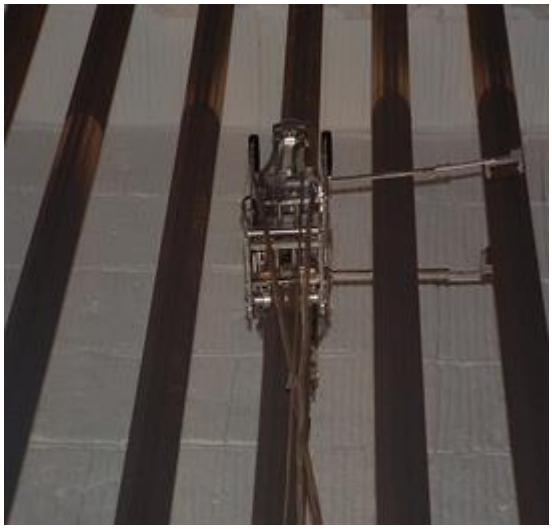

Figure 2-16 MP LEO-SCAN Reformer Tube Inspection system

Shown in Figure 2-16 is the unique LEO-SCAN tube crawler designed and built by MP. The basic construction is relatively similar to the ARTiS tube crawler, using mechanical drive wheels to climb the tube. Mechanical arms are used to stabilise the device from rotation during the inspection. The system also uses a dual-axis laser diameter measurements to measure diametrical strain. MP encourages clients to perform a baseline inspection of new tubes for a better comparison for creep strain. Key advantages of Eddy Current Inspection are:

- No coupling media required
- Inspection without the need of catalyst removal
- No surface cleaning required
- Automated inspection solution avoiding the need for scaffolding
- Full coverage across the length of radiant tube
- Generally quicker than Ultrasonic Testing

Design of the Eddy Current coil is important to obtain adequate sensitivity, eddy current penetration, and signal to noise ratio. Tube with a high percentage of nickel content, such as HK-40, requires the use of a biased coil or a shield design to reduce effects of material permeability variation. In the NDT industry, it is the elimination of the undesirable responses, such as this, that forms the basis of much of the technology of eddy current inspection [69]. One scheme that has been developed is the segmented “Array” probe which uses 6 to 8 segmented coil design for increased signal to noise ratio, reduced averaging, and provide

more detailed information on defect morphology [14]. Factors that can limit the performance of Eddy Current testing that could potentially lead to false reading are:

- Proximity/Lift-off of the inspection probe, influencing the signal response. Typical examples are scales and welds steps.
- Inner wall defects many not be detected due to penetration levels.
- Ferrous materials with a high percentage of Nickel (such as HP-40) requires the use of magnetically shielded or biassed coils to avoid the effect of material permeability variations.

2.4.3 Infrared Thermography

Infrared Thermography is a technology used to create multi-dimensional thermos image using infrared radiation sensors. Thermographic cameras (infrared) are commonly used to detect radiation in the long-infrared range of the electromagnetic spectrum (wavelength of 8-15µm) and produce a pixelated thermal image (thermogram) presenting the distribution of thermal energy. The principle is that all objects above absolute zero emit infrared radiation according to Planck's law. The amount of radiation produced proportionally increases with the temperature of the object, hence by measuring the infrared radiation level one's environment can be monitored with or without visible illumination.

Described in a study by James, S [17] is the use of infrared thermography as an inspection tool for measuring the surface temperature of reformer tubes during operation. Shown in Figure 2-17 is a thermogram of two different rows of the same reformer, with the image on the left showing normal thermal pattern and image on the right shown signs of flame impingement problems due to burner failure.

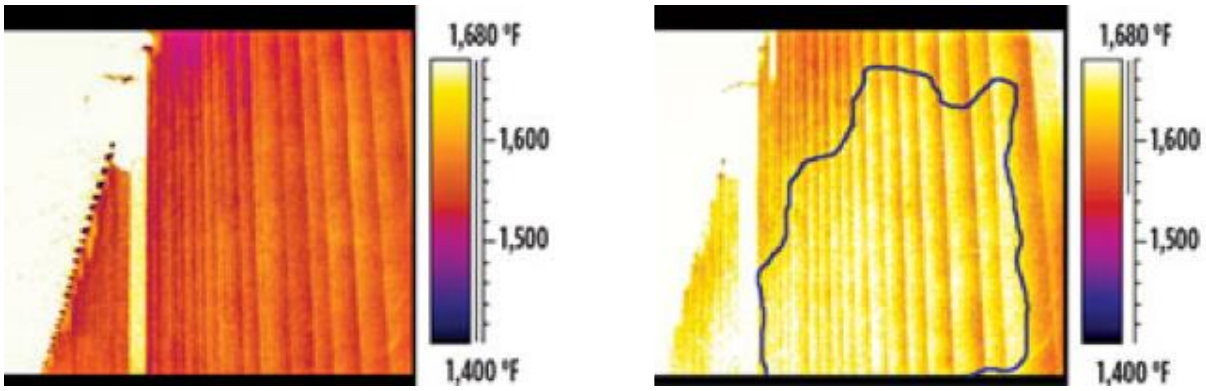

Figure 2-17 Side view of reformer tubes thermal pattern [17]

Infrared thermography is also used in identifying other common reformer phenomena, such as refractory and insulation problems. Shown in Figure 2-18 are various refractory problems indefinable by infrared technology.

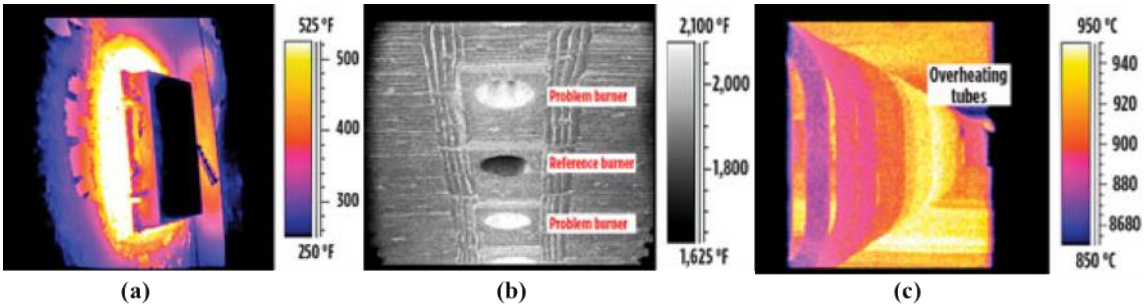

Figure 2-18 Thermal image of common failure detected by Infrared Thermography a)refractory failure located around peephole b)failure of burner tiles c)over headed pigtail tube section [17]

The average temperature of exposure together with the present microstructural condition can be used to correlate stress v/s service time and LMP for life prediction [68]. Unfortunately, numerous study has identified limitations with this technique for estimating the remaining service life of reformer tubes. Because relatively minor differences in temperature have a substantial impact on tube life, a very high resolution and reliability of the temperature measurement is required; typically a 25°C increase in tube temperature will reduce the life by 40% as shown in Figure 2-20. Shown in Figure 2-19 are the common uncontrollable variables stemming from the inaccuracies of Infrared Thermography methodologies such as background radiation, emissivity, and flue gas composition [10]. According to the author, errors of >40°C are quite common.

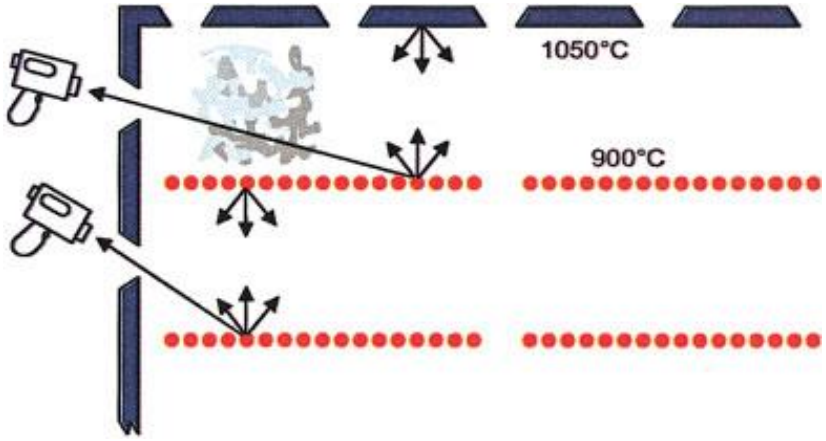

Figure 2-19 IR tube monitoring illustration

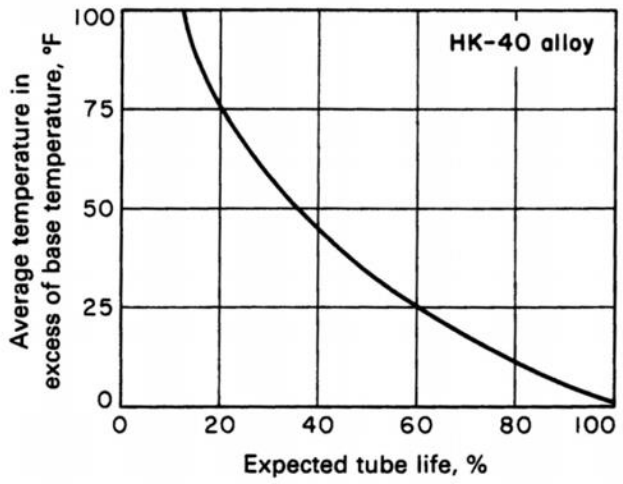

Figure 2-20 Effect of exceeding the design temperature on the expected life of HK-40 alloy reformer furnace tubes [51]

2.4.4 Laser Profilometry

The most recent advancement in the NDT RTIS has been in the introduction of a Laser technology that has traditionally been used in the nuclear power industry.

The fundamental theory is based on the diametrical growth evaluation technique used for creep strain detection in conventional systems. Shown in Figure 2-21 is a schematic diagram of the common arrangement of optical components of a Laser displacement detection. The principal rationale behind this technique is as follows. Using a Focusing Lens the beam from the Laser Diode is projected onto the internal surface of the reformer tube. The photodetector then sees the laser reflection through the Imaging Lens, generating a signal proportional to the spot's position on the detector. As the distance between the target surface and light source changes within the inspection range, the imaged spot on the photodetector shifts due to the parallax. Combined with fast single processing electronics and sensor position detection system, this system is capable of making submillimetre creep strain measurement anywhere along the tube. Although this technology has been used for reformer tube inspection since the 1990's, the patent for this application was not filed until December 2003 [70].

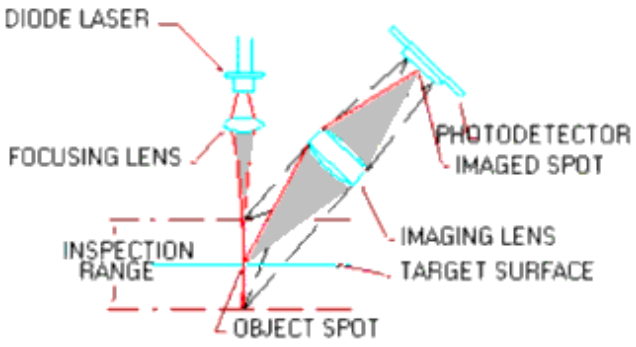

Figure 2-21 Laser Triangulation [71]

One of the best examples of Laser Profilometry technology in the CSR industry is the Laser-Optic Tube Inspection System (LOTIS®) developed and owned by QUEST Integrity Incorporation. Using a unique laser probe, the internal inspection technique collects millions of radial displacement measurements covering the majority of the tube surface circumferentially along the entire length of the tube, including the flange and reducer. Shown in Figure 2-22 is a graphical depiction of the LOTIS system. Using an umbilical cable carrying power and data transmission lines, the LOTIS probe is mechanically driven through the tube with the assistance of gravity. As the probe travel through the tube, the laser head design spins at 1800rpm, scanning the internal surface in two dimensions, generating a helical set of radius data that represents the inside surface topography of the tube. Using 3D contour representation of the collected data the operator can detect non-uniformity in the radial deformation for identifying areas with accelerated creep damage and misbalance in the plant operation. Further, the RLA is evaluated using the Larson-Miller parameter (LMP), based on diametrical growth and the creep staining characteristic of the tube material. Review of this system has been identified with many benefits, such as fast inspection time, accurate measurement of tube diameter, determination of creep damage and RLA, and clear pictorial display of data [11, 16].

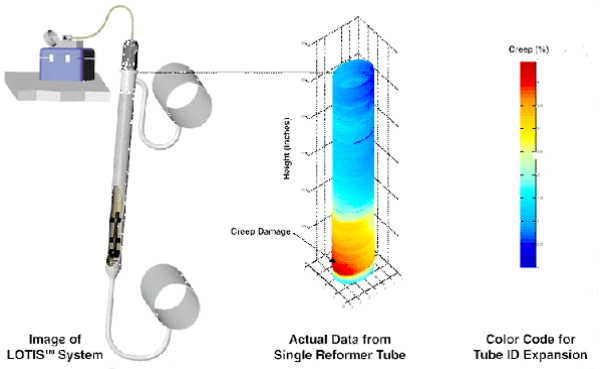

Figure 2-22 Graphic of LOTIS System in Operation [18]

The major advantage of laser inspection over other NDT method reviewed in the preceding section is the amount and accuracy of the profilometry measurement that the system can collect in short period (typically ~3 minutes per tube). The axial and circumferential data density is sufficient for a true average diameter inspection at each axial position. QUEST also recommends that baseline data is collected for each tube before installation. This baseline data will detect an abnormality in the tube, such as machine gouges and hot tears, providing a 'fingerprints' for each tube for better comparison.

There are many industry reports that identified this method to be sufficient for reformer tube inspection of creep calculation and detection [10, 15, 49]. 3D mapping of the measurement data clearly shows the relationships between adjacent, or portion of adjacent tubes, and provides a powerful diagnostic tool that not only unambiguously automatically identifies problematic tubes, but allows the plant personnel to clearly visualize the problem areas and take action to replace tubes, accurately predict lifetimes and rebalance the heat distribution to reduce damage in the future [72]. Plant engineers and inspectors are not only responsible for daily monitoring and reformer operation but also the assets' long-term reliability. Detecting and quantifying creep damage in the early stages of an asset's lifecycle allows equipment owners to manage the reliability of the steam reformer tubes proactively.

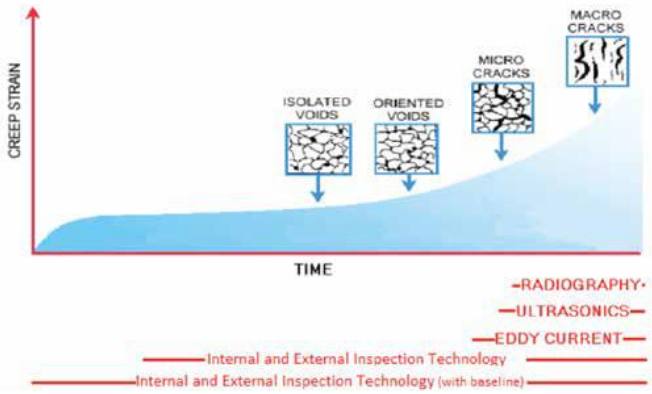

Figure 2-23 Inspection Technology Comparison [11]

There has been numerous study comparing the laser sensing technology with conventional inspection technique to determine the effectiveness of the technique in assessing reformer tube condition. In the chapter in the Handbook of Material failure Analysis [73], a section is published investigating the conformance of the LOTIS system through experimental comparison with the LOTIS result and Metallographic and mechanical testing.

One of the disadvantages of the laser inspection is that the catalyst must be removed to access the tube bore. This limits the application to during catalyst turn around period where the catalyst is loaded/unloaded, around 3-5years. Hence the technique is often compromised with other external techniques, commonly using the eddy current system [74]. However with the benefit of early inspection and frequently planned downtime for catalyst refilling, this technique remarks for a very effect decision-making tool. It should also be noted that the period between schedule plant shut is extending. Improvements in catalyst has extended the life mean that the average run length between turnarounds has steadily increase. This decreases the available inspection times for LOTIS leaving significant gaps in the inspection frequency. Based on this trend, QUEST has developed an external laser inspection called the MANTIS.

Laser Profilometry technique is not limited to just the primary reformer tube but can also apply to other components of the primary reformer such as the inlet and the outlet pigtail tubes. C. Maharaj [27] at the University of West India studied a retired reformer outlet pigtail tube retrieved from a methanol reformer plant constituting 384 catalyst tubes. Although the reformer temperature and pressure parameters were controlled to within the standard operating procedure, the specimen tube failed after approximately six years of operation, resulted in the first unplanned plant outage. The tubes are constructed out of Incoloy 800H material, designed for a nominal life of 100,000hr (11.4 years) provided the operating parameter does not exceed the temperature and pressure of 900°C and 20 bars.

2.4.5 Current Technology Comparison

In this section, four NDT used for Reformer Tube condition assessment were reviewed, discussing the basic principle of each technology and the pros and cons in the context of Catalytic Steam Reforming industry.

Of the four systems, use of infrared thermography and permanently installed temperature sensors is the only technique applicable for continuous plant assessment during plant runtime, along with visual inspection, that providing valuable monitoring of the plant operation. However, due to the limitation of accessibility and sensing technology, significant error is apparent in the collected data hence limiting the full implementation of the technique. As creep damage is an accumulative, time-based phenomenon, visual and thermography technology alone is determined inadequate for accurate RLA evaluation.

Consequently, Eddy Current and Ultrasonic inspection has been the dominant NDT approach commonly used during plant downtime. Using external crawler design, both techniques can accurately detect granular creep damage without the need for the tube being emptied. Because ultrasonic testing is more susceptible to false reading, the tube is required to be cleaned, and acoustic couple media is necessary for accurate ultrasonic testing, giving Eddy Current technique an advantage regarding reliability and repeatability. However, because development of creep void and microcracking is only evident in the last 20% of remaining service life, both approaches are limiting to the later stage of the tube service life. This is typically considered too late in providing the plant operator enough time to make operational changes for extending tube life.

The latest and significant advancement in the NDT industry in the last couple of decades has been the development in the Laser Profilometry technology. Unlike the conventional systems, studies have determined that laser profilometry is the only technique capable of identifying creep strain in its earliest stages, providing valuable insight into the furnace operation from day one of tube being commissioned, creating a unique and powerful decision-making tool [15]. Using optical triangulation, millions of displacement data is able to be quickly collected for generating an accurate 3D reconstruction of the reformer tube internal geometry. Using rupture time models specific to the material (such as the LMR parameter), inlet/outlet temperature records, and a log of cyclic thermal loading, diametrical comparison with baseline data is performed for an accurate RLA evaluation. Also, collective data analysis using 3D contour representation allows for a powerful debugging tool for a better-balanced furnace. However, as access to the internal cavity of the tube is required for conducting the evaluation, the implementation of this technique must typically be in line with catalyst replacement procedures when the tube is emptied, hence requiring great emphasis on fast assessment to reduce the overall plant downtime.

There are no decisive advantages between the methods in making a conclusive decision in selecting one universal system. Hence their application is dominantly subjective to the plant condition, company maintenance philosophy and owner's preference. There have been reported cases where reformer tube fails with minimal creep strain, and structural changes occur with minimal creep straining. Correlating remaining life with microstructural degrading are found to be difficult as the microstructural changes occur in a non-monotonic way hence limiting the performance structure evaluation methods[7]. Consequently, with numerous tube failure mechanism that exists the degree of damage within a particular tube may not lead

itself to that specific NDE technique; tube condition cannot be accurately determined by one stand-alone technique [10, 12, 13, 16, 33, 50, 67, 75-78]. To this, there are many inspection equipment designs to be complementary or integrated with numerous NDT technology for a comprehensive inspection.

Quest Integrity recommend a combination of the internal and external system to accurately evaluate the remaining life assessments based on Laser Profilometry and Eddy Current inspection [79]. Using their LOTIS and MANTIS technologies, a comprehensive data collection strategy coupled with sophisticated remaining life assessment software model. Shown in Figure 2-24 is the overlay comparison of the creep strain and the Eddy Current detection. Similarly, ARTiS [67], LEO-SCAN, and the BRUCE system [32] use an automated robotic crawler to aid ultrasonic or eddy current testing and diametrical growth inspection. Further, there are publication of the H-Scan system (Figure 2-25) which in cooperates Ultrasonic and Eddy Current technology, as well as dimensional measurements and wall thickness data for a combined NDT methods to complement the lacuna of the various NDTs when performed alone [16].

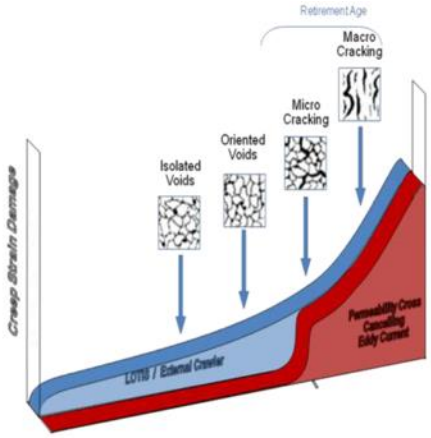

Figure 2-24 Creep Strain detection versus Eddy Current Detection Overlay comparison[80]

Figure 2-25 H-Scan® of Reformer Tubes [16]

It is seen that diametrical growth evaluation is common to all advanced NDT systems that are currently available. While this measurement is relatively easy to obtain, it indicates that creep strain data is of great value for RLA. With the advancement of laser technology, mapping of the internal tube geometry through profilometry analysis has proven to have an advantage over conventional technique as the tube can be evaluated from very early stages, well before creep void is evident. Early warning of both tube and the furnace performance allows the operator the opportunity to modify the plant parameters to increase the tube life, while eddy current and ultrasonic testing are applicable only in the later stage of the creep damage.

2.4.6 Need of Futher Research

There are two significant limitations that have been identified with the current laser inspection system. First is the limitation of diametrical calculation of creep strain. Although radial displacement data is collected by the LOTIS, the creep strain is evaluated based on a diametrical evaluation. Because creep is a temperature and time-dependent phenomenon, the degree of creep rate at a given axial layer of the reformer tube wall is never even in practice, resulting in an anisotropic deformation. Consequently, the diametrical calculation will result in an averaging effect of local creep deformation which limits the ultimate precision of the creep strain determination. To achieve accurate radial calculation, the tube centre must be determined and tilting of the measurement plane must be detected or minimise, as discussed in Chapter 3.

Secondly, internal NTD system lacks the ability to determine the angular position of the measurement data relative to the reformer tube. Where external crawler uses neighbouring tubes or the furnace wall as guidance for stabilisation internal system is driven mechanically using umbilical cords with no guidance as to counter any rotational movement while performing the inspection, other than roller wheels. While tube axial (depth) positioning can

be directly controlled by the length of the suspending cable, the angular orientation of the system is uncontrollable and can rotate from uneven loading on the wheels caused by inconsistency of the internal wall surface, weld step, and localised bulging. Hence, the certainty of the circumferential position of the profilometry data is unknown, especially towards the bottom of the tube. Significant advancement here can lead to improved reformer operation, reducing creep damage, a better-balanced furnace and better planning of tube replacement, eliminating unnecessary/unplanned outages.

2.5 Preliminary Study

In the preceding section, four NDT techniques used in reformer tube inspection was reviewed. From it, we have identified that internal profilometry technology, combined with 3D contouring and diametric analysis, to be a powerful diagnostic tool for early creep strain detection, accurate prediction of remaining service life, and rebalancing of heat distribution. Presented in this section is the preliminary study conducted in collaboration with Methanex NZ that has become the basis of decisions made in this research [24]. This study focused on advancing NDT techniques of reformer tubes using profilometry analysis by proposing new topology for internal inspection. The new system imposes elements that are unique to this study that is explicitly selected to consider the limitations on the LOTIS as reviewed in the preceding section (Chapter 2.4). Main elements discussed in the study are the viability of wireless communication, consideration of full automation, practical modular implementation, and creep strain detection through diametric measurements. The feasibility of this method is evaluated through practical experimentation.

2.5.1 FTIDM testing system design

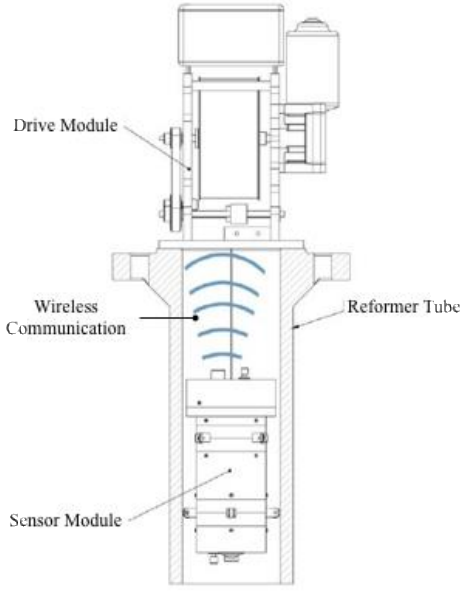

Figure 2-26 Graphical representation of the Internal Inspection system Prototype

Shown in Figure 2-26 is the assembly diagram of the initial Reformer Tube Internal Diameter Measuring system (RTIDM) developed for the preliminary study. This prototype is used to carry out the experimental validations of the proposed system architecture. The design comprises three components; Sensor Module, Drive Module, and a Control Station (not shown in the depiction).

The Sensor Module is constructed out of cylindrical aluminium body (100mm diameter x 200mm Length). The hardware of this module mainly consists of mechatronics sensors, battery bank, electronic control system and a wireless module. Unlike existing Reformer Tube NDT systems, the Sensor Module is completely untethered, made possible by the wireless technology and integrated power bank. The controllers, wireless module, and sensors are selected for minimal power consumption, allowing for sufficient battery life with only three 1.5V Alkaline battery.

The profilometry measurement and control system is composed of diameter measurement and tube end detection sensors. Sensor Module is capable of measuring four diametrical measurements simultaneously in real-time. To achieve this, a 10bit magnetic rotary encoder is used in collaborative with a mechanical linear transducer mechanism. With eight radially projecting encoder arms with 10mm roller bearing, the mechatronics linear transducer is capable of measuring diametrical displacement ranging between 98-110mm at ±0.0146mm accuracy. The encoder arms are mechanically coupled which allows only for symmetrical

movement with the opposing encoder arms. This result is a self-centralisation capability without the need for a separate stabilisation mechanism.

Located at the bottom and top faces of the module are set of mechanical limit switch and SONAR proximity sensors to detect the two ends of the reformer tube. Measurements from the end detection sensors, together with the profilometry measurements, are processed by an 8bit microcontroller into a 46bit data packet and sent to the wireless module for transmission to the Laptop control station.

Selected for the wireless module for this application is a 2.4GHz XBee module manufactured by Digi International. An advantage of using this module is the integrated feature of complete management of secure networking between multiple nodes with minimal processing required by the linked microprocessors. Of the abundant range of XBee modules that are available, the 1mW wired antenna version was used to minimise power consumption. Network topology used for this study comprises of two nodes, a coordinator module located on the Driver Module, and a transmitter End Device found in the Sensor Module. All sensor measurements are collected by a secondary microcontroller, while a laptop computer with custom developed LabVIEW software is used as control software. The operation of the FTIDM system is completely automated with minimal interaction required by the operator during an inspection. The graphical user interface (GUI) has only a few features for activating the inspection cycle, real-time data graphing, and configurable debugging parameters. The acquired data is logged into the computer memory in a Microsoft Excel spreadsheet format.

The Sensor Module is mechanically driven with the means of gravity assisted hoist mechanism, similar to the LOTIS system. However, RTIDM system uses a 1.5mm stainless steel rope, instead of a thick umbilical cable, along with a fully automated spooling system for accurate control of the Sensor Module movement. The spool is directly driven by a 12V automotive DC motor (geared) which is controlled by the control software. Handled in software is an adjustable motor management state-machine, featuring acceleration/deceleration profiling for complete automation using sensor feedback control loop from the ultrasonic sensors. USB serial COM port is used to communicate with the H-bridge Motor Driver, which can provide precise voltage to the DC Motor by adjusting the duty of pulse width modulation (PWM). A 10bit rotatory encoder is used to continually monitor the position of the Sensor Module during operation. This feedback data is sent back

to the control algorithm for a closed-loop control system, with implementation of virtual limit switches for added system robustness.

2.5.2 Experiment Setup

The FTIDM system was tested on a 14m reformer tube intact with both the upper flange and the reducer. This specimen tube, provided by an industrial company, was retired from service as significant creep staining was detected, and is now used predominantly for research applications. The tube is mount vertically against a staircase next to the reformer, mimicking the orientation during operation, and the top opening is accessible from the one of the staircase landing where 240V mains power is available. To evaluate the performance of the prototype system, a total of 30 inspection trails where performed in which the FTIDM system collected profilometry data under full automation. The control parameters were adjusted so that diametrical measurement is obtained at 10mm axial increments. The logged data is then plotted on a diameter-vs-depth plot and then calibrated based on five key observation point on the curve listed in *Table 2-5*. Shown in *Figure 2-27* is the output data from trial number 16.

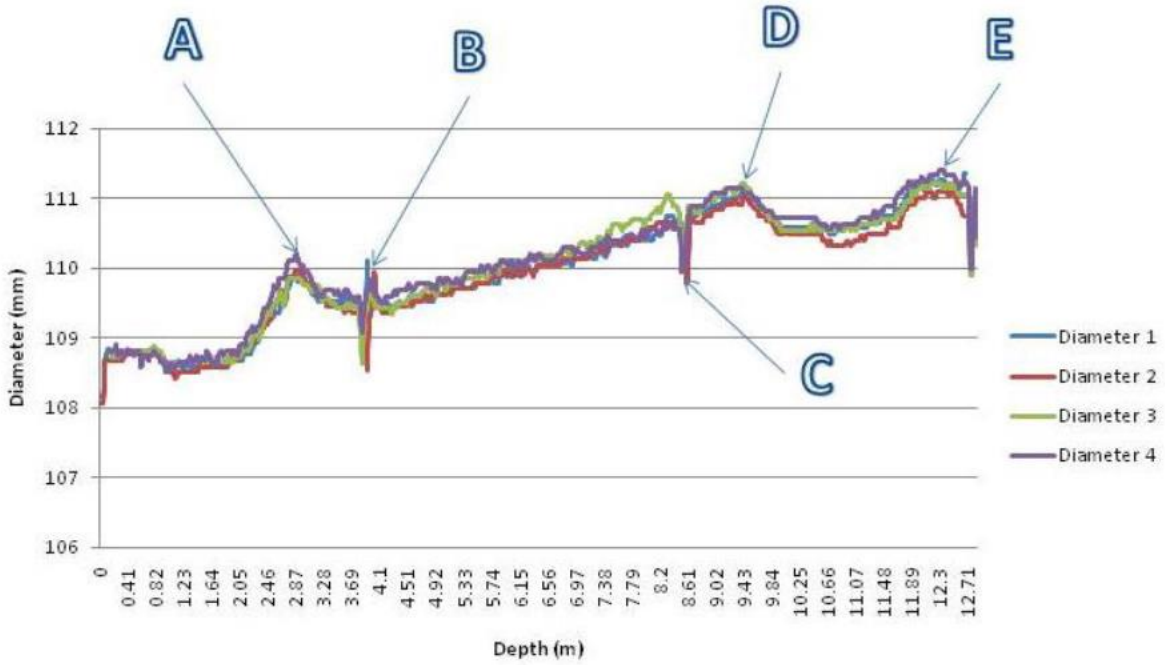

Figure 2-27 Data collected from Trial 16

Table 2-5 Data output feature description

Identifier	*Feature*
A	Diametrical growth seen at bottom of the first radiant tube segment
B	Weld step between first and second radiant tube segments
C	Weld step between second and third radiant tube segment
D	Diametrical growth observed at top half of the third radiant tube segment
E	Maximum diametrical growth observed at bottom of the third radiant tube segment

2.5.3 Results and discussion

Overall, the modular design served to be a very practical solution for Reformer Tube assessment. The compact design allowed for quick and easy setup, and the Control Software allowed to fast and consistent inspection trials, completing a full inspection cycle at a rate of 2~3 minutes per tube. The wireless network was stable throughout the experiment with no losses for measurement data.

Evaluation of the collected data was adequate, showing gradual increase in the tube diameter towards the bottom of the tube. A maximum diametrical growth of 2.5% at the bottom segment of the specimen was consistently detected throughout the trials, which marks the industry standard point at which reformer tube are retired. However, deviation between the four sensors are consistently observed at various location down the tube. This was first considered to be caused by interfering of the radio wave propagation but was later determined to be due to anisotropic deformation in the tube. Observing point A and C in Figure 2-27, a greater diametrical growth in one of the measurement axis is seen. This indicates a localized Creep Straining is occurring, possibly caused by catalyst choking or furnace misbalance from burner misalignment. At point E, a more sever deviation between the diametrical measurement is observed, again, indicating anisotropic deformation is more common towards the bottom of the tube with more creep straining. While assumptions can be made from the collected data, the exact determination of the actual distribution of the Creep Strain at a given location is impossible using diametrical measurements only. If radial measurement was to be determined from the collected data, the tube center axis must first be determined which reasoned not possible with the mechanical stabilization solution.

It has been asserted previously that internal inspection systems driven mechanically on roller wheels are prone weaving against the surface of the internal tube wall causing the system to rotate axially during inspection. This was also obverse during the experiment during the trails. This is best described by comparing measurement collected on trial 4 and trial 5 (Figure 2-28). When comparing the profilometry data between different trial, measurement collected between the top segment to the midpoint of the second segment. When comparing maximum creep straining at the bottom of the second segment of the tube, although the four diametrical curve matches each other, the reading between relative sensors has changed. This indicated that between the adjacent trials between trail 4 and 5, the sensor module followed a different path. One solution to avoid this is to devise a guide mechanism to resist the sensor from rotating. This is deemed unpractical to achieve with the steel rope and hoist arrangement under the spatial constrain inside the tube. Hence it is wiser to implement a sensing technology to track the rotation of the module and correct for the distortion in software.

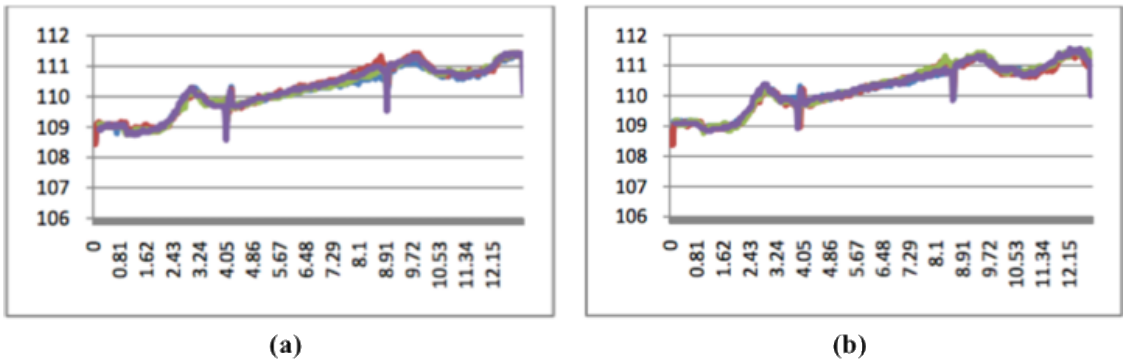

Figure 2-28 Profilometry data (a) Trial 4 (b) Trial 5

One of the drawback of the XBee wireless module is the limited data transfer rate experience during the trial. Although the module benefit with secure and low power wireless solution, the data transfer rate is significantly slower compared with tethered alternative (e.g. Ethernet, USB, CAN bus). On average, a sample rate of 8 Hz was observed during the experimental trials, limiting the maximum speed of the Sensor Module to approximately 0.1m/s when set to 10mm axial resolution. From this the overall data transfer rate can be determined. Taking an average data packet size of 46byte/packet and multiplying by the 8Hz sample rate, the data throughtput of the wireless system can be determined to be 368bytes per second (Bps), equating to 2944 bits per second (bps). Though this figure is far less than the 250kbps transfer rate stated in the XBee module datasheet, it is consistent with the typical performance observed in close proximity application. Shown in Figure 2-29 is the performance of a XBee module S2, throughput as a function of packet length and baud rates,

observed in peer experiment carried out in a 5m X 8m office space [81]. At baud rate of 9600bps and packet length of 46bytes approximately 2900bps throughput is observed. Comparing this figure with the 2944bps seen in the experiment, it indicates that the reformer tube is performing effectively as a waveguide for the 2.4 GHz radio wave and provides a suitable environment for the XBee module application. Using the XBee Series 2 module and higher baud rate, along with improved data packaging protocol, the performance of the XBee module can further be improved for a faster sample rate, hence resulting in quicker inspection.

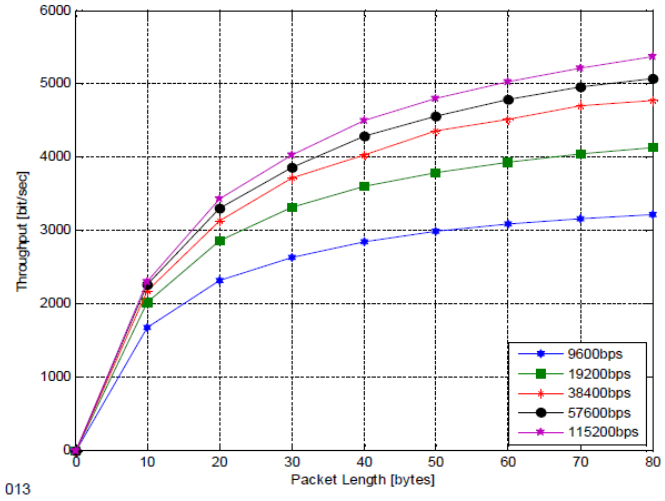

Figure 2-29 XBee S2 Module Throughput versus Packet Length [81]

2.5.4 Preliminary Study Conclusion

Preliminary study conducted in this worked aimed to investigate the feasibility of the fundamental elements of the proposed methodology. Through experimental evaluation using a complete reformer tube assembly, several contributions to the knowledge of performing creep strain inspection using internal profilometry system. Main finds are as follows.

- The creep strain detection capabilities using diametrical are influenced by the distribution of creep strain in the reformer tube wall. With four diametrical measurements, creep strain can be inspected accurately and repetitively for tube used under balanced operation with isometric deformation. However, result has shown that the performance of the method reduces when subjected to tube with anisotropic deformation. The most significant cause of this is the inability of the mechanical stabiliser to keep the measurement datum along the true axis of the reformer tube resulting in an offset in the measurements. The extinct of the reduced performance is directly proportional to the severity of the tube asymmetric deformation and the result

amount of offset. The system requires the capability to detect and correct for measurement datum offset.

- Experiment confirmed that mechanical guided internal inspection probes are vulnerable to axial rotation while traversing through the reformer tube during inspection. This has contributed to the inconsistency in the profilometry measurement, especially in sections of the tube with uneven deformation. Further study is need to either to counter the mechanic wheels tendency of weaving or devise a method of tracking the angular movement.
- The first application of wireless technology as a primary communication method inside reformer tube was presented. The combination of reformer tube and XBee module has proven to provide an adequate alternative to the mechanical data transfer line commonly used in existing NDT inspection systems. Typical reformer tube with an internal bore of greater than 100mm will serve as an effect waveguide to accommodate the low power consumption, bi-directional 2.4GHz XBee modules. However, the throughput of the wireless network is relatively low compared with a hardwired solution (and other wireless alternatives) and consequently becoming a bottleneck to the prototype, limiting the inspection speed. By increasing the baud rate, optimising the data packaging format and handling protocol, the data rate can be improved.

3 Creep Detection Algorithm

Profilometry analysis is one of the best tools for inspecting tubular structures, and the only method that is currently available for detecting early-stage creep damage in reformer tubes in a non-destructive manner. This technology has been implemented in the CSR field for more than two decades and is most commonly recognised by the LOTIS system developed by Quest Integrity [10, 15, 18, 19]. The current method is limited to diametrical analysis of profilometry data, limiting the performance when subjected to unevenly distributed creep straining. Due to averaging effect, anisotropic characteristic in the profilometry measurement is diminished causing inaccuracy in quantifying the severity of creep damage. This chapter presents and discusses the proposed creep damage detection algorithm for evaluating profilometry data for creep straining using radial measurements. Work presented in this chapter is intended to contribute to advance the existing methods for pipe inspection by filling the knowledge gap identified in the Literature Study.

This chapter is structured as follows. In Section 3.1 the current internal profilometry inspection technology is reviewed in the context of the accuracy of the radius measurement and data distortions resulted from measurement datum misalignment. In section 3.2, the creep detection algorithm is presented, discussing the mechanism and practical implementation of the method for reformer tube inspection. In Section 3.4, the performance of the proposed method is analysed in an experimental proof of concept approach, using segments of retired reformer tube. Finally, the result from the experiment is discussed and summarised, highlighting the key finding in the study.

3.1 Introduction

The fundamental principle of reformer tube creep strain inspection is the detection and quantification of the cross-sectional tube deformation caused by granular boundary slippage in the tube wall. Conventional NTD system uses proximity sensors to measure 4 to 6 external diametrical measurements to determine the retirement of the tube based on diametrical growth of 2-3% for HK40 and 5-7% for HP45 is detected [34, 75]. Due to the small number of measurement samples, only a very general insight of the tube creep condition can be evaluated when subjected to uneven creep straining, as confirmed by the preliminary study presented in Chapter 2.5. The laser profilometry system uses high-resolution radial measurements to map the entire tube internal surface. With larger measurement data, better diametric analysis can be performed using the nominal design diameter or baseline data set.

Radial data benefit over diametrical measurements as localised anisotropic values can be identified with 3D contour plotting, allowing for detection of other various tube failure elements such as burner misalignments and effect of portholes. Hence, Creep strain inspection in catalytic steam reformers using the profilometry inspection method has now become the current standard.

3.1.1 Pipe Inspection

Internal pipe and tube inspection is a common topic in many industries and has continuously caught the interest of researchers in both industry and academia. With the practical benefits of circular structures, and often associated with low cost and ease of manufacturability, application of cylindrical component will continue to exist indefinitely in association with the advancement of inspections technology. Standard applications are fluid conveyance, structural members, and pressure chambers. One of the major research areas in internal pipe inspection is in sewer lines and oil & gas industry [82, 83].

The traditional inspection methods uses Pipe Inspection Gauge or PIGs to probe the wall of the pipe using ultrasonic, infra-red, mechanical sensors, eddy-current, and other NDT technology [84-88], like that used for reformer tube inspection described in the literature review. More modern system uses vision technology to profile, detect, and classify pipe defects using self-driven crawler architecture to autonomously travel inside limited access piping, such as the wheeled KANTARO [89] or the multiarticulate systems described in [90-92]. An onboard optic sensor, such as a closed-circuit television (CCTV) camera, is used to collect still image and/or video footage of the structures inner surface for high-resolution data capture for abnormality assessment. Common method used in assessing CCTV inspection data is feature classification. In the most primitive form, the pipe condition is visually inspected by a human operator based on video recording showing the pipe internal surface using standardised coding system such as the EN 13508 *Investigation and assessment of drain and sewer systems outside buildings*. Although the method can be very robust and adaptive, the performance is heavily dependent on the ability of the inspector and the quality of the captures video. In a case study in [93], the consistency of human data assessment was evaluated in terms of defect recognition, defect description, and interpretation of inspection report. The result indicated that the consistency of visual examination conducted by a trained

inspector can be low as 25%. Naturally, this has leaded to advancement in implementing autonomous software based analysis systems.

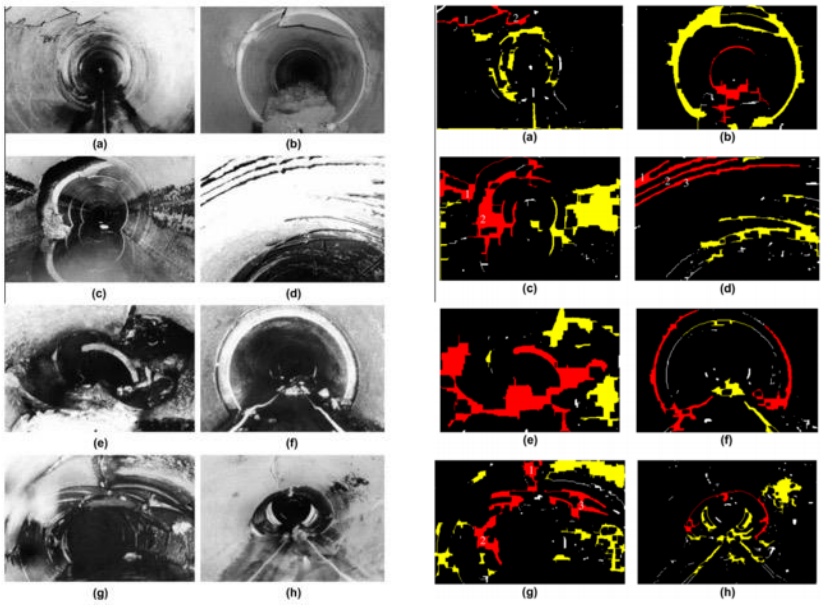

Figure 3-1: Feature Segmentation with Morphological measurement (a) Fracture, (b) Debris, (c) Hole, (d) Spalling, (e) Collapse, (f) Open Joint, (g) Broken, (h) Deformation [94]

Statistical classification and artificial intelligence techniques are used to develop diagnostic systems to assist the interpretation of sewer pipe defects on CCTV images to overcome human's fatigue and subjectivity, and time-consumption. In the work by Tung-Ching Su and his team [94] morphological segmentation based on edge detection is used to classify CCTV inspection images into one of eight categories; fractures, debris, hole, spalling, collapse, open joint, broken, and deformed sewer (Figure 3-1. In the work by Ming-Der Yang [95], machine learning was used classify defect texture features determined based on correlations of 2-dimensional discrete wavelet transfer and co-occurrence matrices. This work showed promising results of the overall accuracy of over 50%, revealing the potential of machine learning with sewer pipe inspection with remains for improves for practical application in the future work. For the application reformer tube, feature classification from 2-dimensional image is conceived to be limited as early stage creep straining gives minimal visual features. For a more convoluted machine learning algorithm, e.g. neural network algorithm, a large amount of training data set is necessary which is deemed difficult as there are minimal grouped set of profilometry measurement associated with creep deformation that is available.

Morphological pipeline profiling using laser triangulation, identical to the approach used in the LOTIS system described in section 2.4.4, is also a preferred method in the sewer industry. Laser range measurement is used for advanced geometry inspection and high-resolution 3D

modelling for pipeline assessment using various robotic platform [96-100]. Although the hardware architecture is very similar to that used in reformer tube inspection a more convoluted software analysis is involved. Illustrated in Figure 3-2 is laser image processing procedure used by D. Krys in his work [96]. First, the laser image is processed using various image filters and interpolation techniques to clean the image from noise and data outliers. Then phase congruency and image segmentation process are used to further repair holes in the measurement and region of interest is identified and segmented. The odometer data is used to stamp each data frame with the acquisition location. The pipes morphological profiles are processed from the estimated pipe centre, determined using numerical analysis such as centre-of-gravity, Hough transformation, or tri-point method [101], discussed later in the chapter. And finally, the result is presented as a 2D map or a 3D model for further data interpretation.

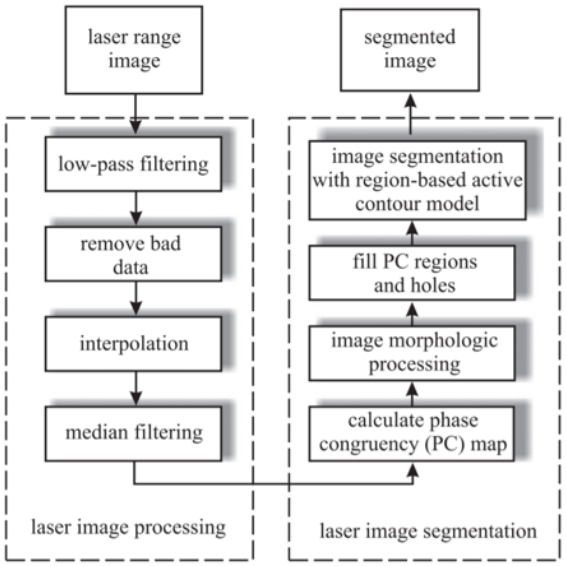

Figure 3-2: Laser image processing procedure example [96]

Alternatively, complicated image processing can be reduced by using 2-dimensional position-sensitive detector (PSD) in collaboration with rotating head mechanism for a faster and electrically power efficient solution that can achieve a radial measurement accuracy of ±0.1mm [102]. Overall when compared other morphological analysis methods, such as ultrasonic profiling, better resolution and accuracy are obtained hence laser profilometry system have proved to be a necessity for sufficient sewer inspection [88].

A modified method of abnormality detection based of laser-triangulation is the laser intensity profiling. In the work by L. Seneviratne [103, 104], an image processing method was studied which utilised light intensity variation to locate and identify defects. Like the previous

technique, a ring of structured light is shown onto the surface of the structure of interest and the image is captured using an onboard camera. After performing a two-stage signal conditioning with edge detection and contrast/brightness adjusting, partial histogram is generated by computing the local averages of pixel intensity along a defined number of segments of the pipe sectional profile. Because the area of defect reflect and scatter light differently to surfaces with no defect, deviation in the light intensity can be used to locate and identify structural features such as cracks and holes. Illustrated in Figure 3-3 is the output from an intensity-data-extraction algorithm with the peak in the profile indicating the location of a potential discontinuity. The benefit of this approach is that the performance is independent of platform misalignment nor deviation from pipe centre axis. Further, very small cracks and surface corrosion can be detected that is not featured in the laser geometric profilometry [105].

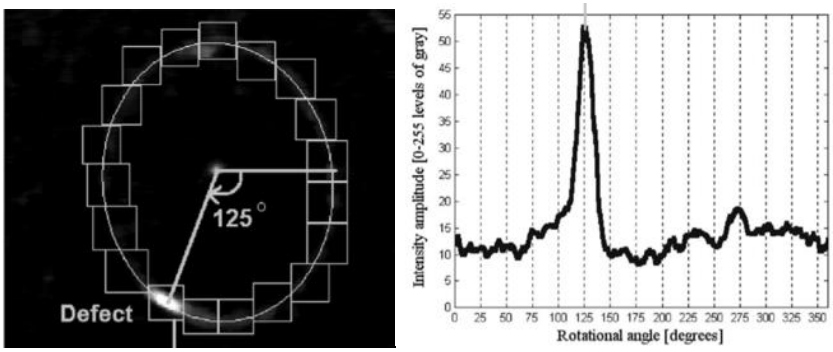

Figure 3-3: Output of intensity-data-extraction algorithm for pipe inner surface defect detection [106]

Like in the case of NDT technology for Reformer Tubes, there are no decisive advantages between the methods in making a conclusive decision in selecting one universal system for pipe inspection, as their application is subjective to elements such as pipe condition, environment, and resources. One approach to overcome this is to combine the technologies into one system. In the work conducted by L.D.Seneviratne a comprehensive system was developed for automated detection and classification of defects in tubular structures [107]. From single sectional line pattern, both geometric and light intensity is evaluated to extract features from the data as shown in Figure 3-4, and used to classify between one of five categories of defects using artificial neural network; hole, long. Crack, Radial Crack, Joint, and obstacle. However, the presented method does not account for anisotropic deformation in the sectional profile in the scale expected for creep damage in reformer tube.

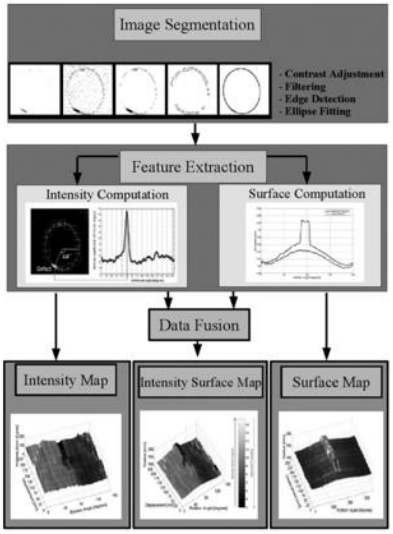

Figure 3-4: Overview of the comprehensive preprocessing and visualization algorithm [107]

In summary, research in the sewer industry is contributing largely to the advancement of pipe inspection technology. Laser profilometry is also recognized in this field as a powerful tool for various internal defect assessment, of which was reviewed for viability with creep inspection of reformer tubes. Centre alignment and system calibration are an issue challenged which ultimately determines the performance of morphological assessment, along with common error occurring in vision-based systems, such as light scattering and impeded visibility. As of this point, no method was identified applicable for direct use with early-stage creep detection in reformer tubes.

3.1.2 Significance of Datum Misalignment

There are two general challenges that are addressed with geometric analysis. One is data filtering of outlier measures in the measurement dataset introduced during sampling. For vision-based pipe inspection system, this is caused by a number on optical phenomenon affecting the image quality such as light reflection, camera resolution, ambient lighting, etc. The second challenge is the detection and calibration of measurement datum with the pipe axis sectional geometric datum. A datum reference (or just datum) is a point on an object that serves as a reference in defining a specific geometry of that object. In the case of defining the sectional profile of a cylindrical object, the object datum is the point at any given measurement plane that is in coincident with the circular axis. The datum is used by the inspection apparatus to create a system reference of the measurement space. Geometric data is prone to misinterpretation when the measurement space deviates from the physical space. In this section, the effect, cause, and significance of datum misalignment and data calibration are discussed.

Depicted in Figure 3-5 is an internal profile of a reformer tube wall with *1%* increase from its nominal diameter of *100mm* (illustrated as a dashed line). The blue dot is the measurement datum located *0.5mm* away from the tube axis along the X-axis. Radii measurements taken from the two measurement space and its relative angular position shown in Figure 3-6. The plot in green and blue is the two profilometry data taken from the tube centre and the measurement space respectively. Data collected during inspection is commonly described in 2D line graphs as it allows for a clear evaluation of the inspection results and creep growth; it also helps in making comparisons with previous inspections baseline dataset for performing trends and forecast assessments [11]. A random fluctuation of *±0.05mm* is introduced to the data point mimicking the error that may be induced during inspection; based on the accuracy of the LOTIS system.

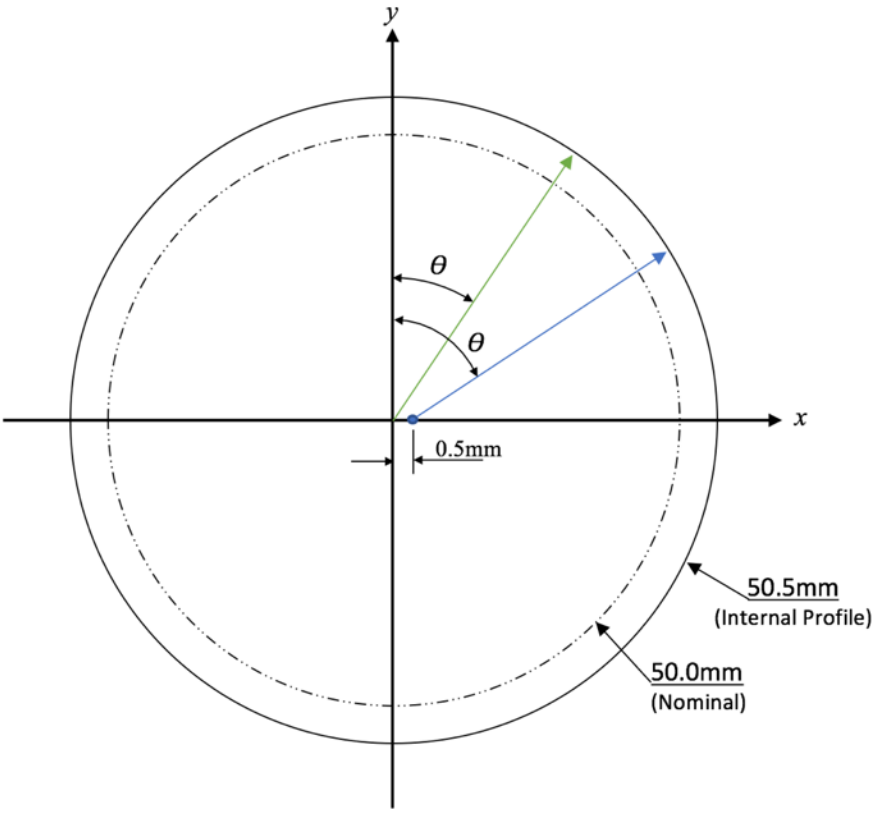

Figure 3-5: Internal Geometry of a Reformer Tube with 1% diametrical increase

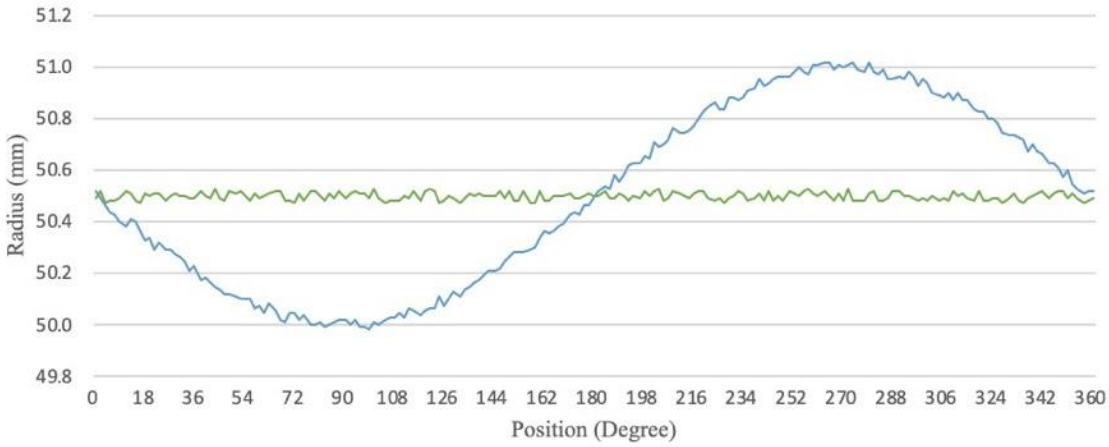

Figure 3-6: Sinusoidal distortion introduced from Datum misalignment of 0.5mm

Looking at Figure 3-6 the green line is the ideal interpretation of the geometry when the radius measurement is taken from the centre of the tube; a horizontal line about 50.5mm radius with minor variation from the sample resolution. From this data, the extent of creep strain can be clearly determined with no ambiguity and numerically determined by subtracting the difference between with the baseline data. When studying the blue plot, it is apparent that a misalignment in the measurement datum with the tube axis induces a sinusoidal characteristic, causing significant deviation from the actual profile. The magnitude of the distortion is proportional to the displacement of the datum offset as defined in-depth in section 3.2.2.1. At *270°* the radius peak at *51mm* which can be interpreted as a growth increase of *2%* in the reformer tube wall. Following the current standards, this will lead to a false retirement of a HK40 tube.

This is not a major problem in this example with isotropic deformation as the datum offset can be determined with simple centroid detection algorithms such as data averaging , circle-fitting, tri-point centre estimation which are seen in existing system. There are other mechanical means for minimising this phenomenon as discussed later in this section. With high-density profilometry dataset collected from systems like the LOTIS, averaging on the dataset at a given cross-sectional plane is adequate to determine a viable creep growth. However, for a tube with asymmetric geometry, this task becomes increasingly difficult.

Let us now study the second example geometry presented in Figure 3-7. The illustration shows an example cross-sectional profile of a reformer tube internal wall experiencing unbalanced creep straining that may have resulted from furnace burner misalignment. Represented in black dashed line in the centre of the Cartesian coordinates is the original profile of the tube before exposed to service (baseline data) with a nominal radius *Rn* of

50.0mm. The current geometry of the tube internal profile is shown by the solid line surrounding the original form. The symmetric region of hoop straining is shown in black line with a general isotopic increase in radius of R_h, and an area of localised bulging of isotropic deformation cause from accelerated creep, shown as a red line. This localised creep damage is further characterised by the angular distribution and a peak radius of R_m. The extent and distribution of creep strain is determined by calculating the difference between the baseline data and the new geometry at different regions. For this particular example, the tube is described as having a general hoop straining of *1%* and region of increased creep degradation distributed between *60°* and *120°* with a maximum creep damage of 2% at *90°*. Presented in Figure 3-8 and Table 3.1 is the corresponding displacement measurement *R* between *0-360°* associated with the relative position *Θ*. In this ideal situation, the profilometry data can be easy interpreted into general and localised creep region. The general creep is identified by flat region between 0-10 and 130-360. The localised creep damage is identified by a protuberance spreading over *50°* to *130°* with a peak radius *Rp* of *51mm* at the position *90°*, indicated by red/purple lines on the figure. The extent of creep damage and the remaining service life can then be determined using Larson-miller parameter and creep curve for the particular material.

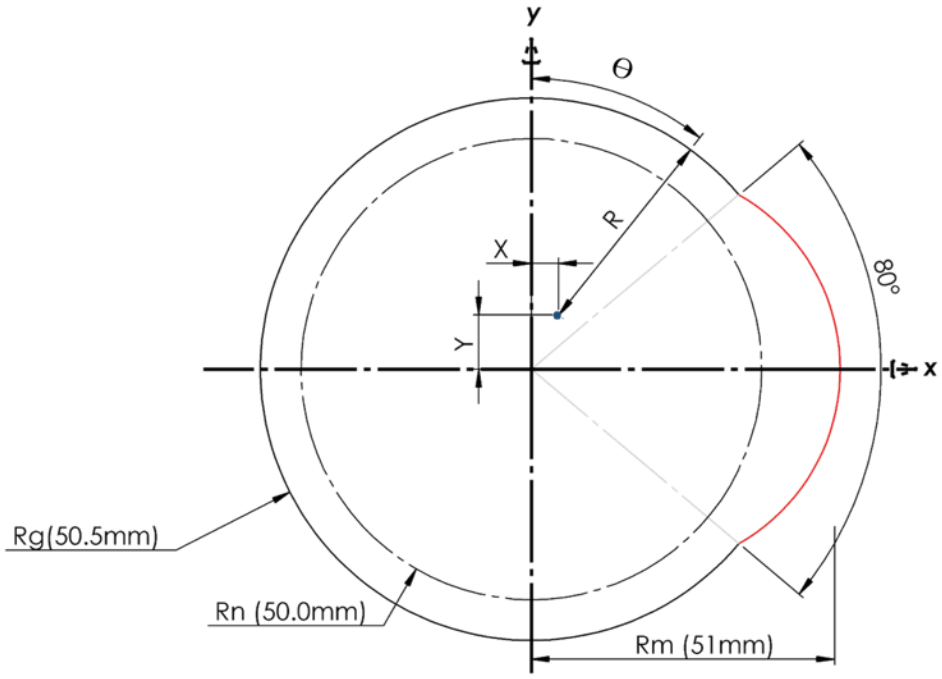

Figure 3-7: Sample Geometry with localized accelerated creep damage (not to scale)

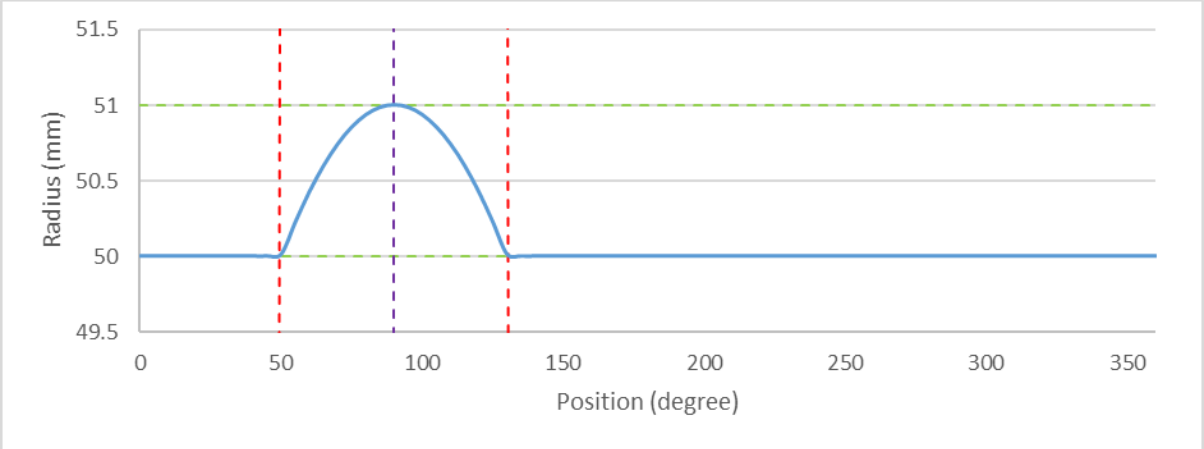

Figure 3-8: 2D Graph of radius vs position of sample geometry (X=0,Y=0)

Table 3-1: Sample Geometry (X=0, Y=0) evaluation

Creep Type	*Description*
Isotropic Hoop Straining	R_h: 50mm Region: 0-60 and 120-360 Creep Strain: 0%
Localise	R_p: 51mm Location: 90 Spread: 60- 120 Creep Strain: 2%

The blue dot indicates the centre axis (measurement datum) of a measurement instrument (e.g. LOTIS probe) where the radial measurements are made. With the limitation of electromechanical system, there always exists a level of calibration error between the measurement space and the tube axis. This is presented by the displacement *X* and *Y*.

The main cause of datum misalignment is due to the mechanical limitation of inspection apparatus guidance mechanism. For small pipe inspection, multi-actuating rollers are commonly used to stabilise the measurement probe to the centre of the pipe axis. In most cases, best stability can be achieved with three points of contact systems.

Figure 3-9: Typical LOTIS Laser probe with the Three-point Centralizing mechanism [10]

Shown in Figure 3-9 is an image of a LOTIS laser probe with the three-point centralising mechanism. Three-point stabilising (TPS) design uses symmetrically moving arms preloaded with outward force (typical using mechanical spring). Roller wheels with rounding edge are specifically used for a point contact with the internal wall of the tube at three locations on the sectional contour at equal spacing of *120°*. The nature of the mechanism drives the probe to a position inside the tube that is equal distance from the three points of contact. In a completely circular tube, this will force the probe to the centroid of the tube which is on the tube axis. However, in an anisotropic tube, this is not always the case as demonstrated further.

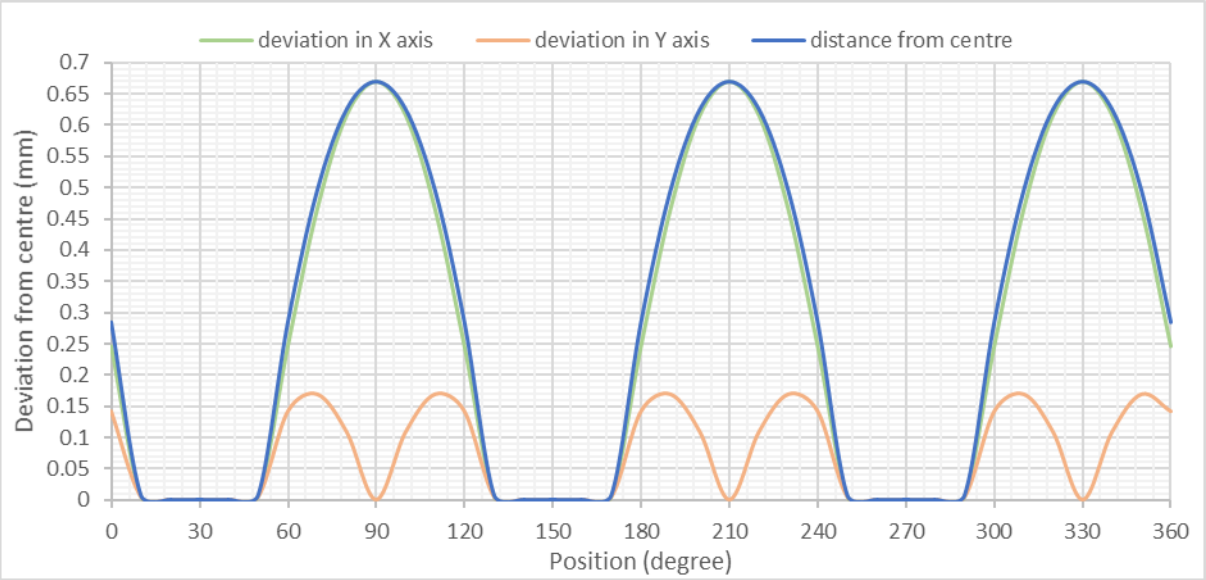

Figure 3-10: Three-point Centralizing mechanism used on LOTIS

Presented in Figure 3-10 is the displacement between the measurement datum and the tube axis as the TPS system is rotated around the sample tube previously presented in Figure 3-7. As each roller falls within the bulged region of increase creep straining the centre of the TPS (measurement datum) is shifted away from the geometry datum in the X-axis. Maximum displacement of *0.6689mm* is seen when the legs falls in line with the peak of the bulge at *90°*, *210°* and *330°*. Shift in the datum of *0.1793mm* is also seen in the Y-axis perpendicular to the direction of the bulge. To this, it can be concluded that even with an ideal TPS design with single point of contact that is evenly distributed and with no back lash in the mechanical construction, mechanical stabilising methods has limited performance in centralising the measurement datum for radius measurement in a deformed reformer tube. Its capability is dependent on the extinct and distribution characteristic of the anisotropic deformation of the sectional contour and the angular orientation of the TPS system.

Now let us study two specific scenarios when the TSP system is in such an orientation that the datum moves away from the tube axis. Presented in Figure 3-11 is the profilometry measurement taken in the first scenario where the TSP is positioned *90.00°* with the maximum datum offset of *0.6689mm* in the *X*-axis and *0mm* in the *Y-axis* as determined previously from Figure 3-10. Shown in Figure 3-12 is the same measurement taken in the second scenario when the TSP is oriented *70.00°*, with a datum offset in the *Y* and *X-axis* of *0.1694mm* and *0.4650mm* respectively. A green and red lines indicate the maximum and the minimum measure *R*, and the spread of the localised creep straining. The purple line shows the true peak radius R_p.

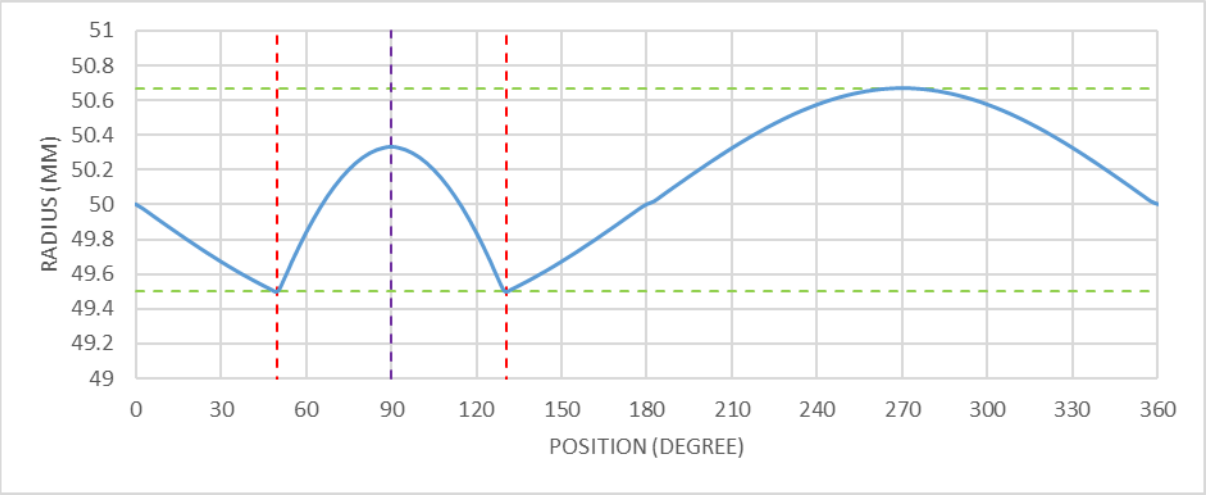

Figure 3-11: Profilometry data from Sample Geometry (X = 0.6689mm, y=0.0000mm)

From Figure 3-11 it is clear that a datum shift in the direction of the localised bulging has created a consequent increase in the radii measurement in the opposing direction with a maximum displacement of *50.6689mm* at *270.00°*. The measurement between the red lines has decreased in value roughly equal to the amount of datum offset, resulting in a peak of *50.3311mm* at *90.00°*, *0.6689mm* (*1.3%*) less than the actual *51mm* (*2.0%*). The distribution of the anisotropic creep straining has spread from *80.00°* to *81.00°* with minimum radius values of 49.4895mm at the positions 49.50° and 130.50°. The general radius R_g nor the peak radius cannot be determined from this plot.

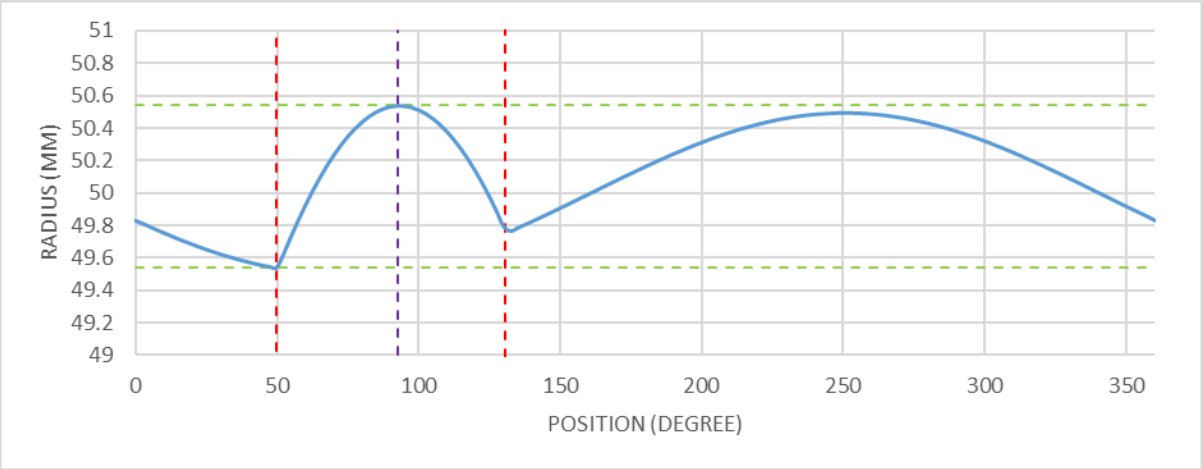

Figure 3-12: Profilometry data from Sample Geometry (X=0.4650mm, y=0..1963mm)

The data in Figure 3-12 shows that in the second scenario the sinusoidal characterise is shifted to the left and the amplitude is reduced. The peak of the consequent secondary bulging is located at 253° with a maximum displacement of 50.5070mm. The spread of the creep damage is 80.69° starting from 49.77° at 49.542mm and ending at 130.46° at 49.77mm. The maximum radius is seen at 92.50° with the value of 50.5390mm, equivalent to 1.06% increase. The isotropic hoop radius R_g cannot be determined from the plot.

Table 3-2: Summary of Sample Geometry Study

Datum Offset (mm)		**X=0 Y=0**	**X=0.6689 Y=0**	**X=0.4650 Y=0.1694**
Rg (mm)	*R*	50 -	50.1411 (average)	50.1446 (average)
Rp (mm)	*R*	51	50.3311	50.539
	Θ	90	90	92.5
R max	*R*	51	50.6689	50.539
	Θ	90	270	92.5
Rmin	*R*	50	49.4895	49.542
	Θ	-	49.5 and 130.5	49.77
Distribution (local creep)		80	80.9956	80.6893

Presented in the table above (Table 3-2) is the summary of the three scenarios of profilometry evaluation conducted on the sample geometry. It is apparent that the characteristic of the error induced into profilometry dataset is dependent on the orientation of the TSP system. Offset in the datum results in a sinusoidal characterises, making distinguishing of isotropic and anisotropic creep damage difficult. In the case of the sample geometry in Figure 3-7, even with an ideal TPS system, maximum radius reading will vary from 1.06% - 2.00%. At

maximum datum offset in the case of scenario 1, the consequent bulging introduced by the sinusoidal feature peak at a larger displacement value than the actual creep damage R_p. Variation in the spread of the creep data is also seen in the three scenarios, with a general increase in the spread from *80.00°* to *81.00°* where it's effect again is dependent on the magnitude of the datum offset.

3.1.3 Summary

Internal Profilometry inspection is a powerful tool for evaluating creep damage in reformer tube with LOTIS bring many benefits of the methodology, but there is area to further improve the quality of the interpretation of the inspection data for more accurate remaining service life assessment. This research aims to extend the system by integrating a programmatic algorithm to correct for the datum offset for better interpretation of the inspection data based on radial measurements.

It has been identified that the biggest challenge in performance accurate profilometry assessment is the calibration on the measurement space with the reformer tube. Misalignment in the measurement space and the tube axis introduces sinusoidal distortion in the profilometry contour. Amount of correction required for a given dataset is dependent on the extinct of the anisotropy creep straining and the orientation of the mechanical stabiliser. In this study, deformation in the reformer tube wall is modelled as two modes of creep strain. One mode is the isometric increase in tube radius caused from evenly distributed hoop straining and the second type being the anisotropic increase in tube radius from localised creep straining. To accurately distinguish between the two modes of failure an accurate detection of datum correction factor is essential. From this, we can classify the profilometry features into three categories to characterise the creep degradation; hoop strain, localised straining, and distribution.

3.2 Creep Detection Algorithm (CDA) data processing architecture

Presented in this section is the Creep Detection Algorithm (CDA) concept and its data processing architecture for analysing profilometry data captured from Reformer Tube inspection measurements. As identified in the preceding section, the primary task for a Reformer Tube profilometry system is to distinguish between isotropic and anisotropic deformation of the tube wall resulted from the hoop and localised creep straining, and further to quantify the extent of the two types of degradation. Accelerated creep damage occurred from localised thermal straining will result in anisotropic bulging which must be distinguished from the overall increase in the tube from the original geometry for accurate assessment of the tube condition. In analysing such elements, the tube axis must be determined from sectional profilometry data and calibrated to achieve an accurate radius analysis. Performance of this will determine the contributions and the significance of this research to the CSR industry. Presented in Figure 3-13 is the structure of the CDA, showing the three stages of the proposed method.

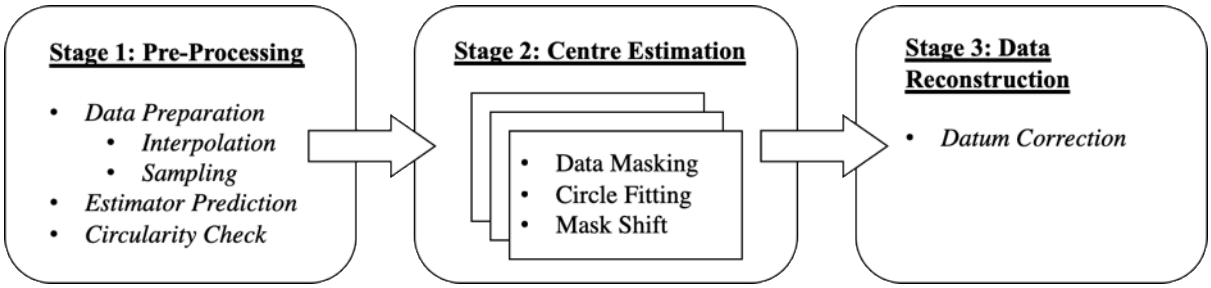

Figure 3-13: CDA flow diagram

3.2.1 Stage 1: Dataset Pre-processing

There are two tasks that are performed in the first stage of the proposed algorithm. First, the input data must be reconstructed into a format compatible with the subsequent processes to handle various profilometry dataset. The second task is for the algorithm to use this data to determine a set of initial parameters used as predictor variables for the regressive analysis to follow. The format required for the creep analysis is a 2-dimension measurement array in a polar coordinate system. The length of the array is defined by the equation below.

$$L = 360° / \theta_d - 1 \qquad [3\text{-}1]$$

where θ_d is the circumferential displacement between the radii measurement, in other words, the resolution of the circumferential position measurement. θ_d of $10°$ degree will result in a 2-dimension array of the length *35*, with the first element being the radius measurement at the angular position of *0°* relative to the measurement coordinate.

3.2.1.1 Data Reconstruction

In Chapter 2.4, five systems currently used for reformer tube RLA were reviewed. From this, we classified the systems into categories based on the two types of dataset generated by each method. The first type is the sampled dataset produced by traditional systems like the MANTIS and the ARTiS systems, which consists of small number diametric measurement samples taken simultaneously at a given transverse plane. The second type is surface-mapped dataset collected from laser systems like the LOTIS. The surface-map dataset has comparatively much higher measurement density than the sampled data and is made up of radii point measurements covering the majority of the tube internal surface. Point measurements are collected along a 3-dimensional helical pattern as represented in Figure 3-14 at a much sample rate of 360 data point per revolution when compared to the sampled dataset, which collect between 2 to 6 diametrical measurements on a 2-D measurement plane.

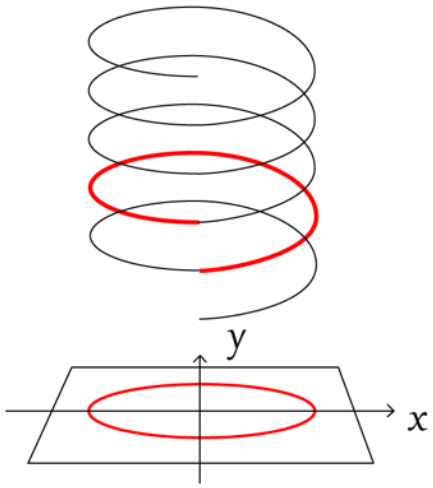

Figure 3-14: LOTIS data point mapping on to 2D Cartesian plane

Proposed analysis strategy is compatible with both types of data set but some limitation exist that will affect the quality of the output data.

When sampled input data type is being processed, new data points within the range of known data points is constructed using numerical interpolation analysis. Interpolation method used for estimating the creep deformation is 3rd order polynomial piecewise interpolation,

commonly referred to as cubic spline interpolation. This method was selected over the other interpolation methods as it yields similar outcome to standard polynomial interpolation of higher degree while avoiding oscillation instability due to Runge's phenomenon. The performance of the selected method is tested and discussed in section 3.4.2. The number of data point reconstructed will potentially yield improved performance but must be compromised with computing power. Model fitting process will significantly take longer to process with increased data size, but too little sample will limit the ability to interpolate localised bulging, especially in the earlier stages of the creep damage where the bulging is less spread out.

For the surf mapping data with much higher resolution, the data size may have to be reduced by removing some of the sample points to improve the processing time. As mentioned earlier, in the practical context, increase downtime from the inspection is not preferred, hence fast inspection and data size must be compromised. Also, because the proposed strategy performs analysis at a given measurement layer, measurement collected along the helical path must be mapped on to a 2-dimensional transverse plane for every revolution of the laser probe as illustrated in Figure 3-14. Although axial position resolution may be lost due to this, this should not affect the output data quality, considering the speed of the laser head for the LOTIS probe rotate at 60rpm.

3.2.1.2 Predictor Estimation and Circularity Check

To improve the regression execution time, the starting point for the set of predictor parameters derived in section 3.2.2.1 must be determined. The parameters required is the estimate of the datum offset X_1 and Y_1, and the radius R of the tube. A suitable candidate that is near to the true profile centre will result in a fewer regression iteration hence faster analysis.

There various methods for fast estimation of centre and radius of profiles which were considered. One is the radius dependent Hough transform which involves drawing circles of a fixed radius in the parameter space as in Figure 3-15, and other the tri-point method which uses three-point (or more) triangulation as illustrated in Figure 3-16. Both methods were tested in a work by M. Johnson [96, 101] to identify pipe centre from image data scanned from a robotic pipeline profiler. In this, two types of circular Hough transforms were evaluated, radius dependent and independent transforms, and found both methods to be a process intensive and prone to error with noise in the positional data, in this case, introduced by calculation of the gradient vector used for profile detection. The tri-point method was

found to be more appropriate for locating circular sections of pipe, but the performance depended heavily on the samples randomly selected from the pipe edge. One can improve the performance by introducing an iterative algorithm to perform regression on all dependent parameters.

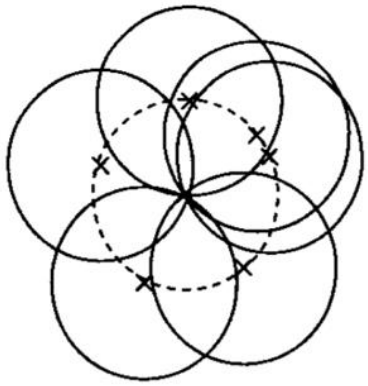

Figure 3-15: Radius dependent Hough transform [101]

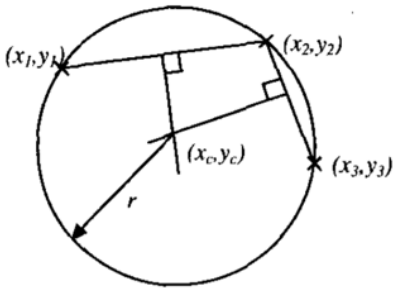

Figure 3-16: Tri-point method for locating circle parameters [108]

While both methods serviced to be viable for estimating a pipe centre without the use of convoluted statistical analysis, the processed required relatively long computing time, especially the Hough Transform method, while not able to handle unsymmetrical deformation seen in reformer tubes. In this research, a more general method has been proposed focusing on computation simplicity and speed in which the measured x and y coordinate values of the raw data point, and the associated displacement measurement *R* is averaged to estimate the centre coordinate and the radius. Although the approach has limited redundancy with dataset with high level of anisotropic features, it is deemed appropriate under early stage creep deformation.

While performing the averaging, circularity of the profilometry data is also calculated. To do this, *the distribution of the R* value for a given data set is determined by comparing the maximum and minimum values. If the distribution is below as predefined threshold, tube is determined to have minimal asymmetrical characteristic, indicating no localised creep

behaviour. This is used as an indicator to skip the rigorous centre estimation algorithm in stage 2 which uses most of the computing time. For this study, a threshold value of *0.10mm* is used equating to *0.1%* symmetricity for a *100mm* reformer tube.

3.2.2 Stage 2: Centre Estimation

When considering analysis of circular geometry, accurate detection of the circle centre plays an important role. In this step, data masking and regressive circle fitting techniques are used to detect and quantify the measurement correction factor and asymmetric creep deformation. As mentioned in the preceding section, this section is skipped if the measurement dataset passes the circularity check in the pre-processor.

3.2.2.1 Circle Fitting

The core of the CDA is based on a circle fitting regression algorithm. In this section, we derive and discuss the method implemented in this study.

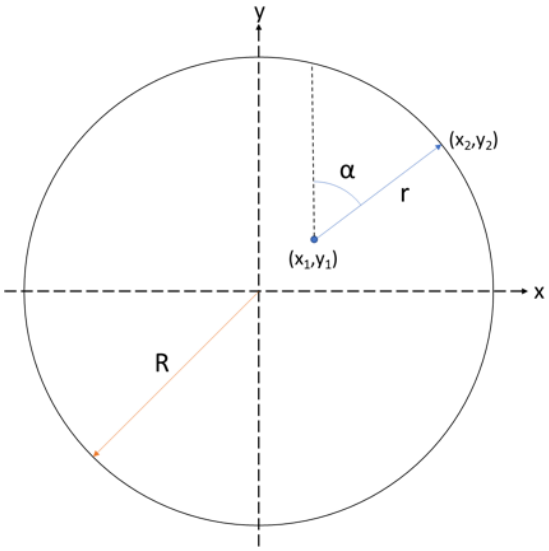

Figure 3-17: Pipe Cross-section parameters

Shown in Figure 3-17 is an illustration of the reformer tube internal profile represented on a cartesian coordinate system. The parameters of interest in deriving the sinusoidal function used in detecting the centre axis are also indicated. Drawn in black line is a circle of a radius *R* located at the centre on the coordinate zero. Represented by the blue dot is the location of the measurement datum with a coordinate (x_1,y_1) representing the correction factor it must calibrate for. Measurement *r* between the measurement datum to any instant on the black line can be described by the two parametric functions [3-3] where Θ is the angular displacement between the radial position of *r* relative to the y-axis. The coordinate at any given point on

the wall profile is described by the coordinate *(x_2,y_2)*. Distance from any point on the internal contour to the tube axis can be described by the Pythagorean equation [3-2].

$$R^2 = {X_2}^2 + {Y_2}^2 \quad [3\text{-}2]$$

$$X_2 = r * \cos\theta + X_1 \quad [3\text{-}3]$$
$$Y_2 = r * \cos\theta + Y_1$$

The two equations in [3-3] is substituted into [3-2] to result [3-4].

$$R^2 = (r * \cos\theta + X_1)^2 + (r * \cos\theta + Y_1)^2 \quad [3\text{-}4]$$

Equation [3-4] is expanded out and rearranged to form equation [3-5].

$$0 = (\cos^2\theta + \sin^2\theta) \times R^2 + (2 \times X_1 \times \cos\theta + 2 \times Y_1 \times \sin\theta) \times R + ({X_1}^2 + {Y_1}^2 - r^2) \quad [3\text{-}5]$$

Equation [3-5] can now be substituted into a standard quadratic function [3-6] taking:

$$f(x) = \frac{-b \pm \sqrt{b^2 - 4ac}}{2a} \quad [3\text{-}6]$$
$$\mathrm{a} = \cos^2\theta + \sin^2\theta = 1$$
$$b = 2 \times X_1 \times \cos\theta + 2 \times Y_1 \times \sin\theta$$
$$c = {X_1}^2 + {Y_1}^2 - R^2$$

To form:

$$\mathrm{R} = \mathrm{f}(\theta)$$

$$= \frac{-(2 \times X_1 \times \cos\theta + 2 \times Y_1 \times \sin\theta) \pm \sqrt{(2 \times X_1 \times \cos\theta + 2 \times Y_1 \times \sin\theta)^2 - 4 \times ({X_1}^2 + {Y_1}^2 - r^2)}}{2}$$

$$= -X_1 \times \cos\theta - Y_1 \times \sin\theta \pm \sqrt{r^2 - (X_1 \times \sin\theta - Y_1 \times \cos\theta)^2}$$

As *R* is always positive, equation [3-7] is derived.

$$f(\theta) = -X_1 \times \cos\theta - Y_1 \times \sin\theta + \sqrt{r^2 - (X_1 \times \sin\theta - Y_1 \times \cos\theta)^2} \quad [3\text{-}7]$$

With the above polynomial function derived the model can be fitted to the profilometry data to estimate the dependent parameters. Fitting quadratic curves (i.e. circles, ellipses) to a 2-dimensional dataset is a nonlinear regression problem [109]. There are number of data fitting methods that is commonly used in statistic modelling which can generally be categories into either “robust” or “non-robust” methods. The most common method by far is the later “non-

robust" method in the form of Least Square Regression (LSR), which estimates regressor parameters based on minimizing the sum of square of the residual between the measurement and response values. While this approach is easy to implement with high accuracy under specific scenario, but is largely influenced by outliers and biased data noise [110, 111]. Alternative is the robust method such as Absolute Least Square [112] or the Least Median Square [113] which has been developed to improve handling of outliers and missing data for a more robust solution. Although these methods (and others) has an advantage over the non-robust method with the robust characteristic, it is compromised by increased computing due to outlier detection and data weigh process.

In this study, it is assumed that the input profilometry dataset has minimal outliers nor data gaps. This may be an unviable assumption for a vision-based system which is vulnerable to such defects as discussed in section 3.1. For this research, the assumption holds with the use of the electromechanic measurement system proposed later in chapter 5.3.1. An LSR criterion for the model fitting is

$$min = \sum_{i=1}^{n} (f(\theta_i) - r_i)^2 \qquad [3\text{-}8]$$

Where $f(\Theta_i)$ is given by [3-7], r_i the measured value and n representing the index of the measurement. Maximum value n is equal to the length of dataset described by equation [3-1].

To implement the regression analysis the Curve Fitting Toolbox is used in MATLAB. Because all of the predefined parametric equations do not match our application, the Custom Equation feature is used to generate an iterative non-linear Least-Square regression function. Under the Fit Options the Trust-Region algorithm is selected and maximum function evaluation and max iterations were set to 300 and 100 respectively. Levenberg-Marquardt method was also considered but under simple comparison using reformer tube profilometry data, the Trust-region had slightly less execution time with no deviation in the output. The number of iterations deviated mainly depending on the variation in the input data. The chosen parameters are those acquired during the experimentation presented in Section 3.3.

3.2.2.2 Data Masking

The standard LSR regression method alone is venerable to inaccurate parameter estimation with the model described by [3-7] as the model does not consider for any asymmetry in the dataset. Hence the technique is used in combination with a technique named shifted data masking. Data masking or data obfuscation is a process of hiding segment or regions of data from a given data field. In the proposed algorithm, this technique is used to exclude portion of the profilometry measurement to locate the region of localised creep deformation. Shown in Figure 3-18 is flow diagram illustrating the use of Circle Fitting algorithm and shifting data masking process.

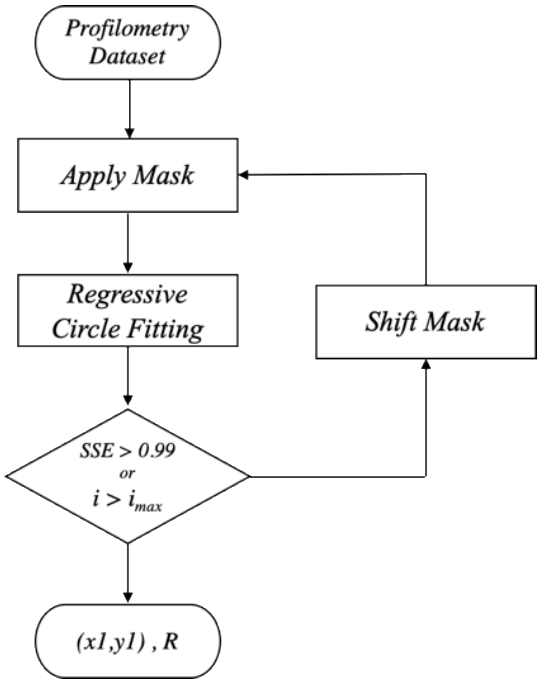

Figure 3-18: Localized Creep and Profile Centre Detection Process Flow Chart

Following the flow chart above, a data mask is applied to the input profilometry data, screening out a portion of measurement from the start of the data field at index 1. The predefined mask size determines the amount of data hiding. Based on this remaining data that is not hidden by the mask, the estimator parameters x_1, y_1, and R is determined using regressive curve fitting algorithm described in section 3.2.2.1. In statistic modelling, regression analysis is a set of statistical process of estimating the relationship among a set of valuables. In this study this is performed using the Curve Fitting toolbox in MATLAB software, a recognised powerful statistical analysis tool designed for and used by scientist and engineers. Using the curve fit toolbox, the data point collected from the inspection can be fitting with custom models other than the standard models, such as polynomial and quadratic functions. MATLAB also features 'goodness of fit' (GOF) reporting tool that gives statistical

indicators to evaluate how well the data fit the model which is used for grading. The structure of the MATLAB GOF report is listed in Table 3-3. The Sum of Square due to Error generally gives a good indication as to how well the function represents a dataset. However, all four parameters will be evaluated for a better insight into the algorithm behaviour. Although Adj R-square value is generally used with multiple linear regressions, it is also included as part of the experiment purely of inclusion in the MATLAB GOF output. Estimator values and the GOF output appended into a result array and the processes repeated while shifting the mask by a set interval. The loop is terminated either when a high SSE value above a threshold value is detected, or when all possible mask position is covered. Resulting in a data array of all possible estimator values calculated in each iteration in relative to each mask location, with x_1, y_1, and R value associated with the SSE grading value. The position of the mask that result in the highest grading value will indicate the region of localised creep deformation.

Parameter	Definition	Mathematical Expression
SSE	Sum of Square due to Error is an indication of the total deviation of the data.	$SSE = \sum_{i=1}^{n} (f(\theta_i) - r_i)^2$
R-Square	R-square is the square of the correlation between the measured and estimated data.	$R^2 = 1 - \frac{\sum_{i=1}^{n} (f(\theta_i) - r_i)^2}{\sum_{i=1}^{n} (f(\theta_i) - \bar{r})^2}$
Adj R-Square	Adjusted R-Square is estimate of degree of relationship in the data.	$R^2_{adj} = 1 - \frac{(1 - R^2)(N - 1)}{N - p - 1}$ P = Number of predictors N=Total sample Size
RMSE	Root Mean Squared Error is an estimation of the standard deviation of the random component in the data.	$RMSE = \left[\sum_{i=1}^{n} \frac{(\int(\theta_i) - r_i)^2}{n} \right]^{\frac{1}{2}}$

Table 3-3: MATLAB 'Goodness-of-fit' statistic parameters

3.2.3 Stage 3: Data Reconstruction

Presented in this section is the final stage of the CDA algorithm. Here, the datum offset values determined in the preceding section is used to reconstruct the input profilometry dataset into a more meaningful format for final evaluation of creep assessment.

To correct for the datum offset each data point is shifted by the $[X_{offset}, Y_{offset}]$ values. This will effectively be transposing the entire data from the original measurement space observed from the measurement system to a new data space observed from the tube centre. In doing this, a

new set of values of displacement and position values must be calculated for each measurement. The relative mechanism for this process is depicted in Figure 3-19.

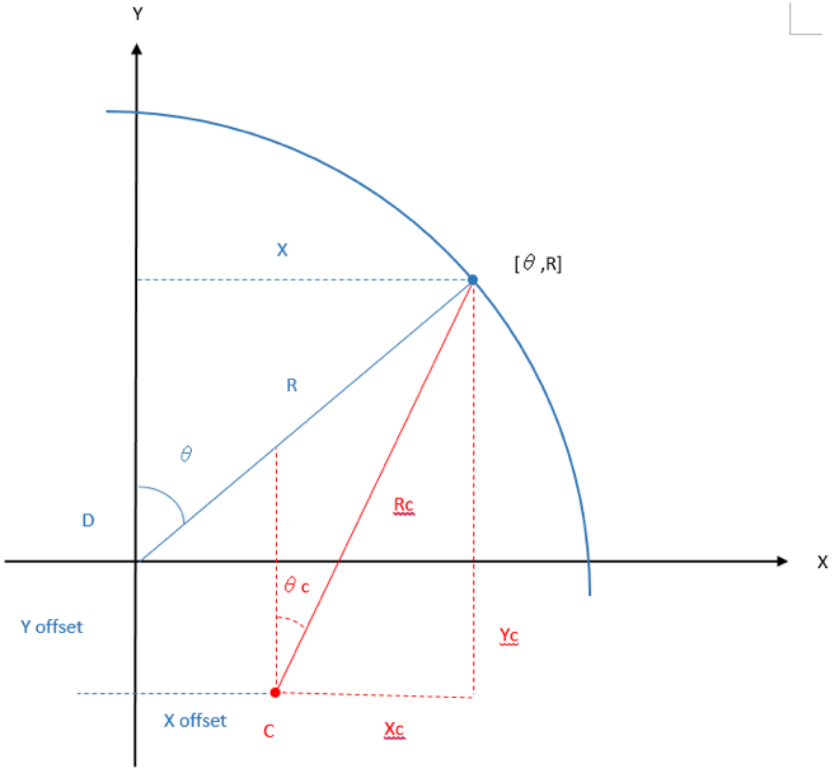

Figure 3-19: Datum offset correction seen in measurement space

Indicated by the blue dot is a measurement point, made up of elements R and Θ, quantifying the relative displacement from the measurement datum D. Horizontal and vertical coordinates $[X,Y]$ for this point can be determined by equations [3-9]. The red dot presents the centre axis of the tube marked C. The coordinate of this point $[X_c,Y_c]$ in the relative to measurement point in the measurement space D can be determined by subtracting the datum offset values $[X_{offset},Y_{offset}]$ from the measurement coordinates $[X,Y]$ as shown in equation [3-10].

$$X = \sin\theta \times R \qquad Y = \cos\theta \times R \qquad [3\text{-}9]$$

$$X_c = X - X_{offset} \qquad Y_c = Y - Y_{offset} \qquad [3\text{-}10]$$

The new data point seen from the tube axis C is represented by the calibrated radius value R_c and its new polar position Θ_c. R_c is determined by the square root of the sum of X_c and Y_c squared [3-11]. Θ_c is determined based on the fourth trigonometric functions shown in the next page [3-12]. The function used for a given data point is determined programmatically

base on the location using the four conditions shown on the left side of each function. The regions of the four quadrants are shown in Figure 3-20.

$$R_c = \sqrt{(X_c{}^2 + Y_c{}^2)} \qquad [3\text{-}11]$$

Quadrant 1 ($X_c > 0$ and $Y_c > 0$)	$\Theta_c = \tan^{-1}\frac{X_c}{Y_c}$	[3-12]
Quadrant 2 ($X_c > 0$ and $Y_c < 0$)	$\Theta_c = \tan^{-1}\frac{X_c}{Y_c} + 90$	
Quadrant 3 ($X_c < 0$ and $Y_c < 0$)	$\Theta_c = \tan^{-1}\frac{X_c}{Y_c} + 180$	
Quadrant 4 ($X_c < 0$ and $Y_c > 0$)	$\Theta_c = \tan^{-1}\frac{X_c}{Y_c} + 270$	

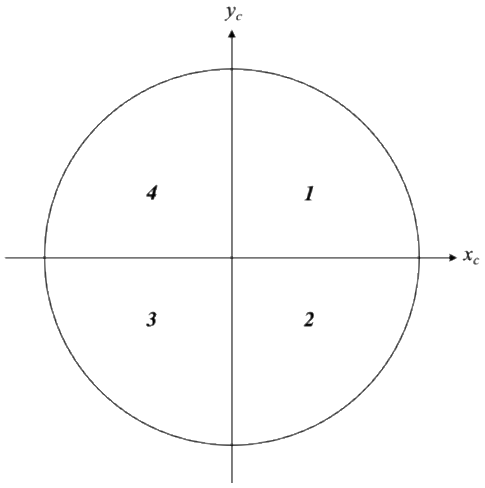

Figure 3-20: quadrant make up for calculating Θc

3.2.4 Discussion

Proposed is a new approach for evaluating profilometry data for two modes of creep straining, tailored for the use of Catalytic Steam reformer tubes. The three-stage algorithm uses iterative circling fitting techniques together with data masking and to detect and quantify asymmetry in the tube profile. Performance is dependent on three parameters which are the data size, mask length, and mask shift step size.

Input dataset must be appropriately sized so enough measurement is contained for accurate RLA. Large dataset with high accuracy and resolution profilometry measurement will contain feature beyond creep deformation, such as surface texture and carbon formation. However, this must be compromised with extended inspection time as process time for the regression

analysis in the second stage of CDA is increased with larger dataset. Excessive data will result prolonged reformer plant downtime with no added benefit. In the context of creep detection, much less measurement is required; as an extreme example, only three point is required for center detection for a perfect circle. Obviously, there must be enough data to distinguish between hoop and asymmetric creep straining.

Mask width must be size accordantly with the size of creep degradation that is to be assessed. If wide spread creep damage is to be inspection, a large mask that encompasses the region of asymmetry must be applied. If the spread if the damage is larger than the size of the mask, the performance of the center detection will be obstructed as equation [3-7] will be fitted to geometric profile not considered by the model. On the other hand, large mask will result in reduce sample size for circle fitting which can reduce the performance but proportionally reduce the time required for computation. The value of the step size of mask shifting will determine that resolution at which the algorithm can locate the region of deformation. Small steps will result in accurate detection of the creep location, but will proportionally increase the iteration number resulting in longer processing time.

Behavior of reformer tube, as discussed in the literature review, is always associated with a number of uncertainties. Especially, characteristics of the tubes creep deformation from unbalanced thermal exposure. The proposed CDA demonstrates a method in assessing localized creep deformation based to radial measurement as to diametric method. Limitation is the occurrence of multiple asymmetric features in the input profilometry dataset, for example, if two or more isolated creep deformation exist on the same measurement plane, in which case the determine datum correction factor will be inaccurate. Extent of this will be dependent to the extent of non-circularity described by the model [3-7]. One solution to is to apply multi data mask to account for more than one region of defections. This was not pursued as it will result in less data for the circle fitting regressing (reduced performance) and increase process time with increase iteration with the added parameter of the additional mask.

3.3 Experiment Design

This section presents the experimental design and results obtain from an this research in examining the performance of the proposed Creep Damage Detection algorithm. It focuses on assessing the algorithm in detecting and quantifying the two modes of creep straining using real profilometer data collected from retired reformer tubes. The experimental results are presented and analysed in both the statistical and observable evaluation. Importantly this section looks at the repeatability and consistency of the system which serves as a validation for the proposed method.

3.3.1 Experiment Design

Prepared for this research are three segments of reformer tubes taken from an ex-service HK40 catalytic Reformer Tube. A various point on the samples are selected, and profilometry data is collected using the custom-built Profilometry Measurement tool. Between each trial, the datum is shifted to mimic the effect of data distortion during an inspection. These four data sets are evaluated using the proposed CDA, and the results are analysed for repeatability and precision.

The implementation of a lab environment, as opposed to performing a complete reformer tube inspection, is due to the inaccessibility to an in-service steam catalytic reformer plant over the later course of this research. Historical data for each tube are not able hence the nominal internal diameter measurement is used as base-line which is required to implement the proposed CDE approach. The remainder of this section discusses the detail of the sample tubes, the consideration made in selecting of the data set, and the acquisition of the profilometer data.

3.3.1.1 Sample Tubes

The ex-service hydrogen reformer tube obtained for this research are the segments taken from different locations of a complete tube. This reformer tube was retired from the Primary Reformer furnace used in a Methanol Production plant in New Zealand. The first segment is taken from the top end of the tube where the body of the primary tube joins with the mounting flange. This segment is from here on in referred to as *Sample A* unless otherwise specified. The second segment is taken midway down the tube with some indication of creep deformation. This segment is from here on in referred to as *Sample B* unless otherwise specified. The third segment is the taken from near the bottom of the tube with visible signs

of significant anisotropic deformation and creep rupture. This segment is from here on in referred to as Sample C unless otherwise specified.

3.3.1.1.1 Sample A

Shown in *Figure 3-21* is the schematic diagram of *Sample A* catalyst tube. The *weld neck flange* is joined to the catalyst tube 90mm from the top surface of the flange. The width of the welding is approximately 10mm. The tube is cut-off *200mm* below the weld ring. The weld neck flange and the catalyst tube are made of SS321 and HK40 steels respectively.

Visually the tube shows minimal signs of creep degradation. Both inner and outer surface showed minimal deposits which indicate that the sample has little exposure to operation above design temperature. Tidy welding between the flange and the tube is seen in both the inner and outer surface with no visual sign of fracturing. The outside surface has rough texture expected from the casting process and the inside face is relatively smooth on touch with visible machine marks. *Table 3-4* presents four diameter measurement taken from the internal surface of the two ends of the sample a radial position *0°*, *45°*, *90°*, and *135°*. A minimal deviation between the measurement on both ends of the tubes indicating circularity in the tube, with minimal anisotropic deformation. Four profilometry data is collected from the approximately *80mm* distance from the bottom face. The four set of data is denoted *A-A1* to *A-A4* and is used as a sample data with minimal creep. The mean internal diameter of *54.7mm* is used as the nominal internal diameter value for the remainder of this chapter.

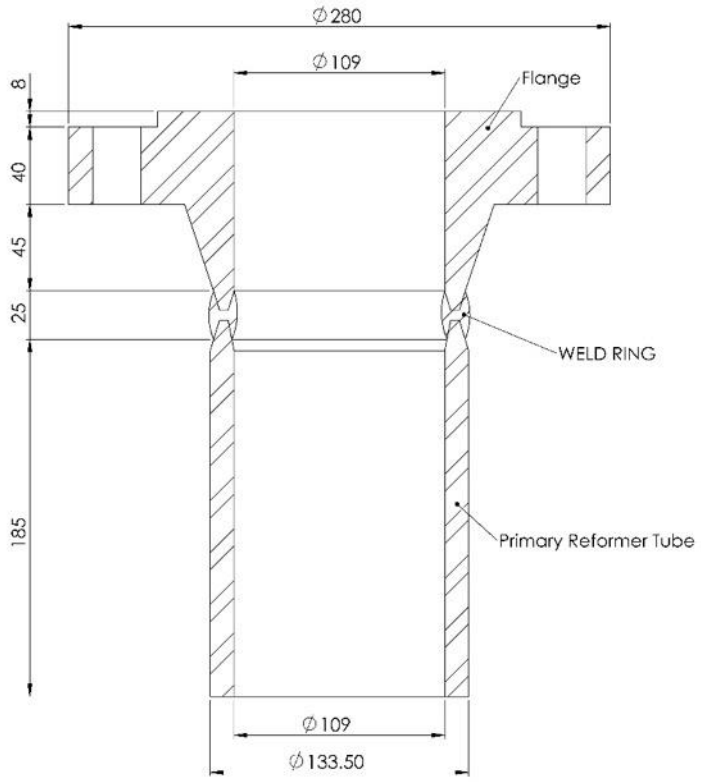

Figure 3-21: Sample A Schematic (mm)

Table 3-4: Sample A top/bottom internal diameter measurement

Position	**0°**	**45°**	**90°**	**135°**	**Mean**	**Deviation**
Top	54.8mm	54.9mm	54.9mm	54.9mm	54.85mm	0.1mm
Bottom	54.6mm	54.6mm	54.6mm	54.7mm	54.63mm	0.1mm

Presented in *Figure 3-22* are the four profilometry data sets collected from *Sample A*. The four profiles present the identical geodesic data collected from different datum coordinates. sinusoidal characteristic described in *Section 3.1.2* is seen in each data set at different extent, indicating the disparity in the datum offset between each data set. The maximum and minimum measurements are indicated by green and red dashed lines respectively. Shown in *Table 3-5* are the maximum and minimum data coordinates. The most radii distribution of *1.78mm* is seen in Data Set *A-A1* indicating largest datum offset and the least distribution of *0.43mm* is seen in Data Set *A-A4* indicating the least datum offset. Note that all the plots are presented with the same scale.

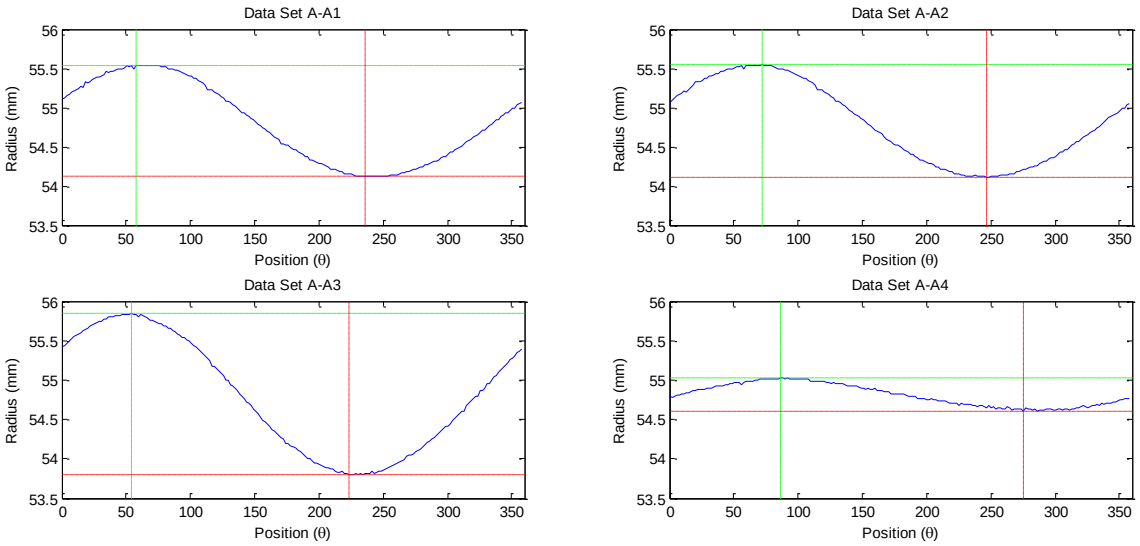

Figure 3-22: Sample A Profilometry data

Table 3-5: Sample A profilometry data maximum and minimum radius

	Maximum		*Minimum*	
Data Set	Radius (mm)	Position (Θ)	Radius (mm)	Position (Θ)
A-A1	55.54	57.6	54.12	235.8
A-A2	55.55	72.0	54.11	246.6
A-A3	55.58	54.0	53.80	223.2
A-A4	55.03	86.4	54.60	275.4

3.3.1.1.2 Sample B

Sample B is a *300mm* length segment taken from the mid-section of the 14m reformer tube. The internal face is smooth to touch but with no visible machine marks. Some dark deposit is visible on the internal wall but no sign of visible asymmetric deformation or pitting. *Table 3-6* presents four internal measurements taken at the two ends of the sample. The bottom of the tube is larger than the top of the tube on average of *0.7mm* indicating that the tube has been exposed to some degree of unbalanced operation and that creep degradation is evident. To better understand this, more measurement where collected from the sample to determine a suitable location for collecting the profilometry sample for testing the CDA method. Presented *Figure 3-23* is a plot of the external diametrical measurements taken at *50mm* steps down the length of the tube, with the blue and green line showing the mean and deviation between the four samples. Compared to *Sample A*, a slightly larger deviation is seen within the four measurements throughout the length of the tube of around *0.15mm* indicating some

level of asymmetry in the tube. The tube diameter increased gradually increases from *133.5mm* to *134.5mm* indicating a general increase of *1.0mm*, equating to *0.75%*. For this experiment, sample profilometry measurement is collected at *250mm* depth with the largest deviation between the four measurements. The four datasets are denoted *B-A1* to *B-A4* and used as a sample with a medium level of creep damage.

Table 3-6: Sample B top/bottom internal diameter

Position	**0°**	**45°**	**90°**	**135°**	**Mean**	**Deviation**
Top	54.9	54.8mm	55.0 mm	54.9mm	54.9mm	0.2mm
Bottom	55.4mm	55.6mm	55.5mm	55.7mm	55.6mm	0.3mm

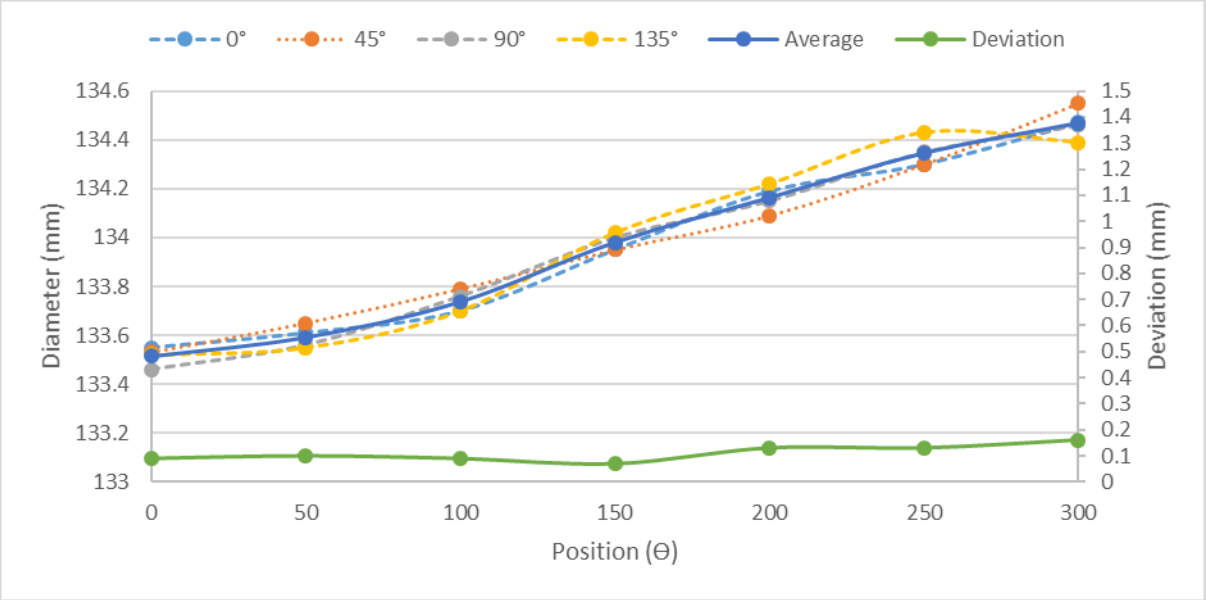

Figure 3-23: Sample B external diameter profile

Presented in *Figure 3-24* are the profilometry datasets collected from *Sample B*. In taking this data, care was taken to minimise the tilting of the sectional measurement plane relative to the axis of the tube. Before the sample tube was placed on the top plate of the Measurement Acquisition Rig, describe in *section 3.3.1.2*, the bottom face of the tube was skimmed off on a lathe. This was done to avoid elliptical characteristic induced in to collected data set as in the case of *Sample A*. Also the amount of the datum offset between each data set is intendedly increased from *Sample A*.

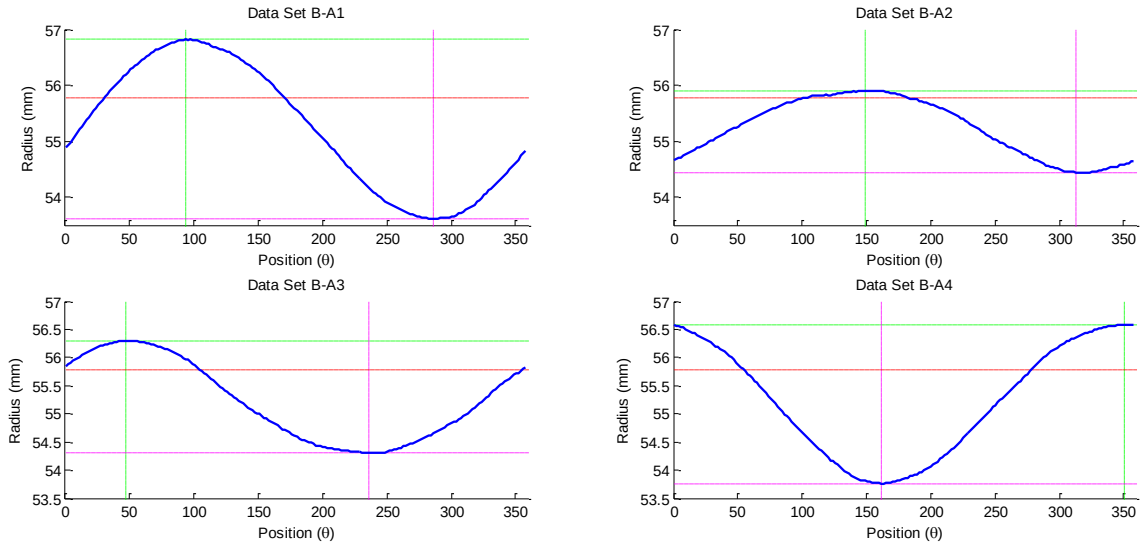

Figure 3-24: Sample B-A Profilometry Data (Data Size =200)

3.3.1.1.3 Sample C

Sample C is the largest segment of tube measuring *970mm*, taken from the bottom section of a reformer tube where the tubes are generally exposed to high operating temperature and internal pressure, resulting in higher risk of creep failure. The sample shows visible signs of deformation through the entire length of the tube with a large crack at the bottom of the tube that had resulted from creep rupture. The tube is significantly larger in diameter than *sample A* and *B*, overall showing evidence of both isotropic and anisotropic creep damage. To determine the appropriate location to acquire the profilometry dataset, the external characteristic of the sample was evaluated in similar fashion as did with *Sample B*.

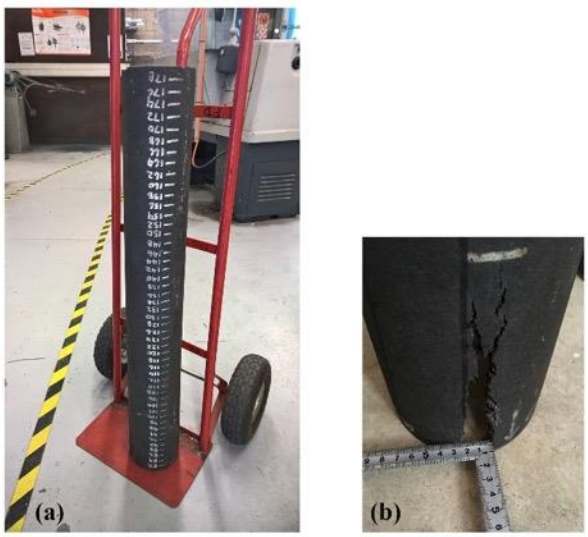

Figure 3-25: Sample C a) Photo of the entire sample b) Photo of Creep Rapture

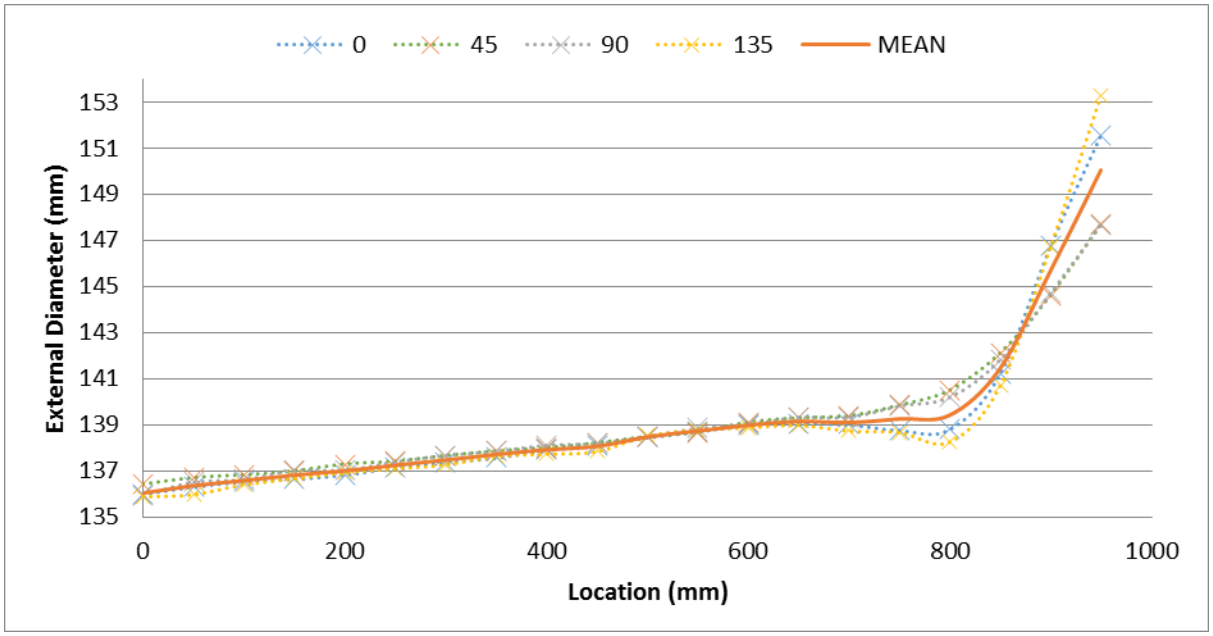

Figure 3-26: Sample C external diameter profile

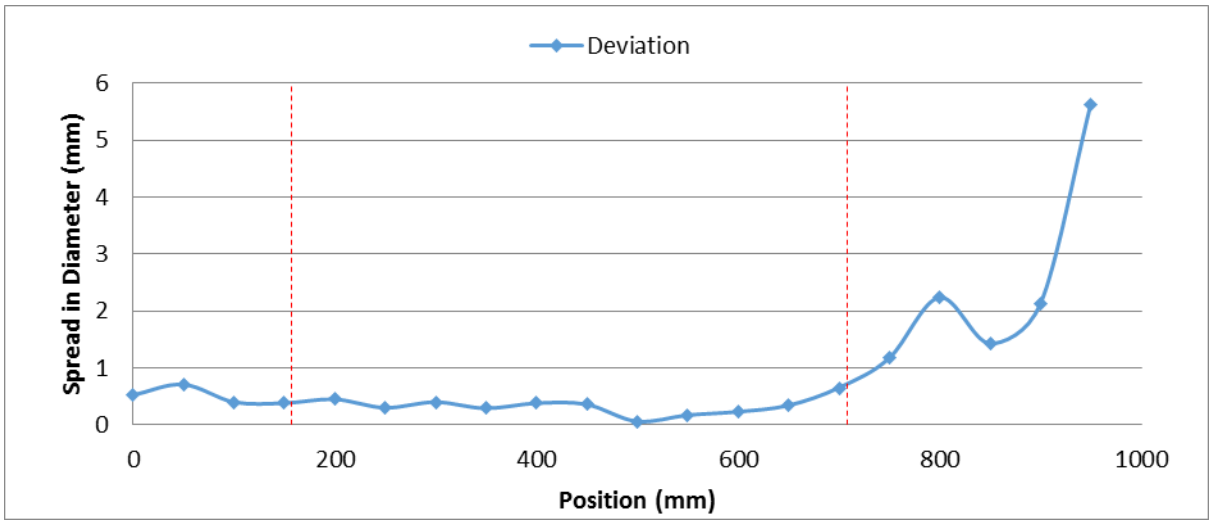

Figure 3-27: Sample B external diameter deviation

It is clear from *Figure 3-26*, showing the profile of the external diameter of the specimen, there is a significant amount of isotropic and anisotropic deformation in the sample. There is general growth in the tube diameter from *136.0mm* at the top of the tube to *139.2mm* at *800mm*. In the region between *800-1000mm*, the diameter readily increases from *139.2mm* to *153.3mm*, ultimately ending at the start of the rupture opening. At *800mm* point there is a large deviation between the four diametrical measurements with measurement at *135°* being smaller than the minimum diameter directly above where the crack starts. This indicates a large amount anisotropic deformation localized at this location. After further study the sample it is determined that this is resulted by buckling mechanism the is thought to have happened as the tube ruptured and the phenomenon is not related to creep damage. To this,

the bottom section of the tube from *700mm* and below is considered invalid for this study and will not be used in this experiment.

Based on the various characteristic evident in the tube, it was decided that two set of profilometry data is collected from *Sample C*, one at *150mm* from the top of the sample. These datasets are denoted *C-A1* through to *C-A4*. The second sample is collected as close as possible to the creep rupture point at *700mm* from the top of the sample. The four samples collected at this point is denoted *C-B1* to *C-B4*. Both data sets are used as sample with high level of creep damage.

Figure 3-28 is the profilometry datasets *C-A1* to *C-A4*. Tube segment was placed on the Test Rig with the bulging face towards the right of the bench hence the deformed face located roughly at *270°*. The bottom face of the tube that is in contact with the test rig is machined true as possible to the tube axis.

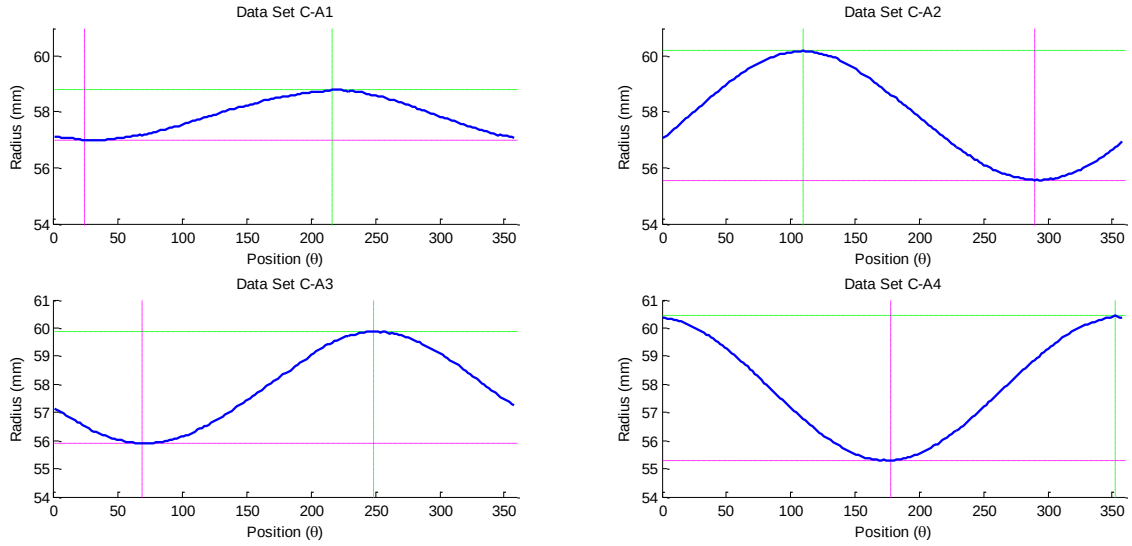

Figure 3-28: Sample C-A Raw Data Set (Data Length = 200)

Figure 3-28 presents the raw cross-sectional internal wall profile data collect *800mm* from the top of the sample tube. Tube segment was placed on the Test Rig with the bulging face towards the left of the bench hence the deformed face located roughly at *90°*. The bottom face of the tube that is in contact with the test rig is machined true as before.

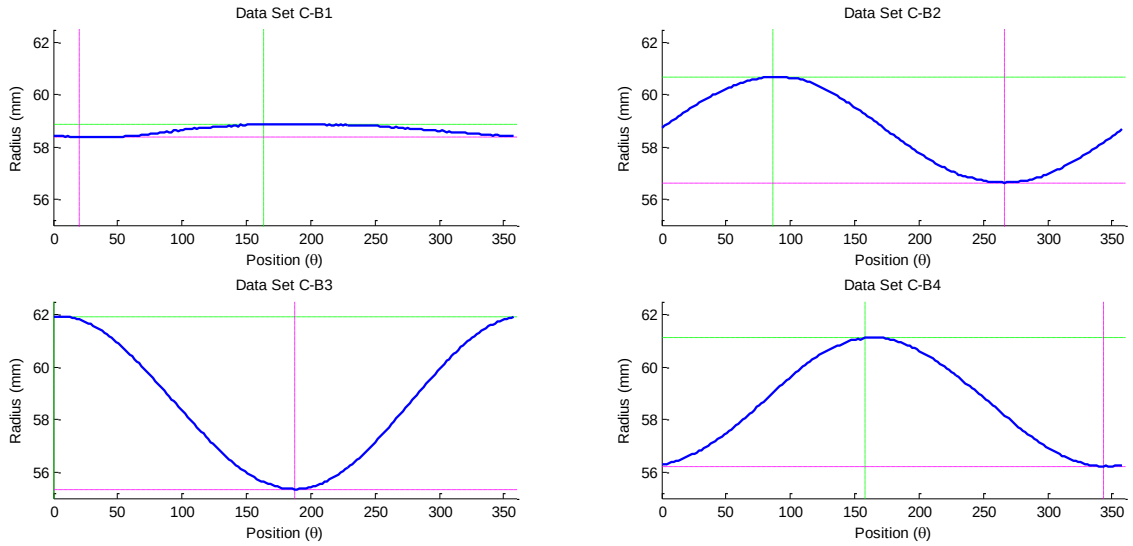

Figure 3-29: Sample C-B Raw Data Set (Data Length = 200)

3.3.1.2 Profilometry Measurement Tool

Key No.	Part Name
1	Mitutoyo Dial Indicator
2	ABS Dial Indicator Mount
3	M5 x 30mm Counter Sunk Hex Screw
4	Top Plate
5	Stepper Motor Mount
6	NEMA 23 Stepper Motor
7	M5 x 10mm Hex Screw
8	Extrusion Base

Figure 3-30: Profilometry Measurement Tool Assembly Diagram

Presented in *Figure 3-30* is assembly diagram of the custom build precision measurement rig designed for collecting profilometry measurement from the sample reformer tube segments described in the previous section. The design is built around a Mitutoyo[1] precision Digimatic indicator and a NEMA 24 *3.1Nm* high torque stepper motor. The stepper motor is used to locate the Mitutoyo gauge over *0-360°* in a controller manner while the iDC-1012E digital indicator probes the internal wall of the sample tube. The radius measurements are collected at a resolution of *0.01mm* at a precision of *±0.01mm*. Measurement data along with its angular position is logged onto a custom written LabVIEW software utilizing the Mitutoyo

[1] www.mitutoyo.com

standard SPC protocol via an ATMEL microcontroller. Stepper motor is driven at full step of *1.8°* for accurate *200* step per revolution using the DM556 universal motor driver. A detailed analysis of this rig performance is given in Appendix A and can be referred to for additional insight.

3.4 Experiment Results and Discussion

This section presents the observed and statistical analysis considered in this research to analyse the performance of the CDA method. Using the sets of four profilometry dataset collected from the sample tubes, the method is evaluated under the topics of creep damage detection, cubic interpolation, and effect of adjusted data mask size.

3.4.1 Creep Damage detection performance

In the first test, the algorithm is evaluated for its ability to detect and quantify creep straining. For this, the profilometry data collected from each sample are processed using the entire *200* raw data points without performing any data interpolation. The mask width is selected per the level of localised creep strain in the tube that gives an adequate result. For each set of data, the results are presented in both graphical and numerically.

3.4.1.1 Sample A

For this dataset, a narrow mask width of *10°* is selected to accommodate the relatively new segment of the reformer tube, as previously discussed in *Section 0*. Presented *in Figure 3-31* and *Table 3-7* is the graphical and numerical result generated from the CDA. The four plot shows the modified data set with compensated datum offset. The maximum and minimum values are indicated by the green and purple lines with the red line indicating the general radius measurement determined by the algorithm. The table presents the average radius, calibration correction factor in *X* and *Y* axis, and the "goodness of fit" (GOF) statistical result generated by the algorithm. This table also includes the execution time of the CDA determined based on the 'time' function built into MATLAB.

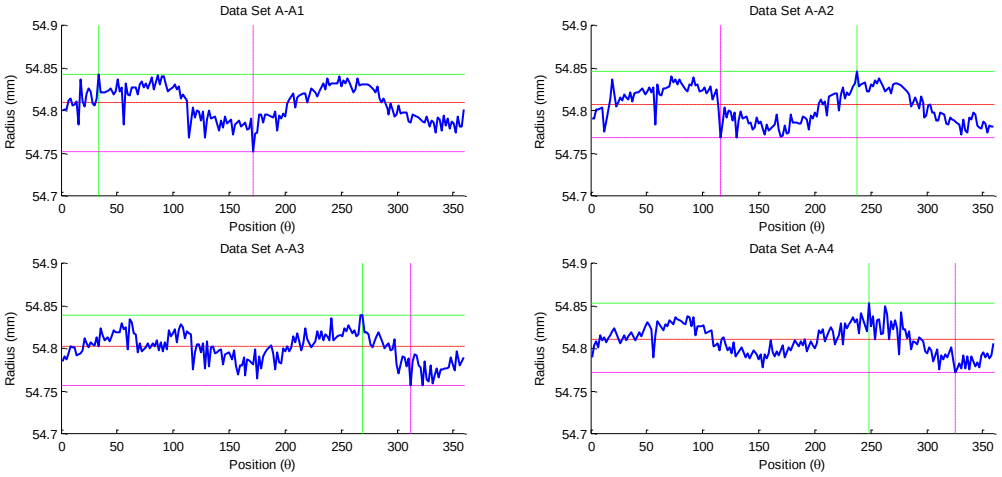

Figure 3-31: Sample A CDA Graphical Results (Data Length = 200, Mask Width = 10°)

Table 3-7: Sample A CDA Numerical Result (Data Length = 200, Mask Width = 10°)

	A-A1	*A-A2*	*A-A3*	*A-A4*	*Average*
R (mm)	54.8096	54.8079	54.8024	54.8115	54.8079
X Offset (mm)	-0.6405	-0.6505	-0.7861	-0.193	-
Y Offset (mm)	0.3125	-0.2922	-0.6357	0.0161	-
Rmax (mm)	54.8426	54.8459	54.8398	54.8536	54.8455
Rmin (mm)	54.7527	54.7685	54.7570	54.7720	54.7626
sse	0.0685	0.0709	0.0469	0.0488	0.0588
rs	0.9986	0.9986	0.9995	0.9868	0.9959
adjrs	0.9986	0.9986	0.9995	0.9866	0.9958
rmse	0.0191	0.0194	0.0158	0.0161	0.0176
cpu time (s)	0.9375	0.7969	0.9375	0.8271	0.8748

From the result, it is evident that the algorithm has detected and corrected for a significant amount of datum offset at large variation between the trials, from most correction in dataset *A-A3* and the least amount in dataset *A-A4*. Similarity between the reconstructed data with the entire data point falling within a distribution window of *0.10mm* between *54.76mm* and *54.86mm* clearly indicated the consistency of the method. It is noted that a consistent level of fluctuation of approximately *±0.02mm* is visible in all four datasets. Because the magnitude of fluctuation is evenly distributed within and between each graph and repeated features, such as remote spikes and local valleys, can be identified, this noise in the data is determined to be the cause of the rough surface texture of the sample surface.

Output in all dataset show conic feature characterized by oblique circular section. Assuming an elliptical cross-section, a difference of *0.06mm* is seen between the semi-minor and semi-

major axis measurement of *54.77mm* and *54.83mm* respectively. From this one can determine the eccentricity (ε) to be *0.047*8 based on equation *[*3-13, hence determine the theoretical tilt angle θ_α of the measurement plane relative to the tube axis to be *2.68°* using equation *[*3-14. Upon careful observation on the specimen, the determined angle θ_α is in agreeance with the angle of the bottom face to the tube axis where the tube was rested on the Profilometry Measurement tool during sampling.

$$\varepsilon = \sqrt{1 - \frac{b^2}{a^2}} \qquad [3\text{-}13]$$

$$\theta_\alpha = \sin^{-1}(\varepsilon) \qquad [3\text{-}14]$$

Per the CDA tabulated result, the radius of the tube is determined to be on average *54.8079mm*, which slightly deviates from the measured tube radius on *54.7mm*. In this case with the tilted measurement plane however, the tube radius is better determined by the radius measurement on the minor axis of the elliptical geodesic, which would give a radius measurement of approximately *54.77mm* which pushes the figure closer to the measured value. Although there is minimal difference in this scenario, this error can increase proportionally with increased measurement plane till angle. To overcome this, the till angle can be mathematically compensated by fitting an ellipse function to the reconstructed data. However, because θ_α can be minimized with mechanical design (*Section 5.3.4*), this method is not considered in this research and left for future work. It should be noted that the detected radius measurement is closely matched between the four data sets with largest deviation of *0.0091mm* between *A-A3* and *A-A4*. This demonstrates the consistency of the proposed CDA and the validity of the experiment setup, especially when considering the large variation in the datum offset factor between each trial.

The accuracy and consistency of the CDA can also be seem in the statistical *GOF* report presented in *Table 3-7*. High average *root square* and *adjusted root square* is indicating an average of over *99.58%* of the total variance in the data about the average radius is accountable by the model. An average R-square value of *0.0588mm* in each data set indicates some level of random component, which are caused by the data noise induced from the tube surface texture. Some deviation in the execution time of the CDA is seen between the four trials but is to some degrees expected on a Windows Operating System used on the

experiment PC. The average process time of *0.8748s* along with the other GOF elements will be used as a base data to be compared with the preceding trails.

3.4.1.2 Sample B

For this data set, again a narrow Mask width of 10° is used as little localised creep is evident from the sample. The result of the CDA is presented in a graphical and numerical format in *Figure 3-32* and *Table 3-8.* The format of the two outputs are identical to that describe in the previous section.

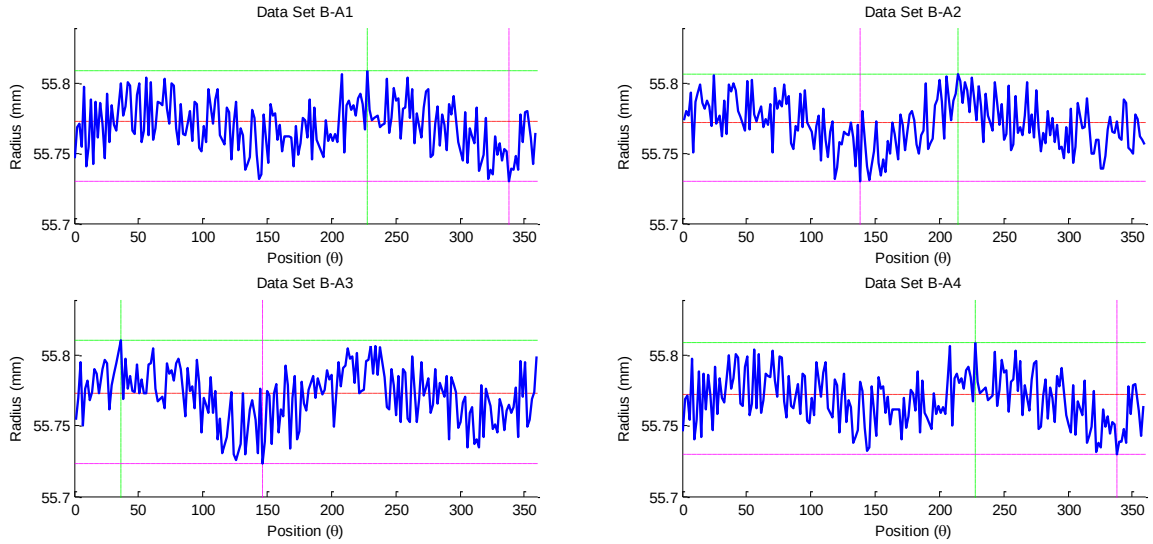

Figure 3-32: Sample B-A CDA Graphical Result (Data Length = 200, Mask Width = 10°)

Table 3-8: Sample B-A CDA Numerical Result (Data Length=200, Mask Width = 10°)

	B-A1	*B-A2*	*B-A3*	*B-A4*	*Average*
R (mm)	55.7728	55.7723	55.7730	55.7702	55.7721
X Offset (mm)	-0.7806	-0.2274	-0.3869	0.172	-
Y Offset (mm)	0.1666	0.2862	-0.3141	-0.675	-
Rmax (mm)	55.8082	55.8064	55.8105	55.8082	55.7283
Rmin (mm)	55.7294	55.7301	55.7233	55.7304	55.7283
sse	0.1008	0.1037	0.1198	0.0937	0.1045
rs	0.9983	0.9916	0.9952	0.9979	0.9958
adjrs	0.9983	0.9915	0.9951	0.9979	0.9957
rmse	0.0232	0.0235	0.0252	0.0223	0.0236
cpu time (s)	1.1719	0.9531	0.9375	0.9688	1.0078

It is clear from the result that *Sample B* has a significant increase in tube radius compared to the nominal 54.7mm. An average radius of *55.7721mm* equates to an overall increase of *1.96%*. Visually larger amount of noise is present in the data indicating a rougher internal surface than *Sample A*. This is clearly has resulted from surface deposit described in *section 0*. This can also be correlated to the increased *sse* and *rmse* value in the *GOF* report of *0.1045mm* and *0.0236mm* respectively.

Although a similar level of data deviation is seen in *Sample B* as with *Sample A*, with a maximum spread of approximately *0.09mm* between *55.81mm* and *55.72mm* seen in dataset *B-A3*, there is overall less sinusoidal characteristic in the data. This indicates that firstly, there is minimal localized creep strain occurring in the tube, and secondly, the measurement plane is perpendicular to the axis of the tube. From observation, the maximum difference in the semi-minor and semi-major axis of the elliptical element is *0.02mm*, seen in data *B-B3*, which would indicate a measurement plane tilt angle of *1.53°*. Ideally tilting of the measurement plane should be completely eliminated, but considering the level of random fluctuation in the radii measurement from the texture of the tube surface, this is not of any practical significance for the application.

3.4.1.3 Sample C-A

Shown in *Figure 3-33* and *Table 3-9* are the CDA results from processing dataset *C-A* collected from the top portion of the *Sample C*. As there is indication of localised creep strain a wide Mask Width value of *100°* is selected.

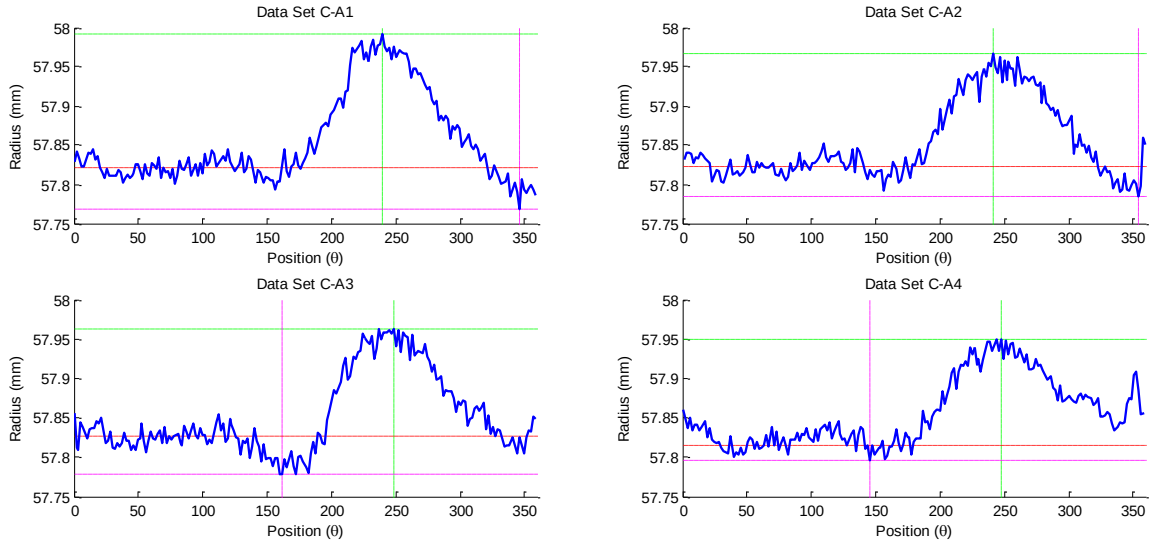

Figure 3-33: Sample C-A CDA Graphical Result (Data Length = 200, Mask Width = 100)

Table 3-9: Sample C-A CDA Numerical Result (Data Length = 200, Mask Width = 100)

	C-A1	*C-A2*	*C-A3*	*C-A4*	*Average*
R (mm)	57.8207	57.8233	57.8267	57.8219	57.8239
X Offset (mm)	0.3998	-2.2012	1.8110	0.1746	-
Y Offset (mm)	0.7179	0.7574	0.6343	-2.5193	-
Rmax (mm)	57.9919	57.9678	57.9627	57.9467	57.9673
Rmin (mm)	57.7687	57.7819	57.7779	57.7946	57.7808
sse	0.0145	0.0137	0.0144	0.0156	0.0146
rs	0.9995	0.9998	0.9997	1.0000	0.9998
adjrs	0.9995	0.9998	0.9997	0.9999	0.9997
rmse	0.0122	0.0118	0.0121	0.0126	0.0122
cpu time (s)	0.8125	0.9219	0.9375	0.9531	0.9063

The reconstructed data plot shows significantly more interesting data than the previous data's. A region of increased radius has been detected between *200*° and *330*°, indicating a region of localised creep straining. While the general radius of the tube has increased to *57.8239mm* (an increase of *5.5%*), the maximum radius of 57.9675mm (on average) between *240*° and *250*° is detected, indicating an area with increased damage of *5.8%*. Note here that if the data was to be assessed based on diametrical analysis, the data will be halves and the maximum radius measurement would reduce to *57.9023mm* as averaged with the opposing data. A small noise in the data of *±0.1mm* indicates a smooth internal surface with minimal material deposit. This can be confirmed with the small *sse* and *rmse* values in *Table 3-9.* This may also correspond to the wider mask width as the model is fitted to a fewer number of data points. At mask width of *100*°, the fitted data size is *260/360* of the *200* data points, equating to *144* data points.

GOF figure shows that the regress model describes the geometry of the tube well. Average adjusted R-square value of *0.9957* shows that the model explains *99.57%* of the total variation of the total variation in the data about the average. The high performance of the CDA model is also justified by the small *rmse* value. Average process time of *0.9063s* was recorded indicating that the process time is not affected by the features of the data and only by the size of the data set.

3.4.1.4 Sample C-B

Presented in *Figure 3-34* and *Table 3-10* is the graphical and numerical result of dataset *C-B* when processed with the CDA algorithm. Again, no data interpolation is performed and a wide Mask Width of *80* is used to accommodate for the localise straining.

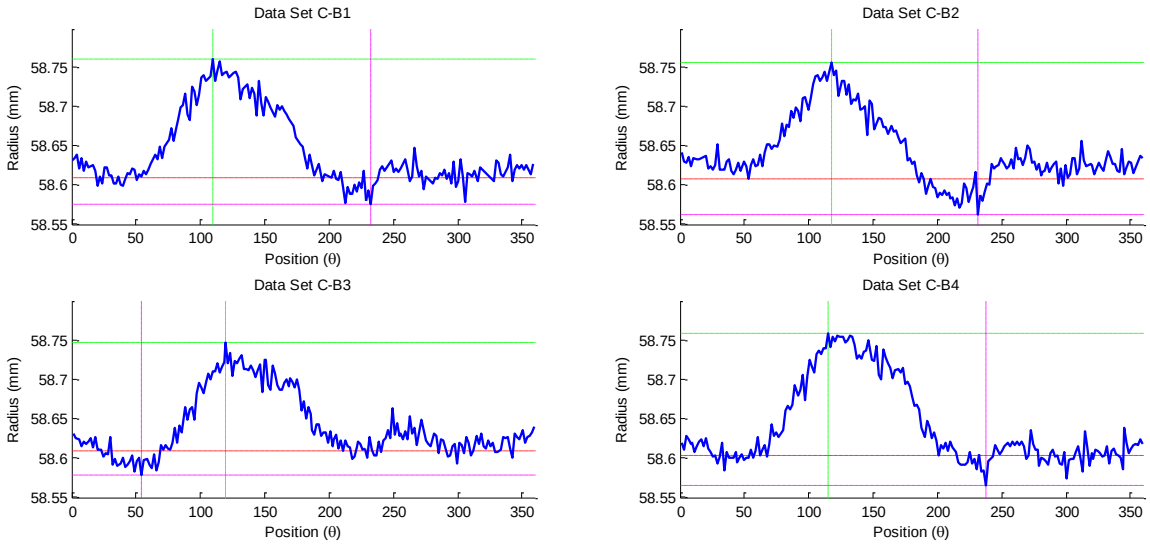

Figure 3-34: Sample C-B CDA Graphical Result (Data Length = 200, Mask Width = 80)

Table 3-10: Sample C-B CDA Statistical Result (Data Length = 200, Mask Width = 80)

	C-B1	*C-B2*	*C-B3*	*C-B4*	*Average*
R (mm)	58.6092	58.6086	58.6094	58.6030	58.6076
X Offset (mm)	0.1224	-1.9820	-0.3017	-0.5487	-
Y Offset (mm)	0.2017	-0.1591	-3.2852	2.3281	-
Rmax (mm)	58.7669	58.7755	58.7621	58.7625	58.7668
Rmin (mm)	58.5708	58.5697	58.5785	58.5679	58.5717
sse	0.0166	0.0221	0.0180	0.0165	0.0183
rs	0.9956	0.9999	1.0000	0.9999	0.9989
adjrs	0.9956	0.9999	1.0000	0.9999	0.9989
rmse	0.0119	0.0134	0.0124	0.0118	0.0124
cpu time (s)	0.9219	0.9219	0.9219	0.0156	0.9453

The result from the analysis has shown that there is a significant amount of localised creep straining occurring in the sample tube, spreading between *75°-200°*. A general increase in the tube radius of *6.9%* can be seen with consistency in all four data sets, verifying the repeatability of the algorithm. A maximum radius of *58.7675mm* on average is detected

between *110°* and *130°* indicating a maximum creep straining of *7.2%*. Considering that the sample was taken within *100mm* from the location of the creep rupture, it is safe to speculate that the absolute maximum straining the material can width stand before rapturing is around *7%*. Larger fluctuation in the flat region of the data indicating non-circularity in the sample section, which can be visually observable on the sample wall with bulking phenomenon. Overall the consistent output of the CDA corresponds with the external measurements presented in *Figure 3-26*, showing good accuracy and viability of the method.

The figures in the *GOF* report presented in *Table 3-10* shows that the proposed model describes the geometry of the tube internal cross-section very well. Average adjusted R-square value of *0.9989* shows that the model explains *99.89%* of the total variation of the total variation in the data about the average. The viability of the CDA method is also justified by the small *sse* and *rmse* values of 0.0183mm and 0.0124mm respectively, similar to result obtained from data43set *C-A*, indicate minimal roughness in the same internal wall. This is expected as the two data is taken from the same sample with similar surface texture. Average process time of 0.9453s was recorded, again indicating that the process time is not affected by the features of the data and only by the size of the data set.

3.4.1.5 Summary

Analysis based on the two data sets collected from Sample C shows that the proposed CDA algorithm is effective in distinguishing between hoop stress and localised creep straining. For both cases, a large Mask Width value of *100°* and *80°* was sufficient in masking the localised straining while accurately determining the tube radius.

The *sse* and *rmse* value can be used to quantify the level of the roughness of the internal surface, where large values indicating rougher internal surface, indicating the likelihood of deposits, and smaller values indicating smoother surface with better balanced furnace operation. *sse* and *rmse* value of 0.06mm and 0.02mm respectively should be used as a baseline value, determined from the values from Sample A-A.

The algorithm is limited in analysing profilometry data with elliptical deformation. There is no mean for the distinguishing between elliptical feature caused by creep strain or tilting of measurement plane. Either would result in an increase radius measurement with it magnitude dependant on the degree of ellipticity.

3.4.2 Performance of Cubic Interpolation

To evaluate the performance of the data interpolation used in the first stage of the CDA, the size of the sample data set is reduced. Then cubic interpolation is used to interpolate a new set of data point and the results are compared with the raw data and its result generated in the preceding experiment. Input data size of twelve is used in this experiment to mimic the sensor number used in the RTIS Prototype presented in *Chapter 5* of this thesis.

A performance of the data interpolation is best determined by observing the error introduced by the process. Shown in *Figure 3-35* to *Figure 3-38* are the comparison of the interpolated data with the raw dataset. Measurements are sampled from each sample at *30°* intervals, starting from *0°*, to generate an input data size of *12*. From this a new data points at *1.8°* interval are generated using the method described in *section 3.2.1.1*, generating a new input dataset with the length equal to the original data of *200*. Shown in figure below is the original and the reconstructed dataset in blue and red lines. The green line indicates that difference between the two datasets with the deviation scale on the right-hand side.

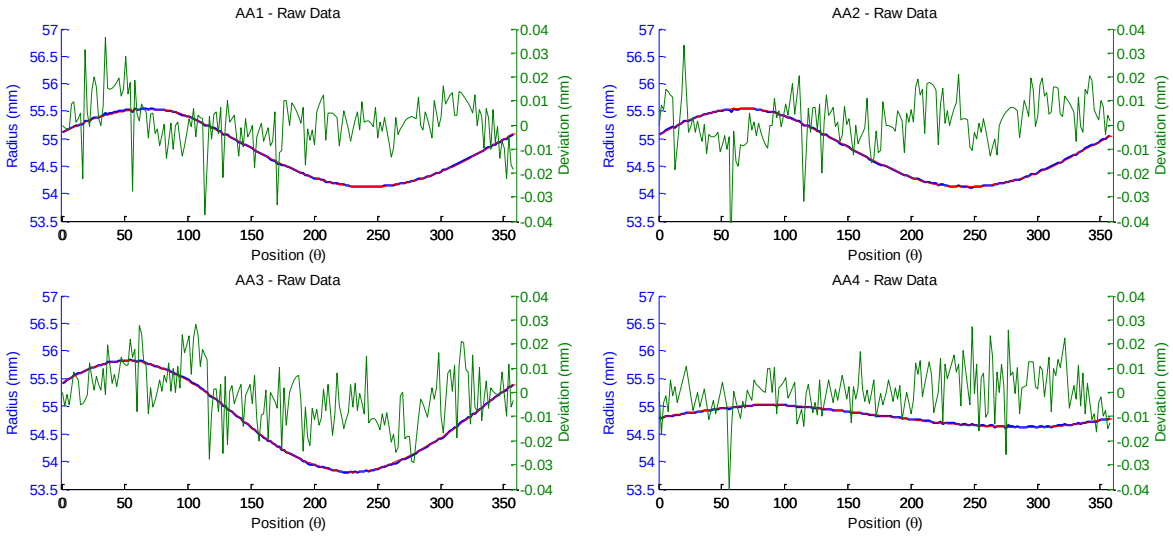

Figure 3-35 Cubic Spline Output of Data Set A-A (Data Length = 12)

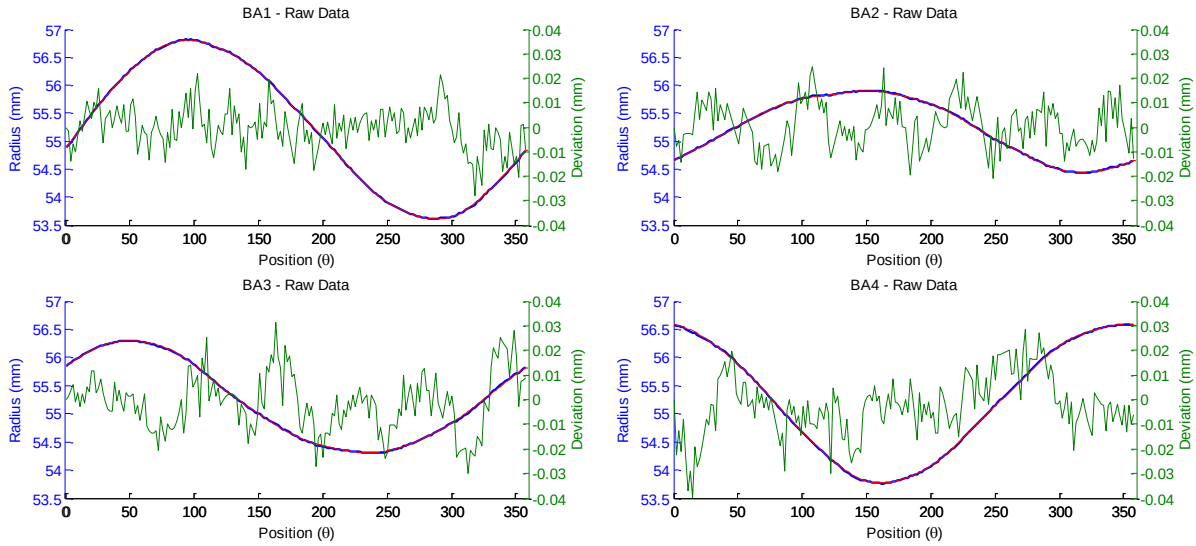

Figure 3-36 Cubic Spline Output of Data Set B-A (Data Length = 12)

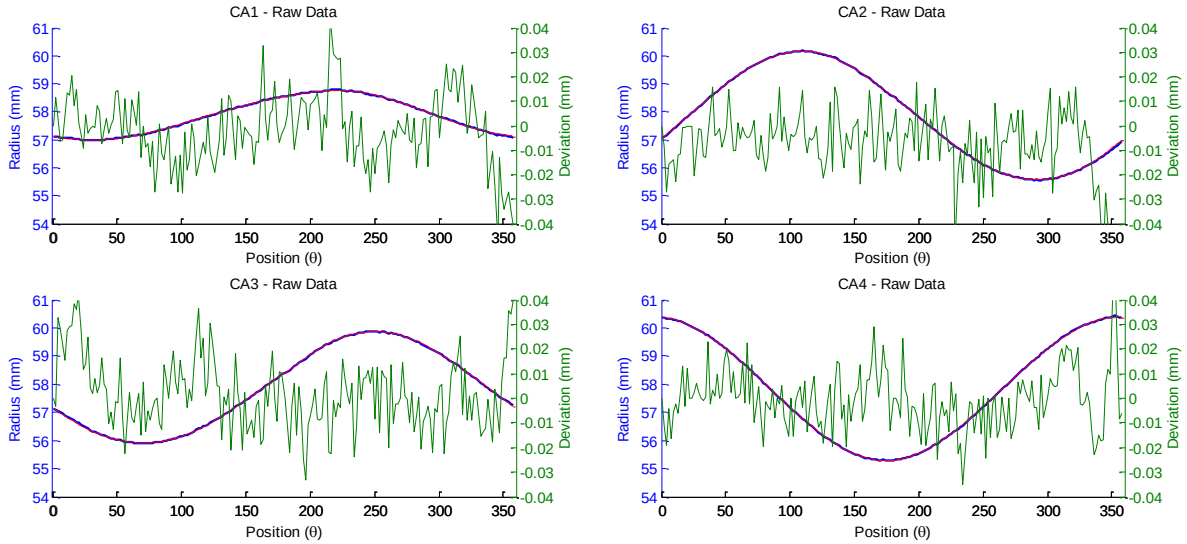

Figure 3-37 Cubic Spline Output of Data Set C-A (Data Length = 12)

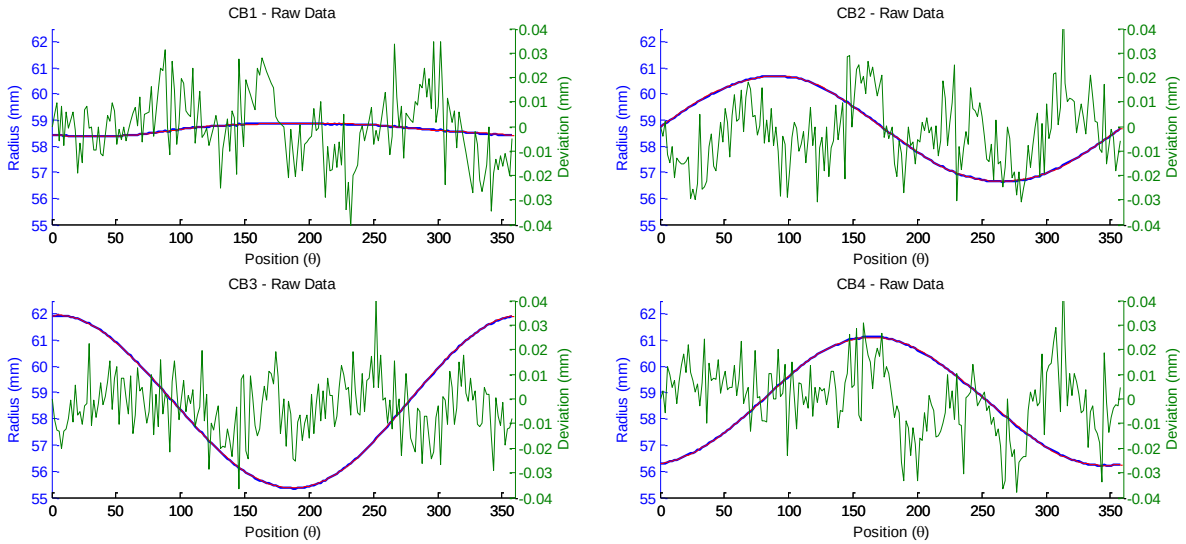

Figure 3-38 Cubic Spline Output of Data Set C-B (Data Length = 12)

Comparison between the interpolated and original data demonstrate that the Cubic Spline interpolation is an effective method for modelling profilometry geometry of a reformer tube. The estimated data points deviates typically within ±*0.015mm* from the original measurement with a random distribution of spikes in various locations. This result is of no surprise considering the *0.01mm* accuracy of the apparatus used in generating the original data and the ±*0.02* surface texture identified previously in *section 3.3.1.1*. A repeated deviation of about 0.04mm is seen between *330°- 360°* region in sample C-A. This can be correlated with the visible in the isolated bulging separate from the isotropic creep deformation in the original dataset *(Figure 3-33).*

The next step is to process the reconstructed data points using the CDA and compare the result with the resulted presented in *Section 3.4.1*. Shown *in Figure 3-39 to Figure 3-42* and *Table 3-11 to Table* 3-14 are the graphical and *GOF* results for each sample set.

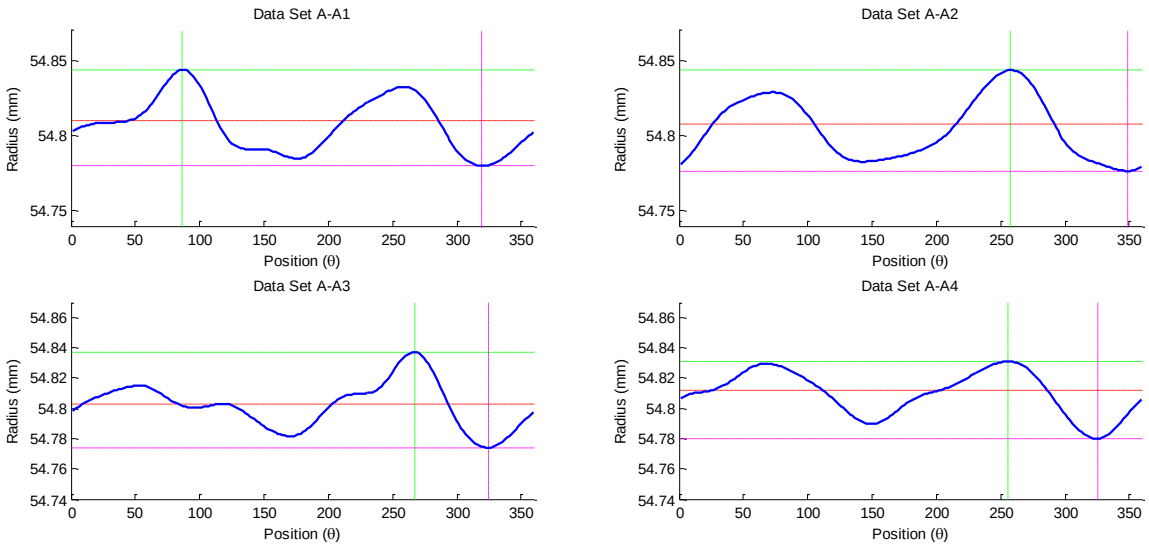

Figure 3-39 Sample A-A Graphical Result (Data Length = 12, Mask Width = 10)

Table 3-11 Sample A-A Statistical Results (Data Width = 12, Mask Width = 10)

	A-A1	*A-A2*	*A-A3*	*A-A4*	*Average*
R (mm)	54.8054	54.8029	54.8002	54.8110	54.8049
X Offset (mm)	-0.6375	-0.6577	-0.7831	-0.1967	-
Y Offset (mm)	-0.3116	-0.2943	-0.6285	0.0151	-
sse	0.0523	0.0704	0.0361	0.0352	0.0485
rs	0.9989	0.9985	0.9996	0.9906	0.9969
adjrs	0.9989	0.9985	0.9996	0.9905	0.9969
rmse	0.0167	0.0193	0.0138	0.0137	0.0159
cpu time (s)	0.8750	0.8750	0.7969	0.8594	0.8516

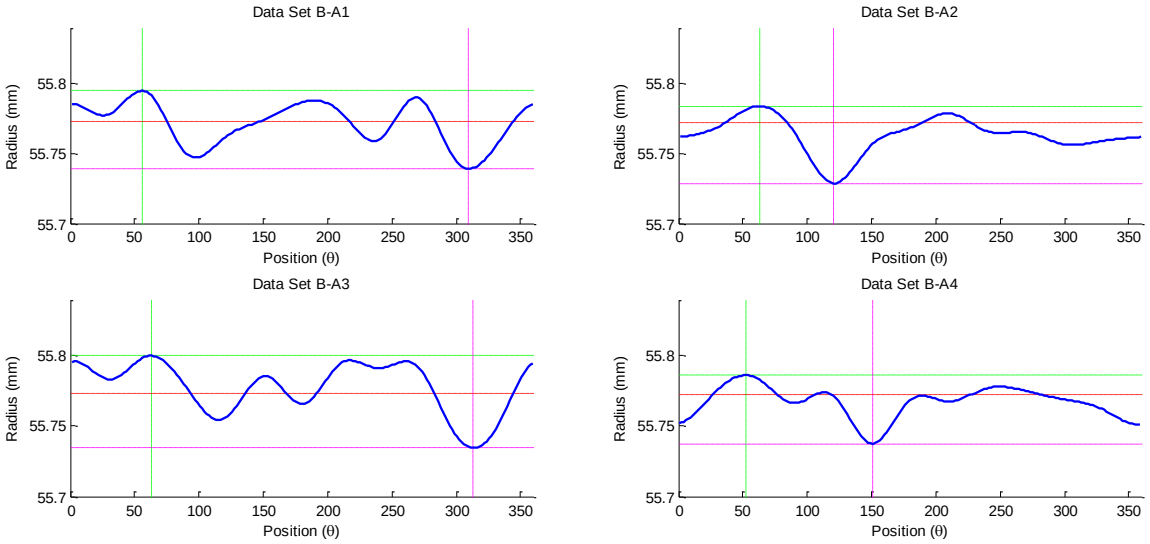

Figure 3-40 Sample B-A Graphical result (Input Data Length = 12, Mask Width = 10)

*Table 3-12: Sample B-A Statistic Result (*Input *Data Length = 12, Mask Width = 10)*

	B-A1	*B-A2*	*B-A3*	*B-A4*	*Average*
R (mm)	55.7728	55.7647	55.7795	55.7686	55.7714
X Offset (mm)	-0.7801	-0.2273	-0.3864	0.1691	-
Y Offset (mm)	0.1658	0.2857	-0.3138	-0.6754	-
sse	0.0936	0.1005	0.1258	0.0752	0.0988
rs	0.9984	0.9918	0.9949	0.9983	0.9959
adjrs	0.9984	0.9917	0.9949	0.9983	0.9958
rmse	0.0223	0.0231	0.0259	0.02	0.0228
cpu time (s)	0.875	0.8594	0.7969	0.875	0.8516

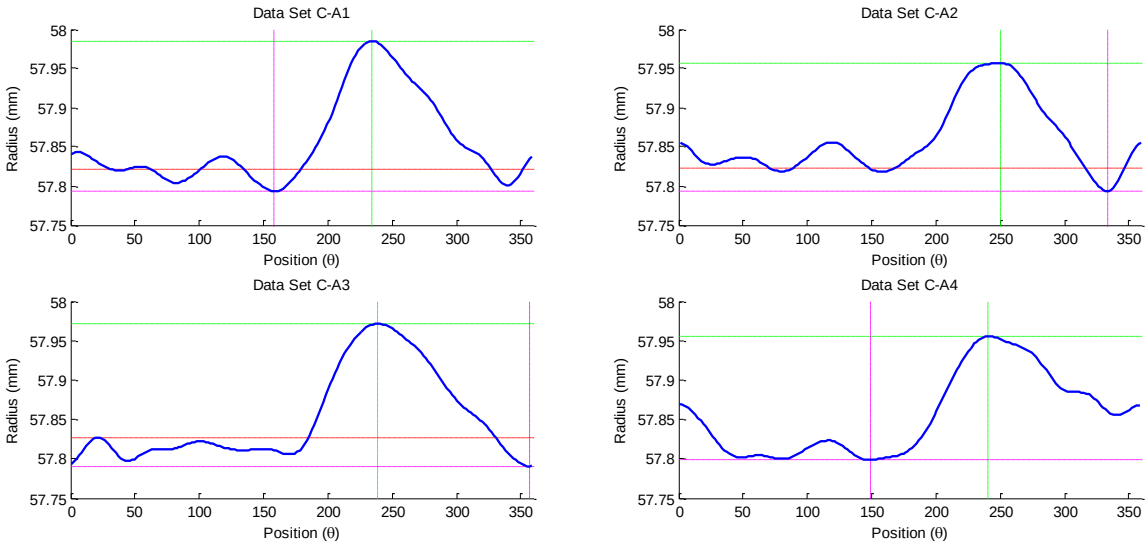

Figure 3-41: Sample C-A Graphical result (Input Data Length = 12, Mask Width = 100)

Table 3-13: Sample C-A Statistic Result (Input Data Length = 12, Mask Width = 100)

	C-A1	*C-A2*	*C-A3*	*C-A4*	*Average*
R (mm)	57.8221	57.8337	57.8131	57.8084	57.8193
X Offset (mm)	0.4019	-2.1886	1.7973	0.1622	-
Y Offset (mm)	0.7289	0.7519	0.6166	-2.5115	-
sse	0.0134	0.0118	0.0049	0.0061	0.0091
rs	0.9988	0.9998	0.9999	1.0000	0.9996
adjrs	0.9988	0.9998	0.9999	1.0000	0.9996
rmse	0.0117	0.0110	0.0071	0.0083	0.0095
cpu time (s)	0.8594	0.9063	0.9531	0.9219	0.9102

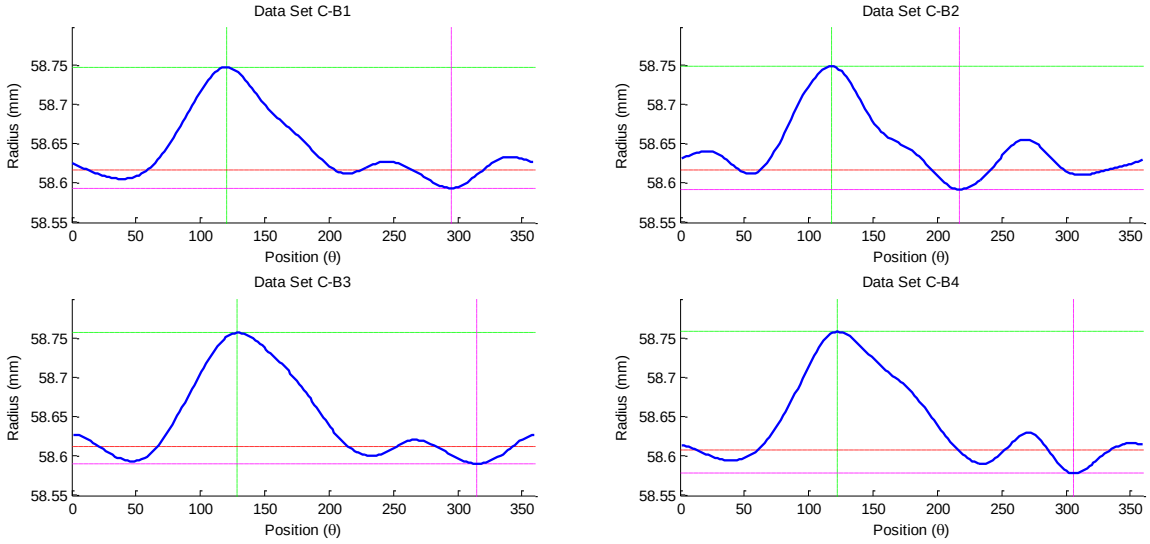

Figure 3-42: Sample C-A Graphical result (Input Data Length = 12, Mask Width = 80)

Table 3-14: Sample C-B Statistic Result (Input Data Length = 12, Mask Width = 80)

	C-B1	*C-B2*	*C-B3*	*C-B4*	*Average*
R (mm)	58.6176	58.6170	58.6121	58.6081	58.6137
X Offset (mm)	0.1155	-1.9886	-0.3008	-0.5477	-
Y Offset (mm)	0.2070	-0.1574	-3.2868	2.3370	-
sse	0.0156	0.0294	0.0186	0.0241	0.0219
rs	0.9963	0.9999	1.0000	0.9999	0.9990
adjrs	0.9963	0.9999	1.0000	0.9999	0.9990
rmse	0.0110	0.0152	0.0120	0.0137	0.0130
cpu time (s)	0.8438	0.9688	0.9688	0.9688	0.9376

The most predominant feature that is noted from the result is the reduction information related to the surface texture of the tube. Although the sample was smooth to touch by human hand, the original data collected from the Profilometry Measurement Tool showed fluctuation of ±*0.02mm* consistently throughout the dataset. As the data is interpolated from series of third-order polynomial functions, the high frequency fluctuation features are attenuated, resulting in an effect of a low pass filtering. Overall the data is clearer and easier to interpret that the original dataset.

For *Sample A*, the elliptical characteristic expected from the tilted measurement plane is still visible, although with reduced clarity and definition. The maximum spread of the data has decreased slightly to *0.08mm*, between *54.77mm* and *54.85mm*, from the *0.10mm* determined form the original data. There is little difference between the average radius value *R*, *0.0050mm* between *54.8049mm* and *54.8079mm* resulted from the interpolated and original data respectively, indicating evidence of consistency in the proposed method. The *GOF* report shows that the model is better fitted with the interpolated data set. The *rs* and *adjrs* values have increased by *0.0011* and *0.0012 respectively*, showing a slightly improved interpretation of the model and the *sse* and *rmse* has also both reduce by *0.056mm* and *0.0077mm*. This makes sense as the model has no consideration for high-frequency features, hence with the filtering effect of the interpolation process the data will match the model better. It is also interesting to note that although with the added process of data interpolation and the same regression data length of *200*, the overall execution time for the algorithm has

reduced by an average *0.1484s*. The main reason for this is the reduction in the regression iteration performed by the MATLAB Curve Fit function. With the *12* point interpreted data the number of iterations required by the fit function to meet the default step tolerance termination condition was reduced from approximately *600* iterations, for the original dataset, to *100* iterations.

A very similar result can be seen in *samples B, C-A* and *C-B* as described with *sample A*. Smoothing effect has taken effect in all three samples, which has slightly improved the statistical results of the *GOF* output. For both *C-A* and *C-B*, the characteristics of local creep deformation is accurately reconstructed with near to nothing 0.0046mm and -0.0061mm deviation between the average radius value R between original and reconstruction dataset. However, the sinusoidal characteristic visible in the original dataset B is indistinguishable in the reconstructed data. This indicates that the performance of the proposed method is limited with tubes with geometrical asymmetry that is equal or less than the signal fluctuation resulted from the surface texture.

3.4.3 Effect of adjusted Mask width

In order to test the effect of adjusted Mask Width used for the CDA model fitting algorithm, the four datasets from the sample tubes are tested with a range of Mask Width sizes. Shown in *Figure 3-43* to *Figure 3-46* are the graphical output generated with mask width ranging between 10 to 100.

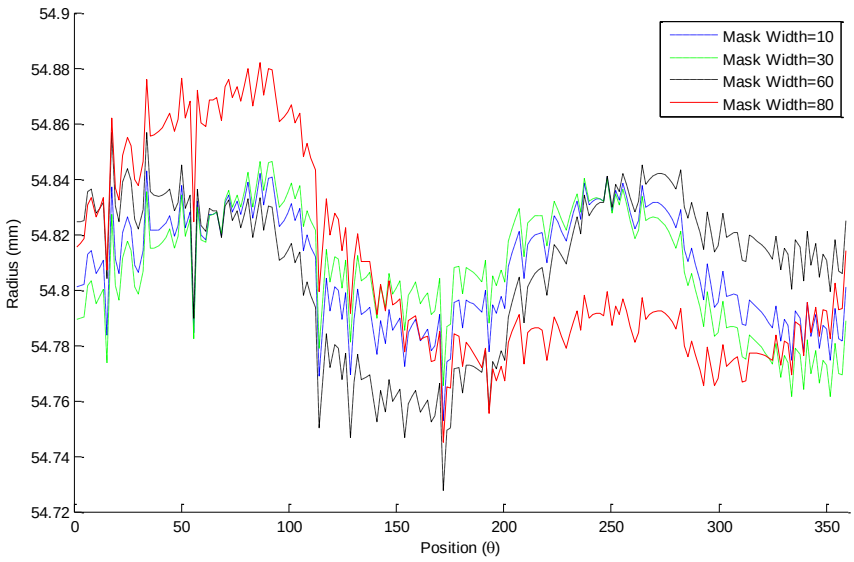

Figure 3-43: Sample A-A Graphical Result with Adjusted Mask Width

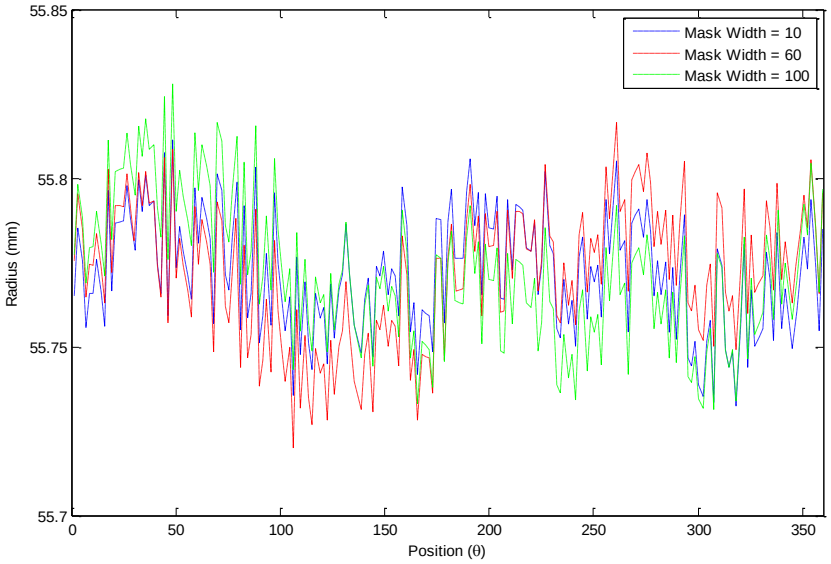

Figure 3-44: Sample B-A Graphical Result with Adjusted Mask Width

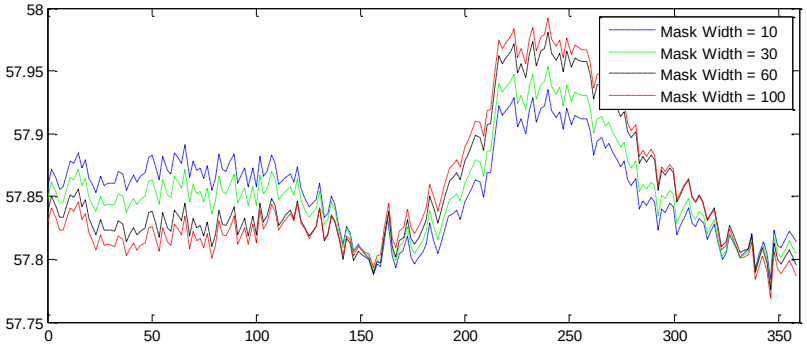

Figure 3-45: Sample C-A Graphical Result with Adjusted Mask Width

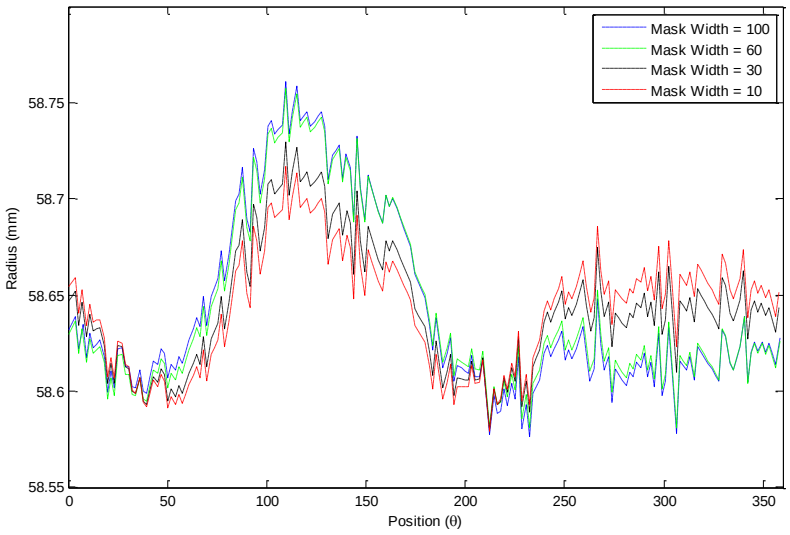

Figure 3-46: Sample C-B Graphical Result with Adjusted Mask Width

Observing *Figure 3-45* and *Figure 3-46*, it is clear that the performance of the proposed method in detecting and quantifying local creep deformation is effected by the size of Mask width used. In both samples, the plot becomes skewed as the mask width is reduced from 100 to 10, resulting in a reduction in the peak radius from *57.99mm* to *57.93mm* for sample C-A and *58.76mm* to *57.72mm* in *sample C-B.* As discussed in *section 3.2.2.2*, the mask width must match the distribution of asymmetry in the tube. It is noted that the CDA was able to accurately locate the position of increase radius regardless of the size of the mask used, *210°-260°* for *sample C-A* and *90°-150°* in sample C-B.

Looking at the result from *Sample B-A, Figure 3-44*, is evident that the Mask width has minimal effect on the CDA performance when there is minimal local deformation in the tube. Between the three mask size of *10, 80,100,* the resulting plot almost overlaps one another. The minor deviation is negligible considering the scale of the variation of the surface texture.

Section 3.2.4 discussed the limitation of the propose CDA, noted that the model derived in *section 3.2.2.1* do not account for multiple asymmetric features. This was clearly reflected in the result from *Sample A-A* as shown in *Figure 3-43.* With elliptic distortion introduced to the dataset resulted from a tilted measurement plane has created two minor and major axis. A small mask width is necessary to best represent this phenomena, but will contradict the large Mask Width required with *sample C-A* and *C-B.* Large mask width will significantly skew the result to one of the semi-major axis, resulting in a false detection.

3.5 Chapter Summary

This chapter identified the phenomenon of datum misalignment that is resulted from conventional three-point stabilising mechanism and its effect on the profilometry measurements. The reformer tube was modelled as makeup of a circle and the anisotropic deformation as hoop and localised creep straining. A sinusoidal distortion induced to the profilometry measurement was derived and used to determine the datum offset by analysing the circular property of the tube using a novel CDA, utilising curving and data masking techniques. A creep damage inspection architecture was presented for practical implementation of the proposed strategy, and its performance was demonstrated on a series of profilometry datasets collected from an ex-service reformer tube. The key attributes, benefits and drawback in using the proposed Reformer Tube Profilometry data analysis strategy for detecting creep damage are as follows.

- The proposed strategy provides a mean of accounting for inspection device misalignment and correction for datum offset distortion. The approach is robust for isotopic and anisotropic tube deformation, and easy to implement with common internal profilometry data.
- Masking technique to locate the direction at which the local deformation is occurring. This data is valuable to plant operators for balancing the reformer furnace for longer lasting reformer tubes. The accuracy and precision of the proposed method in evaluating creep degradation is dependent on the sample size, mask width and step size. More sample data size and masking step size will give a better accuracy and resolution in locating localised deformation but consequently resulting in longer computation time.
- A mean of data reconstruction using cubic spline data interpolation technique and its effectiveness was demonstrated. The experiment has revealed that creep strain can sufficiently be detected from reconstructed dataset from 12 radii measurements using cubic spline interpolation.

4 Optical Position Tracking (OPT) System

As discussed in the literature study, current internal RTIS lacks the ability to track the rotational motion of the measurement probe during inspection creating uncertainties in the collected profilometry data. Associating accurate positional measurement with the profilometry data will result in an improved reformer tube inspection performance, contributing to a more efficient RSL assessment and SMR operational analysis.

Presented in this chapter is a novel optical solution for orientation detecting specifically considered for reformer tube application. In the first section of the chapter, the significance and the challenges of position detection in vertical tubes are presented with examples of existing methods. Then the fundamentals of linear polarisers are discussed and further developed into the proposed Optical Position Tracking (OPT) system. Finally, the approach is verified by developing a working prototype to demonstrate an implementation method with RTIS via practical experimentation.

4.1 Introduction

To understand the significance of orientation detection in the sectional plane let us study the following example scenario.

Considered in this scenario is a CSR plant operating *300* tubes processing natural gas/ naphtha for methanol/ammonia production. After four years of service, the plant was put into maintenance shutdown for catalyst replacement. With no prior history of a major fault in the plant, a decision was made to conduct a profilometry inspection on all the tubes for detection of any early-stage creep damage. After assessing half of the tubes with no major issues, the following data was collected. Shown in *Figure 4-1* is a graphical representation of the top portion of the test tube indicating a localised creep strain of approximately *0.4%* (region of the red gradient). While the damage is well below the retirement threshold of *1.5% or 2.5%* for HK40 and HP40 alloys, the result indicates a misbalanced plant.

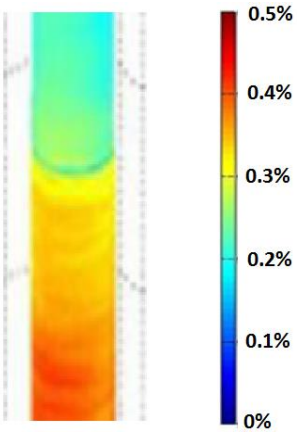

Figure 4-1 Early stage localized creep strain (example)

Based on this knowledge, it is of the company's best interest to adjust the furnace parameters to balance the plant operation, extending the service life of the tubes. To do this, the cause of the localised creep damage must be first be determined. The first and rational step to take is to associate the degrading features with the common causes surrounding the tube, such as burners and tunnel port. For example, if the bulging is oriented towards a particular burner, it can be determined the cause to be associated with either misaligned or a failure of the burner. In another example, if the bulging is towards a particular side hole of the flue gas extraction tunnel, one can assume a thermal misbalance caused by uneven flue gas flow pattern. In a such way, knowledge of the profilometry data location can help debug plant operation and further correct for this to optimise for plant operation.

Profilometry data is typically associated with its relative displacement measurement from the top flange end of the tube along the tube axis and the circumferential orientation relative to the measurement instrument. In the case of the example given, this limits the ability to associating early stage creep detection with its cause when the instrument experiences rotation as the guide wheels track along the uneven tube surface as observed in the sample tubes in *Chapter 3*. To this, manual gauging may be required on the tube walls to accurately identify the direction of the creep degrading, which may be very challenging and time-consuming if the bulge is located in hard to reach places. Such locations might be regions below the extraction tunnel or up high by the furnace ceiling, in which scaffolding is required. If a continuous geometric feature is visible along the length of the tube wall as in

Figure 4-2, the *"twisted"* characteristic can be corrected for programmatically. However, this is not common in many cases hence it is beneficial to implement orientation detection capability into the Profilometry Inspection system for a more comprehensive solution.

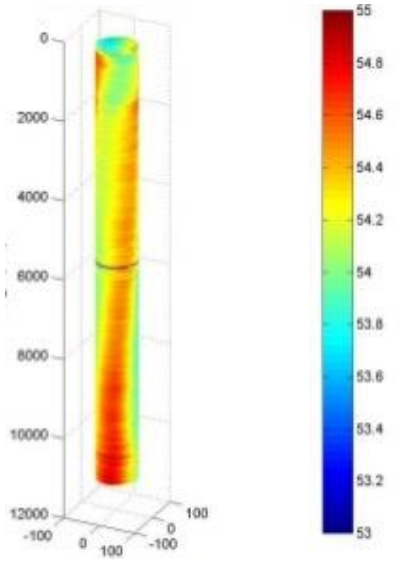

Figure 4-2: Continuous deformation feature in Profilometry Data [18]

Sensing and monitoring motion of a moving object is common task practiced in many engineering disciplines. Historically, academia has worked closely with industry to devise many solutions to various automation and robotics fields. One the most accurate, if not the most accurate, method that is common in measuring rotation motion is the rotary encoder (commonly referred to as just encoder). This prevalent device comes in many form factors, utilizing various sensing technologies for a wide range of application. Common encoder technologies such as optical, magnetic (also called resolver), and capacitive principles are used in conjunction with one another to accommodate a variety of purpose from a dial on a UI control panel to a jet turbine high speed rev-counter for a feedback control system. In robotics, encoders are used to monitor the speed and position of electric motor shafts for precision motion control.

Although with the benefits of flexibility in precision, response time, and cost for manufacturing, the compelling limitation for the rotary encoder is the range that it can operate. Encoders must be installed in close proximity with the moving object (generally 0-10mm) make this technology impractical for this topic. For example, if the encoder was integrated into the reformer tube measurement probe, a rigid mechanical coupling is required between the sensor and a static object outside the tube. This may be a rigid rod that extends the length of the tube or a flat ribbon tape wound on a spool mechanism. Either way, the solution will result in an unwieldy instrument that is impractical for RLA.

In a more remote application, the most established and renounced solution for position sensing is the Global Positioning System (GPS). It is the sophisticated, but yet the most common system that uses global satellites to determine the coordinate of an object

(commonly in longitude and latitude) almost anywhere on the surface of the earth. In robotic mapping, GPS, 3-axis accelerometer, and 3-axis magnetometers are used in conjunction to perform simultaneous localization and mapping (SLAM) algorithm. This comprehensive method has traditionally been used in aerial navigation and autopilot systems. In the last decade, there has been a noticeable development in the automotive industry in self-driving cars, which also deploys onboard vision and LIDAR technology. GPS uses triangulation in 3-dimensional space to determine its exact location. To this, a minimum of three satellite is required for a GPS to work. Because GPS signal is very weak, GPS receivers has limited performance in confined space. Because both GPS signals and earth magnetic field is obstructed within the reformer tube walls due to electromagnetic shielding, both technique is not applicable for this research. Obviously, gravity can still be detected with an accelerometer, knowing the direction of the gravitational force serves little purpose for detecting longitudinal rotation inside a vertically oriented tube.

Another available method used in industry is the fibre optic gyroscope (FOG) [114]. In this method change in orientation is determined using the Signac effect of two light beams trajected through a single mode optic fibre. Work by A Noureldin [115]demonstration the use FOG in downhole surveying to perform real-time measurement-while-drilling at high inclined and horizontal directional boring. Such an approach is adequate for a stable system where the motion is predictable. However, for noisy application with rapid change or vibration, a significant signal-to-noise ratio is induced into the system resulting in time-dependent accumulation of error termed integration drift. To this, this technique and other incremental sensor are typically aided with a frequent update of feedback signals generated from absolute sensors, such as encoders, accelerometer, and GPS modules.

In summary, monitoring the rotational motion of an object travelling through a reformer tube served to be a challenging task - the vertical orientation of the tube combined with the limited access and isolation from GPS or earth magnetic field in large limits the use of conventional sensing technologies. In this research, the effect was invested to devise a new method to handle this task.

4.2 Proposed Method: Optical Position Tracking (OPT) System

Proposed in this research is a conceptually novel method in tracking the angular motion of an object travelling through a cylindrical structure. The method demonstrates an optical solution for long-range motion detection that intends to overcome the limitations found in existing

technology in the application of this research. The orientation independent system is named the Optical Position Tracking (OPT) in this research.

4.2.1 Methodology: Method Development

Shown in *Figure 4-3* is a schematic diagram highlighting the key elements that make up the OPT system. As illustrated, OPT is a two-part system of a light source and OPT sensor which encompasses two-stage data processing algorithm to determine the angular discrepancy between the two modules.

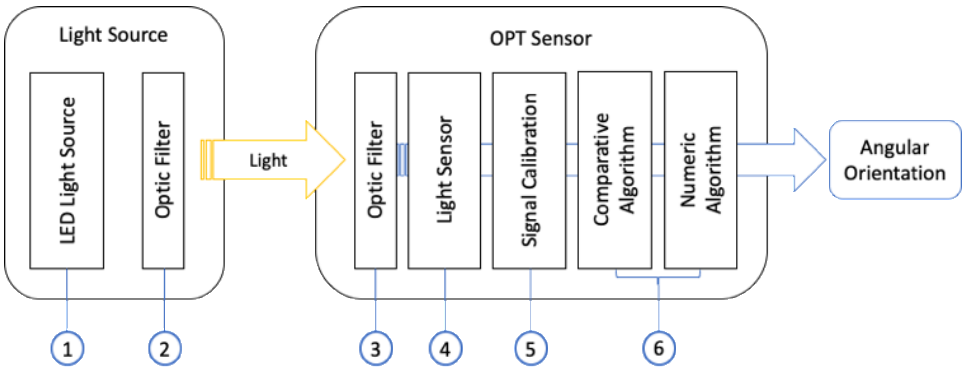

Figure 4-3 OPT Schematic Diagram

The working principle of the propose OPT system is as follows. A light source **(1)** in a form of a narrow conical beam is shown down the reformer tube from the top flange opening of the reformer tube. A linear polarising filter (LPF) **(2)** is placed in front of the light source lens, which plane-polarises the light. This light is observed from inside the reformer tube by the OPT sensor attached to the inspection probe through a second LPF **(3)**. The light passing through the two filters is attenuated proportionally to the relative angular between the transmission axes of the two filters. If the transmission axis of the two filters is in parallel, the transmission through the two filters is maximised. If they are perpendicular, commonly described as the two filters being crossed, then the transmission is minimised. By sensing and analysing the light intensity passing through the two filters with an electronic light sensor **(4)** and a two-stage data processing algorithm **(6),** the angular motion of the Inspection Probe travelling through the tube can be determined. Because the light is contained inside the tube with no other external light source, the optical characteristic of the system is consistent and therefore predictable, making the method feasible compared with application outdoor with lots of lighting variables (e.g. ambient light, sunlight, shadowing).

For a linearly polarised light, the intensity of the light transmitted through an ideal polarizer can be described using Malus' law as shown in equation [4-1].

$$I_t = I_s \times \cos^2 \theta \quad [4\text{-}1]$$

Malus Law states that the intensity of the polarised light (I_s) transmitted through a LPF (I_t) varies as the square of the cosine of the angle (θ) between the plane of transmission of the filter and the plane of the polariser. Shown blue in Figure 4-4 is the characteristic of light beam intensity I_t represented as a percentage of I_s over the full rotation of θ between 0° to 360° according to the Malus' law in the ideal situation. It can be observed that the sinusoidal characteristic repeats twice over the full range of rotation with maximum light passed through when the LPF transmission axes are parallel at *0°* and *180°*. At *90°* and *270°*, the LPF transmission axes are perpendicular (crossed) with the polarisation plane, in resulting passing through the two filters is completely obstructed. By modelling the correlation between the observable light intensity I_t and the given light sensor characteristic, the absolute angular position θ within the repeated phases can be determined. If the initial position is known, the angular motion of the OPT sensor relative to the light source can be tracked throughout the full range of motion.

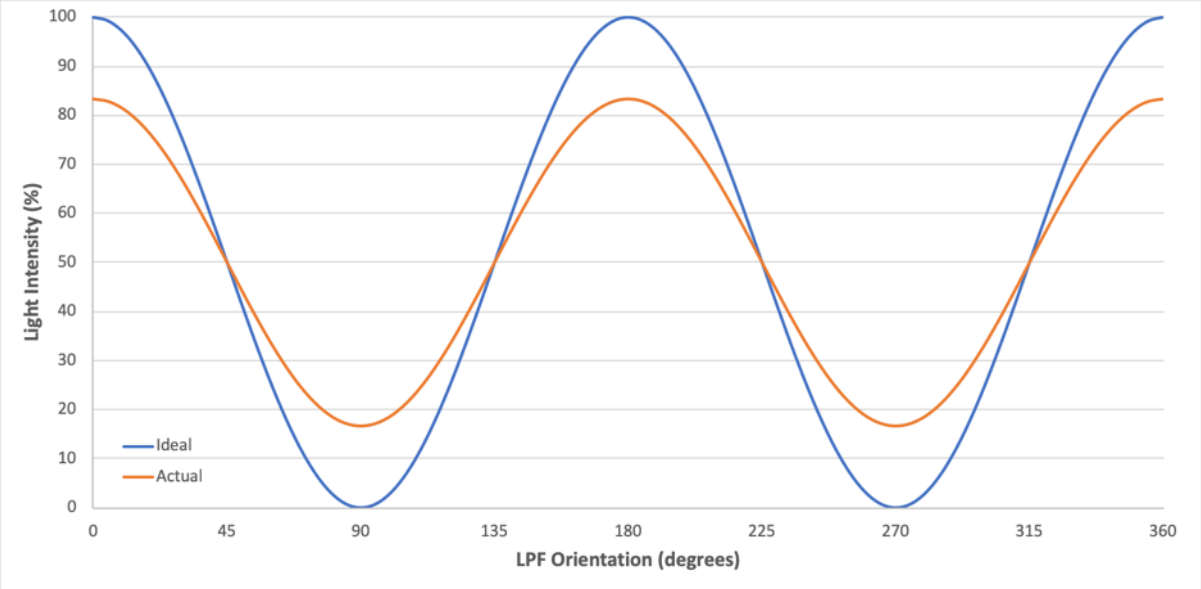

Figure 4-4 Ideal and Actual Comparison of OPT Signal

However, in practice, there are many factors that affects the optical characteristics that is not modelled by Malus Law. Shown in orange in Figure 4-4 is the measured light intensity I_t that better represent the characteristic that is observed in practice. The first aspect to consider is the deterministic error resulted from the practical limitation of LPF. The performance of LPF is dependent on the wavelength passing through the filter and is optimised typically for visible light spectrum between *400-700nm*. Depicted in Figure 4-6 is a specification graph included in the datasheet of a linear polarizer manufactured by TECHSPEC. Shown in blue

line is the transmission characteristics of light pass through a single LPF. In the visual spectrum, an attenuation of typically 55-60% is seen with a almost linear increase between *500nm* to *650nm* wavelength. This makes sense as the majority of the randomly polarised light is blocked by the filter and only the light parallel to the transmission axes is passed through. Shown in purple is transmission characteristic when a light is passed through two filters oriented in parallel axes. Ideally, the output should be identical to the blue as all of the polarised light should pass through the second filter. However, because LPF is not 100% efficient, there is a discrepancy between the Single and Parallel transmission. As a result the transmitted light is attenuated (approximate 5% in this case) by a factor that is dependent on the wavelength of the light source. The green plot in the figure represents the percentage of crossed transmission at a given wavelength between two filters. This indicate the amount of polarise and unpolarised light that leaked through the two LPF. For an ideal filter represented by Malus Law, the light completely blocked by the two filters. But again the physical limitations of the filter causes some light to pass through which is dependent on the wavelength of the light source. According to the datasheet, the average crossed transmission value for this particular filter is 0.15%.

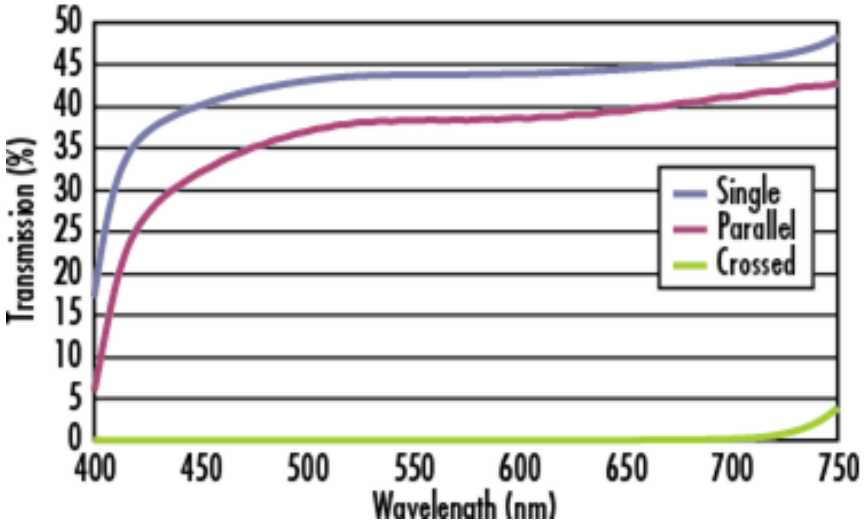

Figure 4-5Characteristic of a TECHSPEC High Contrast Plastic Linear Polarizer

It is common practice to specify the ratio of parallel to cross-transmission of the linear polarizer, and this is known as the Extension Ratio and is typically normalised. An example specification is an extinction ratio of 10000:1 which indicates that the parallel transmission of light is 10000 more than cross transmission within the specified wavelength. For the application of this research, a large Extension Ratio is necessary for a greater deviation between the measured light intensity *I* at parallel and crossed transmission axis.

The second aspect to be considered is the light attenuation and scattering caused by the reformer tube wall. Because the source light is not a collimated beam, as the Inspection Probe move deeper down the tube more of the polarised light is illuminated onto the inner wall of the tube and lesser on the OPT sensor. When the light hit the internal surface of the tube, the direction of the light ray will change accordingly with the law of reflection. The magnitude of each phenomenon is determined by the angle of incidence at which the light approaches the surface, hence the depth of the device, and two materials refractive index. Depending on the amount of service exposure the ID surface condition will change from the original machined finish to a rougher, oxidative surface. Rough surface causes the light to scatter when reflected and become unpolarized. A portion of the light will also be absorbed into the tube wall based on the law of refraction. As a result, an overall attenuation of the detected light is seen, and the amount of unpolarized light transmitted through the system is increased dependent on the distance between the two LPF. Considering the phenoninums, Maxlus Law can be modified to Eq.[4-2] for a better representation for the application.

$$I = a \times I_s \times \cos^2 \theta + b \qquad [4\text{-}2]$$

Addition to the Maxlus Law is the two correction factors a and b that accounts for the element that has been discussed till now. Correction factor a represents the attenuation of the light transmission through the filter. Because measurement of light intensity I can never be negative, a is a value between 0 and 1. Correction factor b represents the amount of light leakage through the filter.

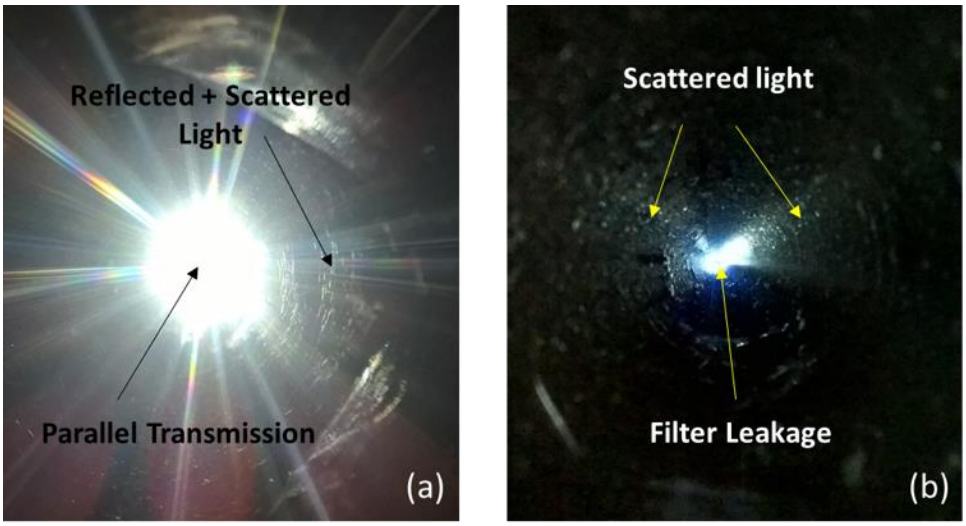

Figure 4-6 LPF performance inside a tube a) parallel b) crossed

Presented in *Figure 4-6* are two images of a polarised light shown through an *8meter* length aluminium tube of *70mm* internal diameter when observed through an LPF filter. In the photo

(**a**) the two filters are oriented parallel and in the image (**b**) the filters are oriented perpendicular (crossed). It is clear that while more light passes through the filters in the orientation (**a**), the filter is not able to completely block the light at the crossed arrangement. Leakage light in the centre of the (**b**) and scattered light reflected off the tube wall is both visible. However, the amount of reflected light is significantly less in image **b** than it is in **a**, indicating that the majority of the polarity is kept in the reflection light off the tube wall.

4.2.2 Data Processing algorithm

If the relative orientation Θ is to be determined based purely on the single light intensity as described in Eq.[4-2], the light attenuation factor *a*, light leakage and random scattering factor *b*, and the transmission factor I_p must be first determined. However, because each element is dependent on the displacement between the two filters and the surface condition of the internal tube wall, it is hard or maybe impossible to formulate a universal model that will accurately reflect on the characteristic of every tube. It is equally impractical to gather characteristic data for every tube in the CSR plant, especially when the elements can differ substantially between and/or within each tube depending on the total service exposure time. For this reason, an alternative OPT data processing algorithm is developed for a universal approach.

Proposed is an orientation detection algorithm based on a comparative analysis of multiple phase-shifted light intensity measurements. Instead of evaluating the magnitude of the light intensity through a single filter, a comparative method is used to analyse three separate sensor reading that is $45°$ phase offset as shown in Figure 4-7. The three light intensity levels *S1*, *S2*, and *S3* is processed using a two-step algorithm, termed the OPT algorithm.

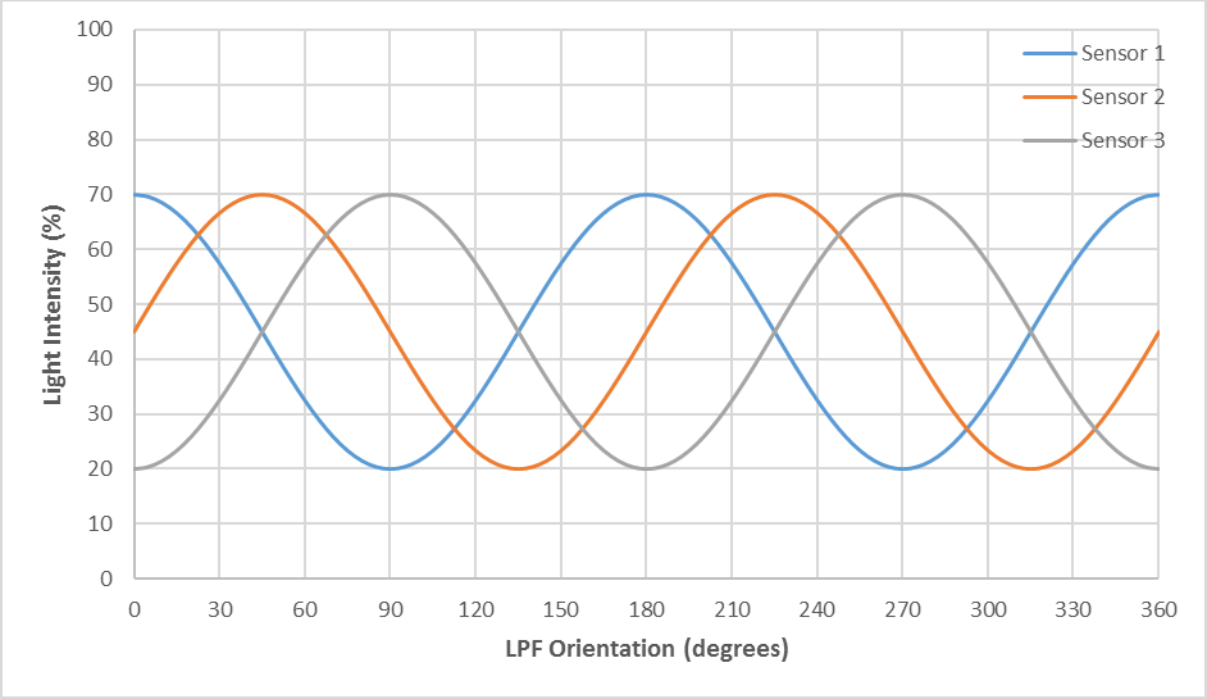

Figure 4-7 Optical Position Tracking Sensor Signal

4.2.2.1 Logic Algorithm

In the first stage of the OPT data processing algorithm, the orientation of the inspection probe Θ is estimated based on logic conditions shown in Table 4-1. Evidently, based purely on the simple logic comparison, angle Θ can be categorised into 16 unique regions and boundaries between *0°-180°* as depicted in *Figure 4-8*.

As the instrument gradually rotates through the tube, the two neighbouring condition statement of the previous location can be used to determine the new location without going through every possible solution. For example, if the probe is located in Region G between 67.6°-89.9°, when the new set of sensor reads are available 'condition G' can first be used to determine if the device has moved out of that original region. If it has then the neighbour conditions E, F, H, and I can then be applied to determine the new location. If the probe rotates pass 180°, then statement A is used with added 180° to indicate that the new position is between 180°-200.4°. In this way, the value of Θ can be tracked within the entire rotation of the filters in 32 unique regions.

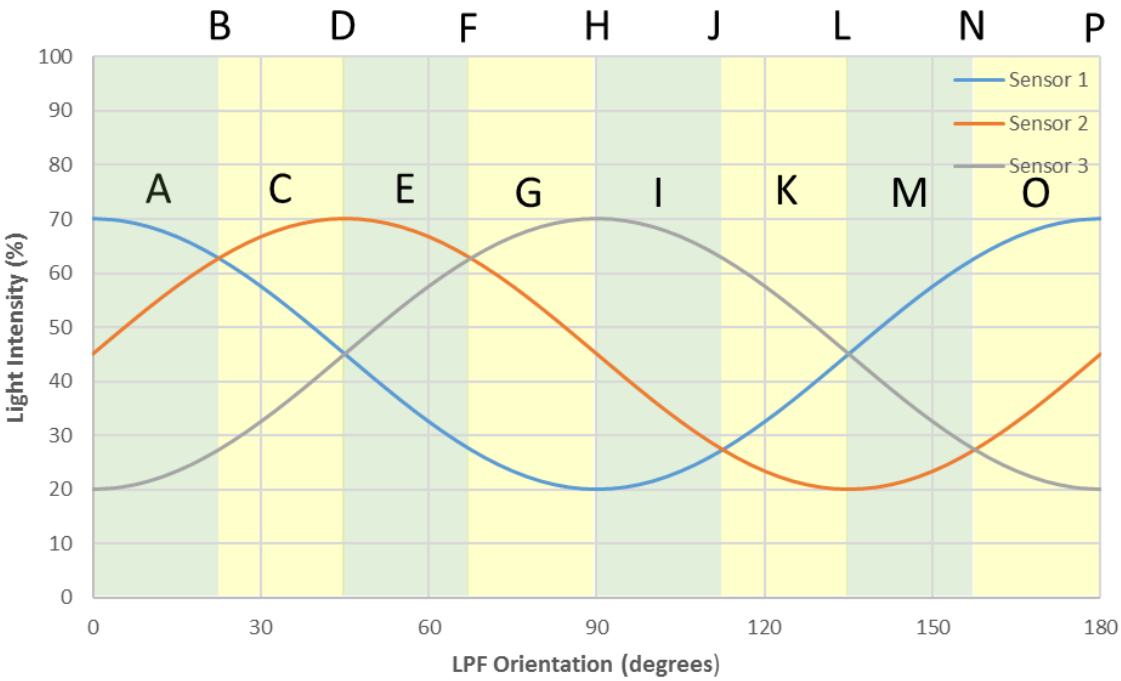

Figure 4-8 Classification of OPT Signal

Table 4-1 Comparison analysis of OPT signal

Identifier	Region	Condition
A	0.1-22.4°	$(S1 > S2 > S3)$ AND $(S2 < \frac{S1+S3}{2})$
B	22.5°	$(S1 > S2\ AND\ S3)$ AND $S2 = S3$
C	22.6-44.9°	$(S1 > S3 > S2)$
D	45°	$(S2 < S1\ AND\ S3)$ AND $S1 = S3$
E	45.1-67.4°	$(S3 > S1 > S2)$
F	67.5°	$(S3 > S1\ AND\ S2)$ AND $S1 = S2$
G	67.6-89.9°	$(S3 > S2 > S1)$ AND $(S2 < \frac{S1+S3}{2})$
H	90°	$(S3 > S2 > S1)$ AND $(S2 = \frac{S1+S3}{2})$
I	90.1-112.4°	$(S3 > S2 > S1)$ AND œ$(S2 > \frac{S1+S3}{2})$
J	112.5°	$(S1 < S2\ AND\ S3)$ AND $S2 = S3$
K	112.6-134.9°	$(S2 > S3 > S1)$
L	135°	$(S2 > S1\ AND\ S3)$ AND $S1 = S3$
M	135.1-157.4°	$(S2 > S1 > S3)$
N	157.5°	$(S3 < S1\ AND\ S2)$ AND $S1 = S2$
O	157.6-179.9°	$(S1 > S2 > S3)$ AND $(S2 > \frac{S1+S3}{2})$
P	180° or 0°	$(S1 > S2 > S3)$ AND $(S2 = \frac{S1+S3}{2})$

4.2.2.2 Numerical Analysis

In the second stage, based on the region determined in the Logic Algorithm, the orientation Θ is determined at a higher accuracy using a numeric analysis algorithm. Based on the *Eq.[4-2]*, the following equations for can be derived for each of the three light intensity signals in *Figure 4-7*.

$$S_1 = a \times \sin(2\theta + 90°) + b \quad [4\text{-}3]$$

$$S_2 = a \times \sin(2\theta) + b \quad [4\text{-}4]$$

$$S_3 = a \times \sin(2\theta - 90°) + b \quad [4\text{-}5]$$

Where *S1-S3* is the three sensor output, *a and b* is the filter transmission factor and the signal offset resulted from the combination of light scatter and LPF inefficiency as previously discussed.

Key Assumption: Here an assumption is made that the amount of light attenuation through the filter (*a*) and randomly polarise light passing through the system from light scattering (*b*) is assumed to be equal to the three signals. This assumption is feasible as long as the three sensors are distance close to each other and the tube axis.

As previously mentioned, deriving the of variables *a* and *b* is impractical with their dependency to the tube surface condition and sensor displacement. Hence, a fractional analysis between the deviation in the signal is formulated as follow:

$$\frac{S2 - S3}{S1 - S3} = \frac{(\mathrm{a} \times \sin 2\theta + \mathrm{b}) - (\mathrm{a} \times \sin(2\theta - 90^{\circ}) + \mathrm{b})}{(\mathrm{a} \times \sin(2\theta + 90^{\circ}) + \mathrm{b}) - (\mathrm{a} \times \sin(2\theta - 90^{\circ}) + \mathrm{b})}$$

Further simplified as:

$$\frac{S2 - S3}{S1 - S3} = \frac{\sin 2\theta - \sin(2\theta - 90^{\circ})}{\sin(2\theta + 90^{\circ}) - \sin(2\theta - 90^{\circ})} \quad [4\text{-}6]$$

In this way, the three sensor values can be used directly to derive the position Θ without the need of knowing the optical characteristic of the reformer tube, displacement between the light source and the OPT sensor, nor the optical characteristics of the LPF. Further, using simple trigonometry the equation can be simplified as follow:

$$\frac{S2 - S3}{S1 - S3} = \frac{2\cos(\frac{2\theta + 2\theta - 90^{\circ}}{2})\sin(\frac{2\theta - 2\theta + 90^{\circ}}{2})}{2\cos(\frac{2\theta + 90^{\circ} + 2\theta - 90^{\circ}}{2})\sin(\frac{2\theta + 90^{\circ} - 2\theta + 90^{\circ}}{2})}$$

$$= \frac{\cos(2\theta - 45^\circ)\sin(45^\circ)}{\cos(2\theta)\sin(90^\circ)}$$

Therefore:

$$\frac{\cos(2\theta - 45^\circ)}{\cos(2\theta)} = \frac{S2 - S3}{S1 - S3} \times \frac{1}{\sin(45^\circ)} \quad [4\text{-}7]$$

Now the left-hand side of the equation can be rearranged to Θ by:

$$\frac{\cos(2\theta - 45^\circ)}{\cos(2\theta)} = \frac{\cos(2\theta) \times \cos(-45^\circ) - \sin(2\theta) \times \sin(-45^\circ)}{\cos(2\theta)}$$

$$= \cos(-45^\circ) - \frac{\sin(2\theta)}{\cos(2\theta)} \times \sin(-45^\circ)$$

$$\frac{\cos(2\theta - 45^\circ)}{\cos(2\theta)} = \cos(-45^\circ) - \tan(2\theta) \times \sin(-45^\circ) \quad [4\text{-}8]$$

By substituting *[4-8]* back into *[4-7]*:

$$\cos(-45^\circ) - \tan(2\theta) \times \sin(-45^\circ) = \frac{S2 - S3}{S1 - S3} \times \frac{1}{\sin(45^\circ)}$$

And rearranging for Θ:

$$\theta = \frac{\tan^{-1}\left(\frac{\cos(-45^\circ) - \frac{(S2 - S3)}{(S1 - S3)} \times \frac{1}{\sin(45^\circ)}}{\sin(-45)}\right) - 180^\circ}{2} \quad [4\text{-}9]$$

Evident from *Eq.[4-9]*, the angular position Θ can be determined based on the three sensor signal, while the key assumption holds, independently to other variables, making this equation universal to tubes of all length and surface conditions.

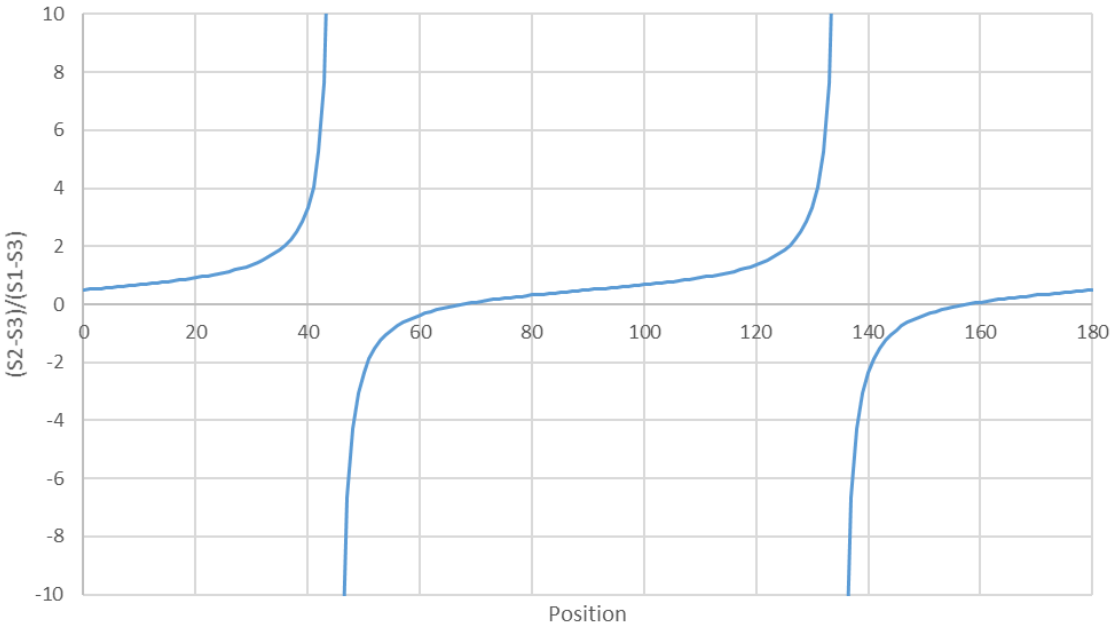

Figure 4-9 Characteristic of Equation 5-8

Figure 4-9 shows the characteristic of the *Eq.[4-9]*. It is clear from the plot that the correlation of the three sensor reading *S1-S2* and the displacement *Θ is tangential*. Because of tis, in the practical sense position within the regions with exponential characteristics (e.g. region near boundary D and L) will be subjected to increased noise-to-signal ratio, causing instability in the algrithm. To avoid such limitation, calculation should be limited to stable regions of the curve. To achieve this while having full displacement coverage, two more equations *Eq.[4-10]* and *Eq.[4-11]* is derived in a similar manner as *Eq.[4-9]*.

$$\theta = \frac{\tan^{-1}\left(\frac{\cos(45^\circ) - \sin(45^\circ) \times \frac{(S1 - S3)}{(S2 - S3)}}{\sin(45^\circ)}\right) + 45^\circ}{2} \qquad [4\text{-}10]$$

$$\theta = \frac{\tan^{-1}\left(\frac{\cos(-45^\circ) + \sin(-45^\circ) \times \frac{(S3 - S1)}{(S2 - S1)}}{\sin(-45^\circ)}\right) - 45^\circ}{2} \qquad [4\text{-}11]$$

The characteristic of the three equation *Eq.[4-9]*, *Eq.[4-10]* and *Eq.[4-11]* is summarised in *Figure 4-10*. Now at any given position *Θ*, there is one or more equation in the stable region. By using the estimated value of Θ determined in the Logic analysis of the OPT algorithm, one of the three equations can be chosen to derive the value *Θ* that gives the optimal performance. The allocation of the equations among the eight regions is shown in *Table 4-2*.

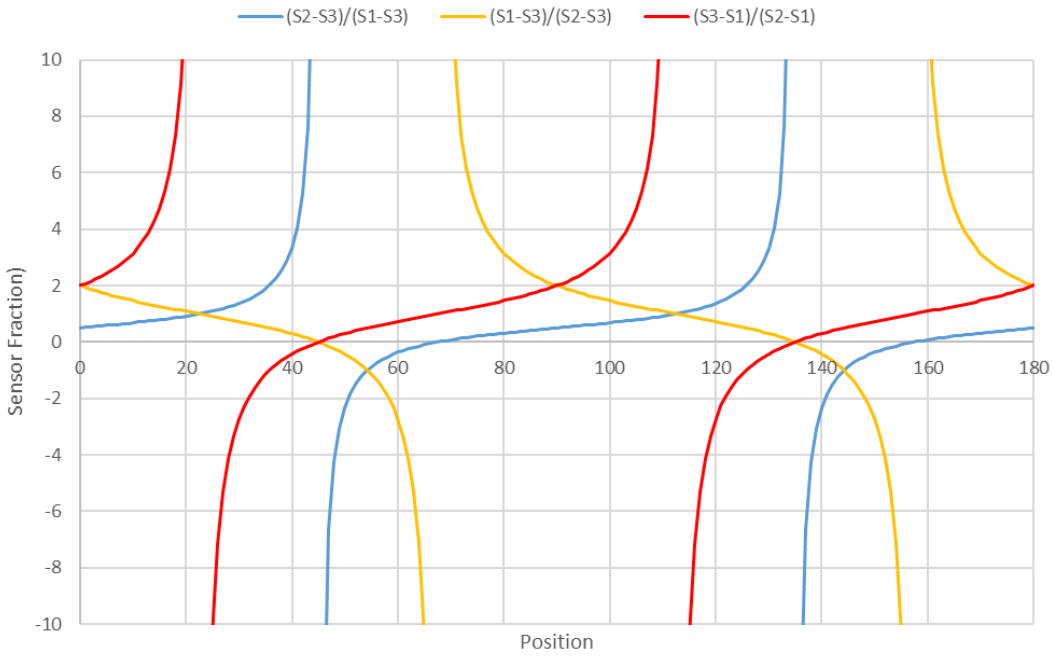

Figure 4-10 Characteristic of the three OPT Equations

Table 4-2 Allocation of Equation for Θ Region

Region	Range	Equation
A	0.1-22.4°	*Eq.[4-9] + 90°*
C	22.6-44.9°	*Eq.[4-10]*
E	45.1-66.9°	*Eq.[4-11] + 90°*
G	67.1-89.9°	*Eq.[4-11] + 90°*
I	90.1-111.9°	*Eq.[4-10] + 90°*
K	112.1-134.9°	*Eq.[4-10] + 90°*
M	135.1-156.9°	*Eq.[4-11] + 180°*
O	157.1-179.9°	*Eq.[4-9] + 270°*

4.3 Implementation and experiment

Having derived a method of monitoring the angular orientation of an object located inside a reformer tube, the next step is to test the concept. Presented in the section is preliminary experimentation conducted in this research to validate the OPT principle and verify its performance.

4.3.1 Experiment Methodology

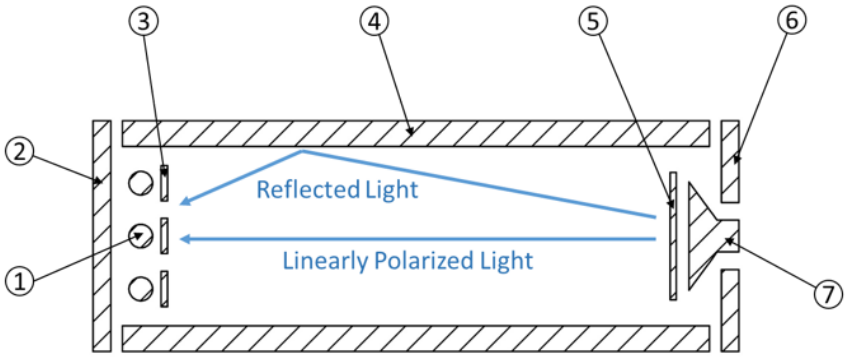

Figure 4-11 Experiment Setup Schematic Diagram

To verify the concept of the proposed OPT system an experiment is set up in an arrangement depicted in *Figure 4-11*. From one end of the sample tube (**4**) a polarised light, generated from a light source (**7**) and a polarising filter (**5**), is illuminated through the length of the tube along the tube axis. At the other end of the tube three digital light sensor (**1**) is used to observe the illuminated light through separate LPF (**3**) with the transition axis oriented *0°*, *45°*, and *90°*. Starting with the two filters in parallel arrangement, the polarity axis of the light beam is rotated incrementally by rotating the polarizer (**5**). At each position, the light intensity measured by each sensor is logged. The data is then used to derive the polarisation axis angle between filters (**1**) and (**5**) using the OPT algorithm and compared with the actual angle of the experiment setup. End caps (**2**) and (**6**) is design to match the tube dimensions so that it block external light entering the sample tube to mimic the intending environment during Reformer Tube inspection. The aim of this experiment is also to demonstrate a practical implementation of the OST system by designing and fabricating a fully functional OST prototype with the intention of integration with the RTIS platform presented in Chapter 5.

Unfortunately, a full reformer tube assembly was not available to be prepared for this section. Therefore two sample tubes of 0.1m and 8.0m length were prepared for this experiment. The experiment conducted on the shorter sample is termed Experiment 1 and testing carried out on the long sample is termed Experiment 2.

4.3.2 Experiment 1

Shown in *Figure 4-12* is the CAD model of the experimental hardware developed for this test. The rig was designed to investigate the OPT performance inside a 100mm length stainless steel tube with an internal diameter of 50mm. The machine finish of the inner wall of the tube was left intentionally to investigate the effect of light reflection. The light sensor used is the TAOS Light-to-Digital Converter, model TSL2561; a single CMOS integrated solution with precision measuring output of 16-bit resolution. The device has programmable features for complete exposure and analogue gain control for a diverse range of application. For this test, a gain of 16 and integration time of 402ms is used. Utilising external addressing feature, a breakout PCB board (**7**) was designed with a single inter-integrated circuit (I2C) communication cable to interact with the three uniquely addressed sensors. Three square cut-outs of EO Edmund high contrast Linear Polarizing Film (**6**) is placed in front of each sensor with the polarisation angle of *0°*, *45°*, and *90°*. The two-part (**8**,**2**) 3D printed enclosure hold the filters and sensor assembly securely. *Figure 4-13* shows the layout of the three filters, labelled *S1-S3*. The red line shows the polarisation axis of each filter. Ideally, the measurements should be made at a single position along the tube axis. However, this is not possible with the physical constraints of the sensor size, resulting in a detection distribution of 21mm and 7mm radius from the tube axis. A 12V LED array of 16 surface mount led (**4**) is used as the light source providing a wide beam angle, flood type illumination.

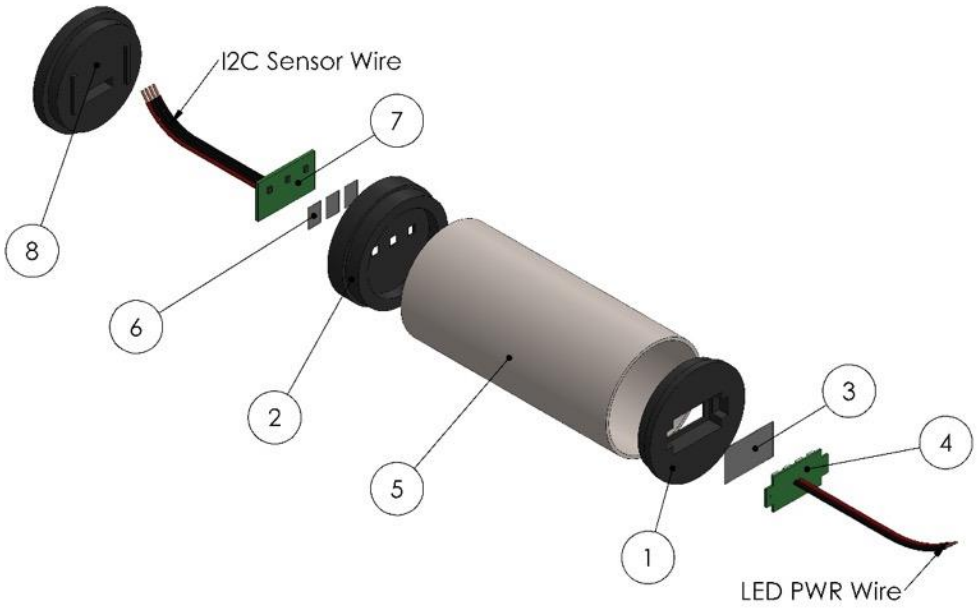

Figure 4-12 Short Range Test Rig Assembly

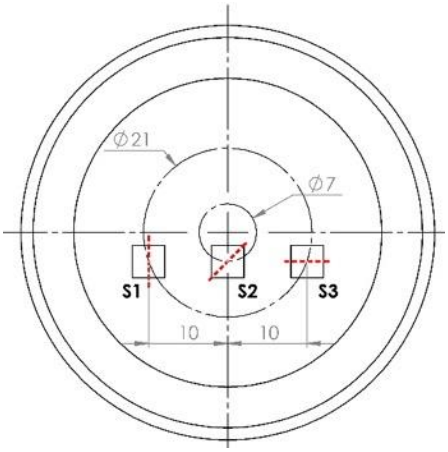

Figure 4-13 Test 1 - Sensor Layout

The light luminosity measured on each sensor was logged over *0°-180°* at an increment of *10°*, and the result is plotted in *Figure 4-14.* Cubic spline interpolation is used to reconstruct the data points between the measured data at 1° increment. From this figure, it can be seen that a good trace of the sinusoidal characteristic described in *Eq.[4-9]*, *Eq.[4-10]* and *Eq.[4-11]* is clearly visible in the three sensor signals, despite the reflective surface of the test tube. Some deviation in the amplitude is seen between the three signals, in particular between Sensor 1 and Sensor 2. This was determined to be caused by inconsistency between the three sensors resulted from general manufacturing specification. It was also noted that there was a slight offset in Sensor 2 signal phase, indicating that the filter was not oriented correctly at *45°*. Causes of both problems are resolved with software calibration and sensor matching.

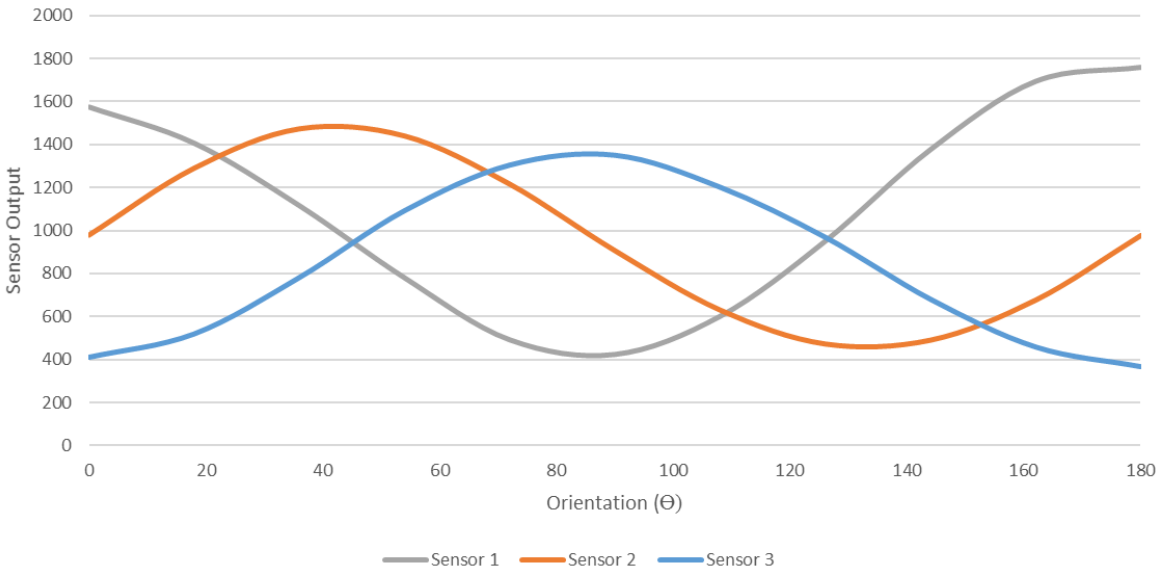

Figure 4-14 OPT Short Range Test - Trial 1 (100mm)

On that regards, multiple experiment trail was performed with minor alterations as listed below:

- The light sensor was replaced with three brand new sensors with the similar characteristic selected from 10 TSL2561 devices batch.
- Sensor calibration scheme was introduced in software to match the sensor performance using simple offset and gain factors.
- A new set of linear polarizer segments was collected from the polarizer film from the similar central region.
- More consideration was made in orient the filters at 0°, 45° and 90°.

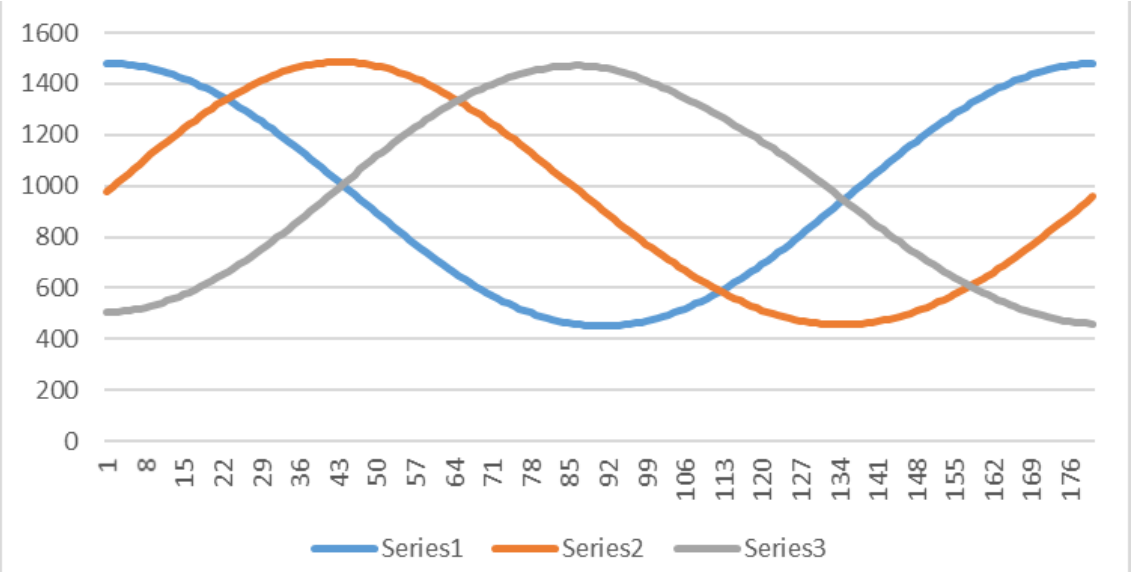

Figure 4-15 OPT Short Range Test with calibration - Trial 2 (100mm)

Figure 4-15 shows the result from the final attempt. It is clear that the signals after the minor correction have significantly improved, indicating that the performance of the OPT system can substantially differ with and without appropriate sensor hardware and software calibration. There is minimal variation in sensor signals over the full range of rotation despite the displacement between the three sensors, indicating that there is an equal distribution of light at the sensor end of the sample. Shown in Table 4-3 Figure 4-14 are the results of the logic and numeric analysis of the OPT algorithm.

Table 4-3 Test1 – Comparison Analysis Result

Detected region	Theoretical	Observed	Error
B	*22.5°*	*21.7°*	*-0.8°*
D	*45°*	*42.8°*	*-2.2°*
F	*67.5°*	*63.8°*	*-3.7°*
H	*90°*	*86.7°*	*-3.3°*
J	*112.5°*	*111.4°*	*-1.1°*
L	*135°*	*133.9°*	*-1.1°*
N	*157.5°*	*156.9°*	*-0.6°*
P	*180°*	*179.7°*	*-0.3°*

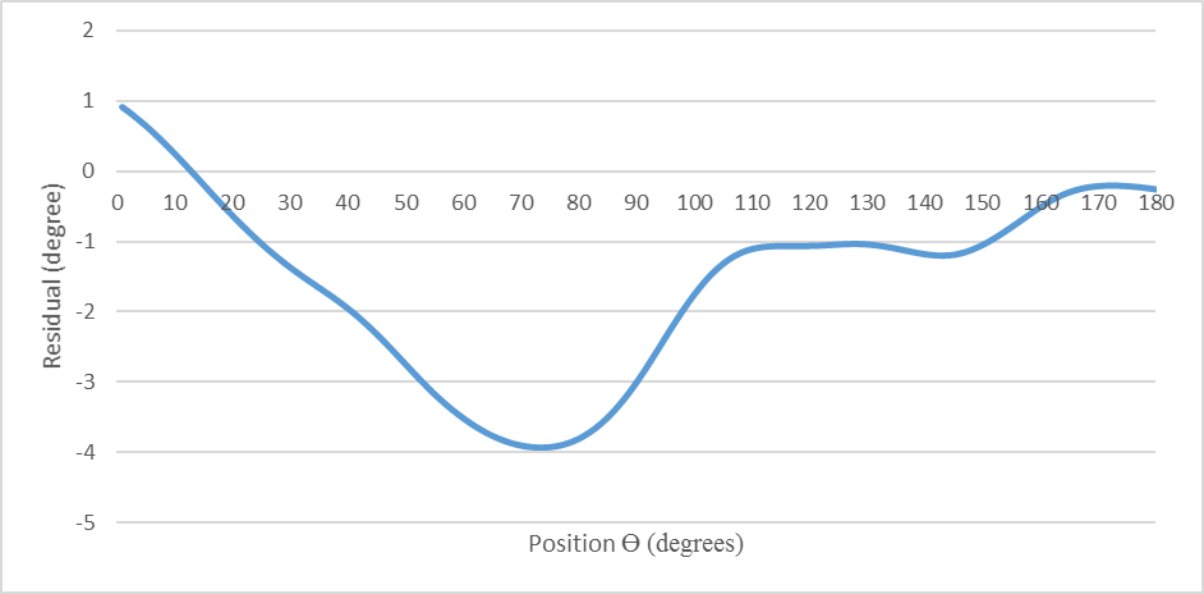

Figure 4.14 Test 1 Numerical Analysis Result

The accuracy can be determined to be approximately ±2°, which is very appropriate specification for FTIS application. However, it should be noted that a general bell curve characteristic is visible in the residual plot in Figure 4-14, which may most likely indicate a misalignment in one of the filter polarity orientation. Because there is no apparent noise in the signals, the actual accuracy of the system is significantly better if curve can be linearized. Conclusively, more attention in the mechanical and electronic setup is required to better evaluate the potential of the OST system in short range application. But regardless, the

current setup has shown excellent orientation detection capability sufficient for reformer tube inspection and hence proved that the principle of OPT is accurate.

4.3.3 Experiment 2

In the similar fashion as in experiment 1, a second test was conducted on the second sample tube. This specimen is an 8.0m long aluminium tube extrusion with 70mm internal diameter and 1mm wall thickness. To match the large internal diameter of the sample the test rig was redesign with improvements based on the knowledge obtained in the first experiment. The OPT system is presented in Figure 4-16 and Figure 4-17.

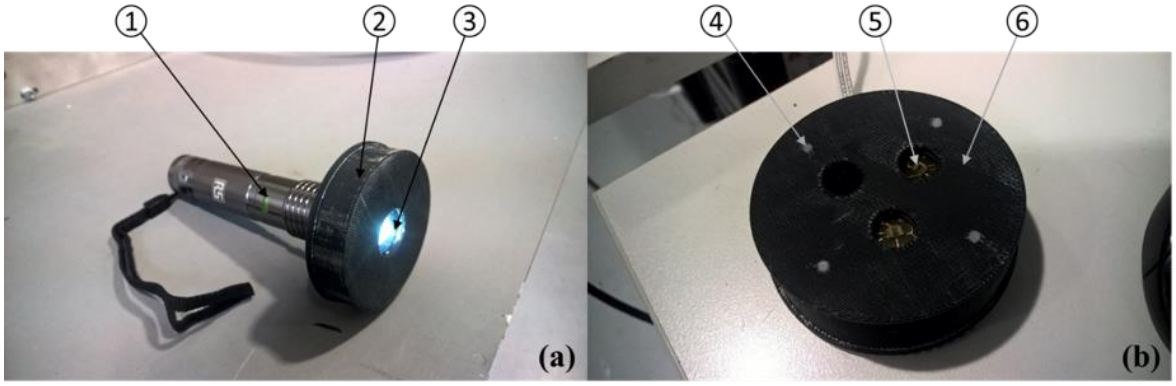

Figure 4-16 Experiment 2 test rig (a)LED Light Source (b) TSL2560 Sensor Assembly

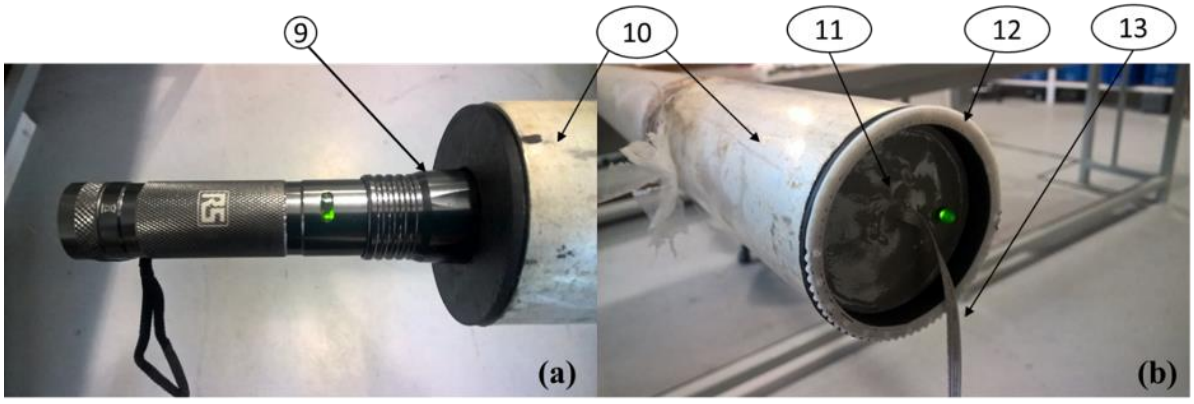

Figure 4-17 Experiment 2 Setup (a) Light Source (b) Potted Senor Unit

Shown in Figure 4-16 is the two OPT units used in the experiment (light source (**a**) and the OPT sensor (**b**)). The two end caps (**2** and **6**) is 3D printed out of black ABS plastic with an interference fit with the sample tube internal wall, giving a secure fit with no ambient light leaking into the sample tube. A 3 watt single LED torch (**1**) is used as the light source, replacing the LED array in experiment 1, featuring a convex glass lens with adjusted beam angle using the rotating head bezel (**9**). A narrow beam angle was used for experiment with approximately 1m spread at 8m distance. The polarising film used in experiment 1 was

replaced with Edmund Optics High Contrast Plastic Linear Polarizers[2] for better filter matching consistency. These filters also have two locating notches on the filters rims indicating the direction of the polarising axis, hence make it easier to orient the filter on the sensor unit. 1.0inch and 0.5inch diameter filters are used for the source light (**3**) and the sensor filters (**5**) respectively. The sensor filters are arranged into a circular layout as shown in Figure 4-18 with an equal distribution of 6mm from the tube axis. The same TAOS TSL2561 light sensors are used, but the PCB breakout board was redesigned to match the new lens layout. The board is mounted on the plastic enclosure (**6**) secured with four nylon screws (**4**) and also potted with an electronic potting compound to avoid any light illuminating through the board (**11**). Using the I^2C interfacing cable (**13**), the TSL2561 sensors are programmed to 402ms integration time and gain of 16, allowing for a steady sampling frequency of 2Hz.

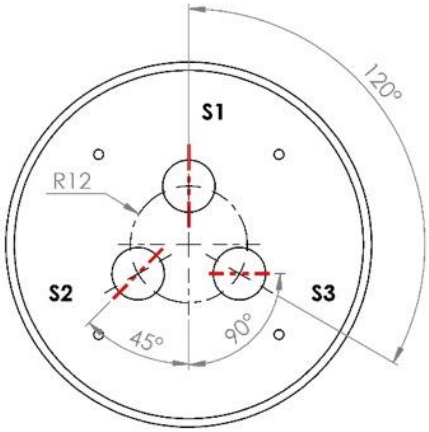

Figure 4-18 Test 2 - Filter Layout

Numerous trials were taken to calibrate the sensors with the appropriate offset and gain values. Three matching sensors were chosen out from 13 brand new sensors batch. To aid the positioning of sensor filter during the experiment, a plastic guide ring (**12**) with notches spaced 5° apart on the out rim was used. In the final trial, a total of 12 measurements were collected. During the series of measurements at each location, the three light measurements were logged, and the results are presented in Figure 4-19.

[2] www.edmundoptics.com

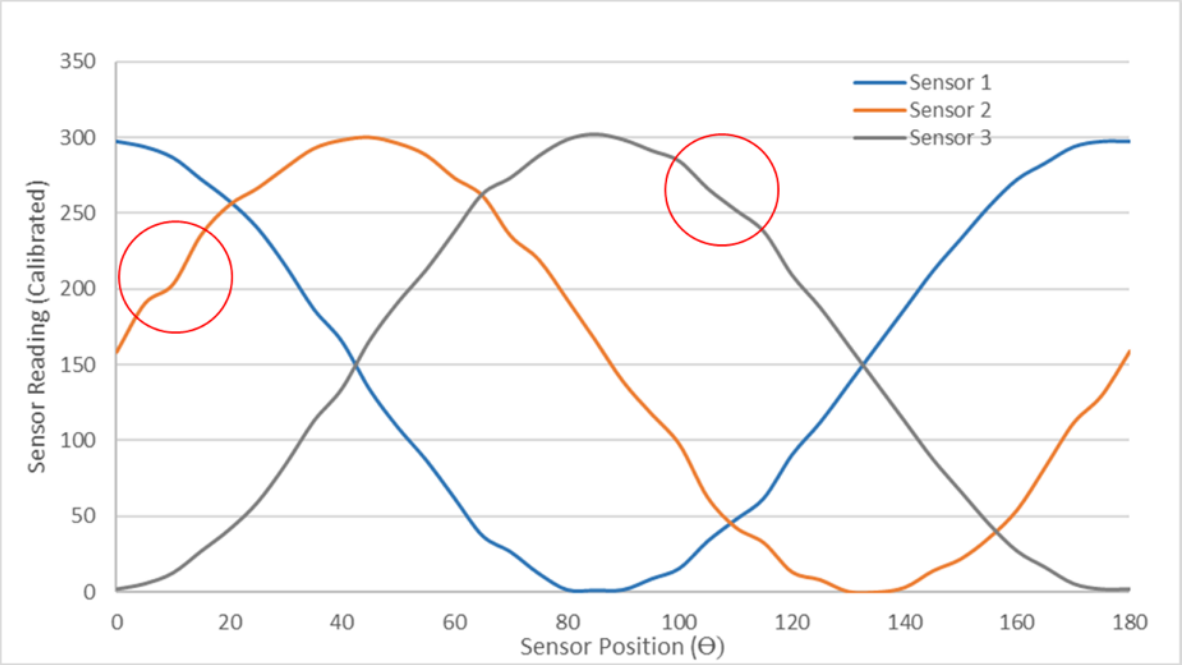

Figure 4-19 Long Range Test - Trial 2 (8m tube)

It is noted that the sensor output is much smaller compared with the results seen in Experiment 1. This is expected as with longer tube sample more of the source light is absorbed by the tube surface resulting in greater signal attenuation. As assumed previously, the magnitude of the attenuation is dependent on the displacement between the light source and the OPT sensor.

All the theoretical analysis in Section 4.2.2 is based on the assumption that the light intensity S1, S2, and S3 is measured from a single point on the tube axis and that the light is distribution evenly at any given cross-sectional plane along the tube. In fact, due to physical constraint with the components size and deviation in the LPF and the light sensor characteristics, error in the signal is inevitable. This is seen as a ripple in the profile of each sensor signal in Figure 4-21. One of the primary element that affects the light distribution is the direction of the light beam emitted from the light source. Figure 4-21 shows the sensor characteristic when the LED torch was significantly tilted away from the tube axis with the majority of the light seen by the sensor is reflected off the wall. It is evident that most of the polarity is kept but excessive skewing in the signal of sensor 1 and 2 is seen, indicating uneven light distribution. The second factor affecting the performance of the OST is the choice of light source. When the torch focus was set to approximately 0° beam angle, the pattern of the LED die is visible in the illumination pattern, as shown in Figure 4-20, creating uneven light distribution. This is determined to be one of the causes of signal dipping indicated with a red circle in Figure 4-19 as the sensor passes over a LED pattern. However,

when the beam angle was increased too much, the signal the signal attenuated dramatically resulting in higher signal to noise ratio.

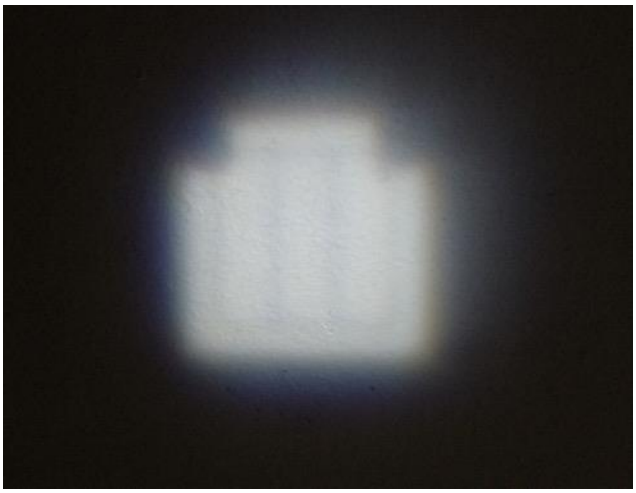

Figure 4-20 LED Light Source Distribution (in focus)

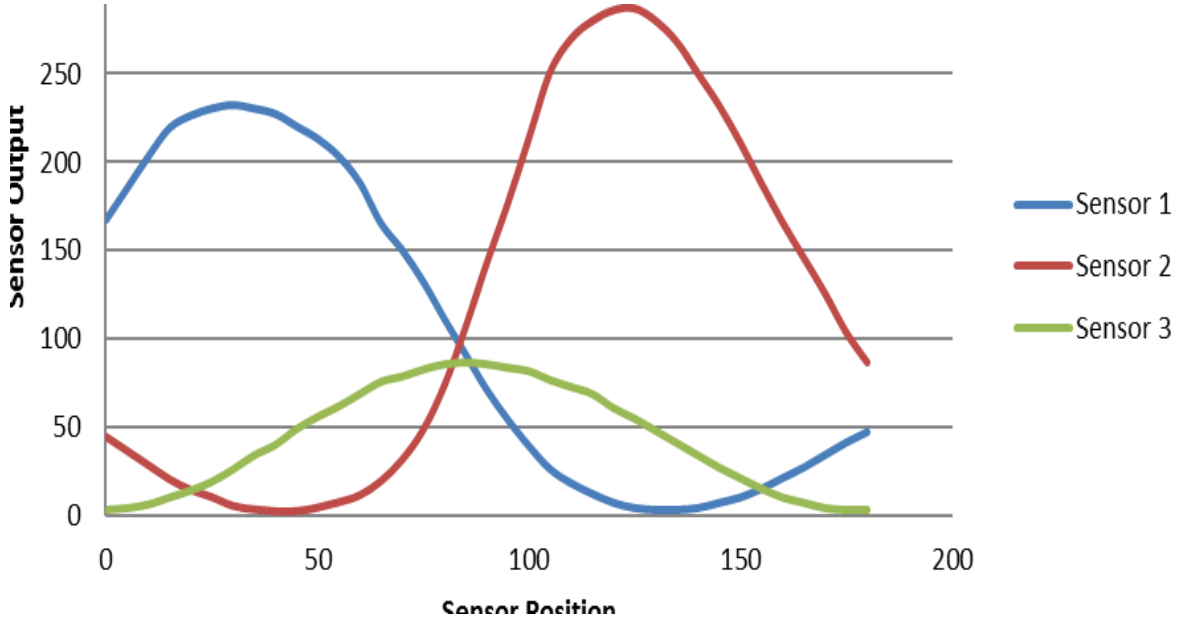

Figure 4-21 OST response to misaligned source light angle

The next step is to evaluate the data by deriving the position Θ using the OST algorithm and comparing the output with the actual position.

Both first and second stage analysis shows consistency between the results. Even spread of the data indicates that the three filters are oriented well with one another, justifying the benefit of the using the new polarizer. The variation of ±1.8° indicates an increase in signal-to-noise ratio compared to experiment 1. This is expected as calculations are based on measurement of smaller scale. An overall offset of 2.5° in the residual plot is an indication that the guide rim used to adjust the filter orientation during the trials is not in line with the

actual orientation of the filters, therefore is not a limitation in the OST concept. To conclude, the results shows an over success in validating the potential of the proposed approach. Important aspects of lighting source and angle have been identified, and overall improvements are seen in the OST design, justifying the benefit of the minor alterations made from the first experiment.

Table 4-4 Experiment 2 OPT Algorithm output – Boundary result

Boundary	Theoretical	Observed	Error
B	22.5	21.7	-0.8
D	45	42.8	-2.2
F	67.5	63.8	-3.7
H	90	86.7	-3.3
J	112.5	111.4	-1.1
L	135	133.9	-1.1
N	157.5	156.9	-0.6
P	180	179.7	-0.3

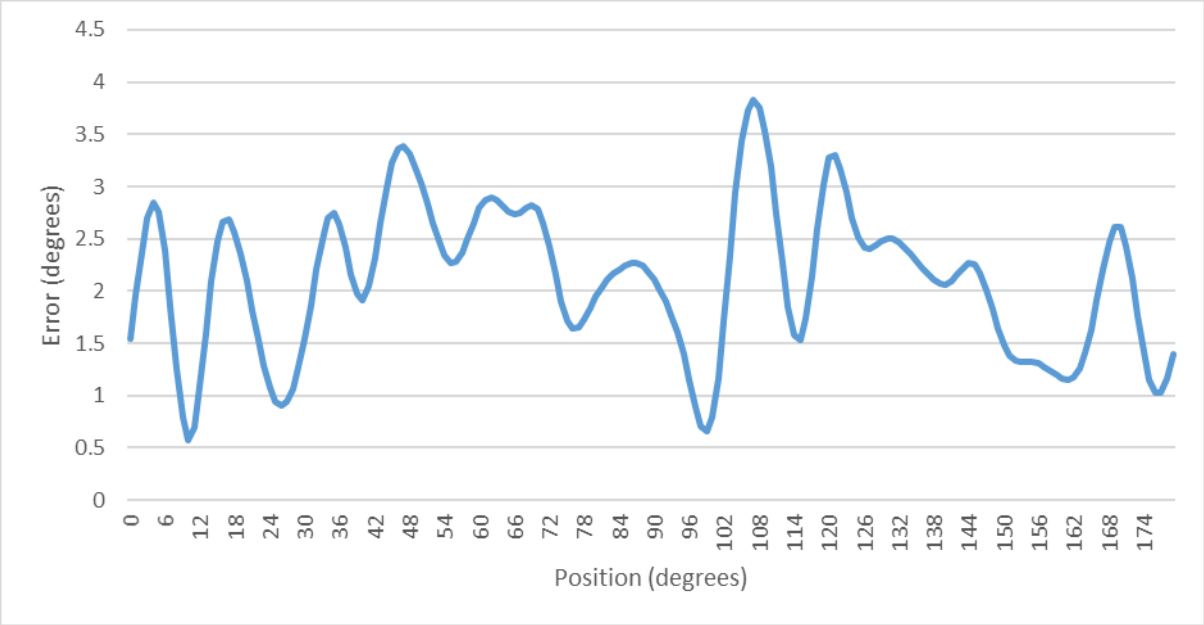

Figure 4-22 Experiment 2 - Residual

4.3.4 Summary

Presented in this section are a theoretical analysis and practical experimentation showing the ability of the proposed OPT sensor performance in short and long distance application. However, the test has only shown the capability within a tube with an internal diameter of 50mm and 71mm at two distances of 0.1m and 8m. For future work, it must be tested under industrial environment inside various size reformer tube. Also, tubes with different level of service exposure should be tested as to evaluate the effect of different internal surface condition. It is assumed that larger diameter will result in better light distribution. In conducting the experiments it was noted that the most difficult task was setting up the lighting. Significant skewing in the measurement is observed when the light beam is off axis of the tube. Hence, different type of light source and light diffusing method should be investigated for improving repeatability. A foreseen problem maybe ununiform reflected light distribution caused from tube bowing that could result in lighting issues similar to Figure 4-21. However, there are minimal to no literature on significance and magnitude of tube bowing under standard operating condition and may be an area for future research.

For implementation with embedded processor with limited processing capacity (e.g. microcontroller), the numerical algorithm can be simplified using a lookup table or an iterative method. Considering the error size of ±1.8° seen in Figure5.21, the predefined look table with 1~2° step size is feasible considering the benefit of reduced processor load and time. A feasible example, the comparison analysis result can be used to pick out one of many lookup tables stored in a separate EEPROM memory, eliminating the need for floating number processing.

One can also investigate in implementing an electrically controllable liquid crystal polarizing filters such as one described in [116] to implement a single sensor solution to the OST system. The light can be observed through a single polariser filter located along the axis of the tube, and the polarity axis can be electrically switched between 0°, 45°, and 90°, eliminating error from ununiformed light distribution.

4.4 Chapter Summary

This chapter introduced a novel optical position tracking system using principles of classic linear polarizer characteristics. Development of the multiple signal analysis technique and two stage analysis algorithms was presented, and the three key equations were formulated. The implementation and performance validation of the approach was demonstrated with short- and long-range experiments. Minor modification and revisions in the lighting and sensing unit were included to account for design and hardware constraints. The key attributes, benefits and drawbacks of using the OPT methodology for reformer tube inspection application are:

- The proposed OPT method provides a robust solution for associating orientation data with the profilometry measurement. The approach has been developed specifically for the unique application of Reformer Tube inspection where the light is contained within a vertical tubular body where conventional position sensing methods such as GPS, Compass, and accelerometer is no usable.
- An OPT algorithm was developed for processing the three light intensity data. The fractional comparison approach eliminates the need for modelling light scattering and attenuation for the individual tube, theoretically making the approach universal for all straight tubular application.
- A Comparison Analysis was used to estimate the position Θ quickly. The algorithm is capable of quickly determining the position over 0°-360° range into 32 unique regions, improving the performance of the numerical analysis strategy that follows.
- The OPT approach has not been fully analysed. Two cases of short and long range experimentation are presented using 50mm and 70mm tubes. To thoroughly examine the methodology, a larger range of trials would be required with various tube sizes and surface conditions to provide a probabilistic performance assessment. For a final application, tests will need to be performed on full-length reformer tubes with different service exposure with varying surface conditions.
- There is area for further development in the OPT design. In this research, two functional OPT prototypes were developed and tested, pointing out a number of design improvements that was made along the way, such as filter selection and electronic potting. However, there is a wide range of sensors, filters, and lighting technology available on the market that would potentially be better suited for the application. The TSL2561 Luminosity sensor had excellent sensitivity performance

with integrated features suited for prototyping. However, inconsistency in the optical characteristic was evident between different sensors making system calibration relatively difficult. While calibration consideration was made with a simple offset-gain approach in software, a better result can be expected with better sensor choice. Additionally, an investigation into the light defusing technique is hugely anticipated by the author. Improvement in a more uniform light distribution inside the tube will improve the reliability and repeatability of the approach.

5 Mechanical Design: RTIS Prototype

5.1 Introduction

This research aims to extend on the currently available NDT inspection technology by testing new set of technology and formulating a conceptual platform for a Reformer Tube Inspection System (RTIS). It is expected that in a similar manner as in the examples in the literature review, the proposed RTIS will result in improve the overall efficiency of Reformer Tube inspection and help optimise the efficiency of methanol, ammonia and other reforming plants. In this section of the research, the main considerations for adapting the OPT and CDA algorithm is given, focusing on the system specification, sensing, communication and modularity.

The primary challenge of integrating new technology into NDT inspection system is in deriving a system framework that is compatible for implementation with practical application. Often application of new technology is limited by practical constrains, where it might be physical accessibility or space limitation, for systematic complication. Although theoretical optimality is desirable, industrial practicality and realistic assumptions is highly considered in this work.

The following chapter is layed out as follows. First the RTIS scheme is introduced. This includes the general components of the system and it implementation in industrial environment. Specifically, practicality design considerations made for practical optimisation is presented. Second, the Reformer Tube Inspection Probe (FTIP) is introduced. The integration of the four novel technology and there overall connections are described. Third the key elements of the FTIP is presented in detail. Specifically, the design of the novel Displacement Sensor is presented. Finally, the RTIS and its key aspects are summarized.

5.2 Proposed System Design

Proposed in this study is a Reformer Tube Inspection System (RTIS), a non-destructive inspection concept which utilizes mechanical sensors to perform creep analysis based on profilometry inspection, based on radial measures opposed to the diametrical measurement used in conventional systems. Using advanced control scheme and higher level of software processing, the inspection process is automated and data interpretation performance are improved. It also uses a novel optical technology to improve the system's ability in locating localised deformation. RTIS system is composed of three components; inspection probe,

probe launcher, and the base station. Figure 5-1 shows a graphical representation of the RTIS system in operation.

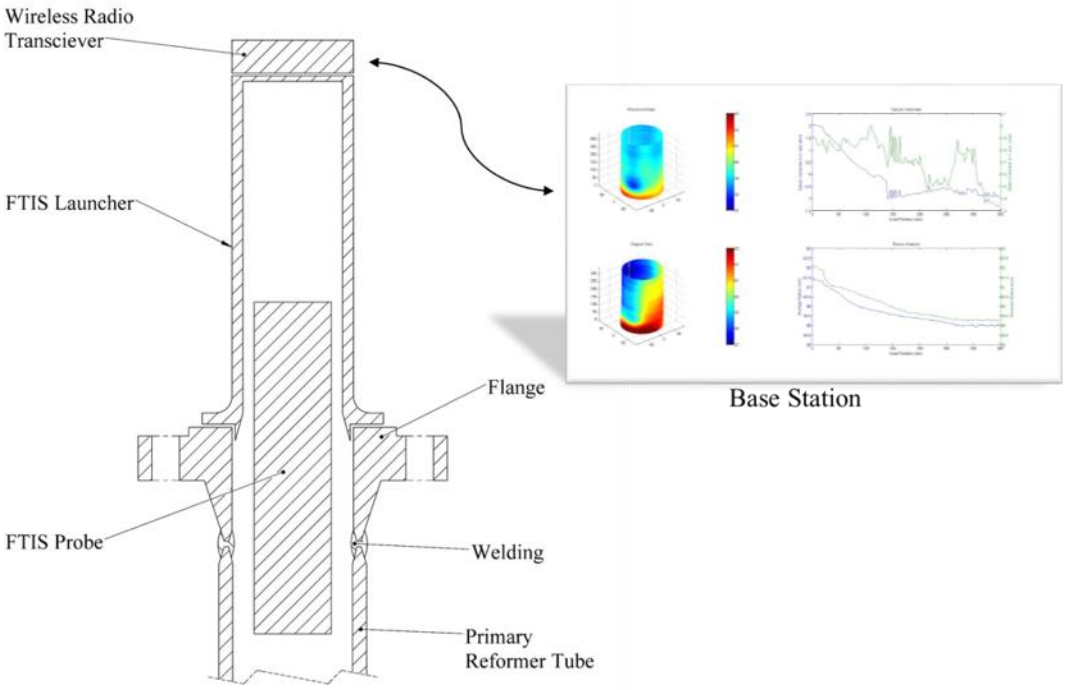

Figure 5-1: Graphic of RTIS system operation

Using modern magnetic position sensing technology, internal radial measurements are collected by the measurement Probe. These measurements are transmitted to the Base Station located outside the tube using wireless radio communication. Using unique data reconstruction and regression algorithm the data is processed in software for datum misalignment, localised radius increase, and general tube increase. Using an electric motor and a spooling mechanism the movement of the Inspection Probe is controlled in software using a 1.5mm stainless steel rope while rotary encoders and optical sensors feedback the actual location. An ultrasonic proximity sensor is mounted on the bottom of the probe for detecting the bottom on the tube.

5.2.1 Inspection process

FTIS Reformer Tube inspection is conducted in line with reformer plant downtime of the reformer plant maintenance typically scheduled at 2 year interval for catalyst replacement [15]. This is the ideal timing as all the tube tops are opened and catalyst are removed. Shown in Figure 5-2 is the four procedures in performing an inspection with the proposed FTIS system.

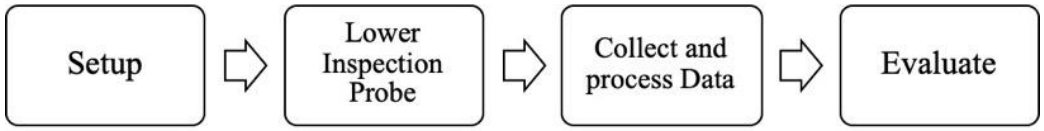

Figure 5-2 FTIS Inspection Procedure

First, the FTIS Launcher containing the FTIS Probe is place over the reformer tube flanged opening and aligned with the tube. As the angular position of the inspection data is detected in relative to the polarised light source it is best to orient the Probe Launcher in the same direction for all tubes for consistency. Then, through the graphical user interface on the Base Station the automated inspection cycle is activated.

In the first step of the automated cycle, the Inspection Probe is automatically lowered into the reformer tube by gravity. The probe is lower at a speed of 0.5m/s until the bottom of the tube, approximately taking 30 seconds to reach the bottom a 15m reformer tube. Up on entering the range of the Ultrasonic bottom detection sensor, at approximately 1m from the bottom, the speed is deaccelerated to a slow coasting speed until the bottom is reached.

Next the Inspection Probe is pulled up the tube collecting profilometry measurements. This is sent in real-time to the Base Station through the wireless radio communication and processed simultaneously. In this step the probe is pulled at maximum speed of 0.250m/s, equating to approximately 1 minute to reach the top for a 15-meter tube. Although mechanical stabilisers are used to steady the Inspection Probe, the speed should not be too excessive during this stage to avoid vibration and resonance noise, that may result from uneven tube internal wall surface, induced into the measurement.

Finally, the tube data can be evaluated on the Base Station. As discussed later in the thesis, the data is represented in a 2D and 3D graphical plot shown extent and location of the maximum radius measurement and the general tube increase in millimetre or percentage. Overall inspection time for a single tube is less than 3 minutes.

5.2.2 Drive

One of the biggest challenges in long distance in-pipe inspection is in developing an efficient and reliable propulsion mechanism. For decades, researchers all over the world have continued to develop new and innovative method of navigating autonomous inspections robots through the variety of world piping network that exists today. Shown in *Figure 5-3* are eight types of smart locomotion methods that are available today.

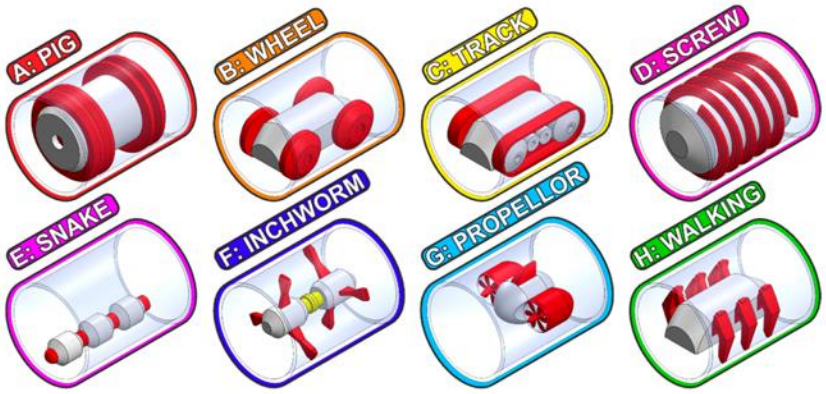

Figure 5-3 Classification of in-pipe robots [117]

Majority of world pipelines are relatively easy to inspect using advanced Pipeline Inspection Gauges (PIG); a passive device that is inserted into the pipe and driven using the means of transportation fluid [87]. PIG is one of the oldest technology around and heavily used in industry for its fast and efficient performance. It is estimated that approximately 99.5% of pipe networks are accessible to conventional 'PIGGING' technology [117]. However, due to the aspect of uncontrollability and necessity for transportation medium, applications with dry pipes with complex pipe infrastructure are generally considered 'unpiggable', like in the case of Reformer Tubes. Naturally, this has instigated the introduction and continued to motivate research and development of self-driven autonomous robots for an in-pipe application.

Wheel and track robot are the two predominate locomotion methods currently used in-pipe inspection robots. With the benefits of speed, control, and adaptability, the two systems are commonly used in combination with other locomotive types. Sole use is prevalent in the sewer industry in flat or low incline environment for vision-based systems [89, 118]. Tracked robot (also known as caterpillar) has a high contact surface area and often chosen over the wheeled system where traction is required. A screw robot uses a helical propulsion motion of rotating drive train. It is generally used in combination with wheels and perform well in the vertical orientation and is resistant to slip due to the angle approach. The HELI-PIPE inspection robot *Figure 5-4 (c)* developed by M. Horodinca [91, 119] demonstrate this using tilted elastic wheel arranges on a rotator head coupled to a motor through a universal joint. Inchworm robot uses a sequence of contraction and expansion segments to create a continuous wave peristaltic motion to create forward motion. This biologically inspired method generally has high wall-friction forces for high payload application. One of the most current work is done by A. Kandari [120], developing a worm-like robot constructed out a modular mesh design, Compliant Modular Mesh Worm robot (CMMR) *Figure 5-4 (b)*. Snake robots comprise of multiple segments with a high number of degrees-of-freedom motion,

benefitting of modular design and adaptable to many in-pipe environments. In work by E. Dertien [121-123], an omnidirectional wheel is used in combination with a V-shape snake robot arrangement as shown in *Figure 5-4 (a)*. Walker robot, or rather a crawler, use legs with multiple DOF to move. Also not as common as other systems, Walkers has advantages of added control and payload as demonstrated by MORITZ robot developed by A. Zagler [124].

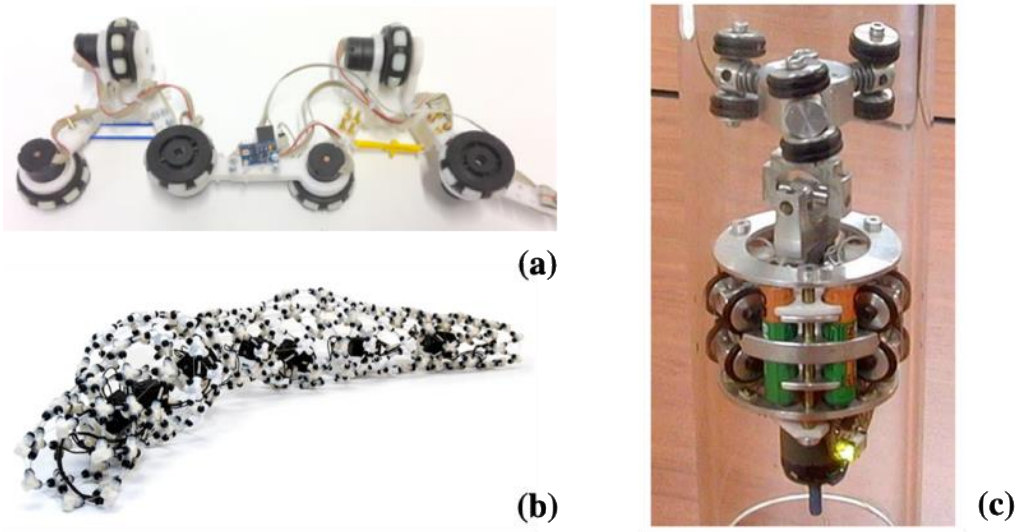

Figure 5-4: a) V-Shapes Snake using Omnidirectional Wheel b) CMMW Inchworm Robot c) Screw Robot

Reviewing the various locomotion method two problems were identified that limits their use for this research. The first problem is the complexity that is associated with essentially all the self-driven systems reviewed. As evident from the image above, the solution for locomotion has seemingly become more sophisticated as if to follow the trend the advancement of electronic technology in the world. Added complexity and moving components are generally compromised with reduced reliability and serviceability, which is not beneficial for a reformer tube inspection tool. The second limitation is the speed at which the systems are designed to operate at a vertical orientation. Studying the literature and watching example videos, it is clear that the presented mechanism struggle at high incline environment. The HELI-PIPE system is capable of *10cm/s* at *3N* of axial payload which is not suitable for a time-depend process. The CMMW inch-worm robot moves slower still at *25.8cm/min*, with no payload, on a horizontal surface.

Based on these remarks, it is decided that the gravity depend cable and spool mechanism used in the preliminary design presented in *Section 2.5* will be used for the proposed FTIS architecture. The module concept in having the drive and the sensing mechanism separate

allows for more design flexibility. The spooling system, and the associated control, battery, and stability mechanism will be located outside the tube with the radio receiver. This will allow for smaller battery capacity, compact form factor, and an overall simplistic and reliable probe design.

5.2.3 Sensor

Vision system is the most prevalent system that is dominating the NDT in-pipe inspection in the oil and gas industry. Using image segmentation and pattern recognition techniques vision system is able to detect cracks, surface corrosion, and other anomalies[125-129], as well as conducting pipe deformation assessments [10, 18, 73, 130]. With the advancement of CPU and GPU processors, a new area of research has opened up for machine learning for improving image classification of surface detect as in the work by [95]. Although with the described benefits of a vision based system, the decision was made early on in the research to implement an electromechanical sensing technology for the propose FTIS design for the reasons as discussed further.

Proposed in chapter 3 of this thesis is a new numeric algorithm for evaluating profilometry data for creep degradation. In deriving this, it was found that accurate measurement of 12 radius measurement is enough to detect two modes of isotropic and anisotropic creep deformation accurately. The accuracy of a vision system in respect for profilometry measurement is relatively low. The work by P. Buschinelli [99] shows that laser triangulation is limited to ±0.2mm radius measurement accuracy for a 100mm nominal diameter pipe in a lab environment, where a standard measurement tools used in machining workshops(such as dial indicators, bore gage, digital callipers, and micrometres) are capable of generally hundreds to a thousand of a millimetre accuracy. Because direct measurement approach does not rely on background and object illumination or dynamic optical focusing, much less power consumption is required to electromechanical systems. For example, 500 series Mitutoyo[3] digital callipers with LCD display has a battery of 18,000 hours from one SR44 coin-cell battery.

In summary, the specification for the sensing system of the FTIS is as follows. The proposed design must perform at least 12 radius measurement simultaneously at low power consumption as possible. To justify the benefit of high accuracy measurement over the high-

[3] www.mitutoyo.co.jp

density output from the vision system, the electromechanical probe must have minimum accuracy ±0.05mm, which is twice the accuracy claimed by existing methods.

5.2.4 Form Factor

Form factor in respect to hardware design is the term used to defines the physical specification of a component. Although there is no standard to following in designing a Reformer Tube inspection systems, various hardware specification has been derived based on good engineering practice, health and safety, and largely on common sense.

Limitation in the physical size of the system is restricted by two aspects. For the FTIS inspection probe, the cross-sectional profile must be less than the size of the reformer tube. As stated in the introduction of the dissertation, reformer tube with internal diameter between *90-150mm* internal diameter is considered in the research, and therefore the diameter of the inspection probe must be less the 90mm with adequate clearance. There is no direct limitation to the length of the probe, but should not be too long that will disrupt the handling of the device. Considering the features of the system the system should not be longer than 1m.

To reduce cost in operating the system the FTIS system must be operable by one operator. This is feasible for the autonomous design as proven in the preliminary prototype. In term of health and safety, the system must not be too heavy to lift and compact enough for portability. Under section four of 'Metal Industry Guidelines for Safe Work' provided by Accident Compensation Corporation (ACC)[4], 20kg is considered as the limit for safe lifting by a single person. Team lifting or other lifting aid is recommended for lifting and moving anything beyond this weight. To this, the FTIS system should be well below 20kg; this includes the weight of the FTIS probe, FTIS carrier, PC base station, and along with other accessories (enclosure, replacement battery etc.)

The last specification is the usable material in the design. Considering the weight restriction of the system, lightweight material such as plastic, carbon fibre, and aluminium is favourable and appropriate to be used for any internal and external component of the design. However, to mitigate the risk of metal embrittlement caused by having material left in the tube with a low melting point, any component in contact or potentially make contact with the reformer tube will be made of stainless steel.

[4] www.acc.co.nz

5.2.5 Wireless Communication

Wireless communication is a technology where data is transmitted over a distance without the need for physical communication cables or wires or other electronic conductors. This eliminates the use of heavy-duty data cables such as the umbilical cable used in the LOTIS system, as a result benefiting in mobility and convenience. With reduced payload, the mechanical spooling system can be designed smaller and measurement probes can be made modular. Reduce cable diameter will also benefit with increased field of view between wireless receiver and the inspection probe, preferred for implementing the OPT system proposed in *Chapter 4*. Other related benefit of the wireless communication in this work is listed in Table 5-1.

Table 5-1 Benefit of wireless communication for FTIS

Benefit	*Description*
Expandability	Wireless system are not wire or cable routing is necessary while easily accommodated multiple devices.
Low Cost	Wireless hardware is very cheap compared to what it was a decade ago to a point where it is negligible for critical devices. Price of the *XBee PRO S2* wireless module used in this research is $39USD. Also financial saving from eliminating the data cable of the length of the reformer tube is significant.
Ease of use	Additional device can be added or remove to wireless network easily for future development. XBee modules are able to accommodate 500 nodes (devices) in a network through software setup.

Despite the abundance of applications and associated benefits, wireless radio communication is not without their drawbacks. One of the weakest aspects of wireless communication in comparison to a wired communication alternative is in the network stability. Under ideal application wireless network can be reliable, such as in the home wifi network, however the stability of radio signal is depended on the physical environment of the magnetic wave propagation path and the distance between the transmitter and receiver, the network can easily be disrupted by external attributes. In the use of radio signal inside a reformer tube, the most essential aspect is attenuation of the signal due to the tube cut off frequency and destructive interference caused by multiple radio wave propagation.

Unique to this work, the reformer tube essentially acts as a circular waveguide structure for guiding the electromagnetic wave between the inspection probe and radio receiver. Appropriate selection of the radio wave frequency will allow for improved wave signal propagation than in open air, with reduced signal attenuation. Equation below is the equation for the circular structure cut off frequency.

$$f_c = \frac{1.8412 \times c}{2 \times \pi \times r} \qquad [5\text{-}1]$$

Where f_c is the circular waveguide cut off frequency in hertz, and c the speed of light constant, and r the internal radius of the tube in metres. The reformer tube of interest in this research has an internal diameter of *90mm* to *150mm*, equating to a r value of *0.045m* and *0.075m* respectively. Using the approximated speed of light value of $3.00x10^8$ the cut-off frequency f_c for the two extremes of the tube sizes are *1.953GHz* for the *90mm* tube and *1.172GHz* for the *150mm* tube. To this, the two common communication frequencies of 2.4GHz and 5GHz protocols are feasible for this application.

Multiple path propagation is a phenomenon that can result in the radio signal reaching the receiver antenna through multiple paths, resulting in destruction and phasing shifting of the transmitted signal. Analysing the propagation inside a cylindrical structure is relatively simple but when ignored can cause complete loss of radio signal. Let us consider the scenario presented in *Figure 5-5*.

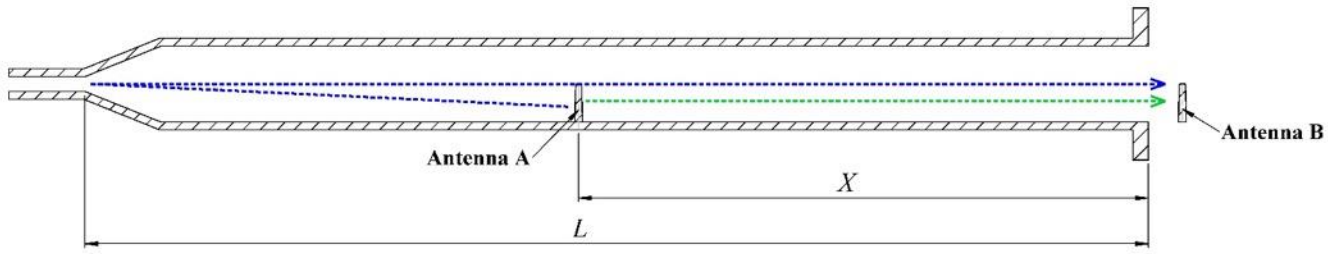

Figure 5-5 Radio wave propagation inside reformer tube

The diagram above show two monopole antennae where the transmitter antenna A is located inside a reformer tube and a receiver antenna B placed outside the tube flange opening. Shown in the red line is the approximate radiation pattern of the antenna in open space. Because reformer tubes are constructed out of conduct HK40 heat-resistant stainless steel alloy the radio signal is confined inside the tube, leaving two propagation paths between the two antennas. One is the signal propagated directly towards the receiver antenna taking the shortest path of distance x and the second is the signal propagated towards the reflector and

reflected to the receiver. The difference in the distance Δd between the two propagation paths are directly proportional to the position of the transmitter antenna A, equated by the formula:

$$\Delta d = 2(L - x) \quad [5\text{-}2]$$

Where L is the length of the reformer tube. Closer the transmitter A is to the reflective face or the bottom of the tube, less the deviation between the two signal propagation paths. When the transmitter is almost at the top of the tube, the largest Δd will be. However, because the strength of the green signal is much stronger than the blue signal reflected from the bottom of the tube the effect of the multipath interference is significantly reduced. As a solution for multipath interference, FTIS uses a metallic reflector plate to direct the radio wave up the tube to the receiver, minimizing the amount of backscatter down the tube. Effectively the radio module is transmitted through a waveguide with varying length.

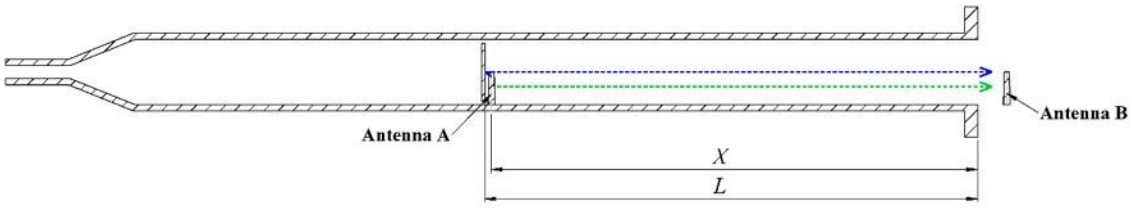

Figure 5-6 Radio wave propagation inside a reformer tube with reflector plate

5.2.6 Summary

In this section the key parameters and specifications has been defined. Presented in Table 5-2 is a summary of the key considerations in developing the FTIS prototype.

Table 5-2 FTIS Design Specification

Form Factor	Maximum cross-sectional profile diameter of 80mm and 800mm in length. Must not weigh more than 20Kg
Material	Components in contact with the tube wall must be Stainless-steel
Communication	Real-time Wireless Communication between the control station and the FTIS probe
Power	Internal DC battery with minimum battery life of 300minutes
Sensor	Point measurement sensor capable of simulation sample at least 12 measurement samples per layer at 20Hz sample rate.
Drive	Gravity fed cable driven mechanism by an electric motor
Layout	A modular design will be used considering the benefit of serviceability and customization.

5.3 Implementation

One of the challenges in developing a Reformer Tube inspection system is the integration of technology in a confined environment Reformer plant and tubes. The design must be compact enough to physically fit inside the reformer tube and have a robust construction for industry environment. Additional, to sufficiently make advantage of the radius based creep damage analyses algorithm, the system must also have the measurement precision and accuracy as defined in section 5.2. Hence in developing the mechatronic design of the FTIS prototype, consideration in many engineering disciplines is necessary.

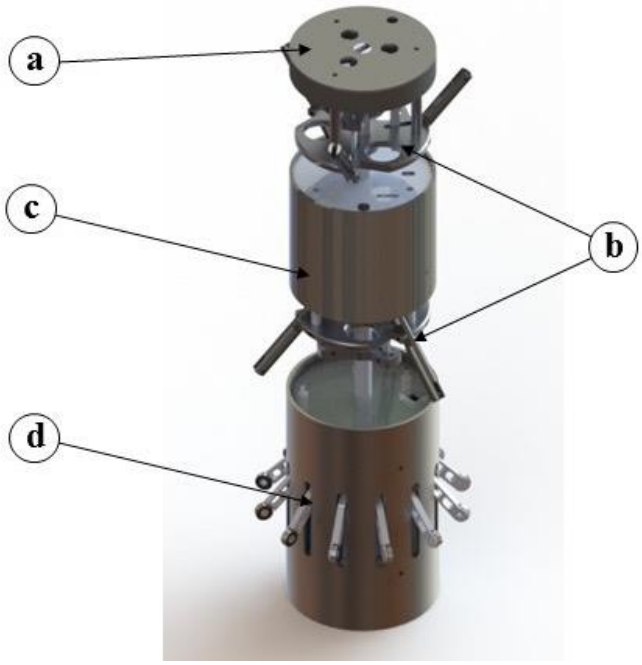

Figure 5-7 Inspection Probe 3D CAD Model

Shown if *Figure 5-7* is a 3D CAD image of the final RTIS probe, depicting the overall system assembly. The working prototype feature every element required to perform creep inspection. The completely standalone design is powered by two lithium ion battery, allowing for simultaneous acquisition of 12 radius measurement continuously for 4 hours. It has two TPS clamping mechanism and a tube bottom detection sensor (not visible in the image). It also features a OPT sensor (discussed in Chapter 4) for tracking the angular orientation of the probe while inside the tube. The system is completely assessable through the 2.4GHz wireless connection. It features a micro USB connection for charging and complete diagnostic of the internal processor. All of this is tightly contained with a cylindrical design envelope of 375mm height by 85mm diameter. To quickly and effectively iterating through

development process, SOLIDWORKS CAD software[5] and Altium Designer[6] has extensively been used to evaluate mechanical and electronic design in a 3D environment. Additive and laser manufacturing technology have been utilized to quickly produce physical prototypes throughout this phase of the research.

Majoriy of the device is enclosed inside a stainless-steel cover, with minimal aluminum and plastic components are visible in places that cannot make contact the reformer tube wall. The system design is divided into four modules with their own specific function; OPT Sensor (**a**), TPS stabilizer (**b**), Radio Module (**c**), and the Sensor Module (**d**). Added modularity is beneficial in the scheme of repair and maintenance: replacing modules can be more effective than system repair at component level. Each module is mounted to a single 12mm stainless steel rod extending through the length of the device, giving a robust and rig structure to the design. The overall weight of the FTIS Probe is 2.3 kilograms.

In the remainder of the section, the main consideration for the individual module is presented, discussing the development and manufacturing considerations, along with theoretical and experimental evaluation. Shown in *Figure 5-8* is a photo of a fully functional FTIS probe fabricated as proof of concept.

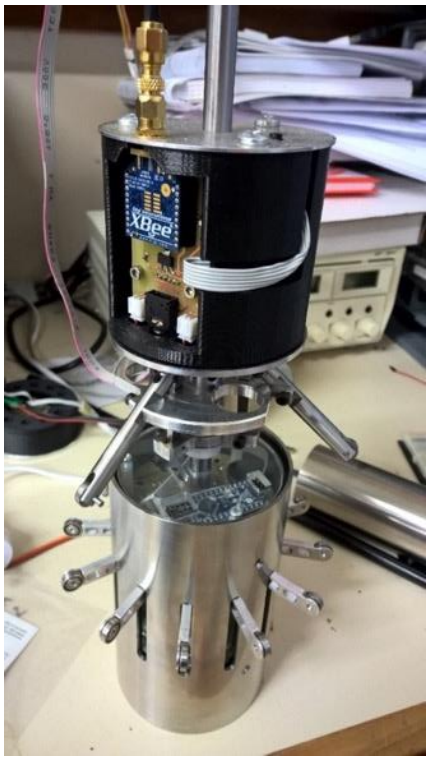

Figure 5-8 FTIS Prototype System

[5] www.solidworks.com
[6] www.altium.com

5.3.1 Displacement Sensor

The performance of the FTIS is determined by the accuracy of the sensors and the method in which the displacement measurements are collected. To make a cohesive estimation of the reformer tube sectional internal profile, the performance of the displacement sensors and its characteristics must be evaluated. In this section, the working principle, performance, and the application of the novel displacement sensor developed for this research is presented, along with numerous design consideration, and the mechanical characteristics that influence the overall behavior of the system.

5.3.1.1 Displacement Sensors

In any design and development process it is good practice to review existing technology so not to *'reinvent the wheel'*. Hence, the first task in designing the displacement sensor for the FTIS is to conduct a market research on potential products that is suited for the task.

As mentioned earlier, the best example of precision electromechanic measurement tool is seen in the manufacturing industry. As long as machining workshop has been around, solution for precise measurement of components has continually explored by many global businesses specialized in this trade, such as Mitutoyo and Starrett. State of the art in electrostatic and electromagnetic induction technology is found in calliper, micrometres and many other handle held devices with ±0.5-10μm accuracy. Such devices generally has long battery life of 18,000hrs with 1~4Hz sample rate through the dedicated SPC protocol.

Another type of displacement sensor that is readily available is the noncontact proximity sensors. The research investigated two common type products based on Sound Navigation and Ranging (Sonar[7]) and time of flight (TOF) laser measurement technology. Figure 5-9 shows two commonly available proximity sensors commonly used in robotics and automation. The HRLV MaxSonar (**a**) module is a low power 5V Sonar sensor heavy used in research and hobbyist. While the performance and durability standard of the sensor is much to what is used in the industrial environment, this is one of the smallest Sonar module available on the market. The acoustic beacon measures measure 16.4mm in diameter, fitting onto a 19.9mmx22.1mm PCB board. The module is fully integrated with serial and analog interfacing capability for measuring object distance of 0.3-5.0m range at a sample rate of 10Hz while consuming on average 3.1mA for continual operation.[8] The limitation of this

[7] Sound Navigation And Range (SONAR)
[8] See HRLV-MaxSonar Series Datasheet by Maxbotic

sensor is that Sonar sensors, in general, has a wide beam angle, low measurement resolution, and large minimum range deadband [9] which is common to all SONAR sensors.

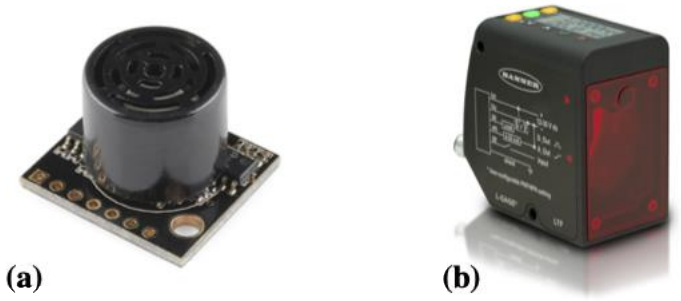

Figure 5-9 Non-contact Proximity Sensor a) HRLV-MaxSonar b) L-GAGE LTF Laser Sensor

The second sensor (**b**) is an L-GAGE Time of Flight (TOF) Laser sensor produced by Banner Engineering[10]. This sensor has a slightly larger form factor of 38mmx68.7mmx66mm but however has better measurement precision of ±0.3mm[11]. the output sample rate is 1Hz and a minimum range dead band of 50mm. With relatively high power consumption of 2.1W the sensor finds its niche in the field of process automation.

From this, one of the initial idea was conceptualised. Based around the HELI-PIPE robot worked by M. Horodinca [119], a TOF laser proximity sensor is mounted to the end of a rotating head facing outwards away from the axis of rotation. Based on the screw locomotion mechanism, the sensor will collect profilometry measurement in a helical pattern the drive wheels pulls the instrument through the tube. By varying the leading angle of the wheels and the speed of the drive head, the speed and pitch of the helical path can be dynamically controlled. A rotary encoder is used to collect the relative position of the rotating head can be determined with each radius measurement. After brainstorming the concept accordingly with back-of-the-envelope calculations, decision was made no to implement the approach for this research, main reasoning being that the concept consists of moving components which generally will result in reduced reliability and increased complex in the electronics wiring. Additional, the self-driving mechanism of the rotating head will result in increased power consumption which is not preferable for a module battery powered system.

After further conceptualising and research, it was determined that there is no sensor currently available for short range displacement measurement, due to limitation of close proximity

[9] Deadband is a region on input that produces no change in the output
[10] www.bannerengineering.com
[11] See L-Gage LTF Time of Flight Laser Distance Sensor Instruction Manual by Banner Engineering

dead band, with low power consumption and small cross-sectional foot print. Therefore, it was decided that for this research a new displacement sensor design will be developed.

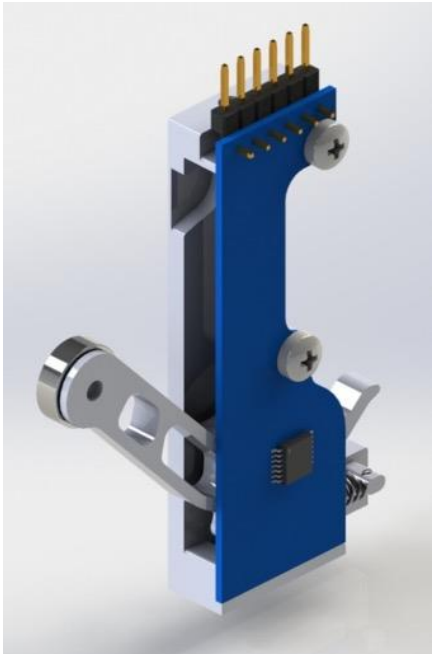

Figure 5-10 Displacement Sensor CAD image in SolidWorks

Shown in *Figure 5-10* is the custom built electromechanic displacement sensor, inspired by studying the mechanical principle of a Dial test Indicator. Based on an electromagnetic inducer, the design has a measuring range of 0-28mm with no deadband, with varying accuracy between ±1µm to 15µm accuracy. The compact design sizes approximately 29mm x 8.5mm x 44.5mm in width, depth and height respectively(Figure 5-14), allowing for 12 sensors to be oriented radially within the 82mm diameter body of the sensor module. Further with lower power consumption of 0.075W, the sensor is capable of sample rate up to 12.4kHz.

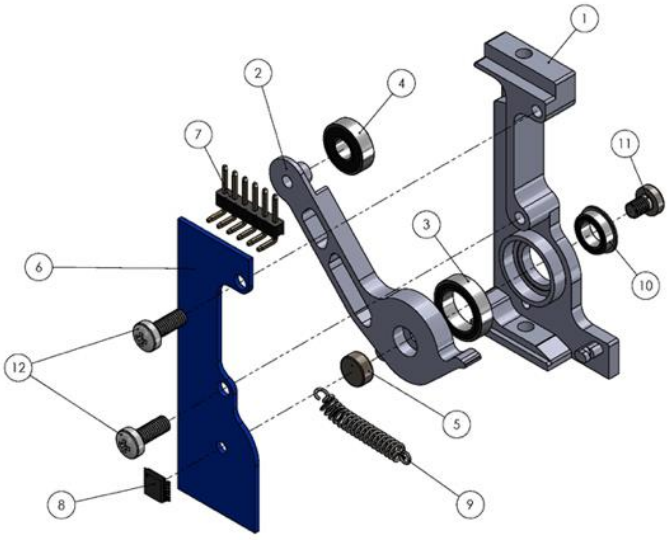

Figure 5-11 Displacement Sensor Assembly Diagram

Depicted in *Figure 5-11* is the assembly diagram of the displacement sensor, consisting of the 12 components. Aluminium housing (**1**) is the main body of the sensor holding the Encoder Arm (**2**) and the PCB board (**6**) in place. Two machine bearings (**3,10**) support encoder arm against the body for a smooth and consistent movement while retaining robustness in the design. The M3 retaining screw (**11**) holds the moving component together against the flanged bearing (**10**). 6mm x 2.5mm axial pan magnet (**5**) is lightly pressed into the recess of the Encoder Arm and fixed with 243 Loctite. 10x4mm sealed bearing (**4**) is mounted on the end of the encoder arm for a smooth running along the wall surface. Custom designed electronic PCB board is located against the bottom lip of the aluminium body and mounted in place with two M3 nylon screws (**12**).

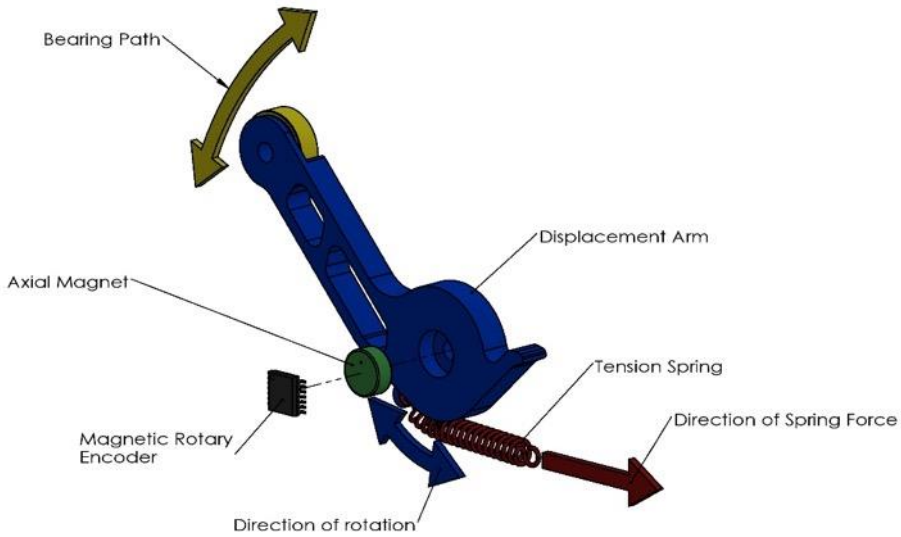

Figure 5-12 Displacement Sensor Schematic Diagram

The working principle of the displacement sensor is as follows. Shown in *Figure 5-12* is a schematic diagram depicting only the moving components. Encoder arm freely rotate about the rotation axis marked with a black dashed line. The range of motion is mechanically limited between *12.88°* to *85.00°*. On the same axis is a encoder magnet recessed into the body of the arm and an absolute magnetic encoder. The tension spring is used to apply a force in the direction of the red arrow, exerting a rotational torque that pulls the outer bearing outwards towards the internal wall of the reformer tube. The response time of the sensor is dependent on the angular acceleration of the encoder arm, which varies depending on the extension of the spring. When the tube wall is in contact with the encoder bearing, the

displacement measurement between the rotation axis to the point in contact can be determined from the angular position of the arm. The absolute rotary encoder eliminates the need for origin point setting at every power-on, allowing immediate starting of measurement while ensuring high reliability without causing an overspeed error.

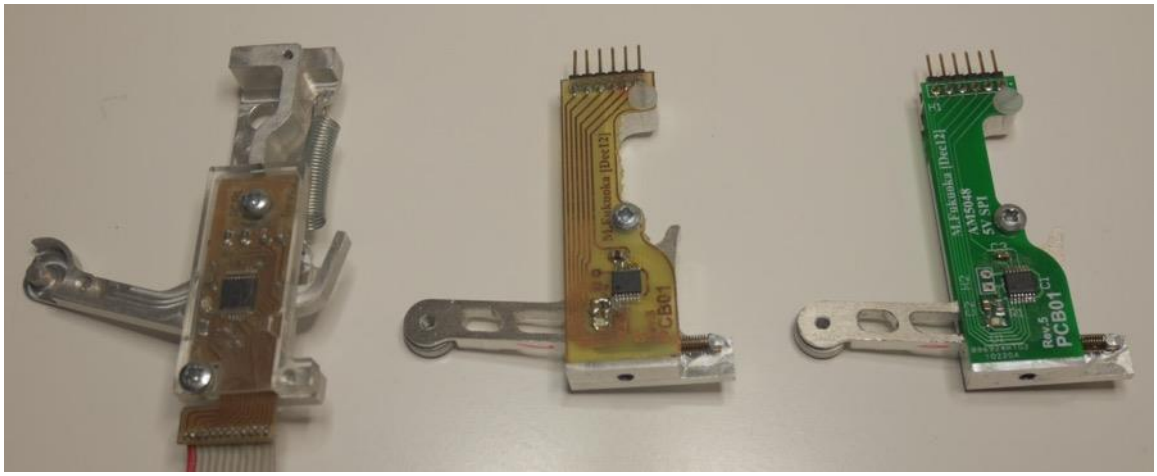

Figure 5-13 Displacement Sensor design iteration

Figure 5-13 shows the three key designs prototyped during the design iteration. On the left is the earlier prototype that features the key elements of the final design. In this iteration, a flat surface on the aluminum housing was first introduced to mechanically limiting the motion of the encoder arm at known position which served to be very useful for initial system calibration. A 12-bit AS5045 magnetic encoder[12] was used, identical to the rotary encoder used in the preliminary system presented in the Literature Review, with acrylic cover to protect the electronics.

In the later design, the encoder was replaced with the 14-bit AS5048 encoder to improve the measurement resolution. Additionally, the aluminum housing was redesigned with simplicity for easy of manufacturing and reduced in size for a smaller cross-sectional footprint. The original spring was replaced with a smaller stainless-steel spring, and the design of the encoder arm was optimized for accuracy and measurement range. With each iteration, effort was made toward a smaller and simpler design. In the final design, the PCB was redesigned for 5V operation, and professionally fabricate at Seeed Studio[13].

5.3.1.2 Design Analysis

In this section, the design of the displacement sensor is analysed, focusing on the resolution, precision, response time and the mechanical loading of the encoder arm. As appropriate

[12] ams.com
[13] www.seeedstudio.com

dimension tolerances and machining procedures have been applied throughout the construction phase, errors from manufacturing, bearing friction and mechanical backlashes are ignored throughout this study.

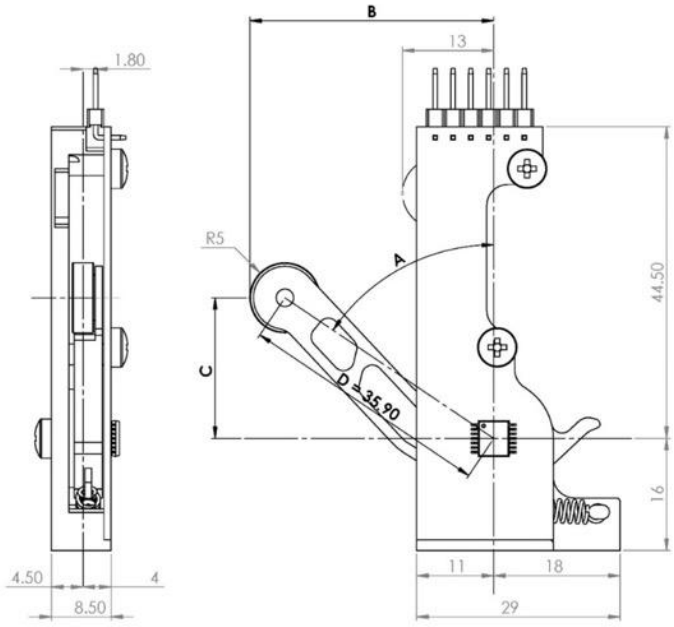

Figure 5-14 2D CAD diagram of the Displacement Sensor

Depicted in *Figure 5-14* is a mechanical drawing of the displacement sensor seen from the front and the side face. The displacement measurement of interest is the distance between the vertical axis of rotation and the point on the encoder bearing making contacting with the tube wall (*B*). This measurement can be related to the angular position of the Encoder Arm as:

$$B = D \,.\sin A + R \qquad [5\text{-}3]$$

Where *D* is the centre -to-centre displacement between encoder bearing and the axial magnet, *A* is the angular displacement been the encoder arm and the vertical axis of magnetic encoder, and *R* the radius of the encoder bearing.

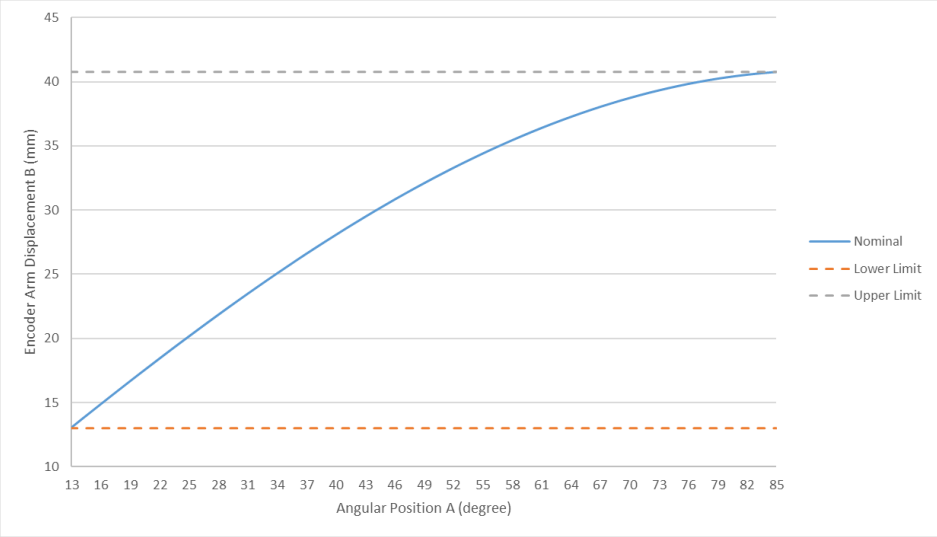

Figure 5-15 Encoder Arm Displacement profile

The range of the Encoder Arm angular motion *A* is mechanically limited between 12.88° and 85.00°. Shown in *Figure 5-15* is the profile of the linear displacement *B* relative to the angular position *A* define by *Eq.[5-3]*. The maximum and the minimum measurement is shown by the two green lines at 13.00mm and 40.76mm. By combining two Displacement Sensor oriented symmetrically along the tube centre, the sensor is capable of measure 81.52mm of reformer tube displacement which is by order of magnitudes greater than the radius deviation resulted from a typical 5% increase of a 100mm reformer tube. An obvious sinusoidal characteristic is seen with varying gradient throughout the entire measurement range, indicating that the rate of change between the distances D for each 14-bit encoder increment is distributed non-linearly. This also indicate that the precision and accuracy of the sensor output is dependent on the angle range.

5.3.1.2.1 Sensor Resolution and Precision

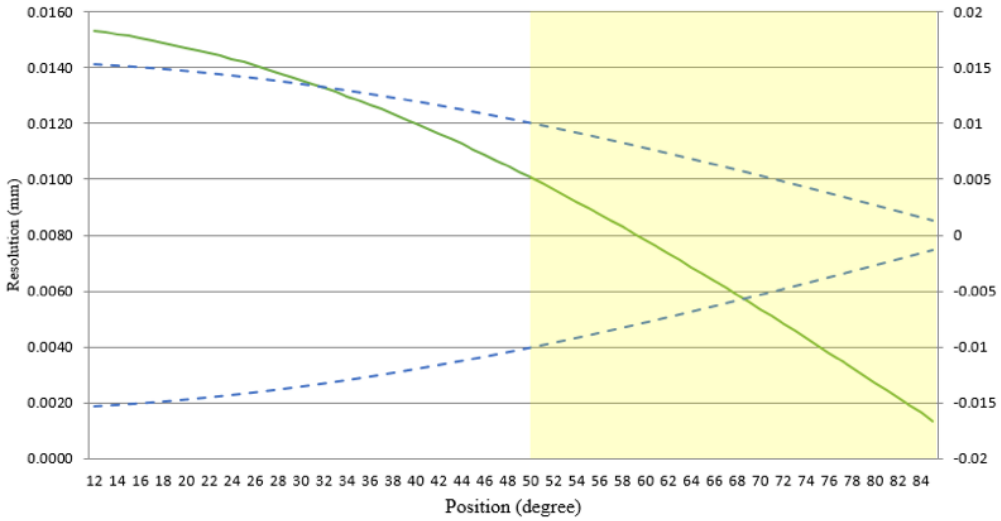

Figure 5-16 Displacement Sensor Precision and Resolution Profile

Figure 5-16 profiles the distribution of the resolution and the precision of sensor output over the full range of the encode arm motion. Plotted in green is the output resolution on the left axis. This data is calculated by the change in the measurement per single increment of the encoder output at a given angle. Finer resolution can be achieved when the Encoder Arm is reaching further away from itself. Best resolution of 0.001mm is seen at full extension and worst case of 0.015mm at home position. On the secondary right axis is the two dashed blue lines shows the precision of the output. This data is based on the 0.05° accuracy of the AS5048 encoder stated in the manufactures datasheet[14]. It is also clear that there is less spread in the output data at greater displacement measurement. The lowest precision of ±0.015mm is seen at Encoder Arm position at 12° and best precision of ±0.001mm at 85°. Highlighted in yellow is the preferred region for reformer tube creep damage inspection of <0.01mm resolution and <0.01mm precision.

5.3.1.2.2 Mechanical loading behaviour

In this section the mechanical loading of the displacement sensor is discussed, evaluating the forces acting on the Encoder arm and how it effects the performance of the sensor for reformer tube inspection. Figure 5-17 is a free-body diagram showing the main forces acting on the encoder arm during inspection.

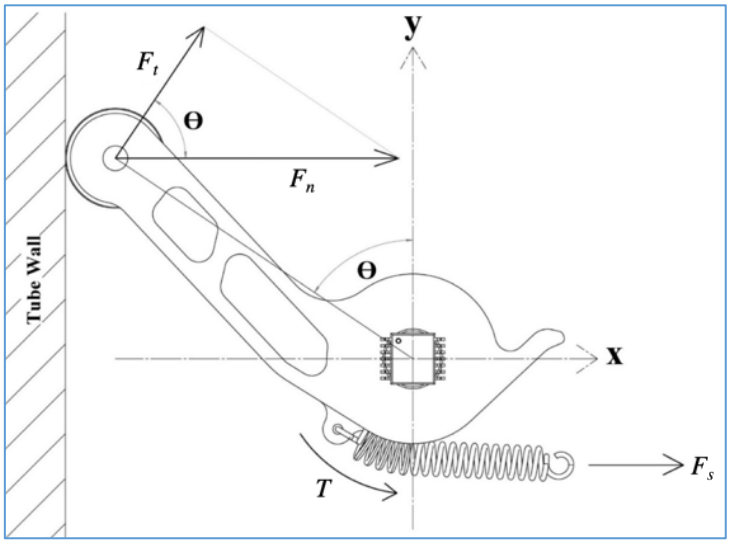

Figure 5-17: Encoder Arm Force Free body diagram

Fs represents the spring force acting on the Encoder Arm along the x axis. Arrow *T* is the resultant torque about the rotational axis. The magnitude of *T* is determined by:

[14] Available from www.ams.com

$$\tau = r \times F_s \quad [5\text{-}4]$$

where r is the radial distance of the spring mounting point and the rotational axis. F_s is determined by the extension of the spring from its nominal length multiplied by the spring constant. The tension spring selected in the design is 2.50mm stainless steel passivated extension spring with a nominal free length of 12.5mm. the spring constant is 0.107N/mm. F_n is the reactant force exerted into the encoder bearing by the internal wall of the reformer tube. Assuming a ideal bearing with no rolling resistance, the direction of F_n will always be in the direction normal to the tube wall. The magnitude of F_n is dependent on the length and position of the Encoder Arm, and the tangential force F_n acting against the force torque T. Value of these three parameters has been selected to achieve a wide region of constant force F_n over the full motion of the Encoder Arm. This has been determined to be of great importance to the system stability as demonstrated.

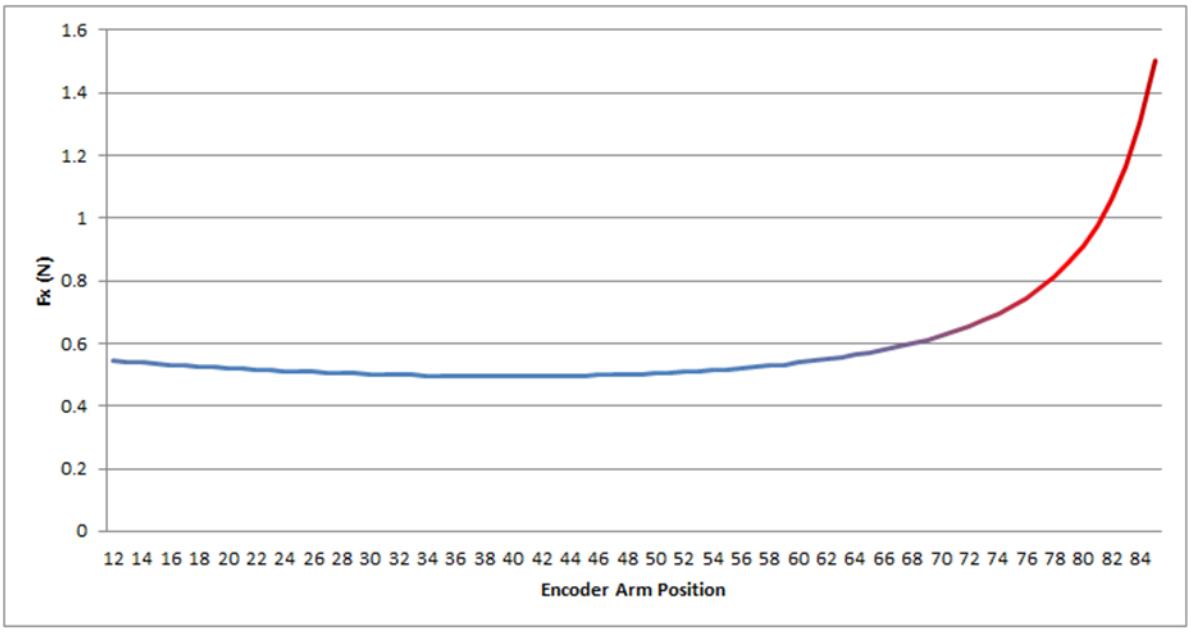

Figure 5-18: Profile of Force acting on the Tube Wall (F_n)

Plotted in Figure 5-18 is the profile of the force F_n over the full range of motion of the encoder arm. The graph shows two region of the output force with almost uniform force of 0.50~0.54N between 12 and 70 and a region with an exponential increase past 70.

In the application where multiple sensors are used back to back for radial measurement, like in the case of the proposed RTIS, it is favourable of the system to operate in the first blue region of the *Fx* force profile. When one or more sensors operates in the exponential region of the Fx profile, the small difference between the encoder arms will exert large difference in

the radial force cause the system to pull onto the tube wall and potentially overcome the strength of the stabiliser system of the RTIS, cause the system to jam inside the tube. Let us consider the four scenarios illustrated in Figure 5-19.

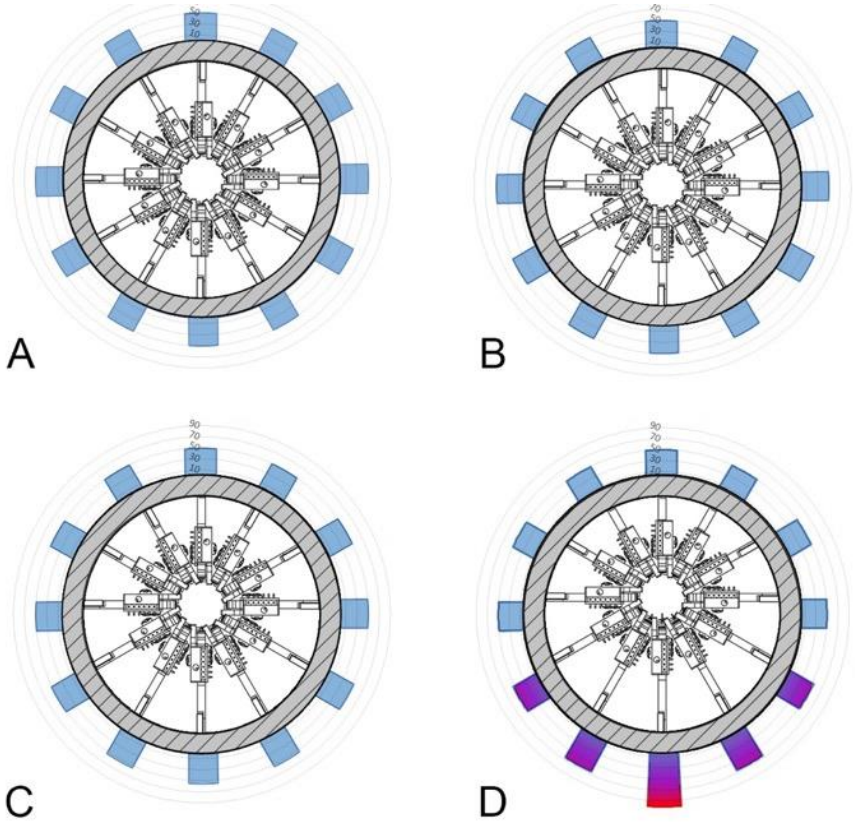

Figure 5-19: Radial loading diagram A) 0mm offset B) 1mm offset C) 5mm offset D) 8.5mm offset

Above are four polar graph diagram show the behaviour of a system with 12 Displacement Sensor inspecting a health tube with an internal diameter of 120mm in different scenarios. The resulting forces and the Encoder Arm positions are presented in Table 5-3. In scenario A, the system is location in the centre of the tube distributing equal amount of outwards force on the tube wall of 0.5017N. In scenario the system is located 1mm offset towards the top of the diagram. In this case some but minimal deviation of 0.79N between the top and bottom sensors loading. For a tube with significant localise creep damage, an offset of 1mm is expected.

Table 5-3 FTIS Radial Loading under four Scenarios

	A		B		C		D	
SENSOR NO.	**θ**	**$F_{x\,(N)}$**	**θ**	**$F_{x\,(N)}$**	**θ**	**$F_{x\,(N)}$**	**θ**	**$F_{x\,(N)}$**
S1	50.17	0.5017	51.24	0.4985	63.02	0.4951	81.37	0.5002
S2	50.17	0.5017	50.88	0.4988	60.05	0.4949	72.08	0.4983
S3	50.17	0.5017	49.94	0.5013	54.68	0.4955	58.81	0.495
S4	50.17	0.5017	48.71	0.5016	48.13	0.5007	47.1	0.4993
S5	50.17	0.5017	48.53	0.5038	42.58	0.5155	38.22	0.5315
S6	50.17	0.5017	46.69	0.5056	38.99	0.5377	32.78	0.6566
S7	50.17	0.5017	46.39	0.5064	37.78	0.5555	31.01	1.0047
S8	50.17	0.5017	46.69	0.5056	38.99	0.5377	32.78	0.6566
S9	50.17	0.5017	48.53	0.5038	42.58	0.5155	38.22	0.5315
S10	50.17	0.5017	48.71	0.5016	48.13	0.5007	47.1	0.4993
S11	50.17	0.5017	49.94	0.5013	54.68	0.4955	58.81	0.495
S12	50.17	0.5017	50.88	0.4988	60.05	0.4949	72.08	0.4983

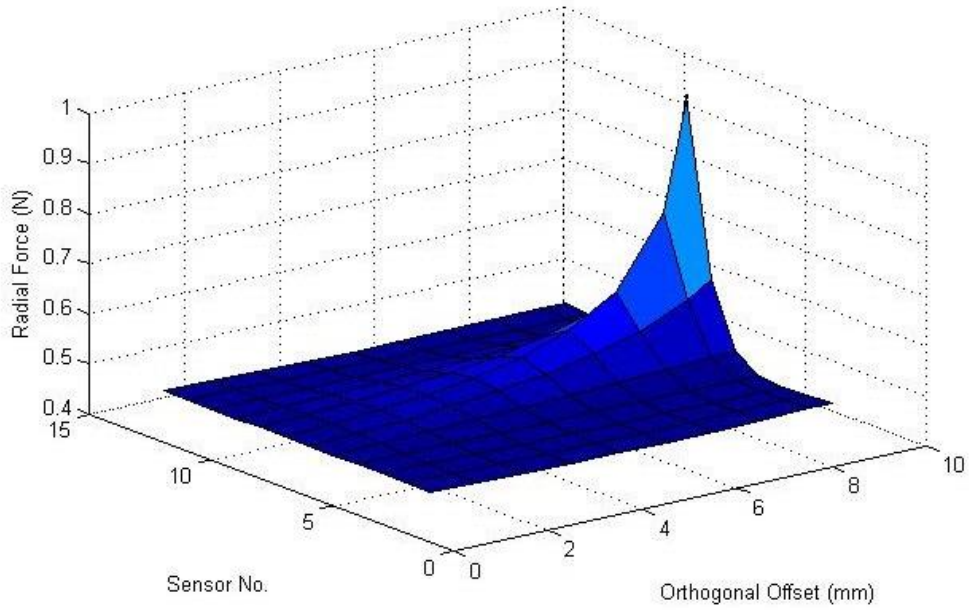

Figure 5-20 Radial Loading vs Orthogonal Offset

5.3.1.3 Experimentation

With the characteristics of the Displacement Sensor theoretically evaluated, the next step to confirm the results through practical experimentation. The single displacement sensor test rig used in this study is shown in Figure 5-21. The rig is comprised of three main components: the position controller (**b**), the sample plate (**d**), and the data acquisition module (**e**). the

sample plate and the position controller is mounted onto a single 6mm aluminium base plate with enough screw clearance for fine adjustments.

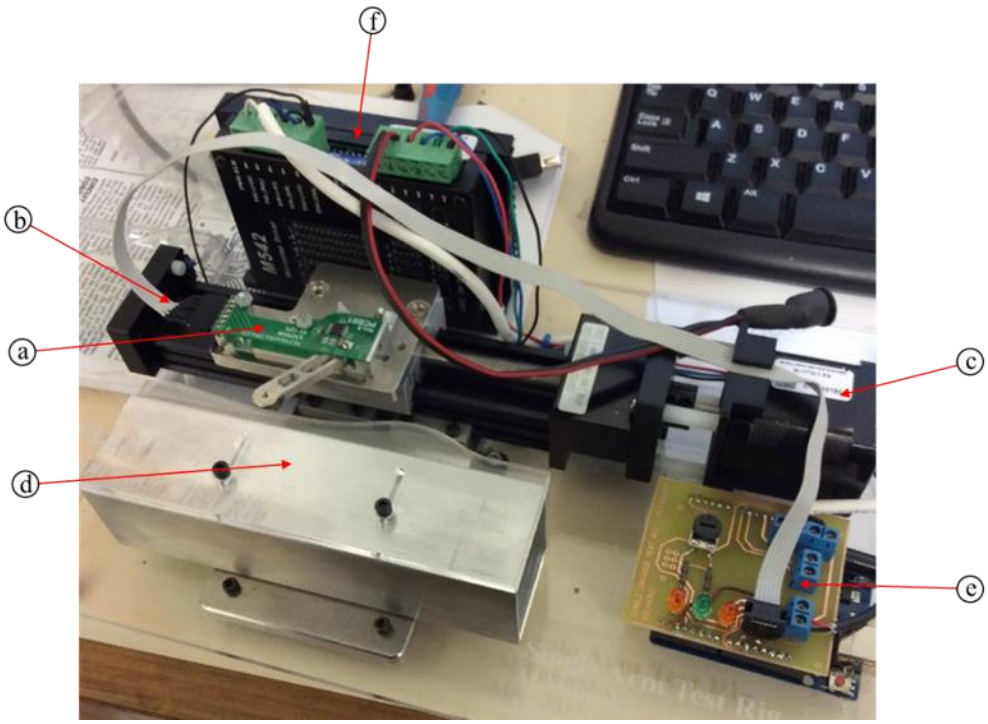

Figure 5-21 Single Displacement Sensor Test Rig

Experimentation Setup

The function of the rig is to simulate the motion of the sensor traversing across the surface with varying profile, mimicking the application during Reformer Tube inspection. The motion of the sensor is controlled using a precision mechanical linear actuator, driven by a NEMA17 stepper motor (**c**) and a 0.5mm pitch lead screw assembly. The position and the speed of the motion is controlled by stepping the motor at 1.8 full-step increment via the TB6600HG[15] base PWM Chopper-Type driver module. System is driven at 12V DC with a current limit of 1.2A per phase. The sample plate is designed with 6 regions of varying geometry. The location of the region is depicting in Figure 5-22 and their characteristic is discussed in the results. The position and the sensor is processed by a microcontroller based control board, and logged directly to a custom build LabVIEW program through a USB interface. The LabVIEW software displays the data onto a GUI plot and logs the measurement into an excel format file. Additionally, the software performing maiden tasks such as software calibration, system homing, and system parameter setting.

[15] toshiba.semicon-storage.com

Presented in Figure 5-22 is the result from the Single Displacement Sensor test. For the test, a sample rate of 100Hz was used with averaging over 10 measurement. The sensor was moved in 0.5mm increments with a 200ms settling period between each step to eliminate potential mechanical resonation. The grey dashed line shows the actual displacement of the sample plate surface at a given position, determined by the design model. The blue line is the displacement measurement determined from the Displacement Sensor. The orange line is the deviation between the two data calculated simply by subtracting the sensor reading from the true value.

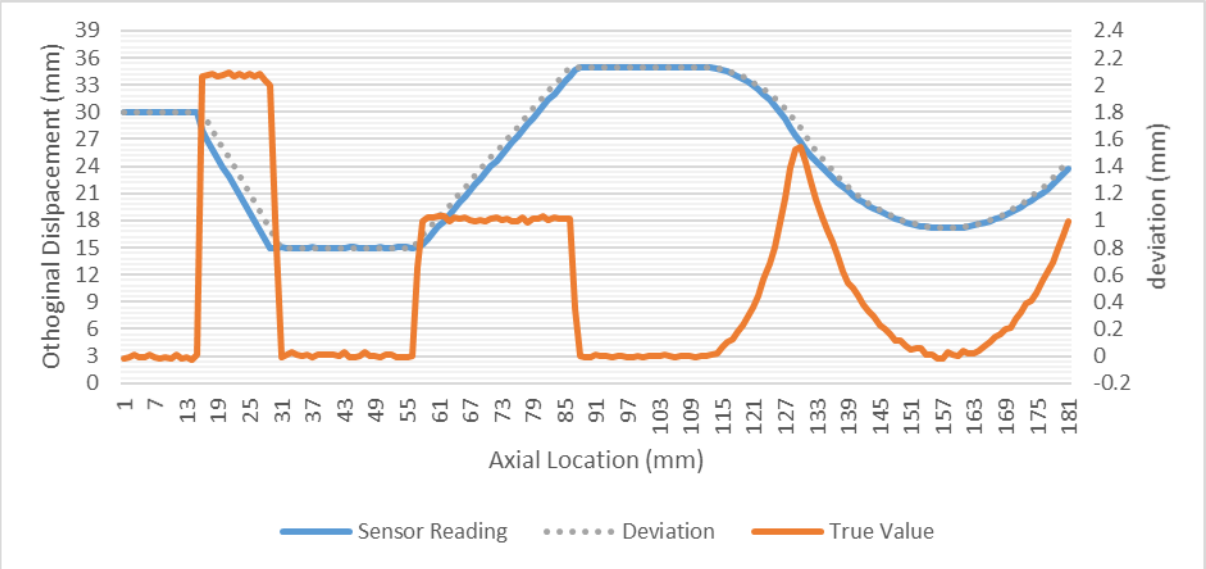

Figure 5-22 Single Displacement Sensor Test Result

Results

First characteristic of the Displacement Sensor from the test result is a deviation in the Sensor Reading along the sloped region on sample. In regions *b*, *d*, and *f* the measurement leads and lag relative to the actual displacement relative to the increasing and decreasing orthogonal displacement respectively, resulting in an increase deviation between the data. The extent of the phenomenon is relative to the gradient of sampled surface. Error in region *b* of 2.071mm is roughly double the error in region *d* of 1.009mm. In region *f* the extent of the error changes between 0-1.532mm relative to the changing gradient of the profile. This can be explained by evaluating the contact point of the sensor bearing. With the nature of the circular geometry of the bearing, the surface in contact with the bearing is always will be tangential to the bearing edge hence the contact point will shift away from sensor orthogonal axis by angle equal to the gradient of the sample plate surface resulting in an error in both x and y axis. The amount of error in the two axes can be determined by the two functions below.

$$e_x = r.\sin(\theta) \quad \textit{Eq. 1}$$

$$e_y = r - r.\cos(\theta) \quad \textit{Eq. 2}$$

Where e_x is the resulted error in the x axis, e_y is the resulted error in the y axis, r is the radius of the sensor bearing, and θ being the angle of the profile surface at the point of contact relative to the y axis.

The second characteristic determined is the variation in the sensor deviation at different displacement of the sample. As discussed in the earlier section, the accuracy of the sensor will vary respectively to the displacement of the detected surface. According to Figure 5-16, the accuracy should in theory decrease from ±0.015mm at 12mm displacement to ±0.001mm at 85mm. to verify this 100 samples were recorded at sample region *a*, *c*, and *e*, and the mean and standard deviations are determined. Figure 5-23 shows the sensor measurement at the three regions of interest and statistically evaluated result presented in *Table 5-4*.

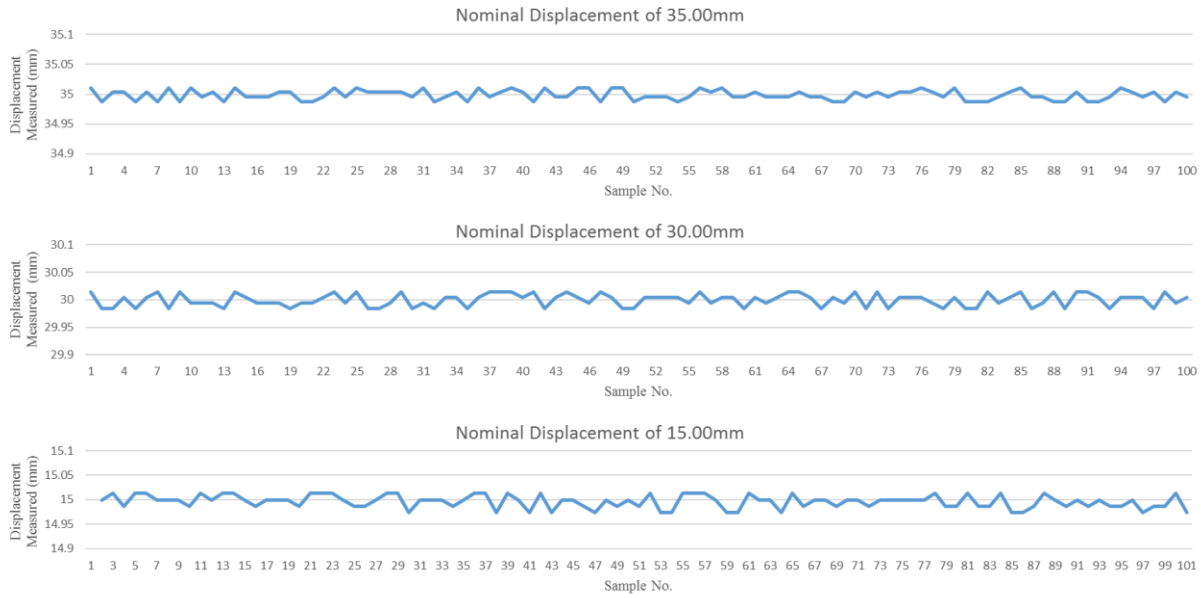

Figure 5-23 Displacement Sensor Static test raw data at 15.00, 30.00, and 35.00mm

Table 5-4 Displacement Sensor Static Evaluation Result

REGION	SAMPLE NUMBER	NOMINAL DISPLACEMENT	MEAN	STANDARD DEVIATION	±2×σ
A	100	30	29.999	0.011	±0.022
C	100	15	14.996	0.013	±0.026
E	100	35	34.999	0.008	±0.016

5.3.2 Radio Transceiver

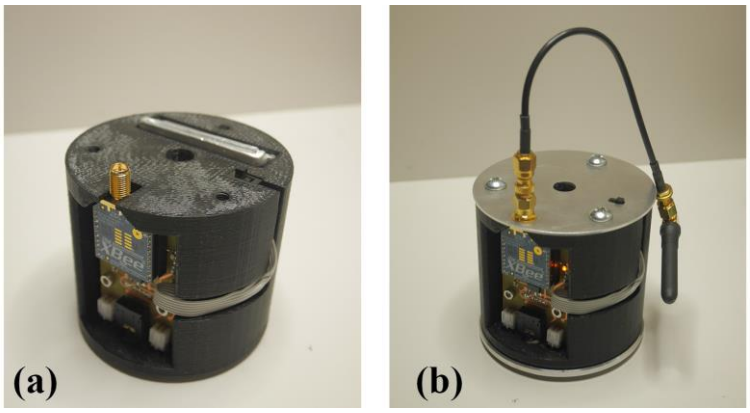

Figure 5-24 Radio Module a)3D Printed ABS Body b) Aluminum Cover Plates

Presented in Figure 5-24 is the Radio Module used in the FTIS prototype. As visible in the left image (a), the bulk of the module is constructed out of black ABS plastic manufactured through FDM 3D Printing process. The body is designed with complex geometry for mounting the radio component, the two Lithium Ion battery, and channeling wires between components. The entire module is designed to fit inside an 83mm stainless-steel cylindrical cover with the top and bottom faces capped with an aluminum plates. The RP-SMA connector is located on the top of the module to connect a 2.4GHz extension to the reflector plate. Power from the battery can be switched off with the power switch on the top plate.

The radio transceiver used for the system is a XBee-PRO ZigBee[16]. Compared with the XBee Znet 2.5 module used in the preliminary study in [24] the new module consumes significantly for power, however benefit from increase transmission range and stability. The UART baud rate is increase to 115200kbps and the measurement packet length reduced to 28bytes, system sample rate of 20.2Hz was recorded. This is a significant improvement to the 8Hz in the preliminary work.

Embedded inside the module is a PCB board designed to perform basic power management tasks. Integrated on it is a Recom 3.3V (500mA) switching regulator[17] to power the 3.3V rail for the XBee module and the TSL2561 sensors used in OPT sensor. The double pole/double throw power switch controls two circuitry arrangement. In the '*on*' state the two 3.7V lithium ion battery is arranged in series to prove the system with a total 7.4V, required to accommodate for the minimum voltage drop of the R-78AA5.0 5V regulator. In the '*off*' state, the batteries are isolated from the system and routed to the 3.5mm stereo jack charging. Due

[16] www.digi.com
[17] www.recom-power.com

to the characteristic of the battery, the cells must be balanced charge with an appropriate charger

5.3.3 Sensor Module

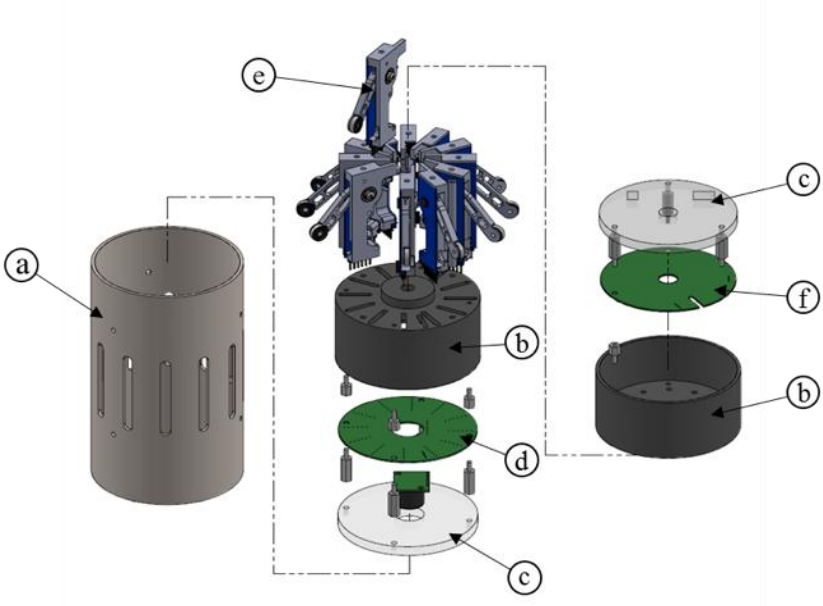

Figure 5-25: Sensor module Assembly Diagram

The sensor module is one of the most defining components of the system design. Not only the system has to accommodate 12 displacement enclosures, but also allow for a robust design with allocation of wiring looming, electronics housing, and electrical insulation and protection. Depicted in *Figure 5-25* is an assembly diagram of the Sensor Module. The module is enclosed inside an 83mm diameter stainless steel tube (**a**) with 1.5mm wall thickness, giving profound robustness and protection for the internal electronics. Two CNC machined plastic sleeves (**b**) holds the sensitive components together while insulating the electronics. Top and bottom faces of the module is protected by a 6mm polycarbonate covers (**c**), allowing transparency for visual indicator. There are three electronic components making up the Sensor Module; Sensor breakout PCB (**d**), Displacement Sensor (**e**), and Processor module PCB(**f**).

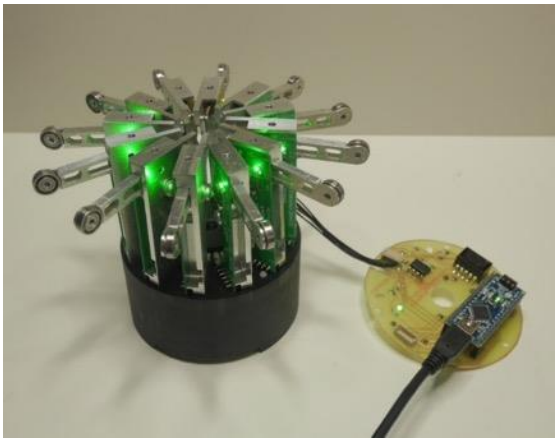

Figure 5-26 Sensor Module development

One of the primary design considerations made during the development of the module is the assembly and serviceability. The polycarbonate covers can be removed for diagnostic purposes without affecting the functionality of the module. The individual displacement sensor is accessible by removing one mounting screw, and be replaced with blanking block to retain functionality during development. Shown in *Figure 5-26* is the setup used during calibration and tweaking the firmware using half of the components, powered off the USB 5V. The detail on the electronics design is presented in *Section 5.4*.

5.3.4 Three Point Stabiliser

Figure 5-27 TPS design 3D CAD Model

Achieving stability of the inspection instrument while moving through the tube is the key for accurate and repeatable data acquisition. While the CDA post-processing algorithm will compensate for the axial misalignment, stability of the system is an essential factor during data acquisition. In the RTID a custom built three-point stabilising system (TPS) has been studied to maintain stability and reliability in the system. Presented in Figure 5-28 is an assembly diagram of the TPS design.

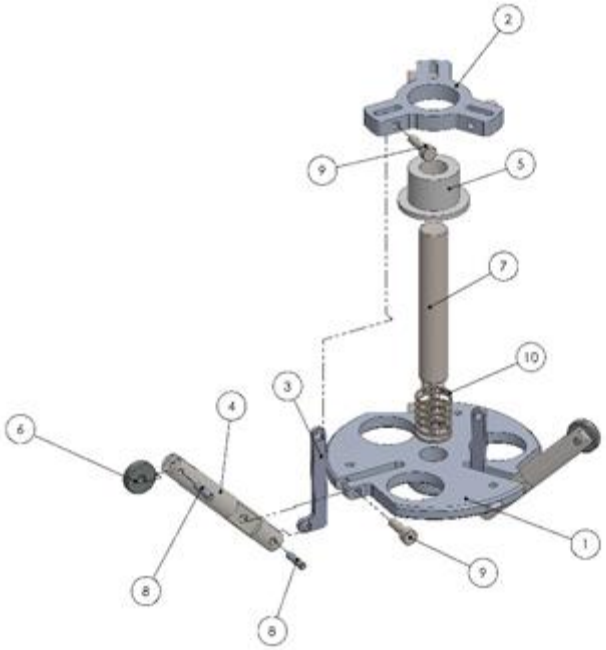

Figure 5-28: TPS system Assembly diagram

The mechanism of the TPS design is relatively simple. The force from the compression spring (**10**) moves the Linkage Ring (**2**), transducing even and equal force on the three Stability Arms (**4**). The mechanics is similar to a common camera tripod used for photography and land surveying. The stability arms and the 10mm rollers (**6**) are made of stainless-steel. Through experimentation, a spring with appropriate spring constant has been selected to ensure the that TPS system can overcome the forces exerted by the Displacement Sensors under the difference scenarios discussed in section 5.3.1.2.

5.3.4.1 Performance Evaluation

The performance of the TSP system is determined by the system's ability to centralise the FTIS system inside a tube. Presented in this section is an sub-experiment conducted on the TPS mechanism using image analysis technique.

Experiment Setup

Figure 5-29 (a) shows the setup used in the first trial of the experiment. The FTIS system is inserted into a 100mm bore aluminium tube positioned along the tube so that the end face of the tube and the core shaft is in line with each other. The two faces are coloured red for a better image filtering. An image is taken from the end of the tube, and then processed to determine the displacement between the two centroids of the faces. A total of 20 trials were conduct, while rotating the probe 60º. In this experiment, the aluminium tube laid on its side so that the weight of the FTIS is directly loaded on to the arm or arms towards the bottom

halve of the tube. Although this is an unlikely scenario for in situ inspection of reformer tube, it will be a good test to determine the performer of the design.

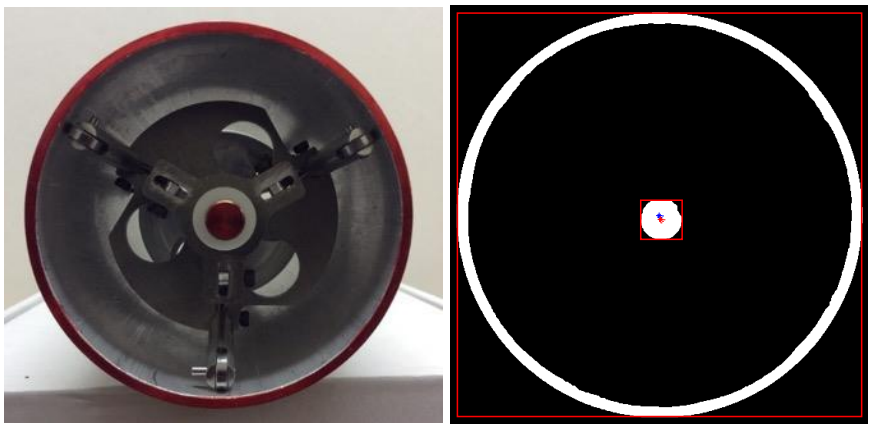

(a) (b)

Figure 5-29 Image analysis of the TPS system performance in MATLAB a) Input Image b) MATLAB output

Presented in *Figure 5-29 (b)* is the output image after processed in MATLAB. To determine the displacement of the TSP inside the tube, a binary mask is generated from the images using colour thresholding in the HSV environment. Masking is used to distinguish the two faces of the Centre shaft and the tube. The two faces are converted into a binary object and a bounding box that meets the *y* and *x* extremities (shown by a red box) is fitted, and the centre of the boundary is located. The centre of the aluminium tube and the FTIS shaft is indicated blue and red dot respectively. The displacement between the two centres are determined in pixel counts and the value is multiplied by a pixel/mm scalar factor determined by the ratio of pixel height of the bounding box and the actual diameter of the sample tube. The output of the 20 trials are shown in *Figure 5-29.*

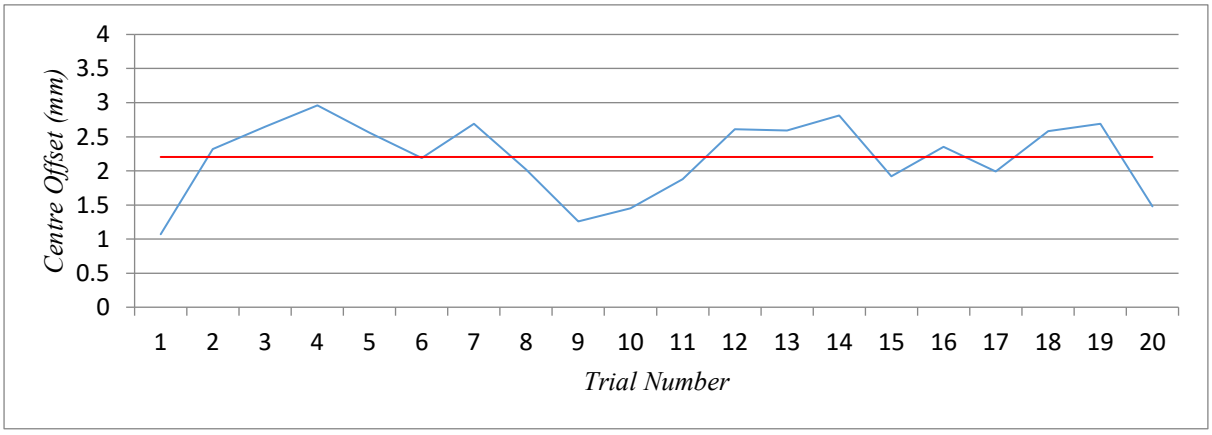

Figure 5-30 MATLAB image analysis out of TPS system

On average, a system misalignment of 2.2mm is measurement within the 20 trials. This indicates that the FTIS system will require a minimum clearance of 3mm around the body of the device to the tube wall. For a conventional system, this level of misalignment will potentially result in an error in the data interpretation and lead false retirement of a reformer tube. However, this should not be of an issue with the use of Creep Detection Algorithm described in Chapter 3. It should also be noted that the maximum displacement is below the 5mm collapsing threshold level of the Displacement Sensor radial force.

5.4 Electronics

The choice for a modular design for the FTIS measurement probe has introduced requirement to the electronics system. Unlike a tethered system with a central computer with external power banking and dedicated hardware drivers, the FTIS system must perform primary tasks, such as power management, system control, and signal filtering within the limited space in each module. In this section, the each elements of the electronic design are present, discussing the choices and design consideration made. Shown in *Figure 5-31* is the entire electronics of the FTIS prototype design.

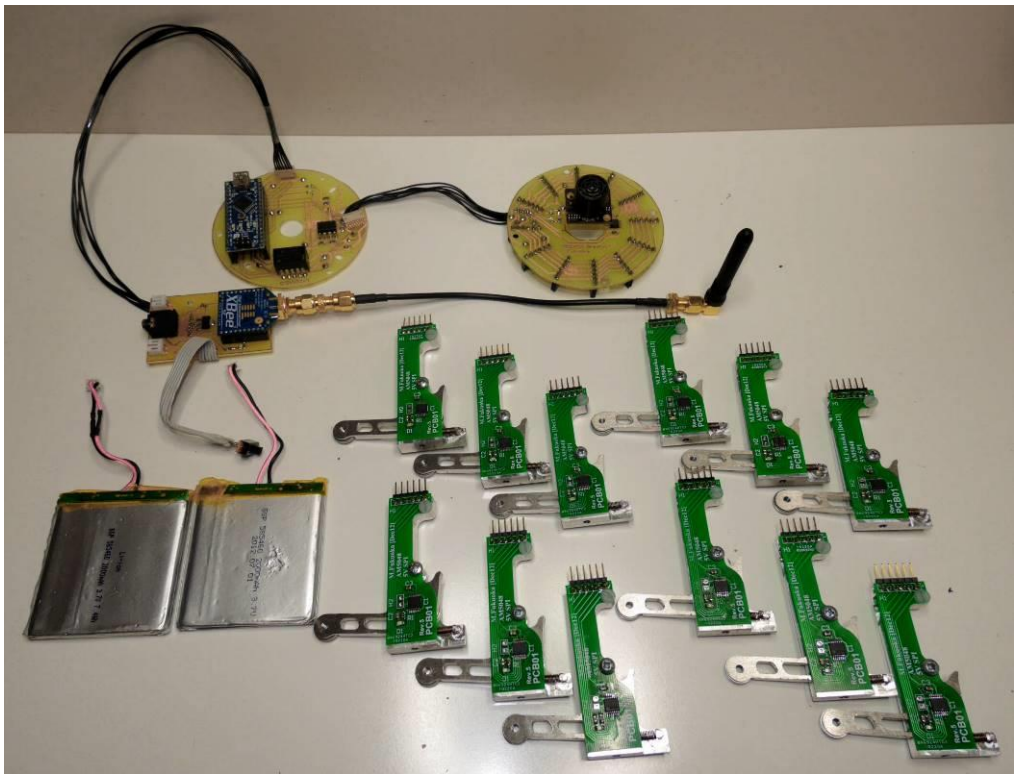

Figure 5-31 RTIS Prototype Electronics Components

5.4.1 Displace Sensor Encoder Board

As the performance of the Displacement Sensor is directly dependent on the quality of the rotary encoder, some time was invested in choosing the sensor for this research. In the preliminary work presented in the literature review [24], a 10-bits MAE3 Absolute Magnetic Kit Encoder from US Digital[18] was used. While the product provided a tidy and robust solution, the module is relatively large considering the size of the actual encoder used inside the sensor. Hence, the use of the MAE3 and other enclosed encoder products were negated in the design, and instead electromagnetic encoder IC's where investigated.

In the early stages of the research 10bit encoders, such as the AS5040 and the AS5043, were evaluated using the PWM signal output. The concept was to convert the PWM into an analogue signal using RC filtering and measure this use the internal ADC to benefit the high sample rate of the internal hardware. For a AVR processor, a maximum sample rate on the 10-bit ADC is 15,384Hz which is faster than most precision encoder ICs. However, even with recommended passive second order RC low pass filter circuit described in the manufactures datasheet, the resolution and the response time of the sensor was largely impeded when passed through the circuit.

In the following iteration, an AMS AS5045 12-bit encoder was used. The PWM protocol was replace with SPI serial bus to accommodate for the added 2-bits of resolution, and later replaced with the successor model. The encoder used for the final design is the AMS AS5048A, a contactless absolute encoder in a compact TSSOP-14 package. With 14-bit output resolution maximum theoretical resolution equating to 0.0219 °/least significant byte (LSB). It has a maximum sample rate of 11.25kHz which is limited by the *Master* side internal hardware. The IC is integrated with a Hall sensors, a Sigma-Delta ADC converter and a digital signal-processor (DSP). The sensors tolerate magnet misalignment, air gap variations, temperature variations, and as well external magnetic field, making the technology ideal for this application. PWM signal and both SPI and I2C serial interface is available with complete serial in-circuit programming capability for zero position and debugging features. Presented in *Figure 5-32* is the electronic schematic of the Displacement Sensor PCB, denoted PCB01.

[18] www.usdigital.com

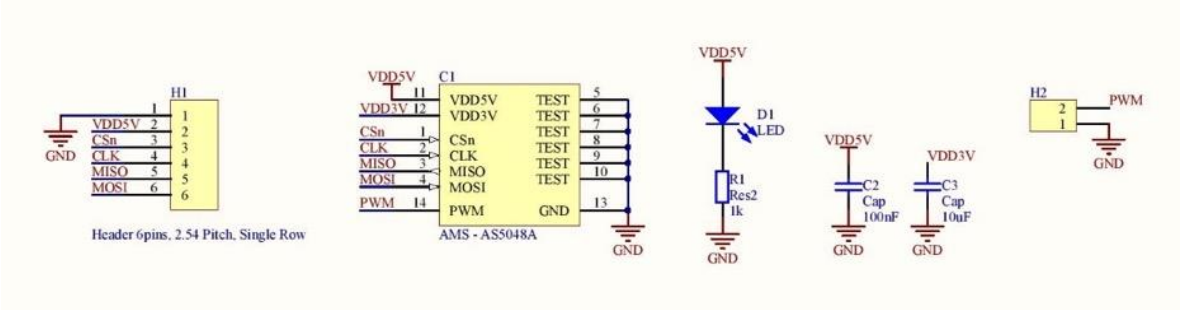

Figure 5-32 AS5048 Encoder Breakout Board Schematic [PCB01]

The sensor is powered by on system 5V rail, provided on pin 1 and 2 on the right-angle header (H1). Combined with the Power Indicator LED (D1) the sensor consumes less than 16mA (experimented), equating to *0.08W*. SPI communication is available on pins 3 to 6 to access the internal registers in the chip for complete control of the IC. In depth descript on the AS5048A encoder is available in the sensor datasheet provided by AMS. PWM on the H2 header is used for debugging purposes during development and is not utilized in the final design. The two decoupling capacitors on the source and 3V low-dropout output pin of 100nF and 10uF respectively has been selected based on the datasheet.

5.4.2 Processor

Presented in Figure 5-33 is the schematic of the main Processor Board, denoted PCB02. The main function of this board is to process the position data from the AS5028 encoder into a linear displacement measurement based on equation X then send the data to the Radio module for wireless transmission to the control station. It also handles other lower level task such as handling the SPI communication bus, data trafficking, battery level monitoring, Polarised Light Tracking etc. This board is powered 7.4V 2 cell lithium polymer battery although the board can tolerate input voltage between 4.75 to 30 DCV. As highlighted in the schematic, the board can be classified as 5 sectors.

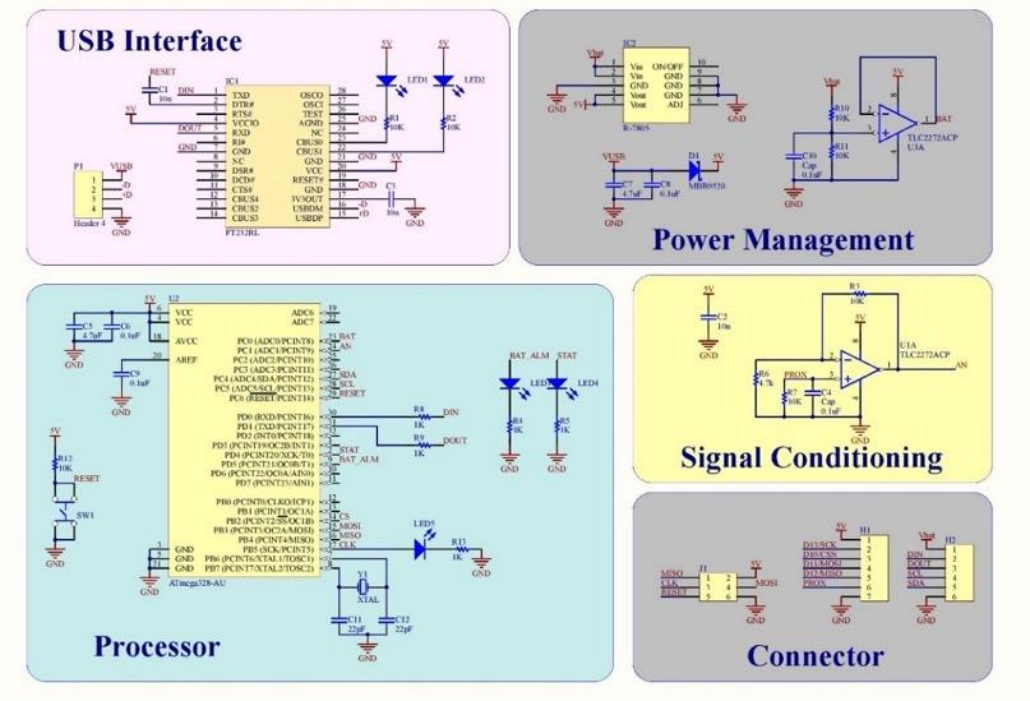

Figure 5-33 Processor PCB Board Schematic diagram [PCB02]

5.4.2.1 Connector

Depicted in Figure 5-34 is the three connector that are available on the PCB02 PCB board. J1 is the JTAG header connector used for debugging and programming the ATmega328 microcontroller. Used for this study is the Atmel-ICE development tool. H1 is a 7 pin JST connector for connecting the data cable between the processor and the encoder breakout board. The cable consists of 5V supply, four SPI bus lines, the bottom detect signal line. Also a JST connection is the 6 pin H2 header. This connection is used for three tasks. Pin 1 and 6 is the external supply rail for power source from the Battery. Pin 2 and 3 is the serial UART data line for communication with the Radio module. Finally, pin 4 and 5 is the I2C communication line to the Polarise Light Tracking module.

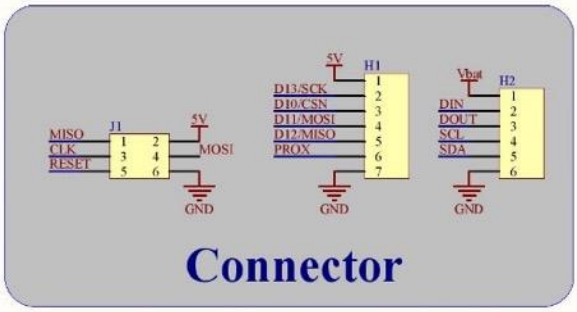

Figure 5-34 PCB01 connector schematic diagram

5.4.2.2 Processor

The core of the board is a 32pin TQFP package Atmel ATmega328 AVR microcontroller operating at 16MHz system clock speed. At board level there is mininal components in the design with only the necessary decoupling capacitors (C5, C6 and C9) , 16MHz crystal oscilator (Y1) and the two load capacitors (C11, C12), and the 10kΩ pull-up resistor (R12) on the reset pin. Current limiting protection resistors R8 and R9 are used on the serial commincation line RX and TX as good engineering practice and two LED circuits are used for program status indicators for debugging purpose.

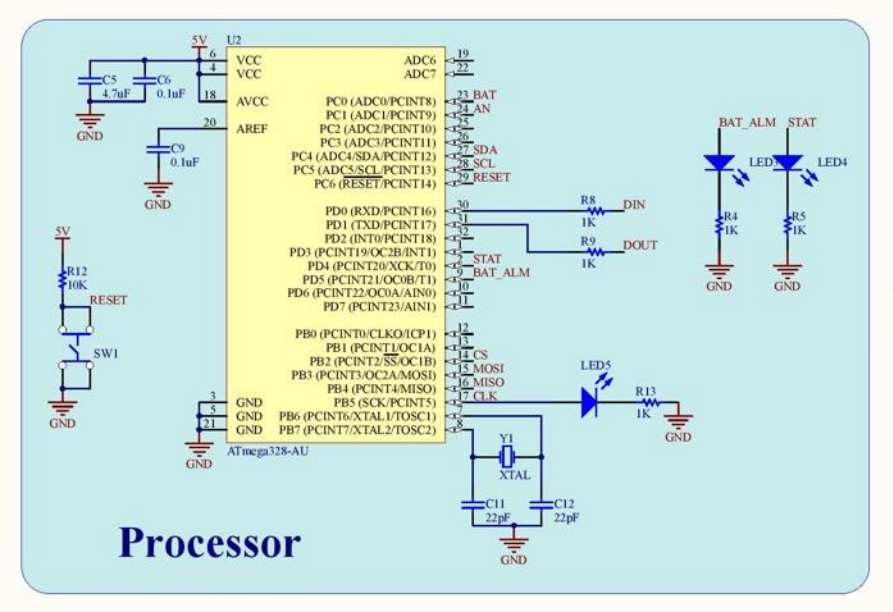

Figure 5-35 Processor Schematic Diagram

The three main features that is of interest on the ATmega328 for this study is the Serial UART, I2C and SPI hardware interfacing periphirals. UART pin TX and RX is used to commincation with the radio module for transmitting and receiving measurement and command datas respectively. Standard 10bit data frame made up of 1 start bit, 8bit of data, and 1 end bit, transmitted at Baud rate of 115200bps is used. I2C interface is used to initialise and measure angular position reading from the Polarise Light Tracking system. Study of this technology is discussed further in Chapter 4. SPI protocol is used to talk to the 12 AS5048 encoders.

Unique to the SPI protocol is the daisychain wiring arrangement with compatible devices. As depicted in the daisy chain four wire connection diagram in Figure 5-36, the MISO and MOSI pins are connected in series with the neighbouring devices. The SPI port of each slave is designed to ouput a copy of the input data in sequence with the clock pulse, creating a

signal shift register communication line. This feature is benefitil as, one, the number of signal lines can be reduced and, two, the sensor measurement can be performed simultaneous.

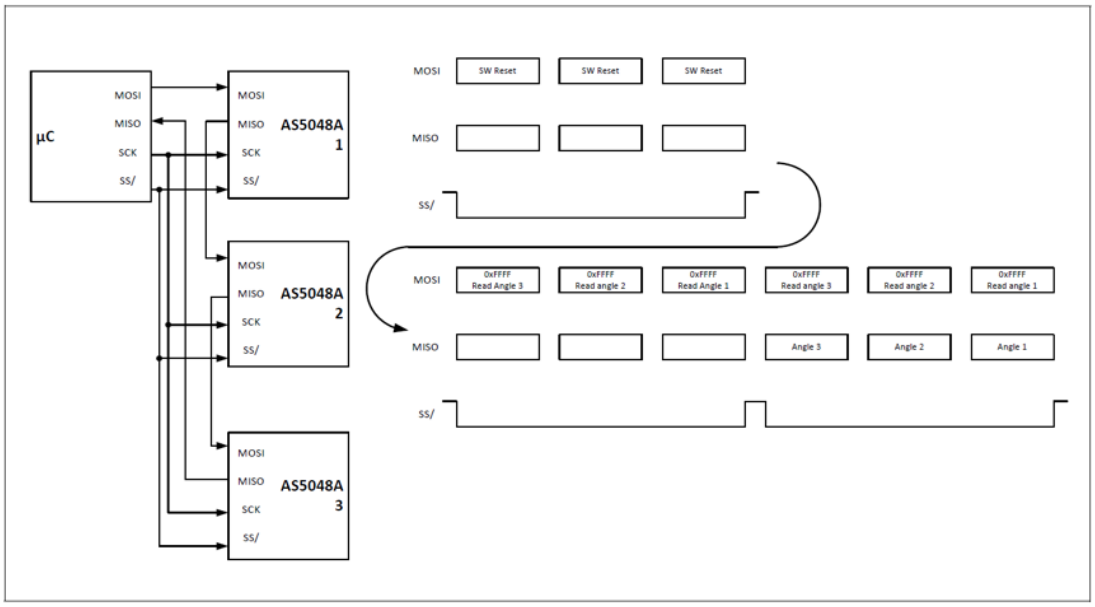

Figure 5-36 4 Wire Daisy Chain SPI connection diagram (image taken from AS5048 Encoder Datasheet)

The configuration of the SPI protocol is shown in Table 5-5. At the given configuration, the processor is capable of process encoder position readings at the maximum sample rate of the AS5048 encoder of 11kHz. This is greater than the through put of the Radio transceivers as discussed later in the chapter, there by an averaging of 10 sample is performed to increase measurement accuracy.

Table 5-5 SPI Communication Configuration

Parameter	*Setting*
Clock Polarity	LOW
Clock Phase	HIGH
Bit Order	MSB First
Clock Speed	8MHz

A Universal Asynchronous Receiver/Transmitter (UART) has been used as the primary method for communicating with the processor. A unique set ASCII command has been generated for a complete control of the FTIS. The full list of accepted commands are listing in Table 5-6.

There are two mode the system can be in; standby and continues read. Standby mode is the default mode the system enters on board power up. In this state the process waits for a three character ASCII command on the RX UART line. The battery level is continuously

monitored at 1min interval and an alarm is sent out on the TX line and the BAT_ALM LED is illuminated if the battery voltage level drop below 6.2V indicating that the battery is 90% discharged and due for charging. The system is turned off if the voltage level drop below 5.8V to avoid battery damaging.

In Continuous Read Mode the processor continuously access the ANGLE register in the AS5048 encoder to collect 14bit position data at 10 kHz. The measurement is averaged over 10 readings than transmitted to the radio module packaged with the Bottom Detect Sensor and the Polarise Light Tracking signals. In this mode 'Return to standby' command is only acknowledged.

Table 5-6 FTIS Command List

Command (ASCII)	*Action*
bat	Read battery level: Returns a number equivilant to the battery voltage level on the Vbat rail.
rXX	Single Read: Perform a measurement on the encoder number XX (01 to 12). Returns four Hexadecimal characters between 0 and 16,383 equivilant to the encoder position (0.0219°/LSB).
ral	Read All: perform measurement on all 12 encoders. Returns four Hexadecimal characters between 0 and 16,383 equivilant to the encoder measurements seperated with a coma between each encoder position (0.0219°/LSB).
rcn	Read Continiously: Enter contineous read mode.
Stp	Return to Standby: Exit continous read mode and return to standby mode. If measurement in is process on the SPI finish return to standby mode on the next measurement. If already in standby a mode do nothing.
cXX	Calibrate Encoder: Set zero position on the encoder number XX to the current position.
mXX	Single Read (mm): Perform a measurement on the encoder number XX (1 to 12). Returns a string equivilant the battery voltage reading ('7.1' = 7.1V).
mal	Read All (mm): perform measurement on all 12 encoders. Returns encoder measurements in millimeters seperated by coma between encoders.
bds	Bottom Detection Sensor:
pol	Polarised Light Tracking Sensor:

5.4.2.3 USB Interface

Shown in Figure 5-37 is the schematic diagram of the USB interface circuitry. Using is a FT232R IC, a USB to serial UART interface is made. This allows for the user to directly communicate to the system with an USB cable bypassing the wireless communication line. This is useful for debugging and bench top experiment purposes as the system can be powered from the USB cable without the worry of battery exhaustion. Also, if a USB bootloader is loaded into the microcontroller (Arduino[19]) the system firmware can be flashed through the USB port without used the JTAG programmer.

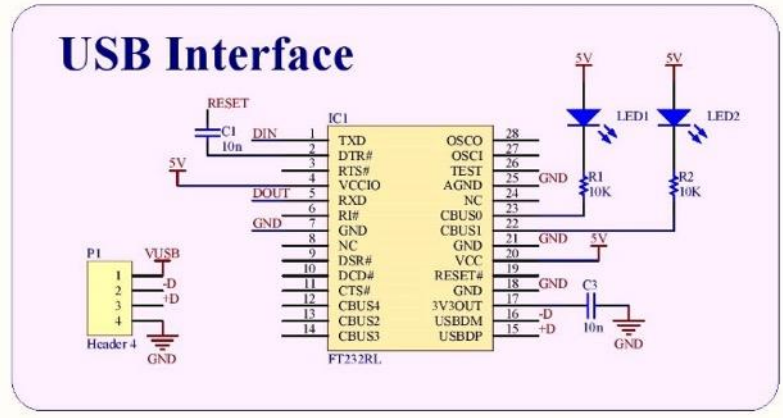

Figure 5-37 USB Interface circuit schematic diagram

5.4.2.4 Power Management

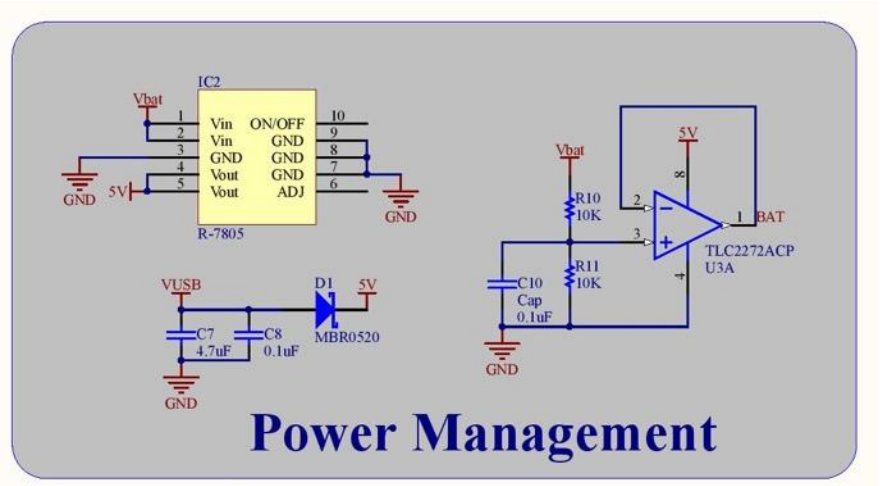

Figure 5-38 Power Management schematic diagram

Presented in Figure 5-38 is the electronics schematic diagram of the power management circuitry. IC2 is a RECOM R-78AA5.0 5V 0.5amp DC to DC switch mode regulator used to

[19] www.arduino.cc

provide power to the processor, Encoder Breakout and the all 12 Encoder board with a stable 5V supply rail. The efficiency of up to 97% means that very little energy is wasted as heat even at input voltage of 32V. In addition, the module features short circuit protection and thermal overload shutdown.

PCB02 can be powered off both USB and/or external supply from header pin H2. To avoid the current flow into the PC USB port from the external source an automatic voltage selector schottky diode (D1) is used to isolate the USB power line from the 5V rail when external power is available. Capacitor C7 and C8 is used to smoothen the *Vusb* line to avoid unnecessary switching of D1 when *Vusb* is unstable.

In the right on the diagram is the operational amplifier based battery voltage monitoring circuit. Because the battery voltage range of 6V to 8.4V is too high for the microcontroller ADC a voltage divider (R10 and R11) is used to halve the voltage level, dropping the range of the BAT signal to 3-4.2V. The signal is then buffered by the unity gain buffer amplifier (U3). The theoretical resolution of the 10bit ADC of the microcontroller will achieving measurement increment resolution of 5mV.

5.4.2.5 Signal Conditioning

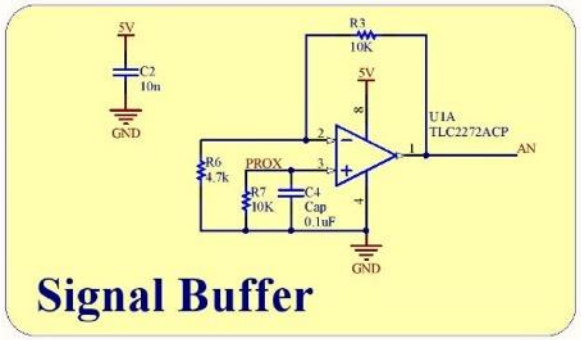

Figure 5-39 Signal Conditioning schematic diagram

Shown in Figure 5-39 is a schematic diagram of the signal amplifier circuit. The amplifier is used to amplify the PROX signal from the ultrasonic proximity sensor to a suitable voltage range for the microcontroller analog input pin. The ultrasonic sensor used for reformer tube bottom detection output a signal voltage range of 0.5V to 2V when used inside the reformer tube of 110mm. Used is a non-inverting op amp gain stage, also known as a voltage follower with gain. The circuit is similar to a unity voltage follower circuit used for signal buffer in the other part of this system but with added feedback resistor networks to add a gain G to the output.

This op amp stage processes the input voltage PROX by a gain of G, so a generalized expression for this gain is:

$$G = \frac{Van}{Vprox} = \frac{R3 + R6}{R6}$$

The feeback resistor network of R3 and R6 set the stage gain of the follower. A gain value of 3.1 can be achieved with the R3 value of 10k ohms and R6 value of 4.7k ohms.

10k ohm pull-down resistor is used on the PROX line to pull the signal down to ground when the Encoder Breakout board is not connected. Capacitor C4 is used to smoothen any noise that may be induced on the line. C2 is a decoupling capacitor for the TLC2272 op amp IC.

5.4.3 Sensor Breakout Board (PCB03)

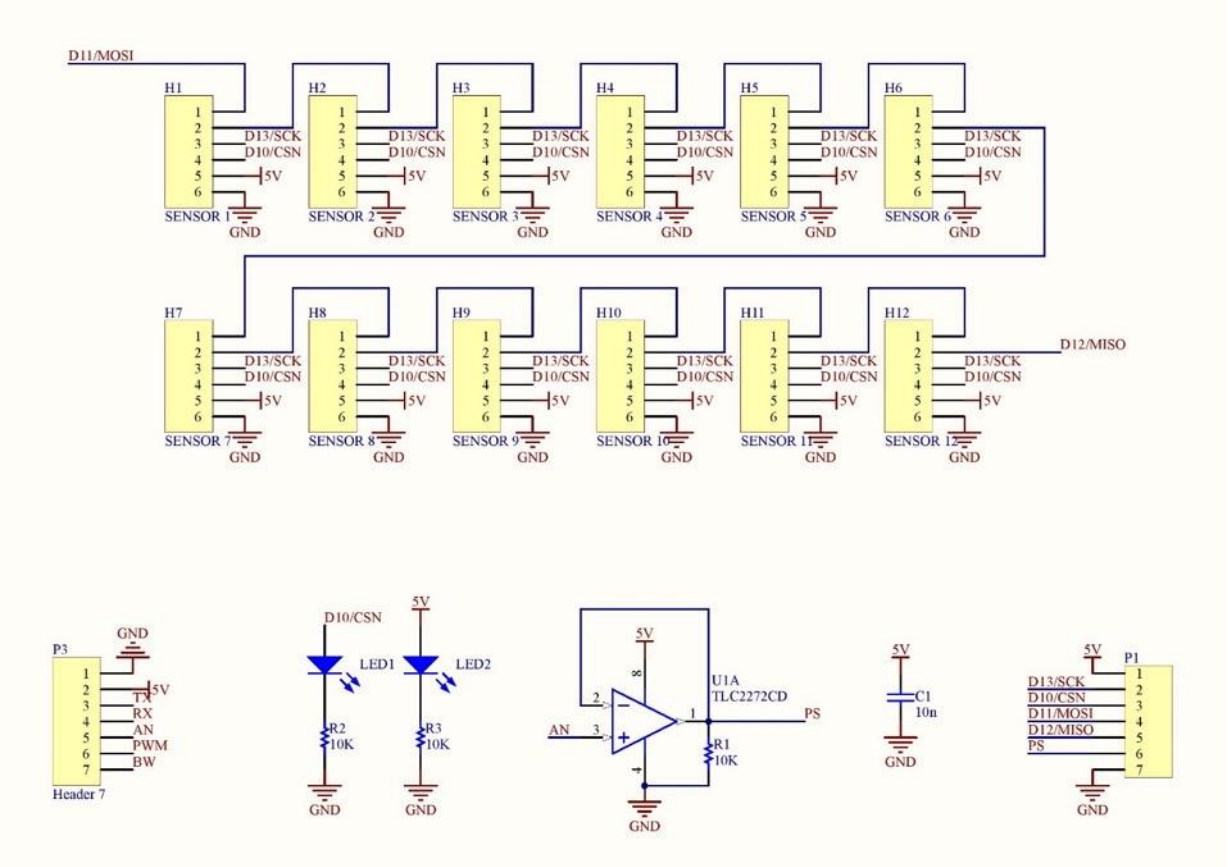

Figure 5-40 Sensor Breakout Board Schematic [PCB03]

Depicted in *Figure 5-40* is the schematic of the sensor Breakout board, identified as PCB02. The displacement sensor is connected via the 12 6x1 female headers from H1 to H12. These 12 modules are configured in a Daisy Chain topology, identifiable by the shared Chip Select CS and System Clock SCK lines, and the connection between the MISO and MOSI pins between the neighbouring modules. Daisy Chain is an interconnection of electronics devices

in a series circuit commonly used in IC SPI devices. This setup was selected over the parallel interface that is also available to the AS5048 chip, as Daisy Chain communication topology generally has benefit of more efficient data transfer rate and simultaneous processing ability. Daisy Chain, in the author's opinion, is beneficial for prototyping and experimental application as devices inside the SPI bus can be replaced with a jumper wire between the MISO and MOSI pins without disturbing the communication. Two LEDs are also used to monitor 5V power line and activity on the SPI CSN signal.

Figure 5-41 Photo of the MaxBotix LV-MaxSonar-EZ4 sensor extruding through the bottom acrylic cover

Connected to the 7x1 female header (P1) is the bottom detection Ultrasonic Proximity sensor. The sensor used in the design is the MaxBotix LV-MaxSonar-EZ4. Of the available EZ range this EZ4 model has the narrowest beam pattern, necessary for Reformer Tube enclosed environment to minimise acoustic propagation from the tube wall. The proximity measurement is available on the AN pin as an analogue output voltage with a scaling factor of -9.8m/inch at 5V supply. As a precaution for future development a Voltage Buffer Amplifier circuit is used to isolate the sensor circuit from the secondary circuit on the output side that may have a low input impedance level. This is implemented using a unity gain buffer amplifier based on the TLC2272 op-amp. C1 is a decoupling capacitor for the op-amp. Serial and PWM output of the MaxSonar sensor is not used.

5.4.4 Power Consumption

Table 5-7 Inspection Probe Current Consumption Table

	Current Consumption (mA per unit)	*Quantity*	*Subtotal Current Consumption (mA)*
XBee Module	120	1	120
AS5048B Encoder	15	12	180

ATMEGA328 Processor	16	1	16
Proximity Sensor	3.5	1	3.5
Signal Conditioning Circuit	6	2	12
Light Sensor	0.6	3	1.8
Total			321.3

Shown in Table 5-7 is the distribution of the maximum power consumption between the three modules of the Inspection Probe. The total power consumption of the Inspection Probe per the table is 321.3mA. Considering current draw of the LEDs indicator and the power loss from the voltage regulator efficiency let us increase this value to roughly 330mA. Knowing the battery capacity and the total current draw, the runtime of the system can be estimated using the following formula.

$$\tau = B \div C \times 0.7 \quad [5\text{-}5]$$

where τ is the estimated runtime in hours, B is the battery capacity, C is the device current consumption, and a correction factor of 0.7 for the allowances for external parameters which can affect the battery life (temperature, battery age .etc). By substituting 2000mAh and the current consumption of 330mA, the estimated runtime can be determined approximately 4hours.

It should be mention that the numbers in *Table 5-7* is the maximum power consumption reflect the current draw during the measurement phase of the inspection; while displacement measurements are processed, and transmitted by the XBee module. During low activity, such as during transport between tubes and probe lowering, the system will consume much less power. For example, in active state the with no radio activity the XBee module will draw around 40-50mA. Although not used in the prototype, the ATMEGA328 processor and the XBee module both has sleep mode feature that will reduce the current consumption to 1mA and 30-50µA respectively. Additionally, a transistor switch circuit can also be implemented to isolate the 12 displacement sensors when it is not in use, reducing the current consumption to zero. In this sense, if the above features where add to the system, the 4hour run time can be allocated exclusively during the 1minute sample period on each tube, allowing for inspection of maximum 400 tubes on one charge.

5.5 Experimentation Evaluation

Till now, the elements of the FTIS prototype design has individually been analyzed. The next step is to evaluate the complete design through a practical experimentation. Best way to do this is to use the system to perform Creep damage inspection on an actual reformer tube.

5.5.1 Experiment Design and Procedure

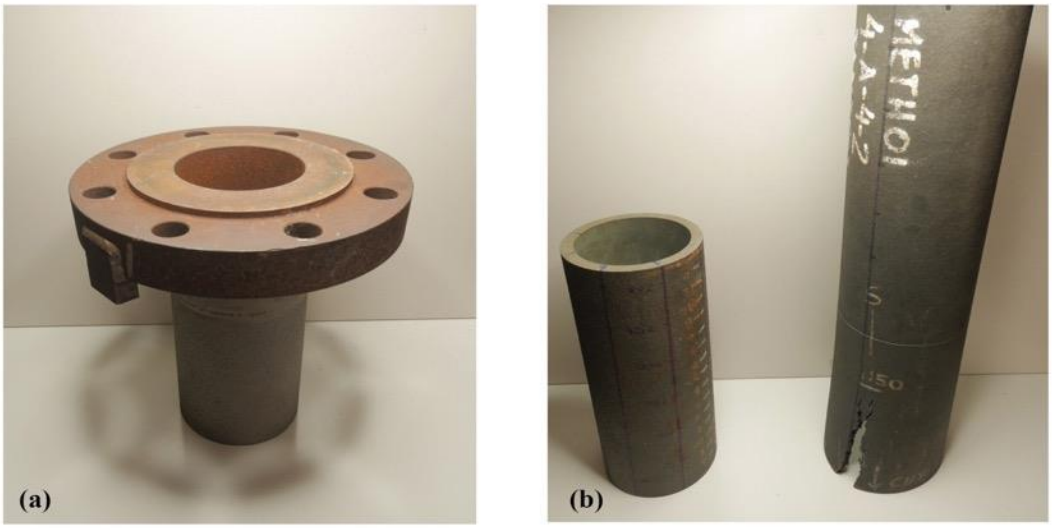

Figure 5-42 Sample Reformer Tubes Used for Testing RTIS Prototype Design a) Sample A, b) Sample B(left), Sample C (right)

Shown in Figure 5-42 are the three sample tubes used in this experimentation. The three tubes are collected from a retire reformer tube of nominal internal diameter of 109mm with different degree of creep failure. It is the same samples used in evaluating the Creep Detection Algorithm presented earlier in this thesis and reference will be made to the experiment presented in Chapter 3. Sample A (a) is the collected from the top of segment of the tube, consisting of the top flange and the segment of the reformer tube. Welding between the two component is visible external but hardly noticeable in the internal surface of the tube. Sample B (b left) is taken from the middle region of a tube with indication of bottom isotropic and anisotropic creep deformation. Sample C (b right) is a longer segment of a tube, measuring 1m, collected from the bottom of a tube. This sample has suffered Creep rapture, as seen in the photo, with significant creep deformation visible throughout the length. IT should be noted that this sample is cut into two smaller segments for experimental purposes in Chapter 3.

Figure 5-43 Experiment Setup of FTIS system measuring Reformer Tube Sample A

The experiment is designed to mimic the use of the system in industry. Shown in Figure 5-43 is the experimental setup used in this section of the research. The FTIS system in inserted from the top of the sample tubes with the measurement probe facing down. Starting from the bottom of the tube, the system is manually pull out of the tube at approximately 0.25m/s, equating to an inspection time of 1minute for a 15m reformer tube. With the limitation of sample tube length, only the bottom TSP mechanism is used to stabilize the system during the experiment. Although this is not the case for the actual application of the design, the added instability is favorable for this experiment to better test the capability of the Creep Detection algorithm. The collected profilometry measurement is transmitted to a PC computer through the XBee radio module. With the data packet size reduced to 24byte and the system UART baud rate increased to 115200kbsp an average sample rate of 23.6Hz was recorded.

The collected measurement is then processed using the CDA presented in chapter 3, implemented in MATLAB. Regression mask window width of 30degree was used throughout the experiment. The code has further need modified for added 3D modelling capability. The final output is four graphical presentation consisting of two 3D model of the profilometry measurement before and after post-processing, and two 2D plot made up of datum correction values and general/ maximum radius measurement determined by the algorithm. Ideally the output data should be evaluated against base-line data for each sample, however because the data is not available for this study the nominal diameter of 109mm will be used.

5.5.2 Result

Sample A

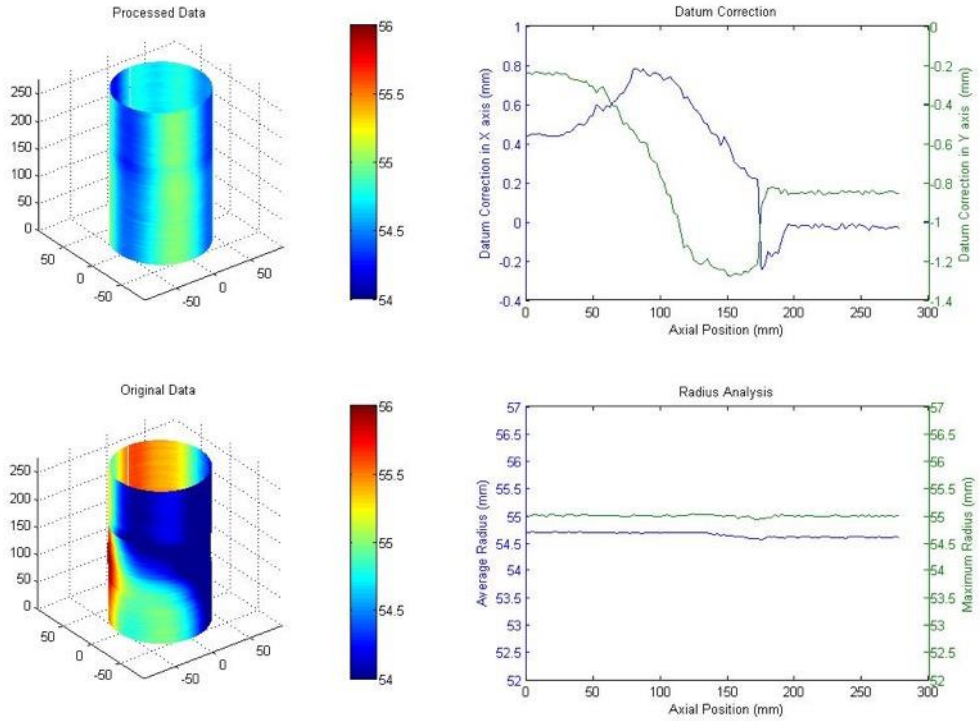

Figure 5-44 MATLAB Graphical Output (Sample A)

Figure 5-44 shows the measurements from Sample A generated by post-processing algorithm. Shown in bottom left is a 3D representation of the raw profilometry data collected from the FTIS. Measurement between each encoder are reconstructed using Cubic spline interpretation technique. It is clearly that significant amount of distortion exists in the data from datum misalignment, resulting in a deviation of almost 2mm. Interruption in the measurement is also visible between 170-180mm location as the surface texture changes over the welded region. A total of 324 measurements where collected and 5400 measurements where reconstructed for further processing.

Shown in the second 3D graph is the same measurement after being processed by the post-processor. Majority of the distortion has been corrected and spread of the radius measurement is significantly reduced. The Datum Correction plot shows the system dynamically correct for the datum misalignment with the tube axis in ‘x’ and ‘y’ axis, between -0.2mm and 0.8mm, and -1.3mm to 0.2mm respectively. The Second plot shows that the tube has isotopically increased in the radius 0.36% and anisotropic increase of 0.92%. Some disturbance in the measurement is seen over the weld region with slight decrease in the radius. Overall the geometry of the sample is uniform indicating a balanced operation with minimal creep

damage. If base-line data is available, over boring from manufacturing defect can be determined to better determine the significance on the increased radius.

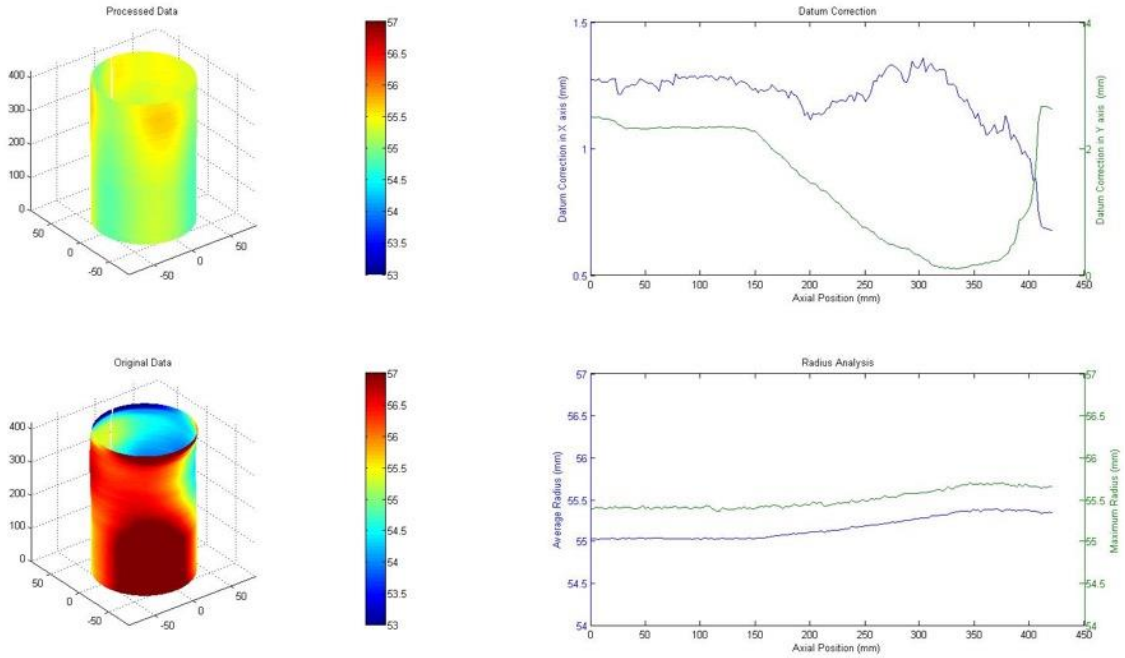

Figure 5-45 MATLAB Graphical Output (Sample B)

Figure 5-45 shows the inspection output of sample B. In this trial, greater amount of datum deviation can be observed from the unprocessed data. The measurement is largely biased towards the negative x and y direction, resulting in a deviation of 4mm between 53-57mm. from the 'Datum Correction' plot it can be seem that the system has actively detected and corrected for the offset, resulting in a much more realistic model of the tube. An overall creep deformation of 0.92% is measured at the bottom 0-150mm of the sample, and gradually increase to a peak at 370mm. The 'Processed Data' 3D model shows signs of localized creep damage in the top region towards the negative x axis, indicating an unbalanced operation. From this information, an investigation can be instigated to determine the cause of degrading (i.e. burner misalignment, catalyst deactivation).

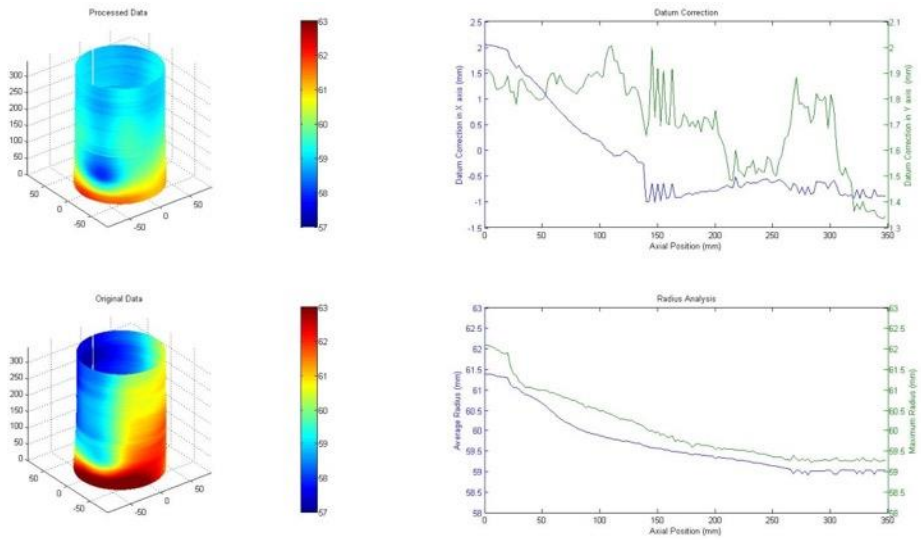

Figure 5-46 MATLAB Graphical Output (Sample C)

Figure 5-46 shows the analysis output of the FTIS system when trailed on sample C. As expected from visible features both the pre and post processed measurements showed significant deformation at the bottom of the tube towards the creep rupture. The data was sampled from end of the creep rapture hence the open in the tube visible in Figure 5-42 is not included in the analysis. Key features in the tube has detected by the system justifying the performance of the prototype design. First interesting feature is the inward buckling of the tube just above the point where crack from the creep rupture starts. This feature was not initially not noticeable but a very common phenomenon considering the sudden bending of the material as the rupture flares the edges of the crack. This feature is completely lost in the original data. Second feature is the

5.5.3 Summary

The Prototype design evaluated using segments of retired reformer tube was successfully able to reconstruct and correct for measurement distortion under various condition. The statistical algorithm presented in chapter 3 is sufficient in dynamically correction of datum misalignment at levels beyond expected by TSP instability. Experiment result proved the viability of the displacement encoder design, and the effect of data distortion resulted from datum misalignment was further emphasised. With considerably less measurement data, in comparison to the existing laser based system, viability of the XBee wireless communication and numerical data reconstruction was shown. Overall it can be concluded that the proposed FTIS prototype design is a viable platform for implementing the pot-processing algorithm for radius based profilometry analysis proposed in this research

5.6 Chapter summary

In this chapter a mechanical design of a Reformer Tube Inspection System prototype was presented and discussed. The concept design was implemented into a module mechatronic system made up of four modules; TSP, Optical Position Tracking, Radio, and the probe. Each element was designed and evaluated to meet the system specification and for easy of manufacturing. Various manufacturing process include CNC milling, Laser cutting, and additive manufacturing was used for a low cost, high precision system. Although not fully documented in this dissertation, many of the multidiscipline design consideration necessary in the mechatronics has been dealt with through multiple design iterations, such as selection and placement of sensors, electronic component distribution, wiring and signal communication protocols etc. The final prototype is a completely modular cylindrical design integrated with low power embedded electronics and wireless communication features.

The FTIS prototype was tested in the lab using reformer tube segments with various degrees of creep damage. Improvements were made on the MATLAB post-processor code for better representation of the analysed data using 3D modelling. The result showed that the system is sufficient for rapidly performing tube inspection while providing accurate profilometry data for both tube RSL assessment and providing insight of the furnace operation. Although the XBee wireless solution has less data throughput rate then existing systems (LOTIS), the optimised system UART protocol combined with the statistical algorithm prove to have compatible inspection performance. In conclusion, the proposed CDA data processing method combined with the integrated mechatronic design presented in the chapter creates a viable solution for better analysis for creep straining in reformer tubes.

6 Conclusion

The main contribution of the research is the development and propose a novel NDT system for the purpose of remaining life assessment of catalytic reformer tube, which is envisaged to provide a solution to the fundamental limitation of existing inspection systems. The proposed methods presented through this research comprises of novel profilometry data processing algorithm, long-range orientation monitoring system, and unique modular hardware design for a practical application, making the concept unique and innovative. Very Encouragingly, the proposed innocative profilometry inspection method and the design methodlogy has been sussessfully implemented in reformer tube pig-tail inspection in a major chemical process industrial campany. The following summarises the major research activities, outcomes, and the general contributions made towards the knowledge of NDT technology.

A literature review explored relevant NTD technology in reformer tubes and revealed three significant knowledge gaps relating to the creep assessment which formed the basis of the three research problems. First, there is very literature on working methods for evaluating profilometry data for creep deformation, such as signal processing, system calibration, data interpolation, and classification of creep deformation. Secondly, while methodology exists to monitor the movement of in-tube inspection instrument along the axis, no dynamic method exists to monitor the instrument motion in the sectional plane. Thirdly, literatures show that remaining life assessment from profilometry inspection is limited to diametrical growth measurement. These research problems were then explored in three studies.

Study 1: a contribution in this study recognised with the success in devising a method of processing profilometry data for creep analysis. The process began by examining the phenomenon and significance of datum misalignment in profilometry dataset to understand the relative challenges of conducting profilometry creep analysis from radius measurement. This was done by exploring case studies on profilometry dataset generated based on a model where creep is distinguished between isotropic and anisotropic deformation. The finding showed that measurement is induced with sinusoidal characteristic dependant on the magnitude of asymmetry in the tube and the orientation of the mechanical stabilisers. The sinusoidal distortion is modelled, and a method for processing profilometry dataset is derived, termed as Creep Detection Algorithm (CDA). Using combination of data interpolation, regressive model fitting and data masking technique, the proposed three-stage algorithm is

designed to locate the tube axis and classify region of anisotropic characteristic, allowing for creep deformation assessment based on radius measurements.

The Creep Detection Algorithm was implemented in MATLAB and testing using samples with various creep phenomena collected from ex-service reformer tube. The experiment demonstrated stability and repeatability between the total of 32 datasets, indicating consistency in the method. CDA successfully distinguished and quantified two modes of hoop and localised creep deformation with *goodness-of-fit (GOF)* statistical reporting to verify the result. Although unanticipated, results indicated that the texture of the measured surface is correlated with the Sum of Square due to error *(SSE)* and Root Mean Squared error *(RMSE)* values in the GOF report, suggesting a potential for other application of the CDA. It was also verified that the 3rd order cubic spline interpolation used is an adequate model for characterising creep deformation. Comparative analysis revealed that only 12 radius measurements is required for the CDA to successfully perform creep assessment. This is significant as it allows for faster data transition with reduced data set, justifying the use of wireless communication, and reduces the overall processing load for a quicker inspection.

Study 2: The second study comprised the development of the long-range orientation detection system intended for correction of distortion in profilometry measurements evident in current profilometry system. This research proposed the use of linear polarisation filters to form an innovative approach to track the rotational motion of an object moving through a reformer tube, termed the Optical Position Tracking (OPT) system. Based on Malus Law, the transmission axes between the OPT light source and sensor side polariser is measured to determine the angular displacement between the two. Implementation of 3 shaft offset signal is discussed and a two-stage programmatic algorithm, comprised on logic and numerical analysis, is derived for a universal solution that is independent to the object displacement or optical characteristic of the tube wall.

To verify the concept, two experimental analysis was conducted. The first experiment is designed as a preliminary study to verify the working principle of the OPT system. Designed around a 100mm long aluminium tube, a working prototype was constructed. With the aid of Additive Manufacturing, a two-part OPT system was developed using LED array light source, Edmund polarizing film, and TAOS digital luminosity sensor. Through multiple design iteration and system calibration, the experiment confirmed the principle of the propose OPT method, with results of ±2.0° accuracy. The experiment also identified key elements of the

system such as the importance of filter orientation and illumination consistency between the sensors. In the second experiment, another working prototype was developed but designed around an 8.0m aluminium test tube. The OPT design was modified based on the findings from the first experiment, with improved polarizer quality, better arrangement of sensor, and electronics potting and general consideration to handle ambient lighting. Experimental result showed attenuation in the measurement luminosity as expected with the increase displacement between the sensor and the light source, but an improved performance with measurement accuracy of ±1.8°.

This study succeeded in devising and verifying a method to determine the orientation of an object inside a tube at long range. Although the results are limited to the two sample tubes used in the test, high potential has been demonstrated to justifying for further development.

Study 3: Presented in the final study is a system architecture of a reformer tube inspection system (RTIS) developed based on the findings from the first two studies. The proposed design integrates the CDA and OPT system in a mechatronics design, inspired by the work conducted in the preliminary study. Based on practical consideration and specification derived from the working principles, a prototype of the measurement probe is fabricated for experiment and demonstration purposes.

The FTIS probe prototype features a four-part modular design consisting of OPT sensor, TPS stabilizer, radio, and sensor modules. A 1.5mm stainless steel body accounts for robust and rig construction, with an overall cylindrical size of 375mm x 82mm, weighing approximately 2.3kg. Design features custom-built displacement sensors yielding significantly high performance when compared with other in-pipe vision systems, with maximum sample rate as high as 11.25kHz. Based on a 14bit electromagnetic rotary encoder, the design is capable of making radius measurement ranging 0-28mm with an accuracy between ±1μm to 15μm, determined from experimental analysis. With a small cross-sectional footprint of 29.0mmx8.5mm, a total of 12 radially oriented sensors are contained within the Sensor module for simultaneous measurement. Using OPT sensor, downfacing ultrasonic proximity sensor, and gravity dependent cable drive mechanism, FTIS system has complete control in positioning the measurement probe anywhere along the main body of the tube with remote access to the internal microcontroller through wireless communication. All of which is contained within the 82mm x 375mm cylindrical body, weighing approximately 2.3kg. The overall power consumption of the design is 1.65W. With the internal 2.0Ah lithium-ion

battery design into the Radio module, the system is able to continuous transmit profilometry measurements for 4.0 hours, with room for hardware and software optimisation for extended battery life.

Although wireless communication has been implemented with in-pipe inspection robots, this research was first to successfully implement wireless technology within a reformer tube. Upon examining the radio wave propagation and waveguide characteristic, it was determined that a 100mm reformer tube act as a passive waveguide for frequencies above 1.95GHz. This was verified through experimental demonstration on a 14m reformer tube. Using the XBee modules, it was proven that 2.4GHz wireless communication is feasible within the reformer tube for real-time data transmission at equal baud rate as when used in an office space, allowing near real-time parallel processing. Data throughput rate of 2800bps was confirmed, which is suitable for the application reformer tube inspection. Although considerations were made only around the XBee module the results are not limited to the Zigbee protocol. Hence, the work conducted is a good initiative for investigating the implementation of other modern wireless technology on the 2.4GHz frequency and above, such as Wi-Fi and Bluetooth.

Overall this study successfully developed a fully functioning FTIS system that is able to perform profilometry inspection of catalytic reformer tubes with improved detection and classification of creep deformation using the novel CDA and OPT systems.

6.1 Future Work

Over the course of the research, a number of insights and discussion around the area of improvement on the proposed method were made. To further the advancement of NDT technology in the Catalytic Steam Reforming industry the following area should be considered for future work.

- **Improve the algorithm for elliptical deformation**: Investigation into enhancing the performance of the creep strain detection algorithm to accommodate tube with elliptical deformation. A new mathematical model for detection the datum offset will need to be formulated, and accordingly, a suited localised creep detection algorithm must be investigated. This is considerably difficult compared to the current work as not only the x and y datum offset must be determined, but the major and minor axis of the ellipse along with the angular orientation must also be fitted.

- **Further work into OPT system:** The current work is subjectable to error when the light beam is not directly illuminated along the tube axis. This insight suggests that the system performance can be improved with other optic technology such as light diffusers and electrically controllable liquid crystal polarising filters. Also, to fully justify the approach for commercial use, the OPT system must be tested on full-length reformer tubes with various service exposure time and surface condition. The effect of tube bowing should also be investigated.
- **Consideration of other wireless technology:** Consideration of implementing other wireless modules for improved wireless communication. While the XBee benefit from low power consumption, which is essential for this application, with sufficient data transfer rate, it is still considered the main bottleneck for the speed at which the proposed FTIS can operate. Investigation into the implementation of other wireless technology, such as Wifi and Bluetooth with different antenna forms, may result in better a wireless solution with improved performance. It should be noted that power management will also need to be considered, especially if wireless module with high power consumption is to be used.

7 Reference

1. Packer, J.E., J. Robertson, and H. Wansbrough, *Chemical Processes in New Zealand*. 1998: New Zealand Institute of Chemistry.
2. Ramachandran, R. and R.K. Menon, *An overview of industrial uses of hydrogen.* International Journal of Hydrogen Energy, 1998. **23**(7): p. 593-598.
3. Shu-Ren, H., *Hydrocarbon steam-reforming process: Feedstock and catalysts for hydrogen production in China.* International Journal of Hydrogen Energy, 1998. **23**(5): p. 315-319.
4. Neiva, L. and L. Gama, *The importance of natural gas reforming*. 2010: INTECH Open Access Publisher.
5. Swaminathan, J., et al., *Failure analysis and remaining life assessment of service exposed primary reformer heater tubes.* Engineering Failure Analysis, 2008. **15**(4): p. 311-331.
6. Rogers, M., *Lessons learned from an unusual hydrogen reformer furnace failure.* 2005.
7. Labanowski, J., *Evaluation of Reformer Tubes degradation after long term operation.* Journal of Achievements in Materials and Manufacturing Engineering, 2010. **43**(1).
8. Szkodo, M. and G. Gajowiec, *Studies of the mechanism of metal dusting of 10CrMo9-10 steel after 10 years of operation in the semi-regenerative catalytic reformer.* Corrosion Science, 2016. **102**: p. 279-290 %@ 0010-938X.
9. Wahab, A.A. and M.V. Kral, *3D analysis of creep voids in hydrogen reformer tubes.* Materials Science and Engineering: A, 2005. **412**(1–2): p. 222-229.
10. Roberts, R.D. and J. Brightling, *Maximize tube life by using internal and external inspection devices.* Process Safety Progress, 2005. **24**(4): p. 258-265.
11. Hevner, K., *Effective Integrity Management Programs for Steam Reformers.* Inspectioneering Journal, 2014. **20**(6).
12. Shannon, B., C. Jaske, and M. Smith, *Optimizing reformer tube life through advanced inspection and remaining life assessment.* Process Safety Progress, 2010. **29**(4): p. 299-304.
13. Goel, A., *Refinery Reliability Through Advanced NDT Methodologies*, in *Proc. National Seminar on Non-Destructive Evaluation*. 2006: Hyderabad, India.
14. Beresford, B., *Inspection of Heat Exchanger, Condenser & Fin Fan Coolers Tubes - An Update.* Inspectioneering Journal, 2007. **21**(6): p. 3-10.
15. Roberts, R.D., *Managing Creep Strain in Steam Reformer Tubes Using Laser Based NDT*. 2005, NACE International.
16. Das, G., et al., *Advanced NDTs for Inspection of Catalyst Tubes of Reformer Furnace*, in *Asia Pacific Conference on Non-Destructive Testing (14th APCNDT)*. 2014: India.
17. James, S., *Inspect steam reformers and catalyst tubes with infrared thermography.* Hydrocarbon Processing, 2014(FEB 2014).
18. Robers, R.D., *Advancements In Laser Profilometry Applied To Reformer Tubes For Detection Of Creep Damage Provides A Step Change In Steam Methane Reformer.* NDT.net, 2003. **9**(9).
19. Roberts, R.D. and P. Tait, *Laser profilometry applied to catalyst tubes in reformers.* Ammonia Plant Safety and Related Facilities, 2000. **40**: p. 287-291 %@ 0360-7011.

20. Alvino, A., et al., *Damage characterization in two reformer heater tubes after nearly 10 years of service at different operative and maintenance conditions.* Engineering Failure Analysis, 2010. **17**(7–8): p. 1526-1541.
21. Begum, S., et al., *Wall thinning and creep damage analysis in boiler tube and optimization of operating conditions.* Journal of Mechatronics, 2013. **1**: p. 1-6 %@ 2326-2885.
22. Brear, J.M., et al., *Life assessment of steam reformer radiant catalyst tubes — the use of damage front propagation methods.* International Journal of Pressure Vessels and Piping, 2001. **78**(11–12): p. 985-994.
23. Chaudhuri, S., *Creep and life assessment of engineering components in power plants and process industries.* 2008.
24. Fukuoka, M., *Reformer tube internal diameter measuring system : a thesis in the partial fulfilment of the requirements for the degree of Master of Engineering in Mechatronics at Massey University, Turitea Campus, Palmerston North, New Zealand*. 2010, Massey University, Palmerston North, 2010. p. 1 v. (various pagings).
25. Jenabali Jahromi, S. and M. NaghiKhani, *Creep life assessment of primary reformer HP40-Nb modified steel tube of an ammonia plant.* International Journal of Engineering-Transactions B: Applications, 2004. **17**(2): p. 183.
26. Le May, I., T.L. da Silveira, and C.H. Vianna, *Criteria for the evaluation of damage and remaining life in reformer furnace tubes.* International Journal of Pressure Vessels and Piping, 1996. **66**(1–3): p. 233-241.
27. Maharaj, C., C.A.C. Imbert, and J. Dear, *Failure analysis and creep remaining life of hydrogen reformer outlet pigtail tubes.* Engineering Failure Analysis, 2008. **15**(8): p. 1076-1087.
28. Martinez-Ona, R. and M.C. Perez, *Research on Creep Damage Detection in Reformers Tubes by Ultrasonic Testing, TECNATOM SS, Madrid.* Proc. 15WCNDT Roma, 2000.
29. Materia, T. *Creep and Stress Rupture Properties*. 2010 [cited 2015 Jan, 20]; Available from: http://www.totalmateria.com/page.aspx?ID=CheckArticle&site=kts&NM=296.
30. Ramzan, N., et al., *Root cause analysis of primary reformer catastrophic failure: A case study.* Process Safety Progress, 2011. **30**(1): p. 62-65.
31. Ray, A.K., et al., *Analysis of failed reformer tubes.* Engineering Failure Analysis, 2003. **10**(3): p. 351-362.
32. Searle, D., *Detection and Measurement of Reformer Tube Creep.* NON DESTRUCTIVE TESTING AUSTRALIA, 2003. **40**(2): p. 48-51 %@ 0157-6461.
33. Shannon, B. and M.M. Fiaqp. *Assessing creep damage in cast material for reformer tubes utilizing multi-parameter approach*. in *4th Middle East NDT Conference and Exhibition, Kingdom of Bahrain*. 2007.
34. Shannon, B.E., C.E. Jaske, and M.C. Smith, *Optimizing reformer tube life through advanced inspection and remaining life assessment.* Process Safety Progress, 2010. **29**(4): p. 299-304.
35. Shipley, D., *Creep damage in reformer tubes.* International journal of pressure vessels and piping, 1983. **14**(1): p. 21-34.
36. Swaminathan, J., et al., *Mechanical strength and microstructural observations for remaining life assessment of service exposed 24Ni–24Cr–1.5Nb cast austenitic steel reformer tubes.* Engineering Failure Analysis, 2008. **15**(6): p. 723-735.
37. Wahab, A.A., C.R. Hutchinson, and M.V. Kral, *A three-dimensional characterization of creep void formation in hydrogen reformer tubes.* Scripta materialia, 2006. **55**(1): p. 69-73 %@ 1359-6462.

38. Zhou, C. and S. Tu, *A stochastic computation model for the creep damage of furnace tube.* International Journal of Pressure Vessels and Piping, 2001. **78**(9): p. 617-625.
39. Brightling, J., *A long history in steam reforming at Billingham*, in *Nitrogen+Syngas*. 2014. p. 46-50.
40. Xu, J. and G.F. Froment, *Methane steam reforming, methanation and water‐gas shift: I. Intrinsic kinetics.* AIChE Journal, 1989. **35**(1): p. 88-96 %@ 1547-5905.
41. Xu, J. and G.F. Froment, *Methane steam reforming: II. Diffusional limitations and reactor simulation.* AIChE Journal, 1989. **35**(1): p. 97-103.
42. Molburg, J.C. and R.D. Doctor. *Hydrogen from steam-methane reforming with CO2 capture*. 2003.
43. Lippmann, D. and N. Frisse. *First Application of the Uhde Dual Pressure Ammonia Process for the 3300 Mtpd Ammonia Plant for SAFCO in Saudi Arabia*. in *IFA Technical Conference*. 2004.
44. Nielsen, S.E., *Latest Developments in Ammonia Production Technology*, in *FAI International Conference in Fertiliser Technology*. 2007, FAI International Coference in Fertiliser Technology: New Delhi, India.
45. Kalamaras, C.M. and A.M. Efstathiou, *Hydrogen Production Technologies: Current State and Future Developments.* Conference Papers in Energy, 2013. **2013**: p. 9.
46. Dahl, P., et al., *Proven autothermal reforming technology for modern large-scale methanol plants.* Nitrogen+ Syngas, 2014: p. 12.
47. Beyer, F., et al. *Steam reforming–50 years of development and the challenges for the next 50 years*. in *AIChE 50th Annual Safety in Ammonia Plants and Related Facilities Symposium, Toronto, Canada*. 2005.
48. Standard, A., *530: Calculation of Heater Tube Thickness in Petroleum Refineries*. 2003, American Petroleum Institute.
49. Guglielmino, E., et al., *Damage investigation on welded tubes of a reforming furnace.* La Metallurgia Italiana, 2015(1).
50. Mateša, B., R. Bodenberger, and V. Pecić. *Non-Destructive Testing in Predicting of Processing Furnace Remaining Life*. in *International Conference" NDE for Safety", November 7-9, 2007., Prague, Czech Republic*. 2007. Citeseer.
51. da Silveira, T.L. and I. Le May, *Reformer Furnaces: Materials, Damage Mechanisms, and Assessment.* Arabian Journal for Science and Engineering, 2006. **31**(2): p. 99 %@ 0377-9211.
52. Ray, A., et al., *Damage mechanism of service exposed reformer tubes in petrochemical industries-a review.* 2015.
53. Wu, X., et al., *The eutectic carbides and creep rupture strength of 25Cr20Ni heat-resistant steel tubes centrifugally cast with different solidification conditions.* Materials Science and Engineering: A, 2000. **293**(1): p. 252-260.
54. Garbiak, M., W. Jasiński, and B. Piekarski, *Materials for reformer furnace tubes. History of evolution.* Gas, 2011. **700**(800): p. 900.
55. Gong, J.-M., S.-T. Tu, and K.-B. Yoon, *Damage assessment and maintenance strategy of hydrogen reformer furnace tubes.* Engineering Failure Analysis, 1999. **6**(3): p. 143-153.
56. Pippel, E., J. Woltersdorf, and R. Schneider, *Micromechanisms of metal dusting on Fe-base and Ni-base alloys.* Materials and corrosion, 1998. **49**(5): p. 309-316.
57. Turi, I.H., *Primary reformer tubes failure due to corrosion attack.* Process Safety Progress, 2011. **30**(2): p. 157-163.
58. Annesini, M.C., V. Peumonte, and L. Turchetti, *Carbon Formation in the Steam Reforming Process: a Thermodynamic Analysis Based on the Elemental Composition*,

in *8th International Conference on Chemical and Process Engineering*, S. Pierucci, Editor. 2007: Ischia, Naples, Italy. p. 21-26.
59. Carlsson, M., *Carbon Formation in Steam Reforming and Effect of Potassium Promotion.* Johnson Matthey's international journal of research exploring science and technology in industrial applications, 2015: p. 313.
60. Pei, W.Y. and L.C. Dian, *Properties of HK40 Steel after Long Time Service.* Journal of East China University of Science and Technology, 2006(3): p. 323-328.
61. Hong, X., et al., *Degradation and Resifual Life Assessment of Reformer Furnace Tubes after Long-term Service at Elevated Temperature.* Journal of East China University of Science and Technology, 2001.
62. Raj, A., et al., *Performance and Life Assessment of Reformer Tubes in Petrochemical Industries.* High Temperature Materials and Processes, 2014. **33**(3): p. 217-230.
63. Bhaumik, S.K., et al., *Failure of reformer tube of an ammonia plant.* Engineering Failure Analysis, 2002. **9**(5): p. 553-561.
64. *Kubota HK Alloy Data Sheet*.
65. Palma, V., et al., *Experimental and numerical investigations on structured catalysts for methane steam reforming intensification.* Journal of Cleaner Production, 2016. **111**: p. 217-230 %@ 0959-6526.
66. Schillmoller, C., *HP-Modified furnace tubes for steam reformers and steam crackers.* NiDi Technical Series, 1991. **10058**.
67. Upadhyaya, K., V. Bafna, and P. Haribhakti, *An Integrated Approach For RLA Of Reformer Tubes By NDT (ARTiS).* 2014.
68. Upadhyaya, K., V. Bafna, and P. Haribhakti, *An Integrated Approach For RLA Of Reformer Tubes By NST (ARTiS)*, in *Asia Pacific Conference on Non-Destructive Testing (14th APCNDT)*. 2014: India.
69. Buckley, J.M., *An introduction to Eddy Current Testing theory and technology.* technical paper eddyc. pdf available from the internet at http://joe. buckley. net/papers, downloaded on Sep, 2003. **8**: p. 7.
70. Bondurant, P., et al., *A method for reformer tube in situ inspection radius calculation*. 2003, Google Patents.
71. Roberts, R.D., *Laser profilometry as an inspection method for reformer catalyst tubes.* Materials evaluation, 1999. **57**(4): p. 420-422.
72. Bondurant, P., et al., *2D and 3D display system and method for reformer tube inspection*. 2006, Google Patents.
73. *Handbook of Materials Failure Analysis With Case Studies from the Chemical, Concrete, and Power Industries*, ed. A.S.H. Maklouf and M. Aliofkhazraei.
74. Fortinberry, T. and J. Widrig, *Safely Operating Steam Reformers between Turnarounds: A Holistic Approach to Steam Reformer Maintenance and Reliability.* Inspectioneering Journal, 2013. **March/April**(2013).
75. Shannon, B. and C. Jaske, *A Comprehensice Approach to Reformer Tube Inspection and Assessment.* NDT.net, 2004. **9**(6).
76. Shannon, B. *Reformer Tube Inspection Using a Multiple Technique Approach for Condition Assessment*. in *CORROSION 2005*. 2005. NACE International.
77. Knowles, D., K. Buchanan, and M. Kral. *Condition assessment strategies in centrifugally cast HP steam reformer tube alloys*. in *ECCC Creep Conference, Zurich*. 2009.
78. Middleton, C.J., R. Timmins, and R.D. Townsend, *The integrity of materials in high temperature components; performance and life assessment.* International journal of pressure vessels and piping, 1996. **66**(1): p. 33-57 %@ 0308-0161.

79. Rich Roberts, *Intergrated Steam reformer Tube Inspection and Remaining Life Assessment Methodologies Enable Methanol Plants to Operate Reliably Between Turnarounds.* Nitrogen + Syngas Magazine, 2012. **November**.
80. Roberts, R., *Enhanced Steam Reformer Tube Inspection and Remaining Life Assessment Methodologies Provide the Hydrogen, Ammonia and Methanol Industries Confidence to Extend Catalyst Tube Operating Life beyond the Standard Prescribed 100,000 Hours.*
81. Piyare, R. and S.-r. Lee, *Performance analysis of XBee ZB module based wireless sensor networks.* International Journal of Scientific & Engineering Research, 2013. **4**(4): p. 1615-1621.
82. Clarke, T., *The development of an optical triangulation pipe profiling instrument.* Optical 3-D Measurement Techniques III-Applications in inspection, quality control and robotics, 1995.
83. Ritter, M. and C.W. Frey. *Rotating optical geometry sensor for inner pipe-surface reconstruction*. in *IS&T/SPIE Electronic Imaging*. 2010. International Society for Optics and Photonics.
84. Ravan, M., et al., *Sizing of 3-D arbitrary defects using magnetic flux leakage measurements.* IEEE transactions on magnetics, 2010. **46**(4): p. 1024-1033.
85. Camerini, C., et al. *Feeler pig: a simple way to detect and size internal corrosion*. in *2008 7th International Pipeline Conference*. 2008. American Society of Mechanical Engineers.
86. Sabino, J.M., *EVALUATION OF SUPERFICIAL DAMAGE ON OIL PIPELINE BY FEELER PIG.* 2009.
87. Davidson, R. *An introduction to pipeline pigging*. in *PPSA Aberdeen Seminar*. 2002.
88. Duran, O., K. Althoefer, and L.D. Seneviratne, *State of the art in sensor technologies for sewer inspection.* IEEE Sensors journal, 2002. **2**(2): p. 73-81.
89. Ahrary, A., A.A. Nassiraei, and M. Ishikawa, *A study of an autonomous mobile robot for a sewer inspection system.* Artificial Life and Robotics, 2007. **11**(1): p. 23-27.
90. Wright, C., et al. *Design and architecture of the unified modular snake robot*. in *Robotics and Automation (ICRA), 2012 IEEE International Conference on*. 2012. IEEE.
91. Horodinca, M., et al. *A simple architecture for in-pipe inspection robots*. in *Proc. Int. Colloq. Mobile, Autonomous Systems*. 2002.
92. Nassiraei, A.A., et al. *Concept and design of a fully autonomous sewer pipe inspection mobile robot" kantaro"*. in *Robotics and Automation, 2007 IEEE International Conference on*. 2007. IEEE.
93. Dirksen, J., et al., *The consistency of visual sewer inspection data.* Structure and Infrastructure Engineering, 2013. **9**(3): p. 214-228.
94. Su, T.-C., et al., *Morphological segmentation based on edge detection for sewer pipe defects on CCTV images.* Expert Systems with Applications, 2011. **38**(10): p. 13094-13114.
95. Yang, M.-D. and T.-C. Su, *Automated diagnosis of sewer pipe defects based on machine learning approaches.* Expert Systems with Applications, 2008. **35**(3): p. 1327-1337.
96. Liu, Z. and D. Krys, *The use of laser range finder on a robotic platform for pipe inspection.* Mechanical systems and signal processing, 2012. **31**: p. 246-257.
97. Inari, T., et al., *Optical inspection system for the inner surface of a pipe using detection of circular images projected by a laser source.* Measurement, 1994. **13**(2): p. 99-106.

98. Liefeng, Z., et al. *Optical Inspection System for the Inner Surface of a Pipe*. in *Electronic Measurement and Instruments, 2007. ICEMI'07. 8th International Conference on*. 2007. IEEE.
99. Buschinelli, P., et al. *Laser Triangulation Profilometer for Inner Surface Inspection of 100 millimeters (4") Nominal Diameter*. in *Journal of Physics: Conference Series*. 2015. IOP Publishing.
100. Zhang, W.W. and B.H. Zhuang, *Non-contact laser inspection for the inner wall surface of a pipe.* Measurement Science and Technology, 1998. **9**(9): p. 1380.
101. Johnson, M. and G.S. Gupta. *A robotic laser pipeline profiler*. in *Instrumentation and Measurement Technology Conference, 2003. IMTC'03. Proceedings of the 20th IEEE*. 2003. IEEE.
102. Wu, E., Y. Ke, and B. Du, *Noncontact laser inspection based on a PSD for the inner surface of minidiameter pipes.* IEEE transactions on instrumentation and measurement, 2009. **58**(7): p. 2169-2173.
103. Duran, O., K. Althoefer, and L.D. Seneviratne. *Automated sewer pipe inspection through image processing*. in *Robotics and Automation, 2002. Proceedings. ICRA'02. IEEE International Conference on*. 2002. IEEE.
104. Duran, O., K. Althoefer, and L.D. Seneviratne. *A sensor for pipe inspection: model, analysis and image extraction*. in *Image Processing, 2003. ICIP 2003. Proceedings. 2003 International Conference on*. 2003. IEEE.
105. Safizadeh, M. and T. Azizzadeh, *Corrosion detection of internal pipeline using NDT optical inspection system.* NDT & E International, 2012. **52**: p. 144-148.
106. Duran, O., K. Althoefer, and L.D. Seneviratne, *Pipe inspection using a laser-based transducer and automated analysis techniques.* IEEE/ASME Transactions on mechatronics, 2003. **8**(3): p. 401-409.
107. Duran, O., K. Althoefer, and L.D. Seneviratne, *Automated pipe defect detection and categorization using camera/laser-based profiler and artificial neural network.* IEEE Transactions on Automation Science and Engineering, 2007. **4**(1): p. 118-126.
108. Johnson, M. *Real time pipeline profile extraction using recursive filtering and circle location*. in *Image Processing, 2003. ICIP 2003. Proceedings. 2003 International Conference on*. 2003. IEEE.
109. Gander, W., G.H. Golub, and R. Strebel, *Least-squares fitting of circles and ellipses.* BIT Numerical Mathematics, 1994. **34**(4): p. 558-578.
110. Coope, I.D., *Circle fitting by linear and nonlinear least squares.* Journal of Optimization Theory and Applications, 1993. **76**(2): p. 381-388.
111. Kåsa, I., *A circle fitting procedure and its error analysis.* IEEE Transactions on instrumentation and measurement, 1976. **1001**(1): p. 8-14.
112. Matheson, I., *A critical comparison of least absolute deviation fitting (robust) and least squares fitting: The importance of error distributions.* Computers & chemistry, 1990. **14**(1): p. 49-57.
113. Mintz, D. and P. Meer, *Least Median of Squares Regression.* Artificial Intelligence and Computer Vision, 1991: p. 61.
114. Culshaw, B. and I.P. Giles, *Fibre optic gyroscopes.* Journal of Physics E: Scientific Instruments, 1983. **16**(1): p. 5.
115. Aboelmagd, N., I.-H. Dave, and P.M. Martin, *Measurement-while-drilling surveying of highly inclined and horizontal well sections utilizing single-axis gyro sensing system.* Measurement Science and Technology, 2004. **15**(12): p. 2426.
116. Fujikake, H., et al., *Electrically-Controllable Liquid Crystal Polarizing Filter for Eliminating Reflected Light.* Optical Review, 1998. **5**(2): p. 93-98.

117. Mills, G.H., A.E. Jackson, and R.C. Richardson, *Advances in the Inspection of Unpiggable Pipelines.* Robotics, 2017. **6**(4).
118. Song, H., et al., *Design of in-pipe robot based on inertial positioning and visual detection.* Advances in Mechanical Engineering, 2016. **8**(9): p. 1687814016667679.
119. Horodinca, M., et al., *THE HELI-PIPE INSPECTION ROBOTS ARCHITECTURE FOR CURVED PIPES*. 2018.
120. Wang, X., et al. *Rhythmic control method of a worm robot based on neural CPG*. in *2018 13th IEEE Conference on Industrial Electronics and Applications (ICIEA)*. 2018.
121. Dertien, E., et al., *Design of a robot for in-pipe inspection using omnidirectional wheels and active stabilization*. 2014. 5121-5126.
122. Dertien, E., S. Stramigioli, and K. Pulles. *Development of an inspection robot for small diameter gas distribution mains*. in *2011 IEEE International Conference on Robotics and Automation*. 2011.
123. Dertien, E. and S. Stramigioli, *Development of an inspection robot for gas distribution mains: a Mars-mission underground*. 2010.
124. Zagler, A. and F. Pfeiffer. *"MORITZ" a pipe crawler for tube junctions*. in *2003 IEEE International Conference on Robotics and Automation (Cat. No.03CH37422)*. 2003.
125. Jahanshahi, M.R. and S.F. Masri, *Adaptive vision-based crack detection using 3D scene reconstruction for condition assessment of structures.* Automation in Construction, 2012. **22**: p. 567-576.
126. Moselhi, O. and T. Shehab-Eldeen, *Automated detection of surface defects in water and sewer pipes.* Automation in Construction, 1999. **8**(5): p. 581-588.
127. Sinha, S.K. and P.W. Fieguth, *Automated detection of cracks in buried concrete pipe images.* Automation in Construction, 2006. **15**(1): p. 58-72.
128. Yang, M.-D. and T.-C. Su, *Segmenting ideal morphologies of sewer pipe defects on CCTV images for automated diagnosis.* Expert Systems with Applications, 2009. **36**(2, Part 2): p. 3562-3573.
129. Kannala, J., S.S. Brandt, and J. Heikkilä, *Measuring and modelling sewer pipes from video.* Machine Vision and Applications, 2008. **19**(2): p. 73-83.
130. Xu, K., A.R. Luxmoore, and T. Davies, *Sewer pipe deformation assessment by image analysis of video surveys.* Pattern Recognition, 1998. **31**(2): p. 169-180.

8 Appendix A

Analysis of Profilometry Measurement Tool

8.1 Introduction:

Proposed in the research is an innovative data analysis algorithm for detecting general and localised creep strain within a profilometry data set. In Chapter 4 the algorithm was evaluated and justified based on experimentation analysis using three sample tube segments collected from ex-service reformer tube. The quality and the accuracy of the experimentation is heavily dependent on the quality of the sample data used for comparison. Presented in this section are design consideration and analysis conducted on the Profilometer instruments developed for this work. The construction, electronic, and the control aspects of the device are discussed, and the series of an experimentation and results evaluating the device is shown.

8.2 Apparatus Design

Presented in Figure 8-1 is the exploded view of the Profilometer measurement apparatus of discussion. The custom-built design weighs slightly over 3kg and made of 8 components as listed in Table 8-1. The dial indicator used is a Mitutoyo IDE series absolute Digimatic indicator (**1**), an industry grade gauging tool marketed at the machining industry. Model IDC-1012E using in this study has a measuring range of 0-12mm with a resolution of 0.01mm at 0.02mm accuracy. Probing surface is a free rolling 8mm diameter ball bearing preloaded at 0.95N by a coil spring, giving a maximum response time of 1,000mm/s.

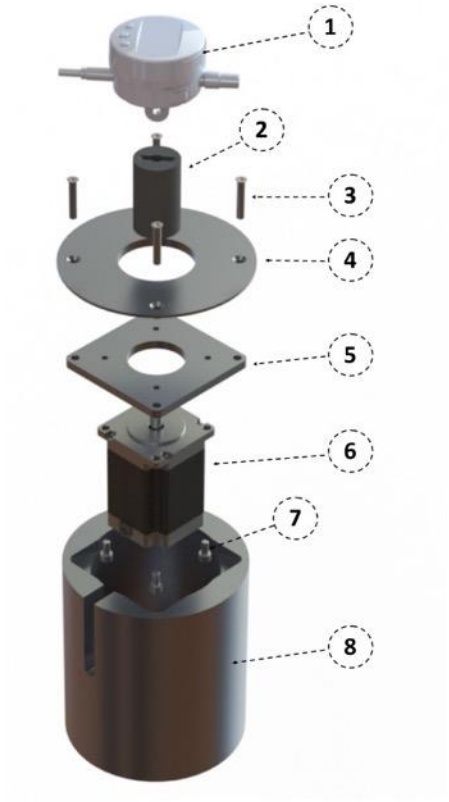

Figure 8-1: Sample Tube Internal Profilometery Analyzer Explode View

Table 8-1: Sample Tube Internal Profilometry Analyzer Component List

Key No.	Part Name	Qty
1	Mitutoyo Dial Indicator	1
2	ABS Dial Indicator Mount	1
3	M5 x 30mm Counter Sunk Hex Screw	4
4	Top Plate	1
5	Stepper Motor Mount	1
6	NEMA 23 Stepper Motor	1
7	M5 X 10mm Hex Screw	4
8	Extrusion Base	1

Dial Indicator is mounted directly to the shaft of the NEMA 23 stepper motor (**6**) via a plastic coupling mount (**2**) printing out of ABS plastic using a UP Plus 2 3D Printer (0.25mm Z axis resolution with solid fill internal scaffolding). The stepper motor used is the bipolar 23H45-3504S model from the high torque series of the Nema23 family, popular for precision control application such as for axial drive of a CNC milling machine. It has full step size of 1.8° (200 steps per revolution) and maximum current rating of 3.5A per phase.

The motor is enclosed inside a 127mm outer diameter aluminium extrusion (**8**). With a wall thickness of 19.05mm, the extrusion base weighs just over 2.5kg, acting as a rigid and robust

platform necessary for the application. The top face of the tube is machined away to mount the 6mm mounting plate (**5**) for suspending the NEMA 23 motor using 4 M5 hex screw (**7**). The 10mm aluminium Top Plate (**4**) is mounted to the extrusion base by 4 M5 screws (**3**) and is a surfaced to provide an even surface to locate the sample tube perpendicular to the measuring plane. M542 Microstep Driver module running at 24V is used to drive the stepper motor.

8.3 Control System and Data Logger

Illustrated in Figure 8-2 is a schematic flow chart of the control system used in the Profilometer. To operate the apparatus, a purpose build software application is developed in LabVIEW environment, with a graphical interface for initiating, terminating, and set up the sampling cycle. An Arduino-based Data Acquisition module used to read the measurement data from the dial indicator and generate digital signals to drive the stepper motor. The processor directly communicates with the dial indicator through the SPC communication port using the custom build interfacing board.

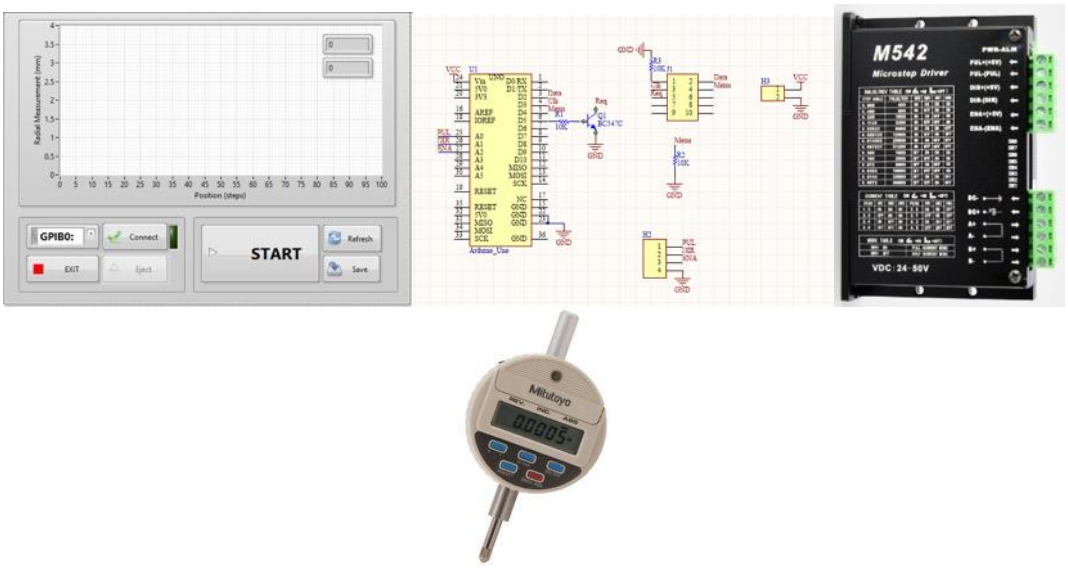

Figure 8-2: Control System Flow Chart

During the sampling cycle, the displacement measurement logged as the stepper motor makes a full rotation. Each data is also associated with the relative angular position Θ. The step size of 1.8° is used with 0.5 millisecond hold period between each sequence to allow for system

settling. The collected data is plotted on the XY graph presented on the GUI before exported into an excel sheet for further analysis.

8.4 Experimentation and Results

In this section series of experimental data collected from a sample tube of 100mm internal diameter is presented. The radius measurement uncertainty is given by the combination of dial indicator performance and the rigidity of the mechanical construction, and the angular positioning accuracy is determined by the consistency of the stepper motors step size. In this study, the error in the step size is not considered. Experimental data is compared with the theoretically calculated data points defined by Eq.(7-1), formulated in Section 4.4, and the overall performance of the Profilometer system.

$$R(\theta) = -X_1 \times \cos\theta - Y_1 \times \sin\theta + \sqrt{r^2 - (X_1 \times \sin\theta - Y_1 \times \cos\theta)^2} \qquad [8\text{-}1]$$

8.4.1 Experiment Setup

Listed in Table 8-2 are the dimensions of the five sample tube specifically designed and manufacture for this study on a 3 axis CNC milling machine. The five samples are machined from a 20mm aluminium disc with 127mm external diameter matching the top plate of the Profilometer. In the centre of the plate is 100mm circular cut out locate 0-2mm away from the plate centre with 0.5mm increments between each sample. The five samples are placed on top of the instrument, and the Profilometry data was collected. For this study, a source voltage of 24 voltages is used with no micro stepping on the stepper motor driver. Between each step, a delay of 500ms settling time is introduced for reduction of potential error from mechanical harmonics.

Table 8-2: Sample Tube Definition

Sample No.	*Internal Diameter (mm)*	*X offset (mm)*	*Y offset (mm)*
1	100.000	0.000	0.000
2	100.000	0.500	0.000
3	100.000	1.000	0.000
4	100.000	1.500	0.000
5	100.000	2.000	0.000

8.4.2 Experiment Result

Figure 8-3,Figure 8-4,Figure 8-5,Figure 8-6, and Figure 8-7 illustrates the data collected on each of the sample plates listed in Table 8-2. The blue plot shows the displacement

measurement at a given angular position, and the orange plot shows the residual measurement between the collected data point and the theoretical data.

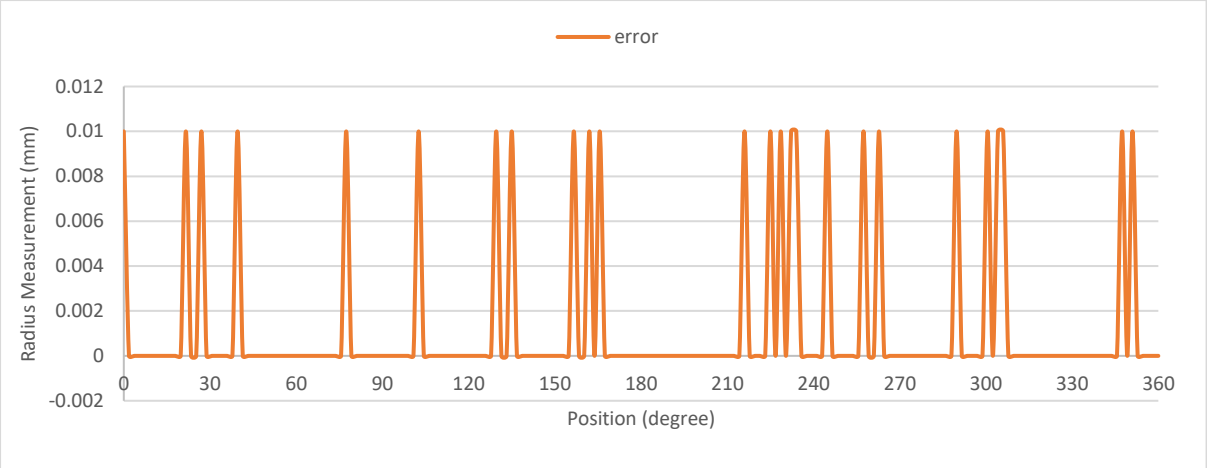

Figure 8-3: STPA Performance Analysis – Sample 1

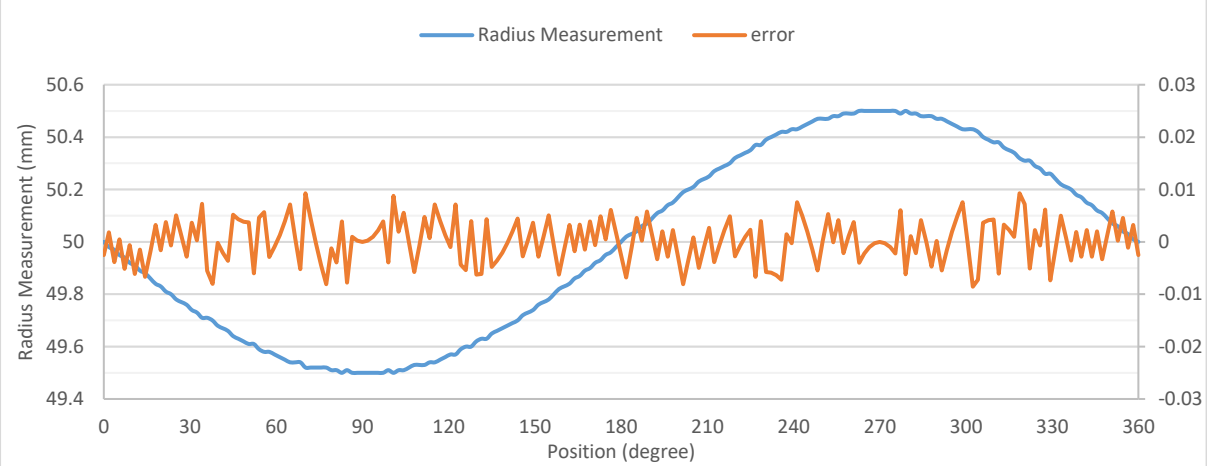

Figure 8-4: STPA Performance Analysis (X = 0.5, Y = 0)

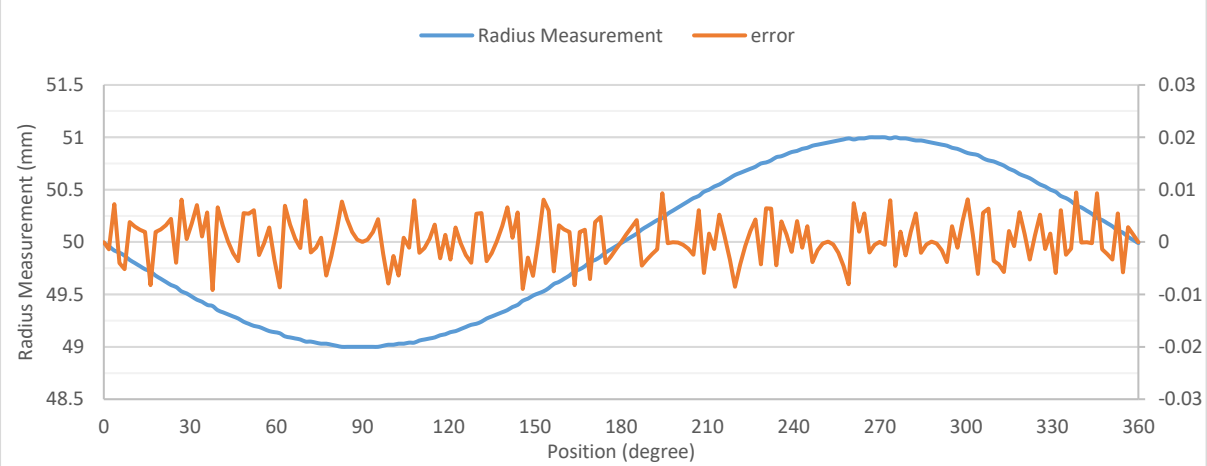

Figure 8-5: STPA Performance Analysis (X = 1.0, Y = 0)

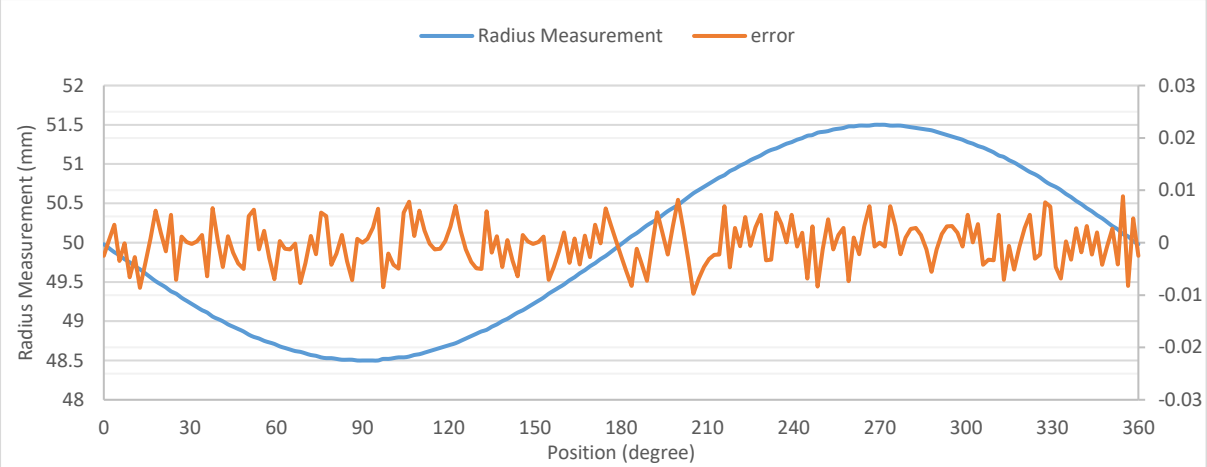

Figure 8-6: STPA Performance Analysis (X = 1.5, Y = 0)

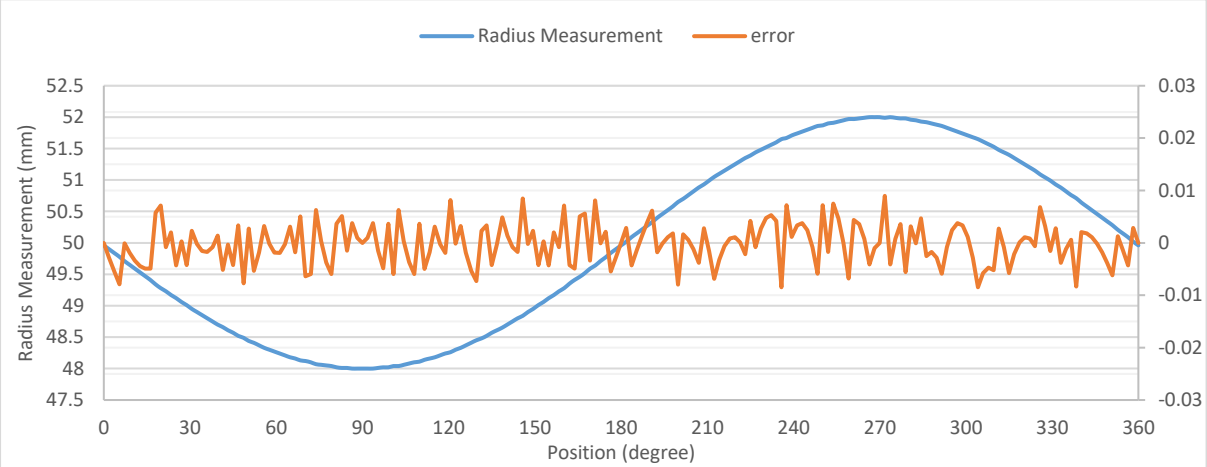

Figure 8-7: STPA Performance Analysis (X = 2.0, Y = 0)

8.5 Summary

Assessing the data presented in Section A.3, the Profilometer instrument is capable of accurately measuring the internal radial displacement and its relative angular position. Although the Mitutoyo dial indicator has in measurement accuracy of 0.03mm according to the datasheet, results from the experiment revealed that the measurements agreed to the theoretical calculation to within ±0.01mm. With appropriate settle time of 500ms, the system is stable and repeatable, performing single sampling cycle within 2minutes. It is concluded that the sample data used in Chapter 4 is accurate to within ±0.01mm.

9 Appendix B

Creep Detection Algorithm Raw Output Data

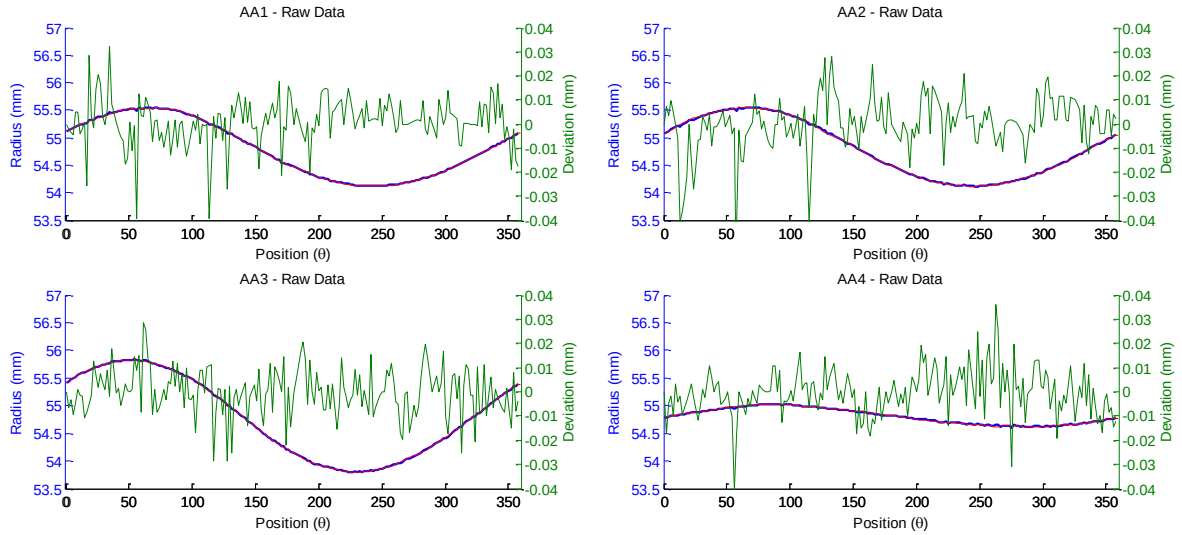

Figure 9-1 Sample A-A: Cubic Spline Output (Data Length = 36)

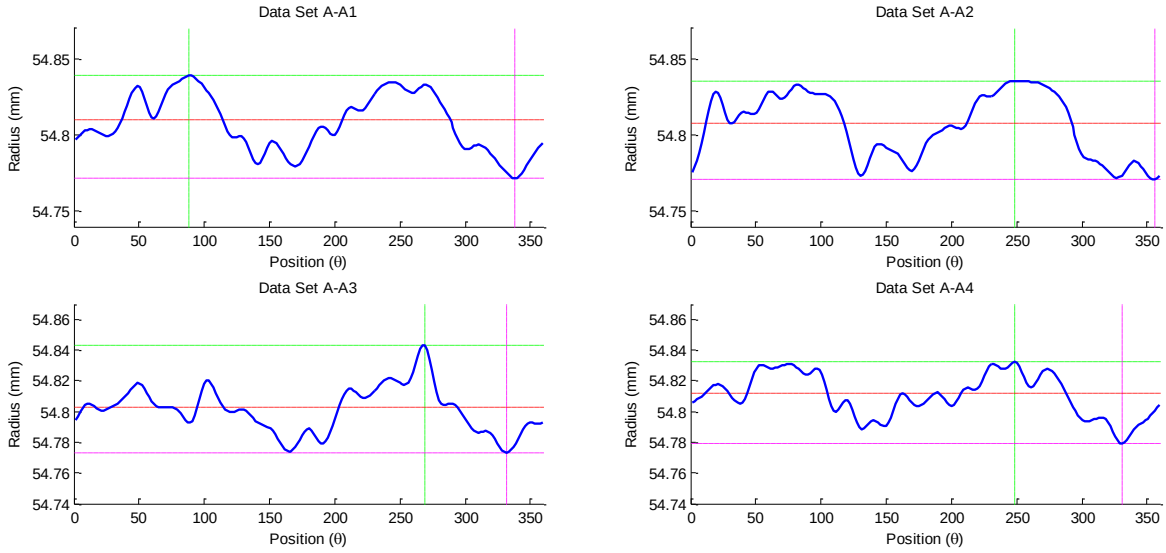

Figure 9-2 Sample A-A: CDA Graphical Results (Data Width = 36, Mask Width = 10)

Table 9-1 Sample A-A: CDA Statistical Results (Data Width = 36, Mask Width = 10)

	A-A1	*A-A2*	*A-A2*	*A-A2*	*Average*
R (mm)	54.8090	54.8079	54.7993	54.8117	54.8070
X Offset (mm)	-0.6420	-0.6523	-0.7897	-0.1959	-
Y Offset (mm)	-0.3188	-0.3007	-0.6331	0.0138	-
sse	0.0601	0.0788	0.0328	0.0319	0.0509
rs	0.9988	0.9985	0.9997	0.9916	0.9972
adjrs	0.9988	0.9984	0.9997	0.9915	0.9971
rmse	0.0179	0.0205	0.0132	0.0130	0.0162
cpu time (s)	0.8438	0.8594	0.8437	0.8125	0.8399

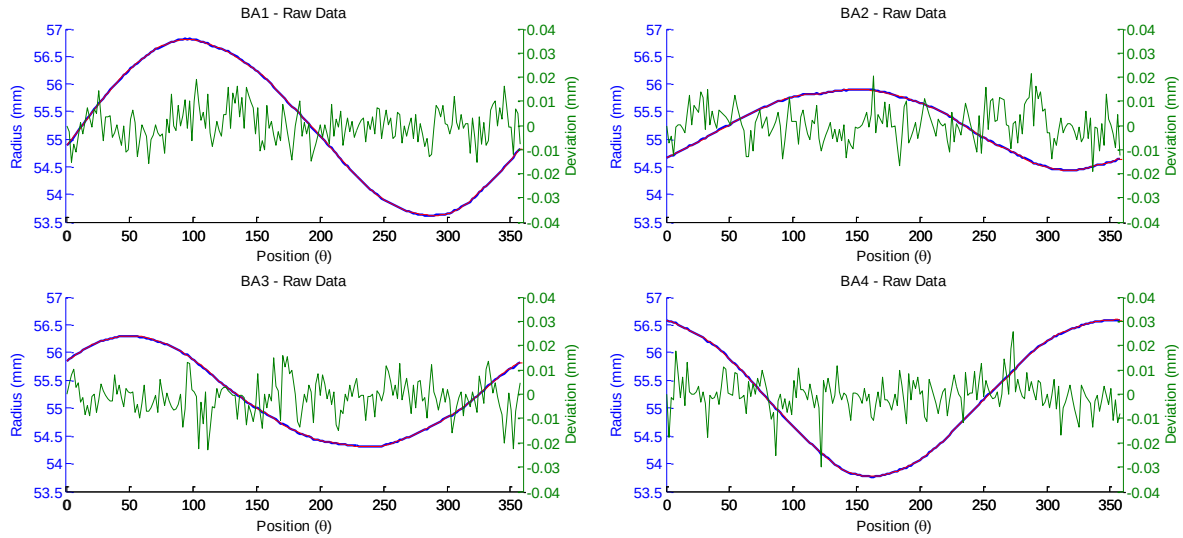

Figure 9-3 Sample B-A: Cubic Spline Output of Data Set B-A (Data Length = 36)

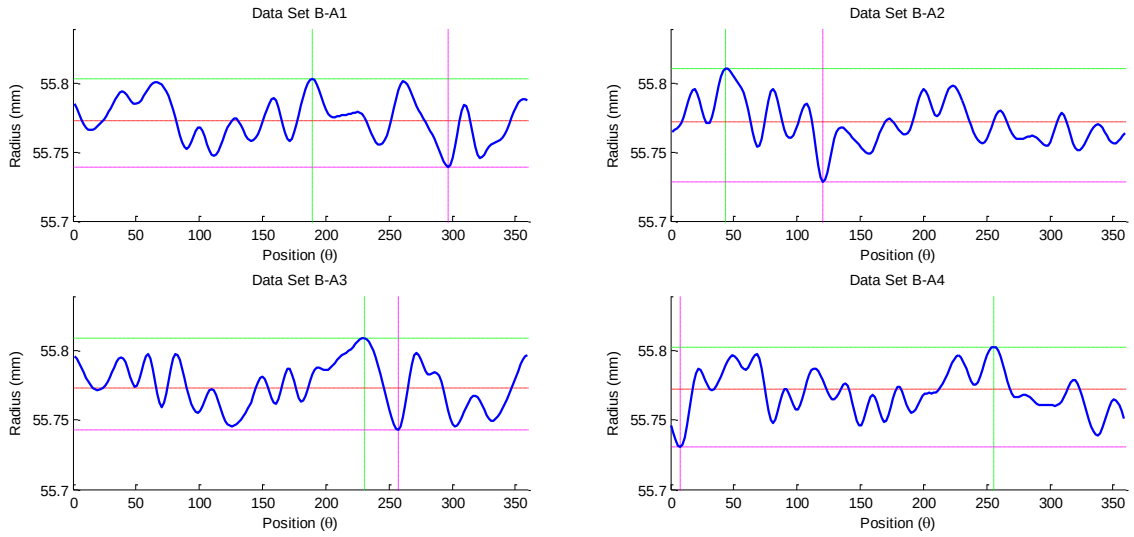

Figure 9-4 Sample B-A: CDA Graphical Result (Data Length = 36, Mask Width = 10)

Table 9-2 Sample B-A: CDA Statistic Result (Data Length = 36, Mask Width = 10)

	B-A1	*B-A2*	*B-A3*	*B-A4*	*Average*
R (mm)	55.7748	55.7694	55.7740	55.7716	55.7725
X Offset (mm)	-0.7797	-0.2278	-0.3881	0.1714	-
Y Offset (mm)	0.1669	0.2863	-0.3147	-0.6751	-
sse	0.1055	0.0979	0.1158	0.0865	0.1014
rs	0.9982	0.9921	0.9953	0.9981	0.9959
adjrs	0.9982	0.992	0.9953	0.998	0.9959
rmse	0.0237	0.0228	0.0248	0.0214	0.0232
cpu time (s)	0.875	0.9219	0.7969	0.8906	0.8711

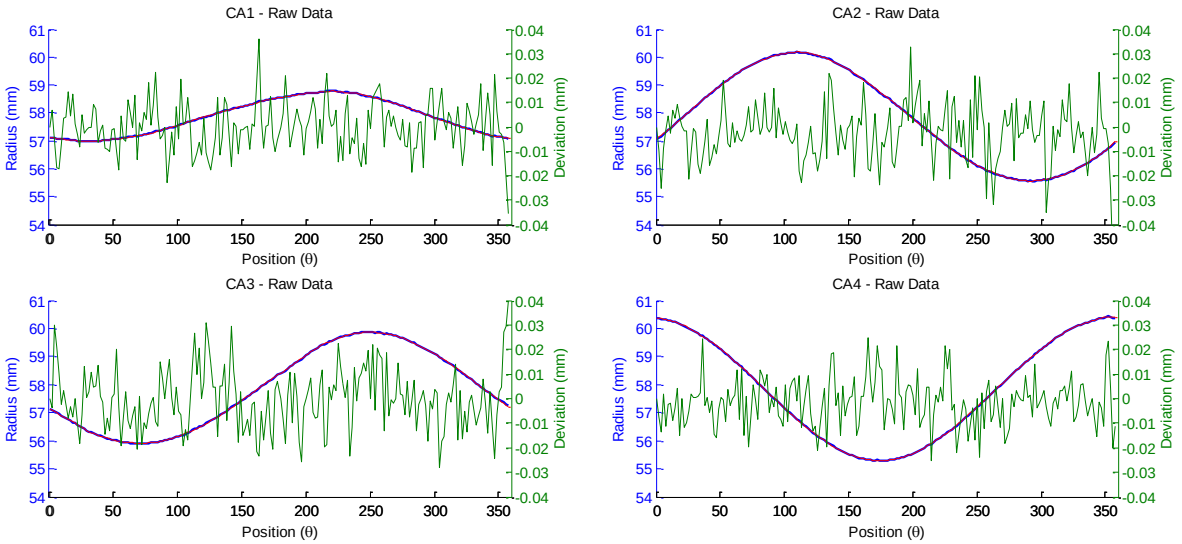

Figure 9-5 Sample C-A: Cubic Spline Output of Data Set B-A (Data Length = 36)

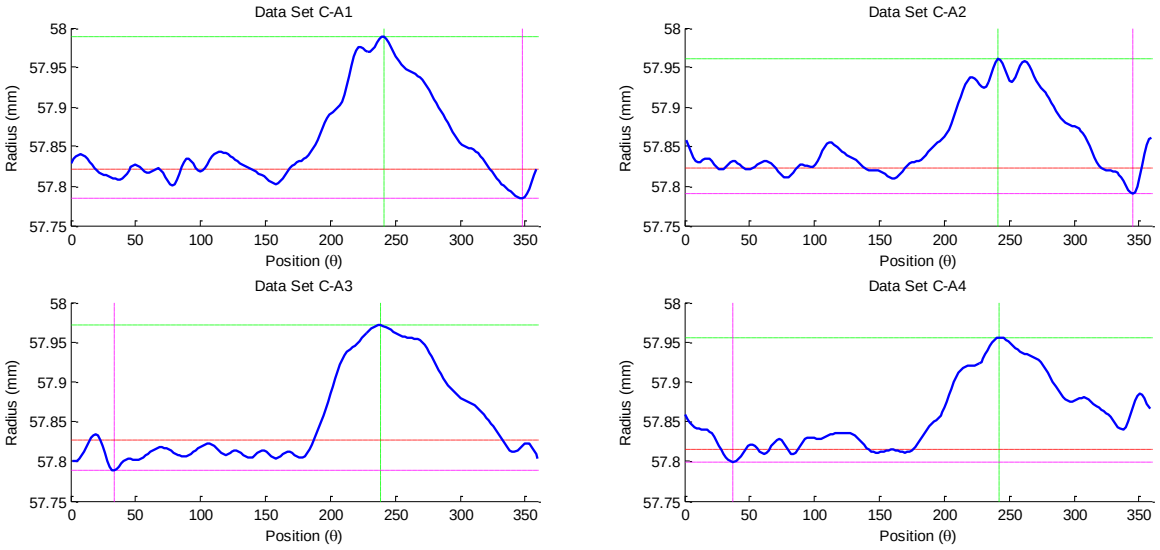

Figure 9-6 Sample C-A: CDA Graphical Result (Data Length = 36, Mask Width = 100)

Table 9-3 Sample C-A: CDA Statistic Result (Data Length = 36, Mask Width = 10)

	C-A1	*C-A2*	*C-A3*	*C-A4*	*Average*
R (mm)	57.8223	57.8282	57.8105	57.8216	57.8207
X Offset (mm)	0.4002	-2.1982	1.7937	0.1725	-
Y Offset (mm)	0.7174	0.7582	0.6229	-2.5216	-
sse	0.0124	0.0111	0.0071	0.0124	0.0108
rs	0.9995	0.9998	0.9999	1.0000	0.9998
adjrs	0.9995	0.9998	0.9999	1.0000	0.9998
rmse	0.0112	0.0106	0.0085	0.0112	0.0104
cpu time (s)	0.8438	0.9375	0.8532	0.9375	0.8930

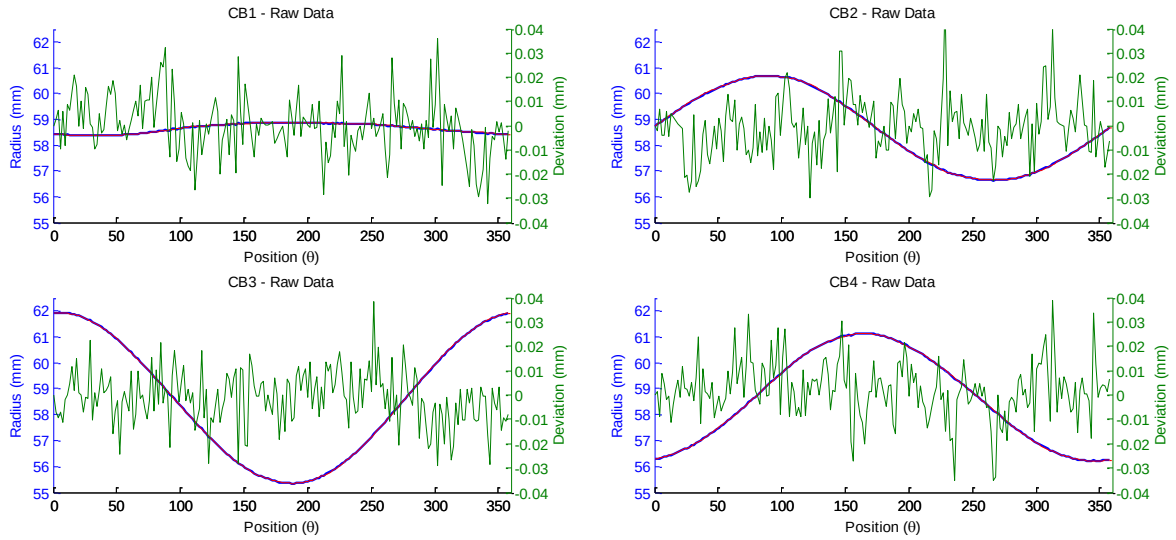

Figure 9-7 Sample C-B: Cubic Spline Output of Data Set B-A (Data Length = 36)

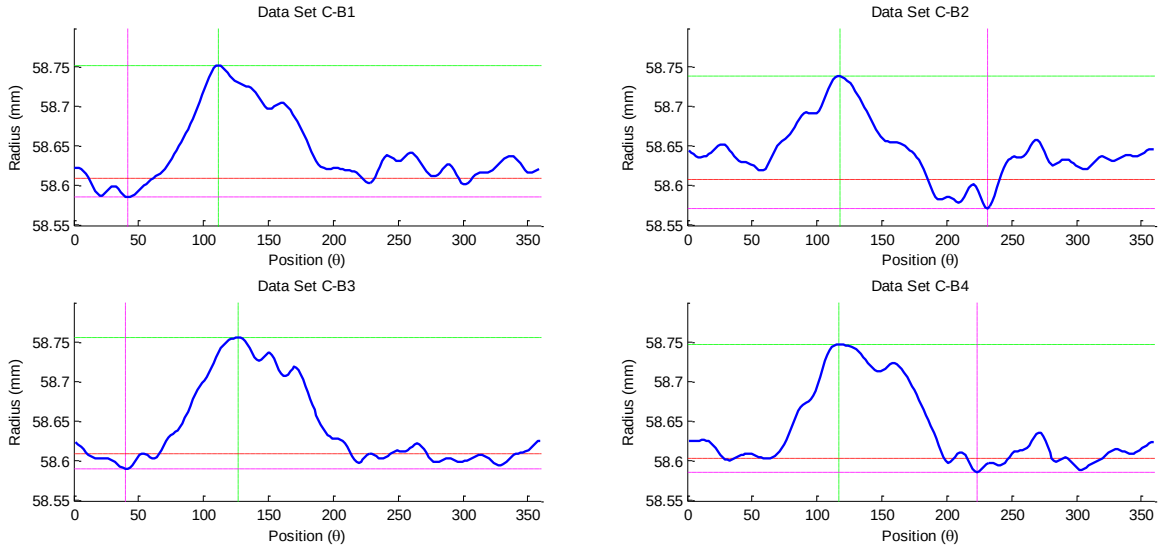

Figure 9-8 Sample C-B: CDA Graphical Result (Data Length = 36, Mask Width = 80)

Table 9-4 C-B: CDA Statistical Result (Data Length = 36, Mask Width = 80)

	C-B1	*C-B2*	*C-B3*	*C-B4*	*Average*
R (mm)	58.6110	58.6137	58.6104	58.6055	58.6102
X Offset (mm)	0.1234	-1.9883	-0.3009	-0.5481	-
Y Offset (mm)	0.2037	-0.1571	-3.2895	2.3347	-
sse	0.1580	0.0228	0.0103	0.0140	0.0513
rs	0.9965	0.9999	1.0000	0.9999	0.9991
adjrs	0.9964	0.9999	1.0000	0.9999	0.9991
rmse	0.0111	0.0133	0.0090	0.0105	0.0110
cpu time (s)	0.8438	1.0000	0.9688	0.9531	0.9414